

ELECTROHYDRODYNAMIC MIXING

by

James Frederick Hoburg

B.S., Drexel University
(1969)

S.M., Massachusetts Institute of Technology
(1971)

E.E., Massachusetts Institute of Technology
(1971)

SUBMITTED IN PARTIAL FULFILLMENT OF THE
REQUIREMENTS FOR THE DEGREE OF
DOCTOR OF PHILOSOPHY

at the

MASSACHUSETTS INSTITUTE OF TECHNOLOGY

June, 1975

Signature of Author
Department of Electrical Engineering & Computer Science, May 9, 1975

Certified by
Thesis Supervisor

Accepted by
Chairman, Departmental Committee on Graduate Students



ELECTROHYDRODYNAMIC MIXING

by

James Frederick Hoburg

Submitted to the Department of Electrical Engineering and Computer Science on May 9, 1975, in partial fulfillment of the requirements for the Degree of Doctor of Philosophy.

ABSTRACT

Theoretical models and experimental configurations are aimed at an understanding of fundamental mechanisms of the coupled interactions inherent in mixing processes resulting from the application of an electric field to liquid systems with components of differing conductivities. Practical operations and mixing quality parameters are described, and the advantages and disadvantages of electrically driven mixing schemes are discussed.

The electroquasistatic form of Maxwell's Equations, with associated boundary conditions, force density, and stress tensor, are employed. Constitutive laws for a binary electrolyte are developed with convection, diffusion, and migration accounted for as ion transport mechanisms. Subject to the applicability of simplifying assumptions, a conductivity is defined and its behavior characterized by a diffusion equation. Electric transfer relations for a charge-free half space are developed. The Navier-Stokes equations, with an electrical force density included, describe a mechanical subsystem. Two characteristic times, the electro-viscous time, $\eta/\epsilon E^2$, and the viscous-inertial diffusion time, $\rho l^2/\eta$, are identified and quantified for familiar fluids. Mechanical transfer relations for a viscous half space are developed.

Surface-coupled stability analyses are performed in two models involving abrupt conductivity changes at the interface between mechanically identical fluids. The effects of a small density difference in a gravity field are retained. Application of a current normal to the unperturbed interface results in temporally growing modes at high wavenumbers, with growth rate characterized by the electro-viscous time. With an electric field applied tangential to the unperturbed interface, no electrical coupling results and all wavenumbers are temporally decaying.

Transfer relations are developed for a layer of exponentially varying conductivity in a tangential electric field in terms of tangential wavenumber, temporal frequency, a time constant ratio, and conductivity gradient. The layer is then bounded on each side with half spaces, and the dispersion relation for bulk fluid motions developed. The system is found to be unstable, with maximum growth rate occurring at a wavelength on the order of the layer thickness. Various eigenmodes are given physical meaning by plotting eigenfunctions on each side of and through the layer region. Maximum growth rate and corresponding wavenumber are determined as functions of model parameters. Replacement of the half-space bounding regions with rigid equipotential walls again results in temporally growing modes, which are identified and characterized.

A numerical integration scheme, appropriate to the transfer relation technique and permitting description of electromechanical continua with smoothly varying equilibrium material properties, is presented and employed in detail to model a region with permittivity a function of normal coordinate. Results are checked against an exact solution for an exponential permittivity distribution. Finite difference equations in correspondence with first order governing differential equations are derived for electromechanical configurations involving varying conductivity layers in equilibrium tangential and normal electric fields.

Experimental results are described, corresponding to application of an electric field tangential to the interface between two miscible fluids of identical mechanical properties, but disparate electrical conductivities. Photographs are presented of slanted propagating fronts at the scale of the interface. Correspondence with the earlier overstability theory, in terms of slant angle, distance between fronts, and propagation velocity, is demonstrated. Photographs corresponding to relatively high values of applied electric field show violent mixing processes of relevance to practical mixing operations. Quantitative descriptions of fluid component distribution as a function of time confirm scaling of the mixing process with the electro-viscous time, except at fields so high that inertia plays a role.

Thesis Supervisor: James R. Melcher
Professor of Electrical
Engineering

. . . Until one is committed there is hesitancy, the chance to draw back, always ineffectiveness. Concerning all acts of initiative (and creation), there is one elementary truth, the ignorance of which kills countless ideas and splendid plans: that the moment one definitely commits oneself, then Providence moves too. All sorts of things occur to help one that would never otherwise have occurred. A whole stream of events issues from the decision, raising in one's favour all manner of unforeseen incidents and meetings and material assistance, which no man could have dreamt would come his way. I have learned a deep respect for one of Goethe's couplets:

Whatever you can do, or dream you can, begin it.

Boldness has genius, power, and magic in it.

--- W. H. Murray

ACKNOWLEDGEMENTS

Through six years of graduate education, Professor James R. Melcher has stimulated, prodded, encouraged, and inspired me. I have deeply respected him as an educator and as a man throughout. His influence on this work is profound.

Professors Louis N. Howard, Kenneth A. Smith, and Alan J. Grodzinsky have been willing and generous contributors of knowledge and stimulation.

Mr. E. Paul Warren has been a constant source of know-how and patient help in the lab.

Mrs. Evelyn Holmes, remaining undaunted by monstrous equations, has typed with the skill and pride of a genuine craftsman.

This work was supported by NSF Grant GK-40021.

TABLE OF CONTENTS

	<u>Page No.</u>
ABSTRACT	2
ACKNOWLEDGEMENTS	5
LIST OF FIGURES	8
CHAPTER I. INTRODUCTION	13
A. Ion Transport Mechanisms	13
B. Electrohydrodynamic Mixing	18
C. Overview	20
Bibliography	24
CHAPTER II. GENERAL MODELS	25
A. Electrical	25
1. Electroquasistatics	25
2. Conduction in a Binary Electrolyte	27
3. Charge Relaxation	31
4. Electric Transfer Relations for a Charge-free Half Space	33
B. Mechanical	35
1. Navier-Stokes Equations	35
2. Characteristic Times	37
3. Mechanical Transfer Relations for a Viscous Half Space	40
Bibliography	47
CHAPTER III. CONDUCTIVITY DISCONTINUITY MODELS	48
A. Introduction	48
B. Equilibrium Normal Electric Field	48
C. Equilibrium Tangential Electric Field	76
Bibliography	81

CHAPTER IV. EXPONENTIAL CONDUCTIVITY DISTRIBUTION IN	<u>Page No.</u>
TANGENTIAL FIELD	82
A. Layer Transfer Relations	82
B. Half-Space Boundaries	92
C. Physical Mechanism	132
D. Rigid, Equipotential Boundaries	138
Bibliography	158
CHAPTER V. NUMERICAL INTEGRATION TECHNIQUE FOR SMOOTHLY	
INHOMOGENEOUS LAYERS	159
A. Varying Permittivity Layer	159
B. Varying Conductivity Layer in Equilibrium Tangential Electric	
Field - Finite Difference Equations	166
C. Varying Conductivity Layer in Equilibrium Normal Electric	
Field - Finite Difference Equations	174
CHAPTER VI. TANGENTIAL FIELD EXPERIMENTS	179
A. Low Field Instability and Correspondence with Theory	179
B. High Field Mixing	186
Bibliography	196
APPENDIX A. SOLUTION OF THE QUARTIC EQUATION (3.38)	197
Bibliography	201
APPENDIX B. MATRIX MANIPULATIONS FOR CHANGING TRANSFER RELATION	
FORMS	202
BIOGRAPHICAL NOTE	205

LIST OF FIGURES

	<u>Page</u> <u>No.</u>
<u>Chapter I</u>	
Figure 1. Taylor's pump	14
<u>Chapter II</u>	
Figure 1. Boundary Geometry	26
Figure 2. Electrical Half Spaces	34
Figure 3. T versus λ	38
Figure 4. τ versus E	39
Figure 5. Mechanical Half Spaces	41
<u>Chapter III</u>	
Figure 1. Normal Field Geometry	49
Figure 2. $[\tau_v/\tau_E]_s$ versus e ($-2 \leq e \leq 2$)	61
Figure 3. $[\tau_v/\tau_E]_s$ versus e ($1 < -e < 10^8$)	62
Figure 4. $[\tau_v/\tau_E]_s$ versus e ($1 < e < 10^8$)	63
Figure 5. $[\tau_v/\tau_g]^3 e$ versus $\frac{\tau_E/\tau_v}{[\tau_E/\tau_g]^3}$ ($0.5 \leq \frac{\tau_E/\tau_v}{[\tau_E/\tau_g]^3} \leq 10.0$)	65
Figure 6. $\left[\frac{\tau_E}{\tau_g}\right]^3 e$ versus $\frac{\tau_E/\tau_v}{[\tau_E/\tau_g]^3}$ ($10^{-7} < \frac{\tau_E/\tau_v}{[\tau_E/\tau_g]^3} < 10^9$)	66
Figure 7. s versus k, $[\rho]/\rho = 0$ ($10^{-1} \leq k \leq 10^8$)	70
Figure 8. s versus k, $[\rho]/\rho = 10^{-7}$ ($10^{-1} \leq k \leq 10^8$)	71
Figure 9. s versus k, $[\rho]/\rho = 10^{-7}$ ($1.36 \leq k \leq 1.37$)	71
Figure 10. s versus k, $[\rho]/\rho = 10^{-6}$ ($1 \leq k \leq 10^8$)	72
Figure 11. s versus k, $[\rho]/\rho = 10^{-6}$ ($13.6 \leq k \leq 13.7$)	72
Figure 12. s versus k, $[\rho]/\rho = 10^{-5}$ ($1 \leq k \leq 10^8$)	73
Figure 13. s versus k, $[\rho]/\rho = 10^{-5}$ ($100 \leq k \leq 200$)	73

Chapter III continued

Page No.

Figure 14.	s versus k , $\frac{\rho}{\rho} = 10^{-4}$ ($10 \leq k \leq 10^8$)	74
Figure 15.	s versus k , $\frac{\rho}{\rho} = 10^{-4}$ ($1000 \leq k \leq 2000$)	74
Figure 16.	s versus k , $\frac{\rho}{\rho} = 10^{-3}$ ($10 \leq k \leq 10^8$)	75
Figure 17.	s versus k , $\frac{\rho}{\rho} = 10^{-3}$ ($10^4 \leq k \leq 2 \times 10^4$)	75
Figure 18.	Tangential Field Geometry	76

Chapter IV

Figure 1.	Layer of varying conductivity in tangential field	82
Figure 2.	$\sigma_0(x)$ versus x for $R = e$	93
Figure 3.	Exponential Conductivity Layer Bounded by Half-Spaces	94
Figure 4.	The Function D in the complex s -plane	103
Figure 5.	$\hat{\phi}$ versus x/Δ , first eigenfunction, $\underline{k}=1$, $T/\tau=1$, $R=e$	107
Figure 6.	\hat{J}_x versus x/Δ , first eigenfunction, $\underline{k}=1$, $T/\tau=1$, $R=e$	108
Figure 7.	\hat{v}_x versus x/Δ , first eigenfunction, $\underline{k}=1$, $T/\tau=1$, $R=e$	109
Figure 8.	\hat{v}_z versus x/Δ , first eigenfunction, $\underline{k}=1$, $T/\tau=1$, $R=e$	110
Figure 9.	\hat{S}_x versus x/Δ , first eigenfunction, $\underline{k}=1$, $T/\tau=1$, $R=e$	111
Figure 10.	\hat{S}_z versus x/Δ , first eigenfunction, $\underline{k}=1$, $T/\tau=1$, $R=e$	112
Figure 11.	$\hat{\phi}$ versus x/Δ , second eigenfunction, $\underline{k}=1$, $T/\tau=1$, $R=e$	113
Figure 12.	\hat{v}_x versus x/Δ , second eigenfunction, $\underline{k}=1$, $T/\tau=1$, $R=e$	114
Figure 13.	$\hat{\phi}$ versus x/Δ , third eigenfunction, $\underline{k}=1$, $T/\tau=1$, $R=e$	115
Figure 14.	\hat{v}_x versus x/Δ , third eigenfunction, $\underline{k}=1$, $T/\tau=1$, $R=e$	116
Figure 15.	$\hat{\phi}$ versus x/Δ , first eigenfunction, $\underline{k}=0.1$, $T/\tau=1$, $R=e$	117
Figure 16.	\hat{v}_x versus x/Δ , first eigenfunction, $\underline{k}=0.1$, $T/\tau=1$, $R=e$	118
Figure 17.	$\hat{\phi}$ versus x/Δ , first eigenfunction, $\underline{k}=10$, $T/\tau=1$, $R=e$	119
Figure 18.	\hat{v}_x versus x/Δ , first eigenfunction, $\underline{k}=10$, $T/\tau=1$, $R=e$	120

Chapter 1V continued

Page No.

Figure 19.	Re \underline{s} versus \underline{k} , $T/\tau = 1$, $R = e$	122
Figure 20.	Im \underline{s} versus \underline{k} , $T/\tau = 1$, $R = e$	123
Figure 21.	Re \underline{s} versus \underline{k} , $T/\tau = 10^{-2}$, $R = e$	125
Figure 22.	Im \underline{s} versus \underline{k} , $T/\tau = 10^{-2}$, $R = e$	126
Figure 23.	Re \underline{s} versus \underline{k} , $T/\tau = 10^2$, $R = e$	127
Figure 24.	Im \underline{s} versus \underline{k} , $T/\tau = 10^2$, $R = e$	128
Figure 25.	\underline{k}^* versus T/τ	129
Figure 26.	Re \underline{s}^* and Im \underline{s}^* versus T/τ	130
Figure 27.	$\hat{\underline{v}}_x$ versus x/Δ , first eigenfunction, $\underline{k}=\underline{k}^*=1.6412$, $T/\tau = 10^{-4}$, $R = 25.9$	133
Figure 28.	$\hat{\underline{v}}_z$ versus x/Δ , first eigenfunction, $\underline{k} = \underline{k}^* = 1.6412$, $T/\tau = 10^{-4}$, $R = 25.9$	134
Figure 29.	Velocity streamlines, $\underline{k} = \underline{k}^* = 1.6412$, $T/\tau = 10^{-4}$, $R = 25.9$	135
Figure 30.	Physical Mechanism	136
Figure 31.	The function D' in the complex \underline{s} -plane	144
Figure 32.	The function D'' in the complex \underline{s} -plane	145
Figure 33.	$\hat{\underline{v}}_x$ versus x/Δ , first eigenfunction, $\underline{k}=10^{-3}$, $T/\tau=1$, $R=e$	147
Figure 34.	$\hat{\underline{v}}_x$ versus x/Δ , first eigenfunction, $\underline{k}=1$, $T/\tau=1$, $R=e$	148
Figure 35.	$\hat{\underline{v}}_x$ versus x/Δ , first eigenfunction, $\underline{k} = 10$, $T/\tau=1$, $R=e$	149
Figure 36.	$\hat{\underline{v}}_x$ versus x/Δ , second eigenfunction, $\underline{k}=10$, $T/\tau=1$, $R=e$	150
Figure 37.	Re $\hat{\underline{v}}_x$ vs. x/Δ , first & second eigenfunctions, $\underline{k}=1$, $T/\tau = 1$, $R = e$	151
Figure 38.	Im $\hat{\underline{v}}_x$ versus x/Δ , first and second eigenfunctions, $\underline{k} = 1$, $T/\tau = 1$, $R = e$	152

Chapter IV continued

	<u>Page No.</u>
Figure 39. $\text{Re } \hat{\phi}$ versus x/Δ , first and second eigenfunctions, $\underline{k} = 1, T/\tau = 1, R = e$	153
Figure 40. $\text{Im } \hat{\phi}$ versus x/Δ , first and second eigenfunctions, $\underline{k} = 1, T/\tau = 1, R = e$	153
Figure 41. $ \hat{v}_x $ versus x/Δ , first and second decaying eigenfunctions, $\underline{k} = 1, T/\tau = 1, R = e$	154
Figure 42. $ \hat{\phi} $ versus x/Δ , first and second decaying eigenfunctions, $\underline{k} = 1, T/\tau = 1, R = e$	155
Figure 43. $\text{Re } \underline{s}$ versus \underline{k} , $T/\tau = 1, R = e$	157

Chapter V.

Figure 1. Planar region with permittivity a function of transverse coordinate	159
Figure 2. Variables at boundaries of an incremental layer	163
Figure 3. Elements of the matrix L as functions of x/Δ	167
Figure 4. Elements of the matrix T as functions of \underline{k}	168
Figure 5. Layer of varying conductivity in normal field	174

Chapter VI.

Figure 1. Experimental flow cell and optical configuration	180
Figure 2. Photographs of experimental cell fluid component dis- tributions	182
Figure 3. Photographs of experimental cell fluid component dis- tributions	183
Figure 4. Photographs of experimental cell fluid component dis- tributions at relatively high electric fields	187

Figure 5. Relative light intensity through experimental cell versus time for various values of electric field	189
Figure 6. Relative light intensity through experimental cell versus cell position, $E = 0.606 \times 10^5$ V/m	191
Figure 7. Relative light intensity through experimental cell versus cell position, $E = 1.21 \times 10^5$ V/m	192
Figure 8. Relative light intensity through experimental cell versus cell position, $E = 1.82 \times 10^5$ V/m	192
Figure 9. Relative light intensity through experimental cell versus cell position, $E = 2.42 \times 10^5$ V/m	193
Figure 10. Relative light intensity through experimental cell versus cell position, $E = 3.03 \times 10^5$ V/m	193
Figure 11. Relative light intensity through experimental cell versus cell position, $E = 4.24 \times 10^5$ V/m	194
Figure 12. Relative light intensity through experimental cell versus cell position, $E = 6.06 \times 10^5$ V/m	194

CHAPTER I. INTRODUCTION

A. Ion Transport Mechanisms

Ion transport mechanisms in liquids consist of migration, diffusion, and convection. ⁽¹⁾ Migration, described in terms of an ion mobility, refers to the motion of charged particles relative to a background of neutral molecules in the face of an electric field. Collisions with the neutral molecules result in a "viscous" retarding force. The diffusion mechanism describes an ion flux independent of charge, proportional to the local concentration gradient, and away from regions of high concentration. Finally, convection refers to motions of the neutral fluid molecules that result in a redistribution of ions contained therein.

Often, the convection mechanism is dominant in liquids. For example, the relative effects of convection and molecular diffusion are described by the Peclet number, $U\ell/\kappa_D$, where U is the fluid velocity, ℓ is a characteristic length, and κ_D is the diffusion coefficient. ⁽²⁾ Taking as typical M.K.S. values $U = 10^{-2}$ m/sec and $\kappa_D = 10^{-9}$ m²/sec, we see that the diffusion mechanism can compete with convection only for length scales on the order of 1μ or less.

Similarly, the ratio of diffusion to migration terms in the ion transport equations is, through the Einstein relation $RT/F\ell E$, where at room temperature, $RT/F = 25.6$ millivolts, E is an applied field and ℓ is a characteristic length. Thus, the dimensionless number comparing convection to migration is $URT/\kappa_D FE$. Taking the same values for U and κ_D as above, we see that an electric field on the order of 10^5 V/m is needed to make migration competitive with convection. In a typical electrolyte, this value of electric field would be accompanied by a high current density

and associated Ohmic heating.

It is, however, part of our purpose here to point out that the convection mechanism is not independent of applied electric field; i.e., that fluid motions, ion concentrations and electric field distribution are intimately related to one another through the two-way electrohydrodynamic coupling of electrical and mechanical subsystems. Thus, at an electric field of 10^5 V/m, fluid motion and ion convection driven by electric forces on a bulk charge distribution are of prime importance.

To be more specific, we picture the coupling mechanisms between the above-cited ion transport processes as follows. First, any local difference in number densities of positive and negative ions results in a net free charge density and, subject to an applied electric field, a net force density on the fluid bulk. Fluid motions in response to the electric force are retarded by viscosity. As a simple example, consider "Taylor's pump" (3) as shown in Fig. 1.

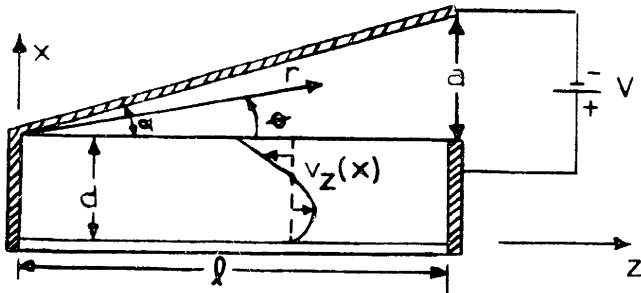


Figure 1. Taylor's pump

A conducting fluid of viscosity η and depth d is contained by a box of length l , with insulating bottom and sides and conducting electrode ends. A slanted electrode extends over the free surface of the

fluid, at angle α to the surface, attaining height a above the fluid at the right end. The left end and slanted electrode are grounded, while the right electrode is at potential V . We wish to describe the motion of the fluid, far enough from the ends of the box so that the flow may be considered one-dimensional. That is, we assume a velocity profile of the form

$$\bar{v} = \bar{i}_z v_z(x) \quad . \quad (1.1)$$

The velocity distribution, driven by a pressure which is a function of z alone, which yields zero net flow over any cross section, takes the form:

$$v_z(x) = A \left[3 \left(\frac{x}{d} \right)^2 - 2 \left(\frac{x}{d} \right) \right] \quad . \quad (1.2)$$

The potential distribution within the conducting fluid is simply

$$\phi = V(z/\ell) \quad . \quad (1.3)$$

The potential distribution in the triangular region, in terms of the polar coordinates shown in Fig. 1, is

$$\phi = - \frac{V}{\ell} r \frac{\sin(\theta - \alpha)}{\sin \alpha} \quad . \quad (1.4)$$

The tangential electric stress on the fluid surface, then, is:

$$T_{zx} \Big|_{x=d} = \epsilon_0 E_x E_z \Big|_{x=d} = - \frac{V^2}{a\ell} \quad . \quad (1.5)$$

Balancing tangential electric and viscous stresses at the fluid surface, we evaluate the constant A in Eq. (2) to finally specify the fluid

velocity distribution:

$$v_z(x) = -\frac{\epsilon_0 V^2 d}{2\eta \lambda a} \left[\frac{3}{2} \left(\frac{x}{d}\right)^2 - \left(\frac{x}{d}\right) \right] . \quad (1.6)$$

If we define a characteristic electric field in the free space region by

$$E^2 \equiv \frac{V^2}{\lambda a} \quad (1.7)$$

and a length characterizing fluid motions by $d/2$, we see that the velocity distribution takes the form:

$$v_z(x) = -\frac{d/2}{\tau} \left[\frac{3}{2} \left(\frac{x}{d}\right) - \left(\frac{x}{d}\right) \right] \quad (1.8)$$

where the characteristic time τ is defined by:

$$\tau \equiv \frac{\eta}{\epsilon_0 E^2} . \quad (1.9)$$

In more general situations, involving for example bulk-coupled rather than surface-coupled interactions, we shall find that we should replace ϵ_0 by ϵ in the definition of τ . This electric-viscous time will assume fundamental importance throughout. It is a characteristic time associated with the fluid convection resulting from an electric force density. Commonly, the electric pressure ϵE^2 is extremely small; hence, of limited usefulness in causing bulk large-scale motions. In many fluids, however, the retarding viscous force is also very small. Even at the modest electric field $E = 10^3$ V/m in water ($\eta = 10^{-3}$ nt-sec/m², $\epsilon = 81\epsilon_0$), we have $\tau \sim 1$ sec. At the high electric field $E = 10^5$ V/m mentioned above as necessary for migration to compete with convection at characteristic

velocity $U = 10^{-2}$ m/sec, we have $\tau \sim 10^{-4}$ sec. Thus, it is only on a length scale of $U\tau = 1\mu$ that the electrically driven convection is characterized by the assumed velocity.

The return link in the coupling of ion transport mechanisms involves the effect of any given ion concentration distribution on the electric field structure. Thus, for example, if the fluid may be characterized by a local conductivity, and fluid convection due to an electric force density results in a conductivity redistribution, then the electric field and force density are, in return, restructured. This two-way coupling between electrical and mechanical subsystems is characteristic of problems in electrohydrodynamics. It allows at least the possibility of instability, i.e., growth in time of any small perturbation from a given equilibrium situation.

As noted above, in reference to the Peclet number, there always exists a small scale on which diffusion effects are dominant. The diffusion mechanism results in a smoothing of ion concentration distribution, hence a lessening of the electrically driven convection effects on the small scale. Typically, in an electrohydrodynamic stability analysis, equilibrium inhomogeneities are limited in sharpness by the diffusion process. The large scale mixing which results from an electrically driven instability may, in the nonlinear stage, yield a new equilibrium configuration, again limited in property gradients by diffusion. Finally, diffusion enters into the instability dynamics on a scale where the diffusion time is comparable to a convection time.

B. Electrohydrodynamic Mixing

The phenomenon of mixing finds practical application in a host of operations designed to reduce bulk nonuniformities in composition, properties, or temperature.⁽⁴⁾ We are concerned here, in particular, with situations involving liquid components. A very common and important application is the bringing together of different molecular species to obtain a chemical reaction.⁽⁵⁾ Mass and heat transfer operations are often enhanced by mixing processes. Bulk flow, eddy diffusion, and molecular diffusion are all mechanisms whereby transfer processes are accomplished.

Two characteristics, scale and intensity, are used to describe the quality of a mixture of two fluids.⁽⁶⁾ Scale refers to the average distance between centers of maximum difference in properties. In turbulent mixing, scale is determined by eddy size and is reduced by break-up of eddies. In laminar mixing, the movement and stretching of layers and strands of components results in scale reduction. Intensity refers to the magnitude of variation in properties within a mixture. Intensity changes as a result of mixing only when scale is reduced to the resolution capability of the diagnostic tool, or when molecular diffusion effects are appreciable.

Equipment used in mixing operations is usually purely mechanical, with a stirring device providing the required external force. Our interest here is in the feasibility of use of an electrical force density to accomplish mixing. We emphasize here that an electrohydrodynamic mixing process inherently involves more than the simple addition of a known force density as a driving term in the fluid equations of motion. Electrical

and mechanical subsystems are coupled "in both directions". That is, the electric field and force density distributions are affected by the fluid motions, and the fluid motions are driven by the electric force density. A self-consistent solution to a set of coupled electrical and mechanical equations must be determined before either the fluid velocity field or electric field is known.

The attractiveness of an electrically driven mixing scheme is readily apparent. Accumulation of free charge in an Ohmic conductor occurs in regions of conductivity variation, in direct proportion to the magnitude of conductivity gradient. Thus, in a situation where mixing of various fluid components is to be accomplished by the application of an electric field, the charge density, and hence the force density, occur locally at places within the mixture where they are most needed. As will be emphasized by the bulk-coupled model of Chapter IV, fluid motions driven by a rotational force density occur on a scale determined by the conductivity gradient scale. By contrast, a mechanically driven stirring device is most efficient in scale reduction of large-scale fluid property variations and least effective with respect to fine-scale inhomogeneity. Thus, an attractive mixing scale might involve the use of mechanical stirring for large-scale mixing, with electrically driven mixing to accomplish scale reduction at the 10^{-2} to 10^{-4} meter wavelength range. Finally, at the finest scale, molecular diffusion times become short enough to compete with the electric-viscous time, $\eta/\epsilon E^2$, discussed in Section A.

Ohmic losses associated with fluid heating in proportion to the square of local current density are responsible for an inherent inefficiency in an electrically driven mixing scheme. Thus, operations employing

the electrical force density as a drive for fluid motions are most attractive when the components to be mixed are poor conductors (for example, oils and other organic liquids). Even in instances of relatively high Ohmic losses, an electrically driven operation may well provide the most efficient means of dealing with small-scale inhomogeneities.

The possibility of use of an electric force density in mixing processes has been recognized in previous literature. For example, in the course of an investigation seeking to employ an electric field to separate xylene molecules on the basis of their dipole moments, Cropper and Seelig⁽⁷⁾ noted turbulent mixing upon application of a dc field normal to the interface between hydrocarbon and solvent phases. The hydrocarbon phase consisted of 10 volume percent each of o- and p-xylene in iso-octane and the solvent was dimethylformamide. (Dimethylformamide is much more conducting than iso-octane.) They reported mixing varying "from spectacular to poor, for reasons not entirely evident".

Holland⁽⁸⁾ continued the investigations of Cropper and Seelig, using a pulsating field in mixing cells of various shapes and sizes. He used a Schlieren optical system to observe fluid motions. Measuring the time required for "complete mixing", he empirically fit an exponential curve to the "field force" time dependence. He also determined the power requirements for the electrically driven mixing technique and found them very near those for a laboratory type baffled blade mixer.

C. Overview

Our development in the chapters to follow is aimed at an understanding at the fundamental level of the coupled interactions inherent in

mixing processes resulting from the application of an electric field to liquid systems with components of differing conductivities. In the process, several interwoven themes are pursued.

After setting down models for electrical and mechanical subsystems in Chapter II, we proceed to develop theoretical descriptions of simple electrohydrodynamic configurations. In Chapter III, we make use of electrical and mechanical half-space transfer relations to perform surface-coupled stability analyses in two models involving abrupt conductivity changes at the interface between mechanically identical fluids. The application of a current density normal to the unperturbed interface results in temporally growing modes at high wavenumbers, with growth rate characterized by the electro-viscous time, $\eta/\epsilon E^2$, first encountered in the "Taylor's pump" example of Section I.A.

With an electric field applied tangential to the unperturbed interface, no electrical coupling results and all wavenumbers are temporally decaying. This fact presents the opportunity for emphasizing the relevance of structure in configurations involving interfaces, where it is natural to use models with abrupt discontinuities in material property parameters. In Chapter IV, transfer relations are developed for a layer of exponentially varying equilibrium conductivity in a tangential electric field. The layer is then bounded on each side with electrical and mechanical half-spaces, and the dispersion relation for bulk fluid motions developed. Thus, the region of varying conductivity between two fluids of differing conductivities, experiencing an electric field tangential to the interface region, is modeled. The system is found to be unstable,

with maximum growth rate occurring at a wavelength on the order of the layer thickness. The maximum growth rate and corresponding wavenumber are determined as functions of model parameters. A viscous-dominated regime, wherein growth occurs in direct proportion to $\epsilon E^2/\eta$, again emphasizes the importance of the electro-viscous time. Simultaneously, the concept of bulk-coupled instability at the scale of interface structure is developed in detail.

The analysis of Chapter IV hinges on the discovery of a conductivity distribution leading to constant coefficients in the governing differential equations. A more general description, with equilibrium material properties arbitrary smoothly varying functions of position, requires the use of a numerical integration technique. In Chapter V, such a technique, appropriate to our transfer relation description, is presented. Thus, means are described for generalization of the concepts pursued in the context of the Chapter IV model.

Chapter VI presents experimental results corresponding to application of an electric field tangential to the interface between two miscible fluids of identical mechanical properties but disparate electrical conductivities. Photographs of slanted, propagating fronts at the scale of the interface, and correspondence in several respects with the overstability theory of Chapter IV, confirm its physical realization.

Relatively high values of electric field lead to violent mixing processes of relevance to practical mixing operations. The complex nature of the phenomena observed here emphasizes both strengths and weaknesses inherent in the models of earlier chapters. Our theoretical descriptions take the form of stability analyses, and involve linearization

of the governing equations, i.e., assumption of small perturbations from an equilibrium. The processes experimentally observed at high field values are grossly nonlinear in nature. However, the importance of the electro-viscous time carries through even here, with a demonstration of scaling in time with $\eta/\epsilon E^2$ of fluid component distributions. Thus, a concept encountered in the context of linear theories is found to have validity in highly nonlinear situations.

More generally, our simple models have as objectives not only an understanding of experimental configurations of deliberately simple geometry. In addition, they point to fundamental mechanisms inherent to all processes involving the same basic ingredients. It is with an understanding of such mechanisms that we can make meaningful observations and predictions with respect to complex electrohydrodynamic mixing phenomena.

CHAPTER I BIBLIOGRAPHY

1. MacInnes, Duncan A., The Principles of Electrochemistry, New York: Dover, 1961.
2. Levich, Veniamin G., Physicochemical Hydrodynamics, New Jersey: Prentice-Hall, 1962, Chapter 2.
3. Melcher, James R., "Electric Fields and Moving Media", IEEE Trans. on Education, E-17, No. 2, May, 1974, pp. 100-110.
4. Uhl, Vincent W. and Gray, Joseph B., Mixing, Theory and Practice, Vol. I, New York: Academic Press, 1966, Chapter 1.
5. Ibid., Chapter 2.
6. Danckwerts, P.V., "The Definition and Measurement of Some Characteristics of Mixtures", Applied Scientific Research, A3, 1952, pp. 279-296.
7. Cropper, W. P., and Seelig, H. S., "Mixing with an Electrostatic Field", Industrial and Engineering Chemistry Fundamentals, 1, #1, February, 1962, pp. 48-52.
8. Holland, Bruce O., "Dielectrophoretic Process for Liquid-Liquid Mixing", Industrial and Engineering Chemistry Fundamentals, 5, #2, May, 1966, pp. 204-207.

CHAPTER II - GENERAL MODELS

A. Electrical

1. Electroquasistatics

We shall be concerned, throughout, with phenomena in which electric energy storage dominates magnetic energy storage, and characteristic lengths are much shorter than an electromagnetic wavelength. Thus, Maxwell's equations, governing electric field \bar{E} , current density \bar{J} , and free charge density ρ_f , for a linear isotropic material with permittivity ϵ , take their electro-quasi-static forms:⁽¹⁾

$$\text{Faraday's Law: } \nabla \times \bar{E} = 0 \quad (2.1)$$

$$\text{Gauss' Law: } \nabla \cdot \epsilon \bar{E} = \rho_f \quad (2.2)$$

$$\text{Conservation of Charge: } \nabla \cdot \bar{J} + \frac{\partial \rho_f}{\partial t} = 0 \quad (2.3)$$

Equation (2.1) is integrated by the introduction of a scalar potential ϕ :

$$\bar{E} = - \nabla \phi \quad . \quad (2.4)$$

In situations where ϵ does not vary with spatial position, Eqs. (2.2) and (2.4) may be combined to yield Poisson's equation:

$$\nabla^2 \phi = - \rho_f / \epsilon \quad . \quad (2.5)$$

The force density \bar{F} on a distribution of free charge density ρ_f experiencing electric field \bar{E} in an electroquasistatic system is:

$$\bar{F} = \rho_f \bar{E} \quad . \quad (2.6)$$

For an incompressible linear dielectric of constant permittivity, \bar{F} is written in terms of the Maxwell stress tensor⁽²⁾ (in index notation):⁽³⁾

$$F_i = \frac{\partial T_{ij}}{\partial x_j} \quad (2.7)$$

where

$$T_{ij} = \epsilon E_i E_j - \frac{\epsilon}{2} \delta_{ij} E_k E_k \quad (2.8)$$

and δ_{ij} is the Kronecker delta:

$$\delta_{ij} = \begin{cases} 1, & i=j \\ 0, & i \neq j \end{cases} \quad (2.9)$$

(The Einstein summation convention is employed.)

Boundary conditions, corresponding to Eqs. (2.1), (2.2) and (2.3) at a surface between regions (a) and (b), defined by normal vector \bar{n} as shown in Fig. 1 are, respectively:

$$\bar{n} \times \llbracket \mathbf{E} \rrbracket = 0 \quad (2.10)$$

$$\bar{n} \cdot \llbracket \epsilon \mathbf{E} \rrbracket = \sigma_{sf} \quad (2.11)$$

$$\bar{n} \cdot \llbracket \mathbf{J} \rrbracket + \frac{\partial \sigma_{sf}}{\partial t} = 0 \quad (2.12)$$

where

$$\llbracket \mathbf{A} \rrbracket \equiv A_a - A_b \quad (2.13)$$

and σ_{sf} is the free surface charge density. [Equation (2.12) does not account for a surface current density.]

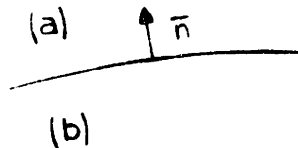


Figure 1
Boundary Geometry

2. Conduction in a Binary Electrolyte

In this section we describe the diffusion and migration of two dilute species of ions, positive and negative, distributed throughout the bulk of a fluid. Conservation of particles, for the positive and negative species respectively, is expressed by:

$$\frac{\partial n_+}{\partial t} + \nabla \cdot n_+ \bar{v} + \nabla \cdot \bar{\Gamma}'_+ = 0 \quad (2.14)$$

$$\frac{\partial n_-}{\partial t} + \nabla \cdot n_- \bar{v} + \nabla \cdot \bar{\Gamma}'_- = 0 \quad (2.15)$$

where n_+ and n_- are particle densities (number per unit volume), \bar{v} is the local fluid velocity, and $\bar{\Gamma}'_+$ and $\bar{\Gamma}'_-$ are particle current densities (number per unit area per unit time) as measured with respect to the macroscopic fluid continuum. In accounting for diffusion and migration as ion transport mechanisms in the fluid frame, we write the local particle current densities:

$$\bar{\Gamma}'_+ = -K_+ \nabla n_+ + n_+ b_+ \bar{E} \quad (2.16)$$

$$\bar{\Gamma}'_- = -K_- \nabla n_- - n_- b_- \bar{E} \quad (2.17)$$

where K_+ and K_- are diffusion coefficients and b_+ and b_- are particle mobilities. We make use of the Einstein relation between diffusion coefficients and particle mobilities:⁽⁴⁾

$$z_{\pm} b_{\pm} = K_{\pm} F/RT \quad (2.18)$$

where z_+ and z_- are charges per ion, F is the Faraday (96,500 coulombs), R is the gas constant (8.3151 joules/^oK) and T is the absolute temperature

in degrees Kelvin. At room temperature,

$$\frac{RT}{F} = 25.6 \text{ millivolts} \quad . \quad (2.19)$$

For incompressible fluid motions,

$$\nabla \cdot \bar{v} = 0 \quad (2.20)$$

(See Section II.B.1.) Thus, combining (2.14) - (2.17) and (2.20):

$$\frac{Dn_+}{Dt} = \nabla \cdot K_+ \nabla n_+ - \nabla \cdot n_+ b_+ \bar{E} \quad (2.21)$$

$$\frac{Dn_-}{Dt} = \nabla \cdot K_- \nabla n_- + \nabla \cdot n_- b_- \bar{E} \quad (2.22)$$

where we have used the convective derivative operator:

$$\frac{D}{Dt} \equiv \frac{\partial}{\partial t} + \bar{v} \cdot \nabla \quad . \quad (2.23)$$

Provided the ion concentrations are small, the diffusion coefficients and mobilities may be considered constants in space and time. Multiplying through Eqs. (2.21) and (2.22) by $z_+ e$ and $z_- e$ respectively, where e is the electronic charge (1.6×10^{-19}), we obtain statements of charge conservation for the two species:

$$\frac{D\rho_+}{Dt} = K_+ \nabla^2 \rho_+ - b_+ \nabla \cdot \rho_+ \bar{E} \quad (2.24)$$

$$\frac{D\rho_-}{Dt} = K_- \nabla^2 \rho_- + b_- \nabla \cdot \rho_- \bar{E} \quad (2.25)$$

where

$$\rho_+ \equiv z_+ e n_+ \quad (2.26)$$

$$\rho_- \equiv z_- e n_- \quad (2.27)$$

Often in liquids, particularly in electrolytes, the difference between

positive and negative charge densities is small relative to the individual charge densities. In such a case,

$$\rho_+ \cong \rho_e + \rho'_+ , \quad \text{where} \quad \rho'_+ \ll \rho_e \quad (2.28)$$

and

$$\rho_- \cong \rho_e + \rho'_- , \quad \text{where} \quad \rho'_- \ll \rho_e . \quad (2.29)$$

The net free charge density, then, is

$$\rho_f = \rho_+ - \rho_- = \rho'_+ - \rho'_- . \quad (2.30)$$

We now combine Eqs. (2.24), (2.25) and (2.30) by multiplying (24) and (25) by b_- and b_+ , respectively, and adding

$$\frac{D}{Dt} (b_- \rho_+ + b_+ \rho_-) = K_+ b_- \nabla^2 \rho_+ + K_- b_+ \nabla^2 \rho_- - b_+ b_- \nabla^2 \rho_f \bar{E} \quad (2.31)$$

or, approximately, ignoring ρ'_+ and ρ'_- in Eqs. (28) and (29) respectively:

$$(b_- + b_+) \frac{D \rho_e}{Dt} = (K_+ b_- + K_- b_+) \nabla^2 \rho_e - b_+ b_- \nabla^2 \rho_f \bar{E} . \quad (2.32)$$

The second term may be neglected compared to the first on the right-hand side of Eq. (32) if the electric field is sufficiently small that

$$|\rho_f \bar{E}| \ll \frac{K_+ b_- + K_- b_+}{b_+ b_-} |\nabla \rho_e| \quad (2.33)$$

or, using the Einstein relation, Eq. (2.18) and characterizing the ∇ operator by $1/\ell$, where ℓ is a characteristic length, we have:

$$|\ell \bar{E}| \ll (z_+ + z_-) \frac{RT}{F} \left| \frac{\rho_e}{\rho_f} \right| . \quad (2.34)$$

When the inequality (34) is satisfied, Eq. (32) becomes:

$$\frac{D\rho_e}{Dt} = K_{\text{eff}} \nabla^2 \rho_e \quad (2.35)$$

where

$$K_{\text{eff}} \equiv \frac{K_+ b_- + K_- b_+}{b_+ + b_-} \quad (2.36)$$

The migration current density due to an applied field \bar{E} is:

$$\bar{J} = \rho_+ b_+ \bar{E} + \rho_- b_- \bar{E} \cong \rho_e (b_+ + b_-) \bar{E} \quad (2.37)$$

Thus, because ρ_e is independent of E , it is natural to define a conductivity:

$$\sigma \equiv \rho_e (b_+ + b_-) \quad (2.38)$$

Combining Eqs. (35) and (38), then:

$$\frac{D\sigma}{Dt} = K_{\text{eff}} \nabla^2 \sigma \quad (2.39)$$

Equation (39) is a conductivity diffusion equation. It reflects no explicit dependence on electric fields. Nonetheless, the electric field plays an implicit role in tending to preserve charge neutrality, as expressed in Eqs. (2.28) and (2.29).

If we characterize D/Dt by $1/t_{\text{diff}}$ and ∇^2 by $1/\ell^2$, we have, from Eq. (39):

$$t_{\text{diff}} = \ell^2 / K_{\text{eff}} \quad (2.40)$$

If we deal with phenomena involving other characteristic times which are small compared to t_{diff} , we are justified in approximating Eq. (39) by:

$$\frac{D\sigma}{Dt} = 0 \quad (2.41)$$

i.e., by modeling the fluid as having a constant conductivity associated with each elementary volume of fixed identity.

3. Charge Relaxation

In order to describe the behavior of the free charge density, ρ_f , in the system considered in Sec. II.A.2, we subtract Eq. (2.25) from (2.24) using Eqs. (2.28) - (30):

$$\begin{aligned} \frac{D\rho_f}{Dt} = & (K_+ - K_-)\nabla^2\rho_e + \nabla^2(K_+\rho'_+ - K_-\rho'_-) - \\ & (b_+ + b_-)\nabla\cdot\rho_e\bar{E} - \nabla\cdot(b_+\rho'_+ + b_-\rho'_-)\bar{E} \quad . \end{aligned} \quad (2.42)$$

Provided the diffusion coefficients are not very nearly equal, we may neglect the second and fourth terms compared to the first and third terms on the right-hand side of Eq. (42):

$$\frac{D\rho_f}{Dt} = (K_+ - K_-)\nabla^2\rho_e - (b_+ + b_-)\nabla\cdot\rho_e\bar{E} \quad . \quad (2.43)$$

Ordinarily, the migration term dominates the diffusion term in (43), i.e.,

$$|\lambda\bar{E}| \gg \left| \frac{K_+ - K_-}{b_+ + b_-} \right| \quad (2.44)$$

or, using the Einstein relation, Eq. (2.18), and neglecting effects of the small integers z_+ and z_- :

$$|\lambda\bar{E}| \gg \frac{RT}{F} \quad . \quad (2.45)$$

When the inequality (45) is satisfied, Eq. (43) becomes

$$\frac{D\rho_f}{Dt} = - (b_+ + b_-)\nabla\cdot\rho_e\bar{E} \quad . \quad (2.46)$$

[Note that, provided Eq. (45) is satisfied, (46) describes the evolution of ρ_f even in the case where the diffusion coefficients are identical in Eq. (42).]. Expanding our Eq. (46) and using the conductivity definition, Eq.

(2.38) and Gauss' Law, Eq. (2.2), we have

$$\frac{D\rho_f}{Dt} + \frac{\sigma}{\epsilon} \rho_f = - \bar{E} \cdot \nabla \sigma \quad . \quad (2.47)$$

Equation (2.47) is the charge relaxation equation. In a uniform conductor, where the right-hand side is zero, it predicts exponential decay in time of any initial free charge distribution for an observer moving with a particle of fluid of fixed identity. Decay occurs with the charge relaxation time:

$$t_{\text{relax}} = \frac{\epsilon}{\sigma} \quad . \quad (2.48)$$

If we deal with phenomena involving other characteristic times which are large compared with t_{relax} , so that the exponential decay occurs essentially instantaneously, we may approximate Eq. (47) by

$$\frac{\sigma}{\epsilon} \rho_f = - \bar{E} \cdot \nabla \sigma \quad . \quad (2.49)$$

Equation (49) is a statement of conservation of charge in the instantaneous relaxation limit. It predicts a free charge distribution at any point where there is a conductivity gradient, and proportional to the electric field magnitude.

It is worthwhile here to restate the two approximations used in arriving at the conductivity diffusion equation in Section II.A.2, Eq. (39), and the charge relaxation equation in this section, (47). Ignoring z_+ and z_- in inequality (34), and combining with inequality (45), we see that the electric field is bounded from both above and below for the equations to simultaneously hold:

$$\frac{RT}{F} \ll |\bar{E}l| \ll \left| \frac{\rho_e}{\rho_f} \right| \frac{RT}{F} \quad (2.50)$$

4. Electric Transfer Relations for a Charge-free Half Space

For later reference, we now consider a region of uniform conductivity and permittivity, consisting of an infinite half space, either $x < 0$ or $x > 0$, as shown in Fig. 2. Because the region is uniformly conducting,

$$\rho_f = 0 \quad (2.51)$$

and Poisson's equation (2.5) becomes Laplace's equation:

$$\nabla^2 \phi = 0 \quad . \quad (2.52)$$

We look for solutions having sinusoidal dependences on tangential coordinate z , and time t :

$$\phi = \text{Re } \hat{\phi}(x) e^{(st-jkz)} \quad (2.53)$$

$$\bar{E} = \text{Re } \hat{E}(x) e^{(st-jkz)} \quad (2.54)$$

Equation (52) is time-independent and becomes

$$(D^2 - k^2) \hat{\phi} = 0 \quad (2.55)$$

where we have used the operator notation

$$D \equiv \frac{d}{dx} \quad . \quad (2.56)$$

Solutions of (55) which decay away to zero in upper and lower half spaces are, respectively:

$$\hat{\phi}^u(x) = \hat{\phi}^u e^{-kx} \quad , \quad x > 0 \quad (2.57)$$

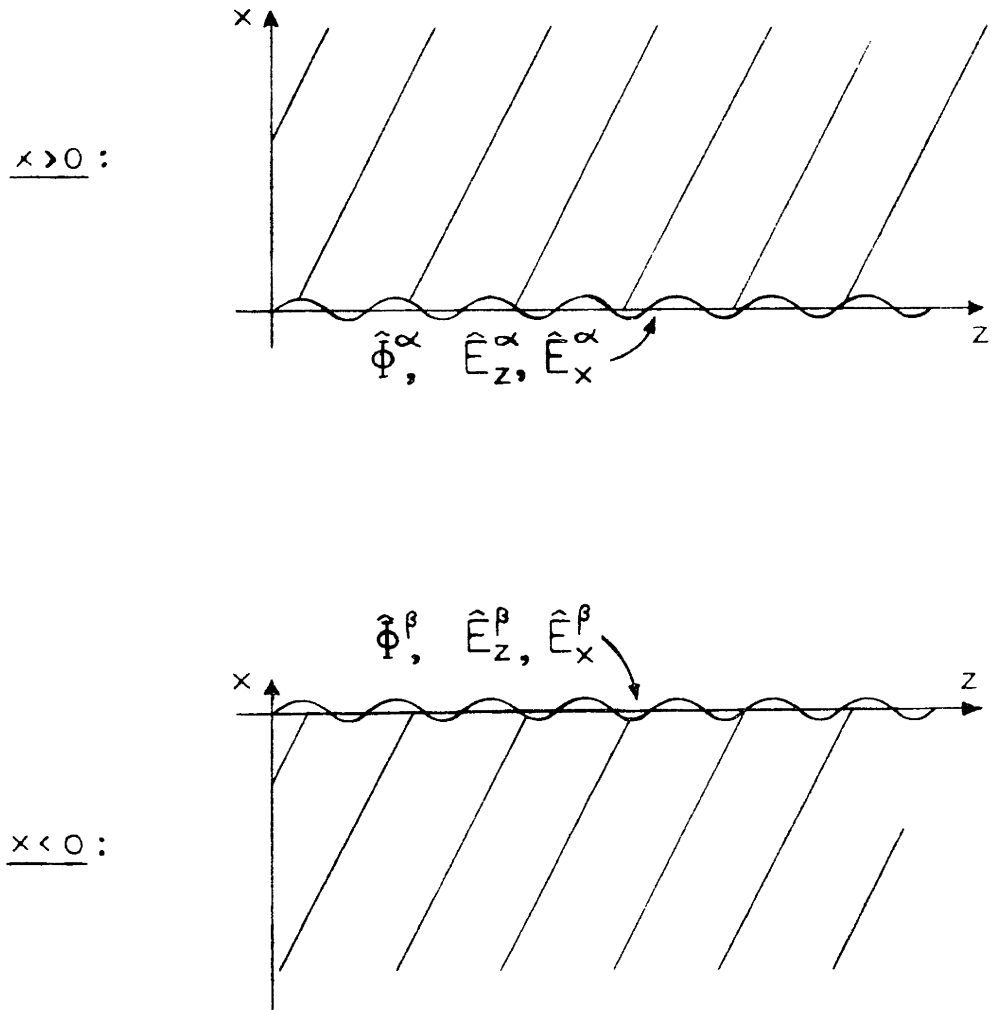


Figure 2

Electrical Half Spaces

$$\hat{\phi}^{\ell}(x) = \hat{\phi}^{\beta} e^{kx} \quad , \quad x < 0 \quad . \quad (2.58)$$

The electric field components at the surfaces, from Eq. (2.4), are:

$$\hat{E}_x^{\alpha} = -D\hat{\phi}^u \Big|_{x=0} = k\hat{\phi}^{\alpha} \quad (2.59)$$

$$\hat{E}_z^{\alpha} = jk\hat{\phi}^u \Big|_{x=0} = jk\hat{\phi}^{\alpha} \quad (2.60)$$

$$\hat{E}_x^{\beta} = -D\hat{\phi}^{\ell} \Big|_{x=0} = -k\hat{\phi}^{\beta} \quad (2.61)$$

$$\hat{E}_z^{\beta} = jk\hat{\phi}^{\ell} \Big|_{x=0} = jk\hat{\phi}^{\beta} \quad (2.62)$$

Combining Eqs. (59) and (60), and (61) and (62), we have the half-space electric transfer relations

$$\hat{E}_x^{\alpha} = -j\hat{E}_z^{\alpha} \quad (2.63)$$

$$\hat{E}_x^{\beta} = j\hat{E}_z^{\beta} \quad (2.64).$$

B. Mechanical

1. Navier-Stokes Equations

We are concerned with two-dimensional motions of viscous, incompressible fluids subject to gravitational and electrical force densities. Thus the Navier-Stokes equations, governing fluid velocity \bar{v} and pressure p for a material with viscosity η and density ρ in a uniform gravitational field, $-g\bar{i}_x$, take the forms:

$$\nabla \cdot \bar{v} = 0 \quad (2.65)$$

$$\rho \left[\frac{\partial \bar{v}}{\partial t} + \bar{v} \cdot \nabla \bar{v} \right] + \nabla p = \eta \nabla^2 \bar{v} + \rho_f \bar{E} - \rho g \bar{i}_x \quad . \quad (2.66)$$

Equation (65) is satisfied by the introduction of a stream function,

$$\bar{\Psi} = \bar{i}_y \psi(x, z, t) \quad , \quad (2.67)$$

such that

$$\bar{v} = - \nabla \times \bar{\Psi} \quad . \quad (2.68)$$

Note that, as \bar{v} is defined in Eq. (67), the gauge has been set to

$$\nabla \cdot \bar{\Psi} = 0 \quad . \quad (2.69)$$

In order to eliminate p as an unknown, we take the curl of Eq. (66); also, we substitute for \bar{v} using Eqs. (67) and (68) and make use of the vector identity

$$\nabla \times \nabla \times \bar{\Psi} \equiv \nabla(\nabla \cdot \bar{\Psi}) - \nabla^2 \bar{\Psi} \quad (2.70)$$

and Eq. (69), to obtain

$$\rho \frac{\partial}{\partial t} \nabla^2 \psi + \rho [\nabla \times (\bar{v} \cdot \nabla \bar{v})]_y = \eta \nabla^2 \nabla^2 \psi + [\nabla \times (\rho_f \bar{E})]_y \quad (2.71)$$

Equation (71) makes it clear that rotational electrical force densities enter into the familiar fluid mechanical competition between inertial and viscous force densities.

The viscous stress tensor, defining stress components in terms of strain rates for an incompressible Newtonian fluid is:

$$S_{ij} = - p \delta_{ij} + \eta \left(\frac{\partial v_i}{\partial x_j} + \frac{\partial v_j}{\partial x_i} \right) \quad (2.72)$$

Boundary conditions at a surface between regions (a) and (b) defined by normal vector \bar{n} as in Fig. 1, are:

$$\mathbf{n} \cdot \llbracket \mathbf{v} \rrbracket = 0 \quad (2.73)$$

$$\overline{\mathbf{n}} \times \llbracket \overline{\mathbf{v}} \rrbracket = 0 \quad (2.74)$$

$$\llbracket S_{ij} \rrbracket n_j + \llbracket T_{ij} \rrbracket n_j = 0 \quad (2.75)$$

where we have accounted only for mechanical and electrical surface force densities in Eq. (75). Surface tension, for example, is not accounted for.

2. Characteristic Times

To gain some "feel" for the implications of Eq. (66), we compare terms to draw out two characteristic times. First, consider the coupling between the first inertial term on the left and the first viscous term on the right. If we characterize the ∇ operator by $1/\ell$ and the $\partial/\partial t$ operator by $1/T$, we obtain

$$\rho \frac{\psi}{\ell^2 T} = \rho \frac{\psi}{\ell^4} \quad (2.76)$$

or

$$T = \frac{\rho \ell^2}{\eta} \quad (2.77)$$

T is the familiar viscous diffusion time. If we think of suddenly exciting a viscous material at its surface at some instant T is the time required for rotational modes to diffuse a depth ℓ into the material. Figure 3 shows T versus ℓ on a log-log plot for some familiar fluids.

On the other hand, consider the coupling between the viscous and electrical terms on the right-hand side of Eq. (66). Again, characterizing the ∇ operator by $1/\ell$, using Gauss' law, Eq. (2), to set

$$\rho_f = \frac{\epsilon E}{\ell} \quad (2.78)$$

and making

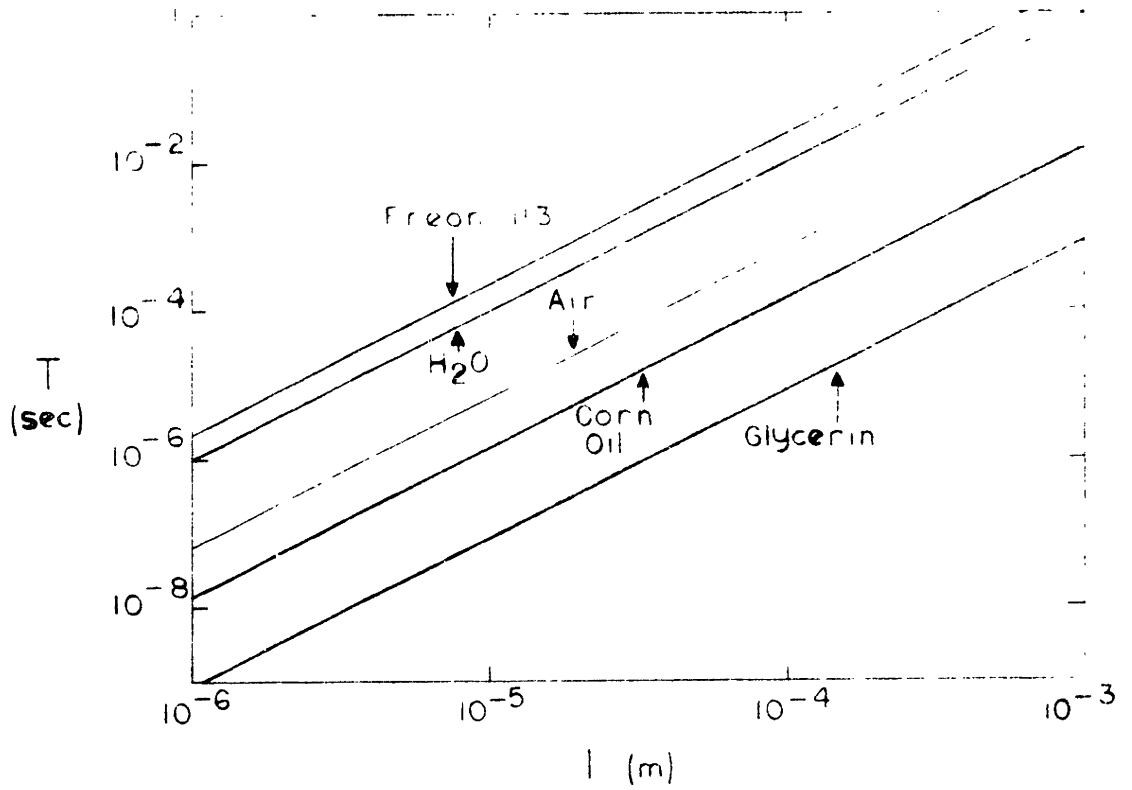


Figure 3

T versus l

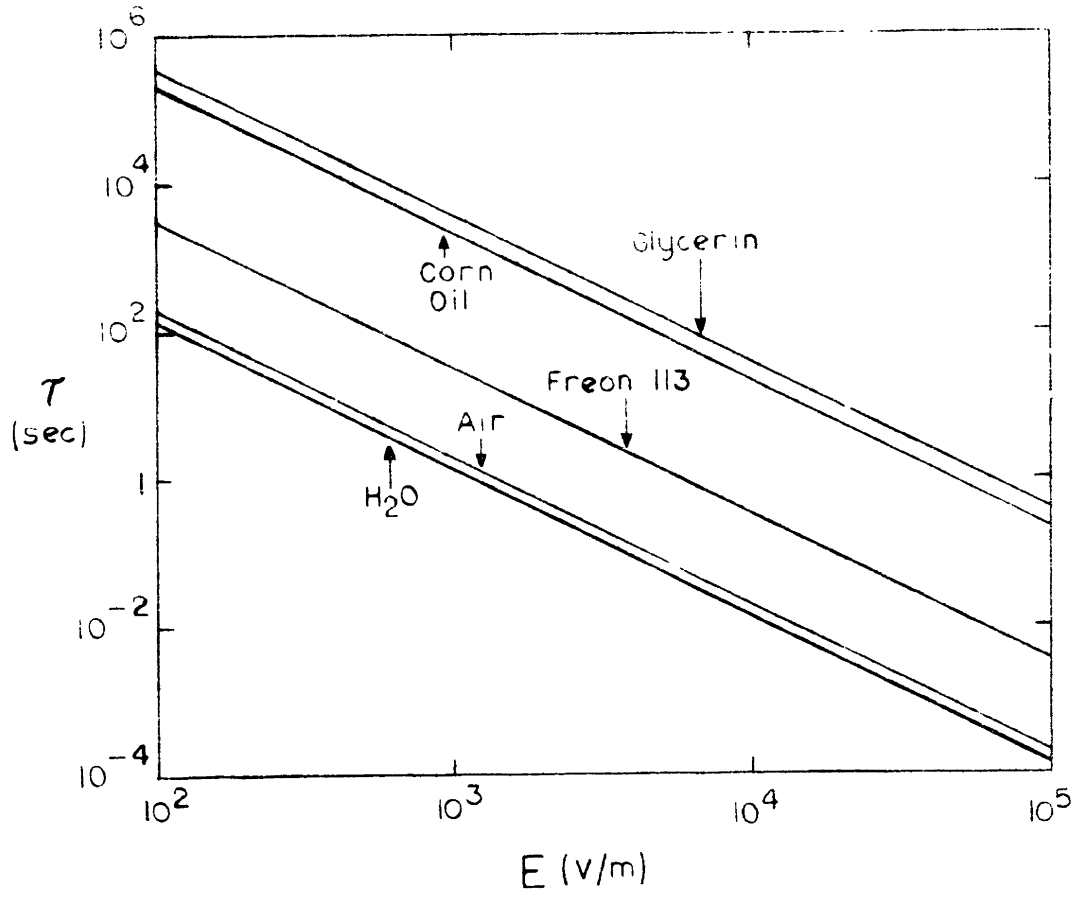


Figure 4

τ Versus E

$$\tau = \frac{\eta}{\epsilon E} \quad (2.79)$$

we find:

$$\tau \frac{\partial^2 \tau}{\partial x^2} = \frac{\partial E^2}{\partial x^2} \quad (2.80)$$

or
$$\tau = \frac{\eta}{\epsilon E^2} \quad (2.81)$$

τ is the characteristic electric-viscous time. Figure 4 shows τ versus E on a log-log plot for the same fluids as Fig 3.

3. Mechanical Transfer Relations for a Viscous Half Space

In the spirit of Section II.A.4, consider an infinite half space of viscous fluid, either $x > 0$ or $x < 0$, as shown in Fig. 5. As in Section II.A.4, the regions are uniformly conducting, hence, are charge free. Thus, there is no electrical force density; i.e.,

$$[\nabla \times (\rho_f \bar{E})]_y = 0 \quad (2.82)$$

in Eq. (71).

In equilibrium, the fluid is stationary; i.e.,

$$\bar{v}^E = 0 \quad (2.83)$$

and (66) is satisfied by the pressure distribution:

$$p^E = -\rho g x \quad (2.84)$$

where the superscript E denotes equilibrium quantities.

We consider perturbations from equilibrium associated with an interface displacement $\xi(z,t)$. Assuming solutions having sinusoidal dependences

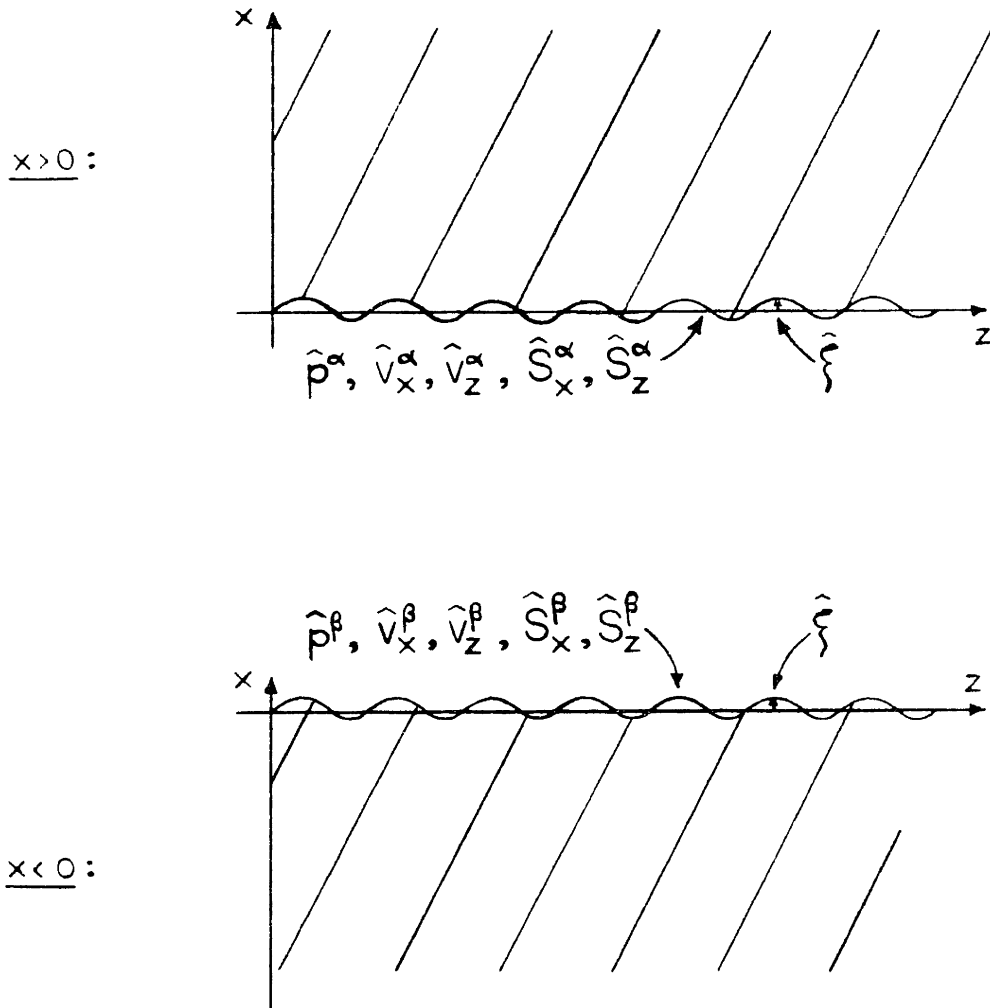


Figure 5

Mechanical Half Spaces

on z and t :

$$[\xi, \bar{v}, \psi, p] = \text{Re}[\hat{\xi}, \hat{v}(x), \hat{\psi}(x), \hat{p}(x)] e^{(st-jkz)} \quad (2.85)$$

Because the perturbation amplitudes are assumed small, we linearize the governing equations, dropping the convective term

$$\bar{v} \cdot \nabla \bar{v} \approx 0 \quad (2.86)$$

in Eqs. (66) and (71).

Equation (68) becomes:

$$\hat{v}_x = -jk\hat{\psi} \quad (2.87)$$

$$\hat{v}_z = -D\hat{\psi} \quad (2.88)$$

The z -component of Eq. (66) becomes:

$$\hat{p} = -\frac{\eta}{jk} [D^2 - k^2 - \frac{s\rho}{\eta}] \hat{v}_z \quad (2.89)$$

and Eq. (71) becomes:

$$[D^2 - k^2][D^2 - k^2 - \frac{s\rho}{\eta}] \hat{\psi} = 0 \quad (2.90)$$

Assuming solutions to Eq. (90) of the form:

$$\hat{\psi} = C e^{\gamma x} \quad (2.91)$$

we have

$$\gamma = \pm k \quad (2.92)$$

and

$$\gamma = \pm q \equiv \pm \sqrt{k^2 + \frac{s\rho}{\eta}} \quad (\text{Re } q > 0) \quad (2.93)$$

as possible solutions. Discarding solutions which grow as $x \rightarrow \pm \infty$, we have two solutions each in the upper and lower half-spaces:

$$\left. \begin{aligned} \gamma_1^u &= -k & ; & & \gamma_2^u &= -q \\ \gamma_1^\ell &= k & ; & & \gamma_2^\ell &= q \end{aligned} \right\} \quad (2.94)$$

Now, writing out the most general stream function solution in each region:

$$\hat{\psi}(x) = \sum_{n=1}^2 \hat{\Psi}_n e^{\gamma_n x} \quad (2.95)$$

(Superscripts u or ℓ on all variables are implied.) Using Eq. (95) in Eqs. (87) and (88):

$$\begin{bmatrix} \hat{v}_x \\ \hat{v}_z \end{bmatrix} \begin{bmatrix} -jke^{\gamma_1 x} & -jke^{\gamma_2 x} \\ -\gamma_1 e^{\gamma_1 x} & -\gamma_2 e^{\gamma_2 x} \end{bmatrix} \begin{bmatrix} \hat{\Psi}_1 \\ \hat{\Psi}_2 \end{bmatrix} \quad (2.96)$$

The velocity components at the equilibrium position of the interface $x = 0$, are then:

$$\begin{bmatrix} \hat{v}_x^\alpha \\ \hat{v}_z^\alpha \end{bmatrix} \begin{bmatrix} -jk & -jk \\ -\gamma_1^u & -\gamma_2^u \end{bmatrix} \begin{bmatrix} \hat{\Psi}_1^u \\ \hat{\Psi}_2^u \end{bmatrix} \quad (2.97)$$

$$\begin{bmatrix} \hat{v}_x^\beta \\ \hat{v}_z^\beta \end{bmatrix} \begin{bmatrix} -jk & -jk \\ -\gamma_1^\ell & -\gamma_2^\ell \end{bmatrix} \begin{bmatrix} \hat{\Psi}_1^\ell \\ \hat{\Psi}_2^\ell \end{bmatrix} \quad (2.98)$$

From Eq. (72), we determine the perturbation stress tensor components:

$$\hat{S}_{xx} = 2\eta D\hat{v}_x - \hat{p} \quad (2.99)$$

$$\hat{S}_{xz} = \eta [D\hat{v}_z - jk\hat{v}_x] \quad (2.100)$$

Using Eq. (96) in Eqs. (89), (99) and (100) we get:

$$\begin{bmatrix} \hat{S}_{xx} \\ \hat{S}_{xz} \end{bmatrix} = \begin{bmatrix} j \frac{\eta}{k} (\gamma_1^2 - 3k^2 - \frac{s\rho}{\eta}) \gamma_1 e^{\gamma_1 x} & j \frac{\eta}{k} (\gamma_2^2 - 3k^2 - \frac{s\rho}{\eta}) \gamma_2 e^{\gamma_2 x} \\ -\eta(\gamma_1^2 + k^2) e^{\gamma_1 x} & -\eta(\gamma_2^2 + k^2) e^{\gamma_2 x} \end{bmatrix} \begin{bmatrix} \hat{\Psi}_1 \\ \hat{\Psi}_2 \end{bmatrix}$$

(2.101)

Finally, the stress components at the equilibrium position of the interface are:

$$\begin{bmatrix} \hat{S}_x^\alpha \\ \hat{S}_z^\alpha \end{bmatrix} \begin{bmatrix} j \frac{\eta}{k} ([\gamma_1^u]^2 - 3k^2 - \frac{s\rho}{\eta}) \gamma_1^u & j \frac{\eta}{k} ([\gamma_2^u]^2 - 3k^2 - \frac{s\rho}{\eta}) \gamma_2^u \\ -\eta([\gamma_1^u]^2 + k^2) & -\eta([\gamma_2^u]^2 + k^2) \end{bmatrix} \begin{bmatrix} \hat{\Psi}_1^u \\ \hat{\Psi}_2^u \end{bmatrix}$$

(2.102)

$$\begin{bmatrix} \hat{S}_x^\beta \\ \hat{S}_z^\beta \end{bmatrix} \begin{bmatrix} j \frac{\eta}{k} ([\gamma_1^\ell]^2 - 3k^2 - \frac{s\rho}{\eta}) \gamma_1^\ell & j \frac{\eta}{k} ([\gamma_2^\ell]^2 - 3k^2 - \frac{s\rho}{\eta}) \gamma_2^\ell \\ -\eta([\gamma_1^\ell]^2 + k^2) & -\eta([\gamma_2^\ell]^2 + k^2) \end{bmatrix} \begin{bmatrix} \hat{\Psi}_1^\ell \\ \hat{\Psi}_2^\ell \end{bmatrix}$$

(2.103)

To arrive at a set of half-space mechanical transfer relations, relating stress components to velocity components at the equilibrium interface position for upper and lower half spaces, we invert Eqs. (97) and (98), combine with Eqs. (102) and (103) and use Eq. (94):

$$\begin{bmatrix} \hat{S}_x^\alpha \\ \hat{S}_z^\alpha \end{bmatrix} = \eta \begin{bmatrix} -\frac{q}{k} (k+q) & j(k-q) \\ -j(k-q) & -(k+q) \end{bmatrix} \begin{bmatrix} \hat{v}_x^\alpha \\ \hat{v}_z^\alpha \end{bmatrix}$$

(2.104)

$$\begin{bmatrix} \hat{S}_x^\beta \\ \hat{S}_z^\beta \end{bmatrix} = \eta \begin{bmatrix} \frac{q}{k}(k+q) & j(k-q) \\ -j(k-q) & (k+q) \end{bmatrix} \begin{bmatrix} \hat{v}_x^\beta \\ \hat{v}_z^\beta \end{bmatrix} \quad (2.105)$$

In a problem involving coupling between a fluid half-space and another region, it is the stresses and velocities at the perturbation position of the interface, $x = \xi$, which appear in the boundary conditions. We denote these quantities by enclosing the superscript α or β in parentheses: $\hat{v}_x^{(\alpha)}$, $\hat{S}_x^{(\beta)}$, etc. We now consider how these perturbation position quantities are related to the stresses and velocities at the equilibrium position of the interface, $x = 0$, appearing in Eqs. (104) and (105).

Consider, for example, $\hat{S}_x^{(\alpha)}$. Because $\hat{\xi}$ is a perturbation quantity, we may expand \hat{S}_x in a Taylor Series about $x = 0$, retaining only terms up to first order in $\hat{\xi}$:

$$\hat{S}_x^{(\alpha)} \equiv \hat{S}_x \Big|_{x=\hat{\xi}} = \hat{S}_{xx} \Big|_{x=0} \hat{\xi} + \frac{\partial S_{xx}}{\partial x} \Big|_{x=0} \hat{\xi}^2 \equiv \hat{S}_x^\alpha + \frac{\partial S_{xx}}{\partial x} \Big|_{x=0} \hat{\xi} \quad (2.106)$$

Now, the second term on the right-hand side of Eq. (106) makes a first order contribution only if $\partial S_{xx} / \partial x \Big|_{x=0}$ has an equilibrium value. The distinction between $\partial S_{xx} / \partial x \Big|_{x=0}$ and $\partial S_{xx}^E / \partial x \Big|_{x=0}$ need not be made, since it can make a difference only to second order. Thus, we have, finally:

$$\hat{S}_x^{(\alpha)} = \hat{S}_x^\alpha + \frac{\partial S_{xx}^E}{\partial x} \Big|_{x=0} \hat{\xi} \quad (2.107)$$

Reconsidering the equilibrium, we have from Eq. (83):

$$v_x^E = v_z^E = 0 \quad (2.108)$$

and from Eqs. (72), (84) and (108) we have:

$$S_{xz}^E = 0 \quad (2.109)$$

$$S_{xx}^E = \rho g x \quad (2.110)$$

Equations (108) and (109), together with (107), generalized to any stress or velocity component, imply that for \hat{v}_x , \hat{v}_z and \hat{S}_z , correct to first order, there is no difference between quantities evaluated at $x=0$ and at $x=\xi$. However, in the case of \hat{S}_x , combining Eqs. (107) and (110)

$$\hat{S}_x(\alpha) = \hat{S}_x^\alpha + \rho g \hat{\xi} \quad (2.111)$$

Finally, referring back to the electric transfer relations, Eqs. (63) and (64), we recognize that, for a half space with the perturbed boundary of $x = \xi$, no distinction need be made between electric field components evaluated at $x=0$ and at $x=\xi$, provided the equilibrium configurations involve no gradients in electric fields within the half spaces.

CHAPTER II BIBLIOGRAPHY

1. Woodson, H. H., and Melcher, J. R., Electromechanical Dynamics, Part I: Discrete Systems, New York: John Wiley & Sons, Inc., 1968, Chapter 1.
2. Woodson, H. H., and Melcher, J. R., Electromechanical Dynamics, Part II: Fields, Forces and Motion, New York: John Wiley & Sons, Inc., 1968, Chapter 8.
3. McConnell, A. J., Applications of the Absolute Differential Calculus, London: Blackie, 1951, Chapter 1.
4. Levich, Veniamin G., Physicochemical Hydrodynamics, New Jersey: Prentice-Hall, 1962, Chapter 2.

CHAPTER III. CONDUCTIVITY DISCONTINUITY MODELS

A. Introduction

Situations involving a junction between two miscible fluids of differing conductivities will, in general, involve the diffusion mechanism described in Sections I.A and II.A.2. It is not meaningful to consider questions of electrohydrodynamic stability by assuming perturbations from an equilibrium state if, due to diffusion, the "equilibrium" is evolving at a rate comparable to the perturbation dynamics. If, however, diffusion times are long compared to times describing instability dynamics (e.g., τ and T as defined in Section II.B.2), we may characterize the junction by an equilibrium conductivity distribution, itself evolving slowly with time, and subject to electrohydrodynamic instability as modeled in a situation of static equilibrium.

Moreover, we might expect that, provided the region over which conductivity variation occurs at the junction between fluids is thin compared with lengths describing instability dynamics, a model involving a discrete jump in conductivity would suffice to describe the interface. We consider such a model in this chapter, subject to an equilibrium electric field, first normal and second tangential to the interface.

B. Equilibrium Normal Electric Field

A plane interface bounds two incompressible fluid half-spaces, stressed by an initially perpendicular current density, $\bar{J} \bar{i}_x$, as shown in Figure 1. The fluids are ohmic conductors, of conductivities σ_a and σ_b , mass densities ρ_a and ρ_b above and below the interface, respectively, and identical permittivity ϵ and viscosity η . If, physically, the lower half-space represents the same fluid as the upper half space, but slightly doped to

increase its conductivity, the density difference $\rho_a - \rho_b$ is small compared to either ρ_a or ρ_b . For this reason, we shall account for the density difference only in the gravitational terms of the governing equations, ignoring it to the extent of using an average density in expressing the viscous decay length. Our aim is to find the dispersion relation for small-amplitude sinusoidal interface motions:

$$\xi = \text{Re } \hat{\xi} e^{(st-jkz)} \quad . \quad (3.1)$$

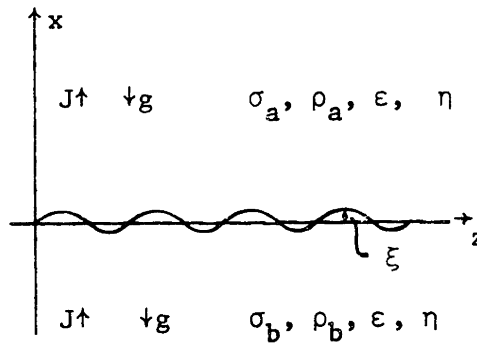


Figure 1. Normal Field Geometry

We have previously characterized each of the fluid half-spaces electrically by the transfer relations of Section II.A.4, and mechanically by the transfer relations of Section II.B.3. We now determine the boundary conditions necessary to tie the fluids together, mechanically and electrically, at the interface. Mechanical stress balance, from Eq. (2.75), requires:

$$\llbracket S_{ij} \rrbracket n_j + \llbracket T_{ij} \rrbracket n_j = 0 \quad (3.2)$$

where S_{ij} are viscous stress tensor components, as defined by Eq. (2.72), T_{ij} are Maxwell stress tensor components as defined by Eq. (2.8), n_j are interface unit normal vector components, and

$$\llbracket A \rrbracket \equiv A_a - A_b \quad . \quad (3.3)$$

The interface unit normal vector components, correct to first order in ξ , are

$$n_x = 1 \quad (3.4)$$

$$n_z = -\frac{\partial \xi}{\partial z} = \text{Re} \frac{jk}{s} \hat{v}_x^{(\alpha)} e^{(st-jkz)} \quad (3.5)$$

where, in writing Eq. (3.5), we have recognized that, to first order in ξ

$$\hat{v}_x^{(\alpha)} = s \hat{\xi} \quad . \quad (3.6)$$

In equilibrium, (3.2) is satisfied by

$$\llbracket p^E \rrbracket = \frac{\epsilon J^2}{2} \left[\frac{1}{\sigma_a} - \frac{1}{\sigma_b} \right] \quad . \quad (3.7)$$

Subject to interface perturbation, we obtain for the $i=x$ and $i=z$ components of Eq. (3.2), respectively:

$$\hat{S}_x^{(\alpha)} - \hat{S}_x^{(\beta)} + \epsilon J \left[\frac{1}{\sigma_a} \hat{E}_x^{(\alpha)} - \frac{1}{\sigma_b} \hat{E}_x^{(\beta)} \right] = 0 \quad (3.8)$$

$$\hat{S}_z^{(\alpha)} - \hat{S}_z^{(\beta)} - \frac{jk}{s} \hat{v}_x^{(\alpha)} \epsilon J^2 \left[\frac{1}{\sigma_a} - \frac{1}{\sigma_b} \right] + \epsilon J \left[\frac{1}{\sigma_a} \hat{E}_z^{(\alpha)} - \frac{1}{\sigma_b} \hat{E}_z^{(\beta)} \right] = 0 \quad (3.9)$$

The boundary conditions on perturbation fluid velocity, from Eqs. (2.73) and (2.74), are:

$$\hat{v}_x^{(\alpha)} = \hat{v}_x^{(\beta)} \quad (3.10)$$

$$\hat{v}_z^{(\alpha)} = \hat{v}_z^{(\beta)} \quad . \quad (3.11)$$

The boundary condition on tangential electric field at the interface is, from Eq. (2.10):

$$\bar{n} \times \llbracket \bar{E} \rrbracket = 0 \quad . \quad (3.12)$$

Writing out Eq. (12) for the assumed equilibrium and perturbation yields:

$$\hat{E}_z^{(\alpha)} - \hat{E}_z^{(\beta)} - \frac{jk}{s} \hat{v}_x^{(\alpha)} \llbracket \left[\frac{1}{\sigma_a} - \frac{1}{\sigma_b} \right] \rrbracket = 0 \quad . \quad (3.13)$$

The boundary condition on normal electric field at the interface, recalling the assumption of instantaneous charge relaxation, is from Eq. (2.12):

$$\bar{n} \cdot \llbracket \sigma \bar{E} \rrbracket = 0 \quad . \quad (3.14)$$

Subject to perturbations, we obtain for Eq. (3.14)

$$\sigma_a \hat{E}_x^{(\alpha)} - \sigma_b \hat{E}_x^{(\beta)} = 0 \quad . \quad (3.15)$$

Equations (2.63), (2.64), (2.104) and (2.105) are now modified so as to be in terms of the perturbation interface variables which appear in the boundary conditions just derived, according to the discussion at the end of Section II.B.3. This amounts to nothing more than substituting perturbation interface variables [superscripted (α) and (β)] for equilibrium interface variables (superscripted α and β), except in the case of S_x^α and S_x^β . For these variables, we make use of Eqs. (2.111) and (6) to write:

$$\hat{S}_x^{(\alpha)} = \hat{S}_x^\alpha + \frac{\rho_a^g}{s} \hat{v}_x^{(\alpha)} \quad (3.16)$$

$$\hat{S}_x^{(\beta)} = \hat{S}_x^\beta + \frac{\rho_b^g}{s} \hat{v}_x^{(\beta)} \quad (3.17)$$

Thus, writing out the transfer relations in terms of perturbation interface variables, we have

$$\hat{E}_x(\alpha) = -j\hat{E}_z(\alpha) \quad (3.18)$$

$$\hat{E}_x(\beta) = j\hat{E}_z(\beta) \quad (3.19)$$

$$\begin{bmatrix} \hat{S}_x(\alpha) \\ \hat{S}_z(\alpha) \end{bmatrix} = \eta \begin{bmatrix} -\frac{q}{k}(k+q) + \frac{\rho_a g}{s\eta} & j(k-q) \\ -j(k-q) & -(k+q) \end{bmatrix} \begin{bmatrix} \hat{v}_x(\alpha) \\ \hat{v}_z(\alpha) \end{bmatrix} \quad (3.20)$$

$$\begin{bmatrix} \hat{S}_x(\beta) \\ \hat{S}_z(\beta) \end{bmatrix} = \eta \begin{bmatrix} \frac{q}{k}(k+q) + \frac{\rho_b g}{s\eta} & j(k-q) \\ -j(k-q) & (k+q) \end{bmatrix} \begin{bmatrix} \hat{v}_x(\beta) \\ \hat{v}_z(\beta) \end{bmatrix} \quad (3.21)$$

We emphasize here the assumption of a slight density difference, $[\rho]$.

While the distinction between ρ_a and ρ_b has been retained in the gravitational terms of Eqs. (20) and (21), it has been ignored in not distinguishing q_a in Eq. (20) from q_b in (21); q is to be determined using an average density

$$q = \sqrt{k^2 + \frac{s(\rho_a + \rho_b)}{2\eta}} \quad , \quad (\text{Re } q > 0) \quad . \quad (3.22)$$

Equations (8), (9), (10), (11), (13), (15), (18), (19), (20) and (21) form a system of 12 homogeneous equations in twelve unknowns. We begin solving the system by algebraically eliminating six unknowns. Combining (13), (15), (18) and (19), we have

$$\hat{E}_x(\beta) = \frac{kJ}{s\sigma_b} \frac{\sigma_b - \sigma_a}{\sigma_b + \sigma_a} \hat{v}_x(\alpha) \quad (3.23)$$

$$\hat{E}_x(\alpha) = \frac{kJ}{s\sigma_a} \frac{\sigma_b - \sigma_a}{\sigma_b + \sigma_a} \hat{v}_x(\alpha) \quad (3.24)$$

$$\hat{E}_z(\beta) = -\frac{jkJ}{s\sigma_b} \frac{\sigma_b - \sigma_a}{\sigma_b + \sigma_a} \hat{v}_x(\alpha) \quad (3.25)$$

$$\hat{E}_z(\alpha) = \frac{jkJ}{s\sigma_a} \frac{\sigma_b - \sigma_a}{\sigma_b + \sigma_a} \hat{v}_x(\alpha) \quad (3.26)$$

Now, using Eqs. (10), (11), (23), (24), (25) and (26) in Eqs. (8), (9), (20) and (21), we obtain a system of six homogeneous equations in six unknowns, as expressed in matrix form below:

$$\begin{bmatrix} -\frac{k\phi\llbracket E \rrbracket}{s} & 0 & -1 & 1 & 0 & 0 \\ -\frac{j\epsilon k\psi\llbracket E \rrbracket}{s} & 0 & 0 & 0 & -1 & 1 \\ \left\{ \frac{\eta q(k+q)}{k} + \frac{\rho_a g}{s} \right\} & j(k-q)\eta & 0 & -1 & 0 & 0 \\ j(k-q)\eta & (k+q)\eta & 0 & 0 & 0 & 1 \\ \left\{ \frac{\eta q(k+q)}{k} + \frac{\rho_b g}{s} \right\} & j(k-q)\eta & -1 & 0 & 0 & 0 \\ -j(k-q)\eta & (k+q)\eta & 0 & 0 & -1 & 0 \end{bmatrix} \begin{bmatrix} \hat{v}_x(\alpha) \\ \hat{v}_z(\alpha) \\ \hat{S}_x(\beta) \\ \hat{S}_x(\alpha) \\ \hat{S}_z(\beta) \\ \hat{S}_z(\alpha) \end{bmatrix} = \begin{bmatrix} 0 \\ 0 \\ 0 \\ 0 \\ 0 \\ 0 \end{bmatrix} \quad (3.27)$$

where

$$\phi \equiv \epsilon J \frac{\sigma_a - \sigma_b}{\sigma_a \sigma_b} \quad (3.28)$$

$$\llbracket E \rrbracket \equiv J \left[\frac{1}{\sigma_a} - \frac{1}{\sigma_b} \right] \quad (3.29)$$

$$\psi \equiv \frac{2J}{\sigma_a + \sigma_b} \quad (3.30)$$

Either by direct substitution of Eqs. (20) and (21) into the first two rows of Eq. (27), or by expanding out the determinant of the 6×6 matrix set equal to zero for nontrivial solutions, we arrive at the dispersion relation:

$$2\eta \frac{q(k+q)}{k} - \frac{g\|\rho\|}{s} + \frac{k\phi\|E\|}{s} = 0 \quad (3.31)$$

Melcher and Smith⁽¹⁾ have considered the problem of two fluid half-spaces stressed by an initially perpendicular current density in greater generality than in the above analysis. We may check Eq. (31) by considering the appropriate limit of the analysis in Reference (1). For the case of instantaneous charge relaxation, Eq. (17) of Reference (1) becomes:

$$\|\sigma_{e_z}\| = 0$$

and, correspondingly, the last row of the determinant in Eq. (18) of Reference (1) becomes

$$0 \quad 0 \quad 0 \quad 0 \quad \sigma_a \quad \sigma_b$$

Expanding out the determinant, then, and setting $\rho_a + \rho_b = 2\rho$ in all terms except the gravitational which involves $g\|\rho\|$, $\epsilon_a = \epsilon_b$, $\mu_a = \mu_b = \eta$, and $T = 0$, we obtain a simplified version of Eq. (19) of Reference (1):

$$\frac{k^2\phi\|E\|}{s^2 2\rho} - \frac{gk\|\rho\|}{s^2 2\rho} + \frac{q}{q-k} = 0 \quad (3.32)$$

Using Eq. (22), we see that Eqs. (31) and (32) are identical.

We now proceed to analyze the dispersion relation. Rewriting (31) we have:

$$v s q(k+q) - gk \frac{[\rho]}{2\rho} - \frac{\epsilon k^2 J^2 (\sigma_a - \sigma_b)^2}{(\sigma_a \sigma_b)^2 2\rho} = 0 \quad (3.33)$$

where $v \equiv \eta/\rho$. (3.34)

Recalling the definition of q , Eq. (22) as

$$s = v(q+k)(q-k) \quad , \quad (3.35)$$

and combining Eqs. (33) and (35), we arrive at a fourth-order equation for q as a function of the wavenumber k :

$$v^2 q(q+k)(q^2 - k^2) - gk \frac{[\rho]}{2\rho} - \frac{\epsilon k^2 J^2 (\sigma_a - \sigma_b)^2}{(\sigma_a \sigma_b)^2 2\rho} = 0 \quad . \quad (3.36)$$

Given a value of k , we determine solutions to Eq. (36) which satisfy the condition $\text{Re } q > 0$. Corresponding values for growth rate s are then given by Eq. (35).

Normalizing (35) and (36) and defining various pertinent time constants, we have:

$$\underline{s} = \frac{\tau_E}{\tau_V} (q^2 - 1) \quad (3.37)$$

$$q(q+1)(q^2 - 1) + e = 0 \quad (3.38)$$

where

$$q \equiv q/k \quad (3.39)$$

$$\underline{s} \equiv \tau_E s \quad (3.40)$$

$$e \equiv \left(\frac{\tau_E}{\tau_V} \right)^{-3/2} \left(\frac{\tau_E}{\tau_g} \right)^{3/2} \left(\frac{\tau_E}{\tau_V} \right)^{-1} \quad (3.41)$$

$$\tau_E \equiv \frac{2\eta}{\epsilon J^2 \left(\frac{1}{\sigma_a} - \frac{1}{\sigma_b} \right)^2} \quad (3.42)$$

$$\tau_v \equiv \frac{1}{k^2 v} \quad (3.43)$$

$$\tau_g \equiv \left(-\frac{2\rho\sqrt{v}}{g\|\rho\|} \right)^{2/3} \quad (3.44)$$

Note that, as defined, τ_E and τ_g are independent of k . τ_v is the only quantity in e which varies as k is varied. Because τ_E is used to define \underline{s} , this normalization is independent of k . Thus, the dependence of \underline{s} on τ_v , with τ_E and τ_g held fixed, is a direct indication of the functional dependence of s on $1/k^2$.

Some understanding of the character of the solutions to Eqs. (37) and (38) may be gained without carrying out a complete solution. First, the critical wavenumber for which growth first occurs, k_c , is defined by

$$s = 0 \quad \text{at } k = k_c \quad . \quad (3.45)$$

From Eqs. (37) and (40), then:

$$q^2 = 1 \quad \text{at } k = k_c \quad . \quad (3.46)$$

From Eq. (38):

$$e = 0 \quad \text{at } k = k_c \quad (3.47)$$

and from Eq. (41),

$$\left(\frac{\tau_v}{\tau_g} \right)^{3/2} = \frac{\tau_v}{\tau_E} \quad \text{at } k = k_c \quad . \quad (3.48)$$

Entering the definitions of Eqs. (42), (43) and (44) in (48) and solving for k_c , we obtain

$$k_c = \frac{g \parallel \rho \parallel}{\epsilon J^2 \left(\frac{1}{\sigma_a} - \frac{1}{\sigma_b} \right)^2} \quad (3.49)$$

For combinations of parameters such that $\left[\tau_v / \tau_E \right]_{\underline{s}} \ll 1$, Eq. (37) yields

$$\underline{q} \approx 1 + \frac{1}{2} \frac{\tau_v}{\tau_E} \underline{s} \quad (3.50)$$

Substituting (50) into (38) and retaining only first order terms in $\left[\tau_v / \tau_E \right]_{\underline{s}}$:

$$2 \frac{\tau_v}{\tau_E} \underline{s} + e \approx 0 \quad (3.51)$$

Combining Eqs. (41) and (51):

$$\underline{s} \approx \frac{1}{2} - \frac{1}{2} \left(\frac{\tau_v}{\tau_E} \right)^{1/2} \left(\frac{\tau_E}{\tau_g} \right)^{3/2} \quad (3.52)$$

or, using Eq. (40):

$$\underline{s} \approx \frac{1}{2\tau_E} \left[1 - \left(\frac{\tau_v}{\tau_E} \right)^{1/2} \left(\frac{\tau_E}{\tau_g} \right)^{3/2} \right] \quad (3.53)$$

If $\tau_v \ll \tau_E$, Eq. (53) becomes simply:

$$\underline{s} \approx \frac{1}{2\tau_E} \quad (3.54)$$

At the other extreme, for combinations of parameters such that $\left[\tau_v / \tau_E \right]_{\underline{s}} \gg 1$,

$$\underline{q} \approx \sqrt{\frac{\tau_v}{\tau_E}} \underline{s} \quad (3.55)$$

Substituting Eq. (55) into (38), and ignoring unity terms:

$$\left(\frac{\tau_v}{\tau_E} \underline{s} \right)^2 + e \approx 0 \quad (3.56)$$

Combining Eqs. (41) and (56) we get:

$$\underline{s} \approx \frac{\tau_E}{\tau_v} \left[\frac{\tau_v}{\tau_E} - \left(\frac{\tau_v}{\tau_g} \right)^{3/2} \right]^{1/2} \quad (3.57)$$

or, using Eqs. (40), (42), (43) and (44):

$$s \approx \left[\frac{\epsilon k^2 J^2 \left(\frac{1}{\sigma_a} - \frac{1}{\sigma_b} \right)^2}{2\rho} - \frac{gk \llbracket \rho \rrbracket}{2\rho} \right]^{1/2} \quad (3.58)$$

If $\tau_v \ll \tau_g (\tau_g / \tau_E)^2$, Eq. (57) becomes:

$$\underline{s} \approx \left(\frac{\tau_E}{\tau_v} \right)^{1/2} \quad (3.59)$$

and (58) becomes:

$$s \approx \sqrt{\frac{1}{\tau_E \tau_v}} \quad (3.60)$$

Appendix I presents a general solution for the quartic, Eq. (38), with parameter e defined in terms of the various time constants by Eq. (41). We summarize the results here. Solutions are computed by the following program:

Define:

$$c_+ \equiv \frac{51\sqrt{17} + 107}{512} \approx .61968$$

$$c_- \equiv \frac{51\sqrt{17} - 107}{512} \approx .20172 \quad (3.61)$$

If $e \leq -c_-$, or if $0 \leq e \leq c_+$, compute:

$$A = \frac{1}{6} \left[\left(1 + \frac{99}{16} e \right) + 9 \left\{ \frac{e}{3} (c_+ - e) (c_- + e) \right\}^{1/2} \right]^{1/3}$$

$$B = \frac{1}{6} \left[\left(1 + \frac{99}{16} e \right) - 9 \left\{ \frac{e}{3} (c_+ - e) (c_- + e) \right\}^{1/2} \right]^{1/3} \quad (3.62)$$

$$\begin{aligned}
 Z_1 &= \frac{11}{48} + A + B \\
 Z_2 &= \frac{11}{48} - \frac{A+B}{2} + j \frac{A-B}{2} \sqrt{3} \\
 Z_3 &= \frac{11}{48} - \frac{A+B}{2} - j \frac{A-B}{2} \sqrt{3} .
 \end{aligned} \tag{3.62}$$

continued

If $-c_- < e < 0$, or if $c_+ < e$, compute

$$\begin{aligned}
 \phi &= \arccos \frac{1 + \frac{99}{16} e}{(1+3e)^{3/2}} \\
 Z_1 &= \frac{11}{48} + \frac{1}{3} \sqrt{1+3e} \cos\left(\frac{\phi}{3}\right) \\
 Z_2 &= \frac{11}{48} + \frac{1}{3} \sqrt{1+3e} \cos\left(\frac{\phi}{3} + \frac{2\pi}{3}\right) \\
 Z_3 &= \frac{11}{48} + \frac{1}{3} \sqrt{1+3e} \cos\left(\frac{\phi}{3} - \frac{2\pi}{3}\right) .
 \end{aligned} \tag{3.63}$$

In either case, choose $\sqrt{Z_1}$, $\sqrt{Z_2}$, and $\sqrt{Z_3}$ such that

$$\sqrt{Z_1} \sqrt{Z_2} \sqrt{Z_3} = \frac{3}{64} . \tag{3.64}$$

Then, the four roots of Eq. (38) are given by:

$$\begin{aligned}
 q_1 &= \sqrt{Z_1} + \sqrt{Z_2} + \sqrt{Z_3} - \frac{1}{4} \\
 q_2 &= \sqrt{Z_1} - \sqrt{Z_2} - \sqrt{Z_3} - \frac{1}{4} \\
 q_3 &= -\sqrt{Z_1} + \sqrt{Z_2} - \sqrt{Z_3} - \frac{1}{4} \\
 q_4 &= -\sqrt{Z_1} - \sqrt{Z_2} + \sqrt{Z_3} - \frac{1}{4}
 \end{aligned} \tag{3.65}$$

Note that, in general, only some of the solutions given by Eq. (65) will satisfy the condition $\text{Re } \underline{q} > 0$. For those roots having positive real parts, we use Eq. (37) to determine corresponding values of \underline{s} .

The behavior of \underline{s} as a function of e is displayed in Figs. 2, 3 and 4. In each case, the ordinate plots $\left[\tau_V / \tau_E \right]_{\underline{s}}$ because only one curve is necessary to define the function $\left[\tau_V / \tau_E \right]_{\underline{s}}$ versus e for all combinations of time constants. If we were to plot \underline{s} versus e , we would obtain a family of curves, with τ_V / τ_E a parameter. It must be emphasized, however, that the quantity $\left[\tau_V / \tau_E \right]_{\underline{s}}$ varies with k not only due to the dependence of s on k , but also due to the dependence of τ_V on k .

Figure 2 shows $\left[\tau_V / \tau_E \right]_{\underline{s}}$ versus e on linear scales in the region near the origin ($-2 \leq e \leq 2$). Solid lines indicate $\text{Re} \left[\tau_V / \tau_E \right]_{\underline{s}}$ and dotted lines $\text{Im} \left[\tau_V / \tau_E \right]_{\underline{s}}$. For $e < 0$, there is one pure real, growing ($\underline{s} > 0$) solution. Only one of the four solutions given in Eq. (65) has $\text{Re } \underline{q} > 0$. For $0 < e < c_+$ there are two pure, real, decaying ($\underline{s} < 0$) solutions, with values 0 and -1 at $e = 0$, and merging with $\left[\tau_V / \tau_E \right]_{\underline{s}} \approx -0.59$ at $e = c_+$. In this region, two solutions in Eq. (65) have $\text{Re } \underline{q} > 0$. Finally, for $c_+ < e$, there are two complex conjugate solutions with negative real part (decaying, oscillatory). Again, in this region, two solutions have $\text{Re } \underline{q} > 0$.

Figures 3 and 4 display $\left[\tau_V / \tau_E \right]_{\underline{s}}$ versus e over a wide range of values. Figure 3 shows $-e$ varying from 1 to 10^8 on a log scale, and Fig. 4 has $+e$ ranging from 1 to 10^8 . In Fig. 4, a dashed line indicates negative real values of $\left[\tau_V / \tau_E \right]_{\underline{s}}$ and a dotted line, again, imaginary values.

For large values of $\pm e$, the curves in Figs. 3 and 4 are as predicted by the approximation under $\left[\tau_V / \tau_E \right]_{\underline{s}} \gg 1$ given by Eq. (57):

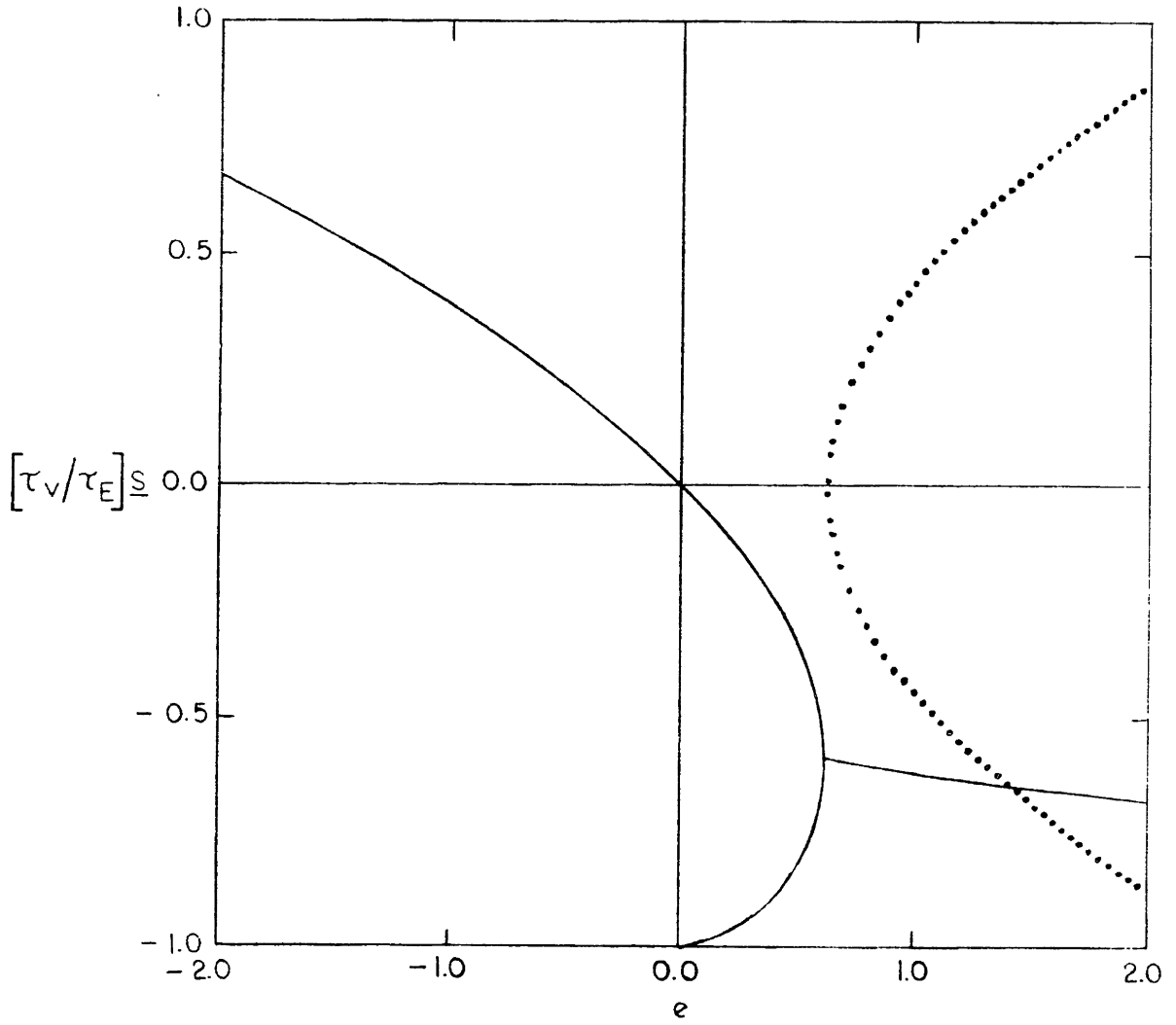


Figure 2

$[\tau_v/\tau_E]_s$ versus e ($-2 \leq e \leq 2$)

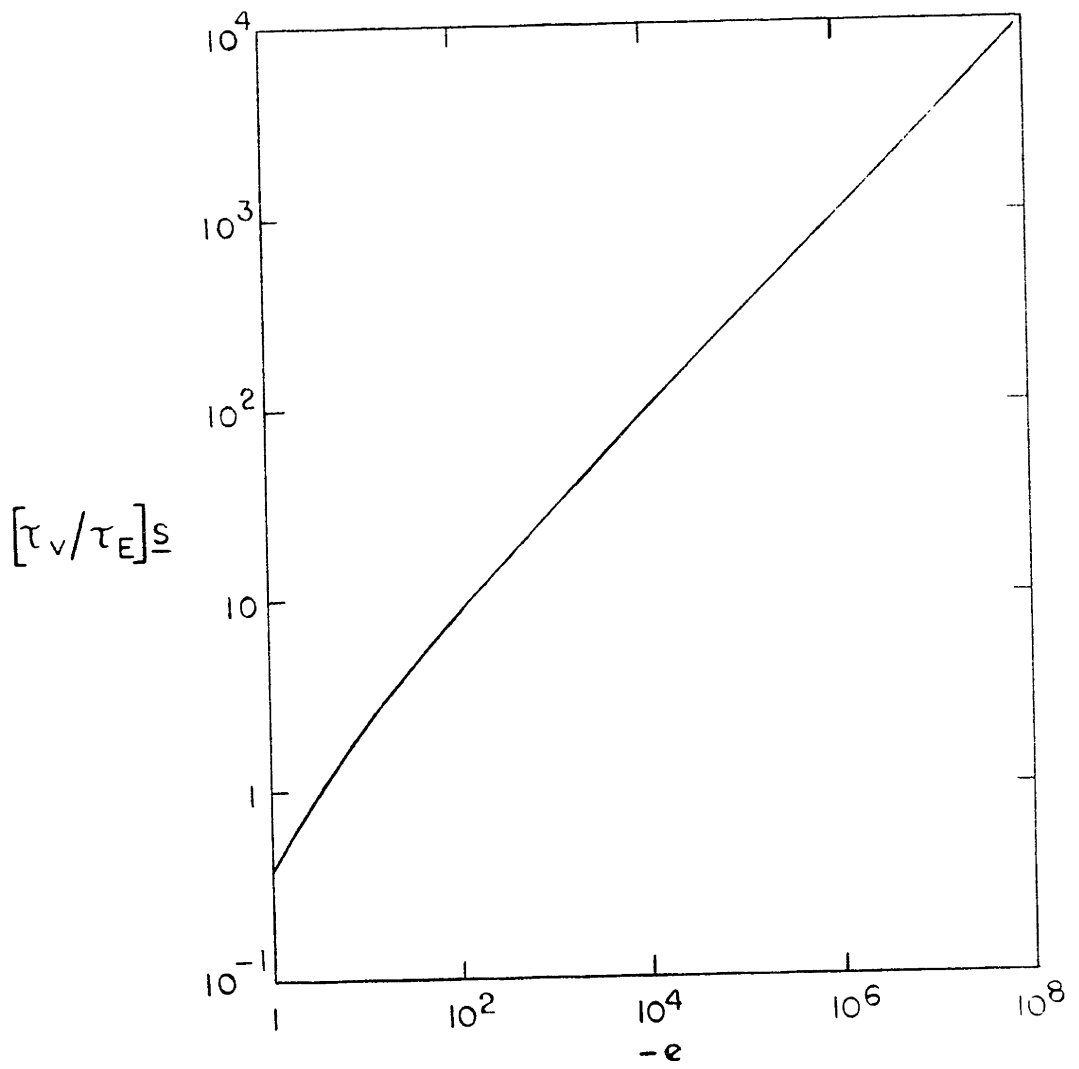


Figure 3

$[\tau_v/\tau_E]_s$ versus e ($1 < -e < 10^8$)

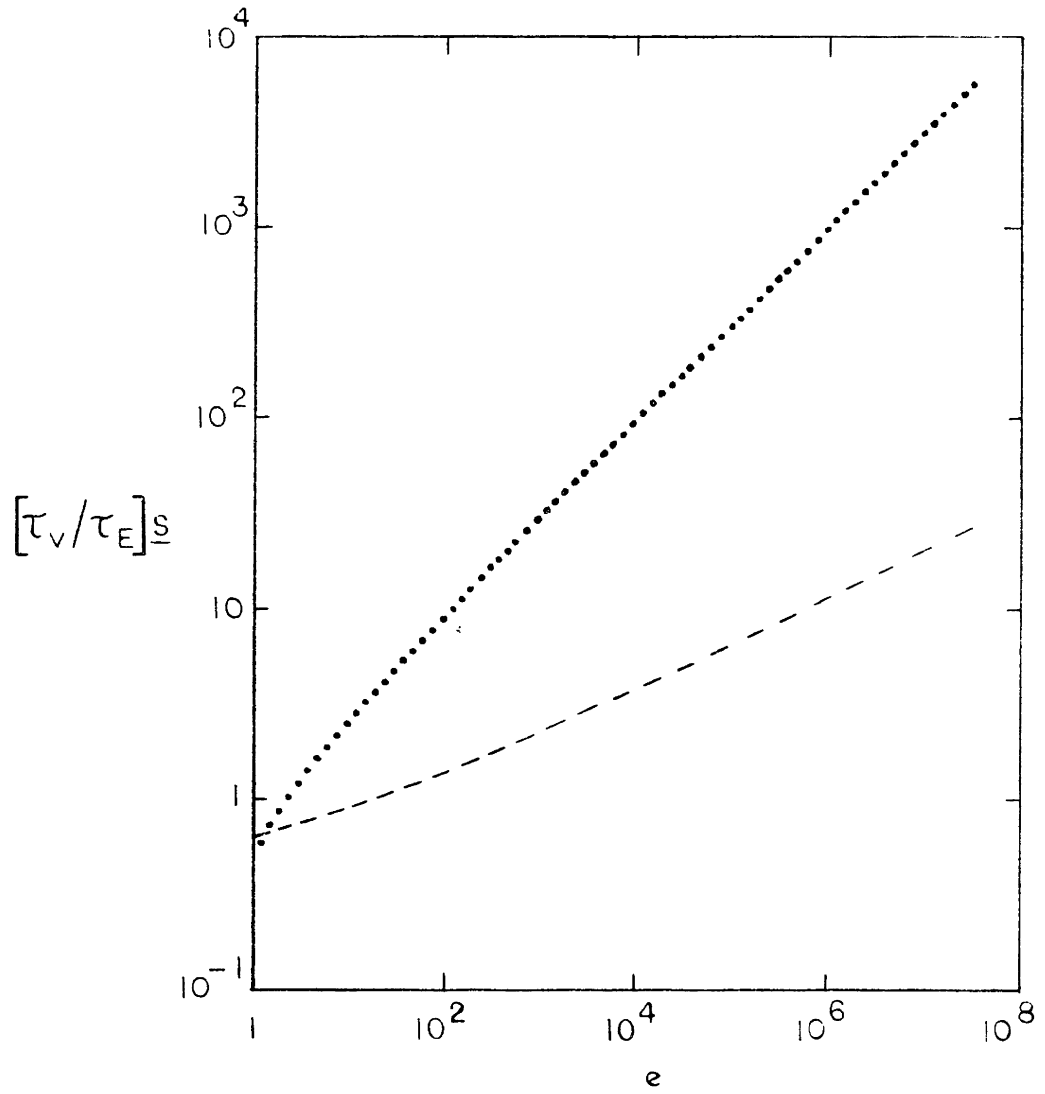


Figure 4

$[\tau_v/\tau_E]_s$ versus e ($1 < e < 10^8$)

$$\left[\tau_v / \tau_E \right]_s \approx \sqrt{-e} \quad (3.66)$$

Figures 5 and 6 show the behavior of e as a function of τ_E / τ_g and τ_E / τ_v . Again, a proper choice of scales allows the display of all information using one curve. Equation (41) is rewritten:

$$\left(\frac{\tau_E}{\tau_g} \right)^3 e = \left[\frac{\tau_E / \tau_v}{(\tau_E / \tau_g)^3} \right]^{-3/2} - \left[\frac{\tau_E / \tau_v}{(\tau_E / \tau_g)^3} \right]^{-1} \quad ; \quad (3.67)$$

the function $(\tau_E / \tau_g)^3 e$ versus $\tau_E / \tau_v / (\tau_E / \tau_g)^3$ is positive for $\tau_E / \tau_v / (\tau_E / \tau_g)^3 < 1$ and negative for $\tau_E / \tau_v / (\tau_E / \tau_g)^3 > 1$. It displays a minimum of

$(\tau_E / \tau_g)^3 e = -4/27$ at $\tau_E / \tau_v / (\tau_E / \tau_g)^3 = 9/4$. Figure 5 shows $(\tau_E / \tau_g)^3 e$ versus $\tau_E / \tau_v / (\tau_E / \tau_g)^3$ on linear scales for $0.5 \leq \tau_E / \tau_v / (\tau_E / \tau_g)^3 \leq 10.0$.

Figure 6 shows the same function, over a wide range of values, on log scales. The dashed line for $\tau_E / \tau_v / (\tau_E / \tau_g)^3 > 1$ indicates negative ordinate values. For $\tau_E / \tau_v / (\tau_E / \tau_g)^3 \ll 1$, or equivalently, $\tau_v \gg \tau_g \left(\frac{\tau_g}{\tau_E} \right)^2$, Eq. (67) becomes:

$$\left(\frac{\tau_E}{\tau_g} \right)^3 e \approx \left[\frac{\tau_E / \tau_v}{(\tau_E / \tau_g)^3} \right]^{-3/2} \quad (3.68)$$

or,

$$e \approx \left(\frac{\tau_v}{\tau_g} \right)^{3/2} \quad (3.69)$$

This behavior corresponds to the solid line with slope $-\frac{3}{2}$ in Fig. 6. On the other hand, for $\tau_E / \tau_v / (\tau_E / \tau_g)^3 \gg 1$, or equivalently, $\tau_v \ll \tau_g (\tau_g / \tau_E)^2$, Eq. (67) becomes:

$$\left(\frac{\tau_E}{\tau_g} \right)^3 e \approx - \left[\frac{\tau_E / \tau_v}{(\tau_E / \tau_g)^3} \right]^{-1} \quad (3.70)$$

or

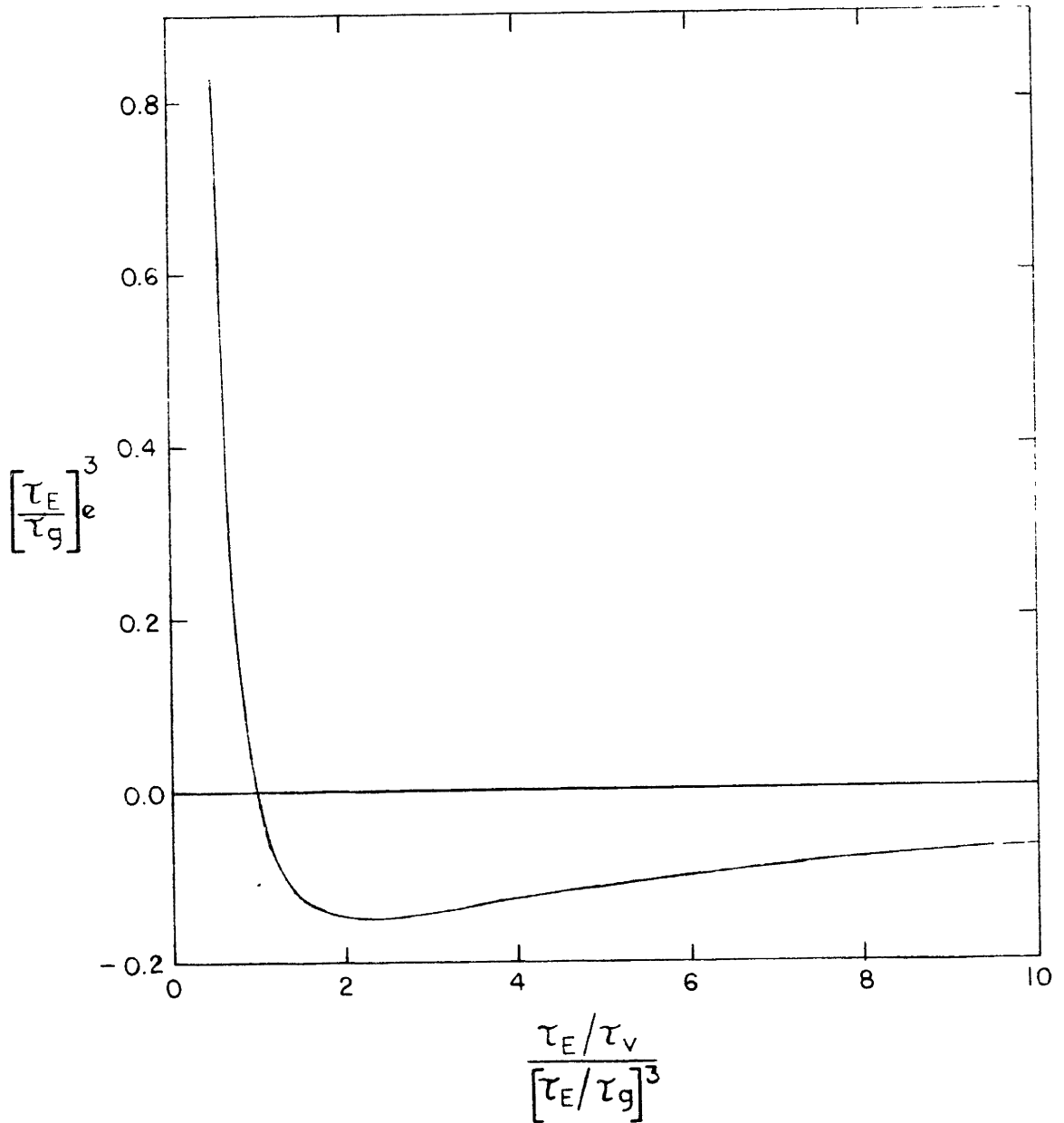


Figure 5

$$[\tau_E/\tau_g]^3 e \text{ versus } \frac{\tau_E/\tau_v}{[\tau_E/\tau_g]^3} \left(0.5 \leq \frac{\tau_E/\tau_v}{[\tau_E/\tau_g]^3} \leq 10.0 \right)$$

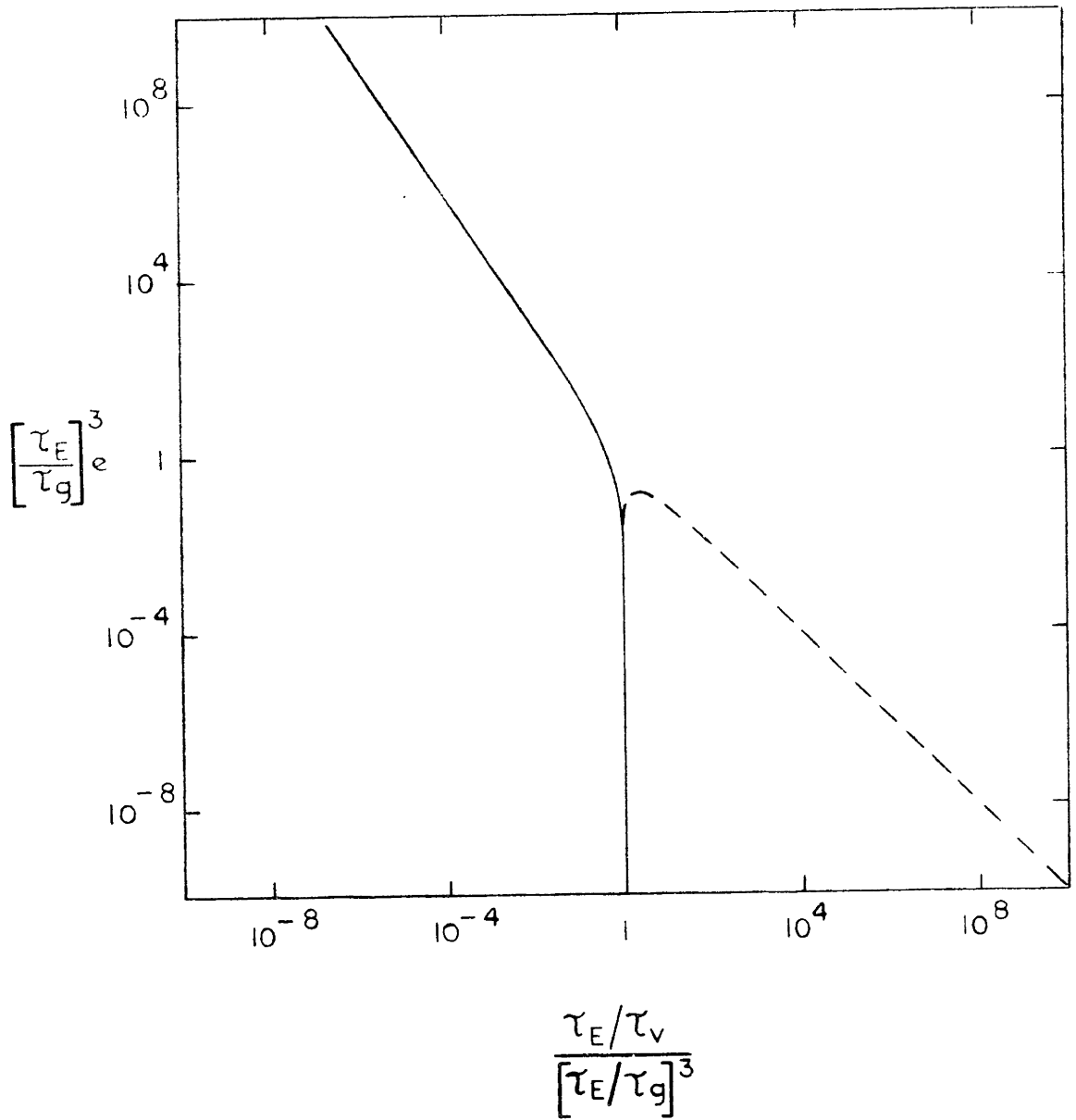


Figure 6

$$\left[\frac{\tau_E}{\tau_g}\right]^3 e \text{ versus } \frac{\tau_E / \tau_v}{\left(\tau_E / \tau_g\right)^3} \quad \left(10^{-7} < \frac{\tau_E / \tau_v}{\left(\tau_E / \tau_g\right)^3} < 10^9 \right)$$

$$e \approx -\frac{\tau_v}{\tau_g} \quad . \quad (3.71)$$

This behavior corresponds to the dashed line with slope -1 in Fig. 6.

We may now consider the behavior of \underline{s} as a function of τ_E/τ_v (k^2 dependence) for a given value of τ_E/τ_g . For small enough τ_E/τ_v , e is positive and large. Hence, $[\tau_v/\tau_E]\underline{s}$ is decaying, oscillatory. In this region, the density difference (a heavy fluid below a light fluid) dominates over electromechanical effects.

As τ_E/τ_v increases, e decreases until, eventually, the value $e = c_+$ is reached. Here, the imaginary part of $[\tau_v/\tau_E]\underline{s}$ has just become zero and the negative real part splits into two negative pure real solutions.

As τ_E/τ_v increases further, one of the solutions becomes less negative and one more negative. When τ_E/τ_v reaches the value $(\tau_E/\tau_g)^3$, e passes through zero. At this point, one solution of $[\tau_v/\tau_E]\underline{s}$ changes from negative to positive pure real, and the other reaches the value -1 and disappears. The value of τ_E/τ_v where the positive solution first appears corresponds to the critical wavenumber defined by Eq. (49).

Further increase of τ_E/τ_v yields further decrease of e , until, at $\tau_E/\tau_v = \frac{9}{4} \left(\frac{\tau_E}{\tau_g} \right)^3$, the minimum value, $e = -\frac{4}{27} \left(\frac{\tau_g}{\tau_E} \right)^3$ is attained. At this point, $[\tau_v/\tau_E]\underline{s}$ reaches a maximum. (Note that this does not imply a maximum in \underline{s} at this point.)

As τ_E/τ_v is increased even more, $[\tau_v/\tau_E]\underline{s}$ becomes less negative, approaching zero asymptotically as τ_E/τ_v is increased without bound. Correspondingly, $[\tau_v/\tau_E]\underline{s}$ remains positive pure real and decreases toward zero. In this region, the condition $[\tau_v/\tau_E]\underline{s} \ll 1$ holds, and Eq. (54) is applicable. Thus, s approaches the value $1/2\tau_E$ as k is made large. Physically, for very short wavelengths, a competition between an electrical surface force density

of the form $\frac{1}{2} \epsilon E^2$ and a viscous drag of the form $\eta \nabla^2 \bar{v}$ leads to a growth rate $\frac{1}{2\tau_E}$.

If the condition $(\tau_E/\tau_g)^3 \ll 1$ holds, then near the minimum in e , $-e \gg 1$. In this case, the condition $[\tau_V/\tau_E]_{\underline{s}} \gg 1$ is satisfied, and Eq. (58) is applicable. In fact, there will exist a range of τ_V for which $\tau_V \ll \tau_g (\tau_g/\tau_E)^2$ also, and hence, Eq. (60) applies. In this case, the competition is between the electrical surface force density, $\frac{1}{2} \epsilon E^2$ and inertia $\rho(\partial \bar{v}/\partial t)$, and leads to a growth rate $k \sqrt{[\epsilon J^2/2\rho](1/\sigma_a - 1/\sigma_b)^2}$. The value of k where transition from inertia-dominated to viscous-dominated solutions occurs may be determined by setting:

$$k \sqrt{\frac{\epsilon J^2}{2\rho} \left(\frac{1}{\sigma_a} - \frac{1}{\sigma_b} \right)^2} = \frac{1}{2\tau_E} \quad (3.72)$$

Combining Eqs. (42) and (72) we obtain:

$$k_{\text{transition}} = \frac{J \left(\frac{1}{\sigma_a} - \frac{1}{\sigma_b} \right) \sqrt{\frac{\epsilon \rho}{2}}}{2 \eta} \quad (3.73)$$

Note that k must be small enough to avoid the viscous-dominated region, yet large enough to avoid the gravity-dominated region, in order for the inertia-dominated region to appear. It is possible for τ_g to be small enough (density difference large enough) so that the condition $(\tau_E/\tau_g)^3 \ll 1$ does not hold; thus, for there to exist no range of values for k in which the inertia dominated solution appears. Stated another way, an inertia-dominated regime will appear only if $k_{\text{transition}} \gg k_c$.

To deal with a real set of physical constants, consider the case of two layers of water, the lower an electrolyte and the upper distilled. We take:

$$\rho = 10^3 \frac{\text{Kgm}}{\text{m}^3} ; \quad \eta = 10^{-3} \frac{\text{Kgm}}{\text{msec}} ; \quad \nu = 10^{-6} \frac{\text{m}^2}{\text{sec}}$$

$$J \left(\frac{1}{\sigma_a} - \frac{1}{\sigma_b} \right) = \frac{10\text{V}}{1\text{cm}} = 10^3 \frac{\text{V}}{\text{m}} ; \quad \epsilon = 81\epsilon_0 .$$

Then, $\tau_E = 2.79 \text{ sec}$. We take several values of $\Delta\rho/\rho$ to see how the value of τ_g affects the solution. Figures 7 through 17 display s versus k on linear and log scales for various values of $\Delta\rho/\rho$. The usual coding is employed: solid curves for real values, dotted curves for imaginary values, and dashed curves for negative real values on log plots.

Note that, in each case, for large enough k , the electric-viscous solution $s = 1/2\tau_E$ is reached. With zero density difference (Fig. 7), we see the electric-inertia solution increasing linearly with k for small k and the electric-viscous solution for large k . The transition wavenumber is as given by Eq. (73).

As a small density difference is introduced ($\Delta\rho/\rho = 10^{-7}$ in Figs. 8 and 9 and $\Delta\rho/\rho = 10^{-6}$ in Figs. 10 and 11), we see the appearance of k_c , the lower bound for growing solutions, two decaying solutions for values of k less than but near k_c , and finally, gravity-dominated decaying oscillatory solutions for small k . In Figs. 8 and 10, the inertia-dominated regime is apparent for $k_c < k < k_{\text{transition}}$.

As the density difference is increased, the inertia-dominated regime becomes narrower and the regime with two purely decaying solutions becomes wider. Figures 12 and 13 have $\Delta\rho/\rho = 10^{-5}$, Figs. 14 and 15 have $\Delta\rho/\rho = 10^{-4}$, and Figs. 16 and 17 have $\Delta\rho/\rho = 10^{-3}$. In Figs. 14 and 16, the inertia-dominated regime is completely absent, with transition directly from viscous-dominated to gravity-dominated solutions. (In Figs. 15 and 17, only

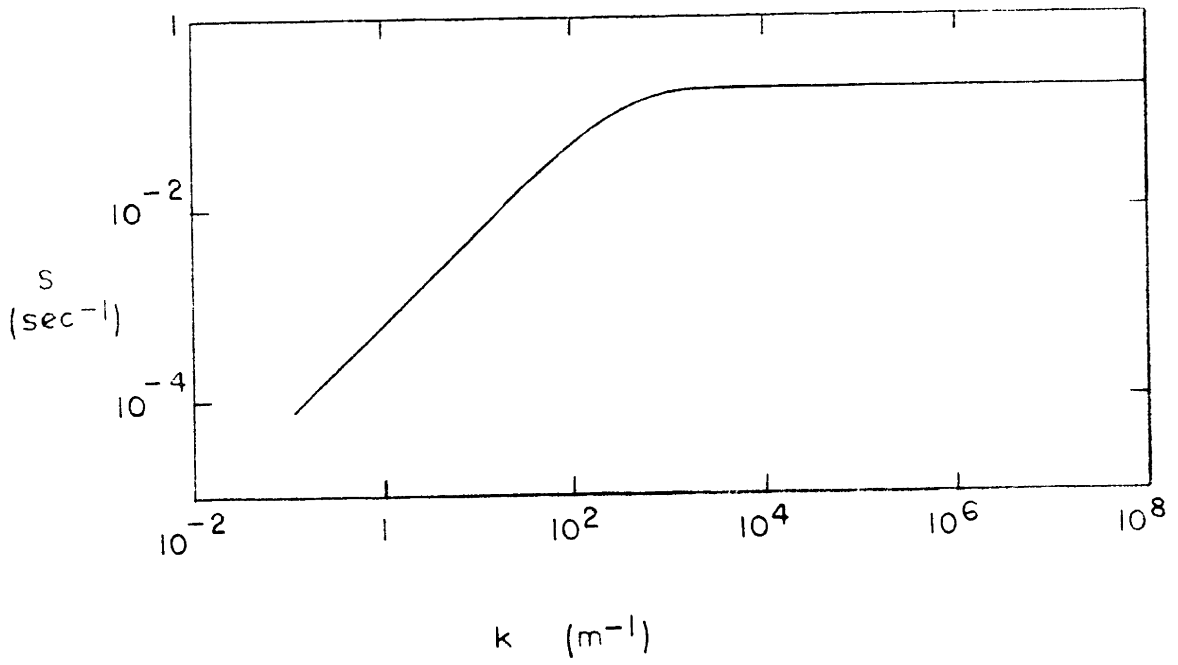


Figure 7

s versus k , $\|\rho\|/\rho = 0$ ($10^{-1} \leq k \leq 10^8$)

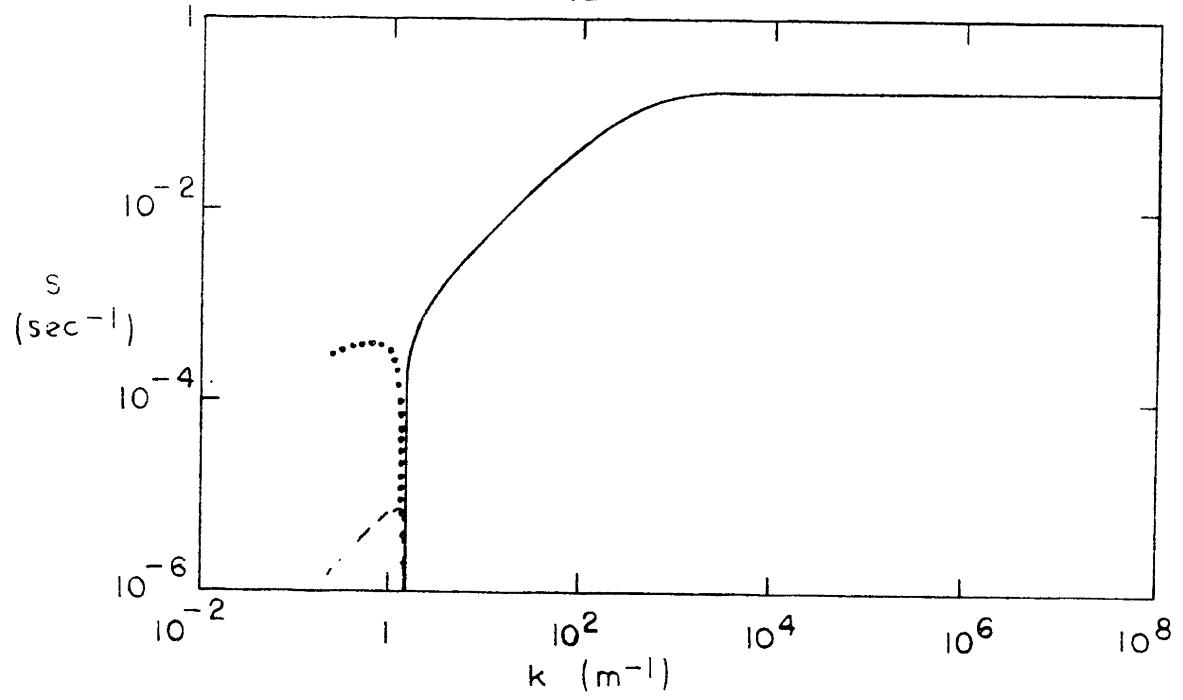


Figure 8
s versus k, $[\rho]/\rho = 10^{-7}$ ($10^{-1} \leq k \leq 10^8$)

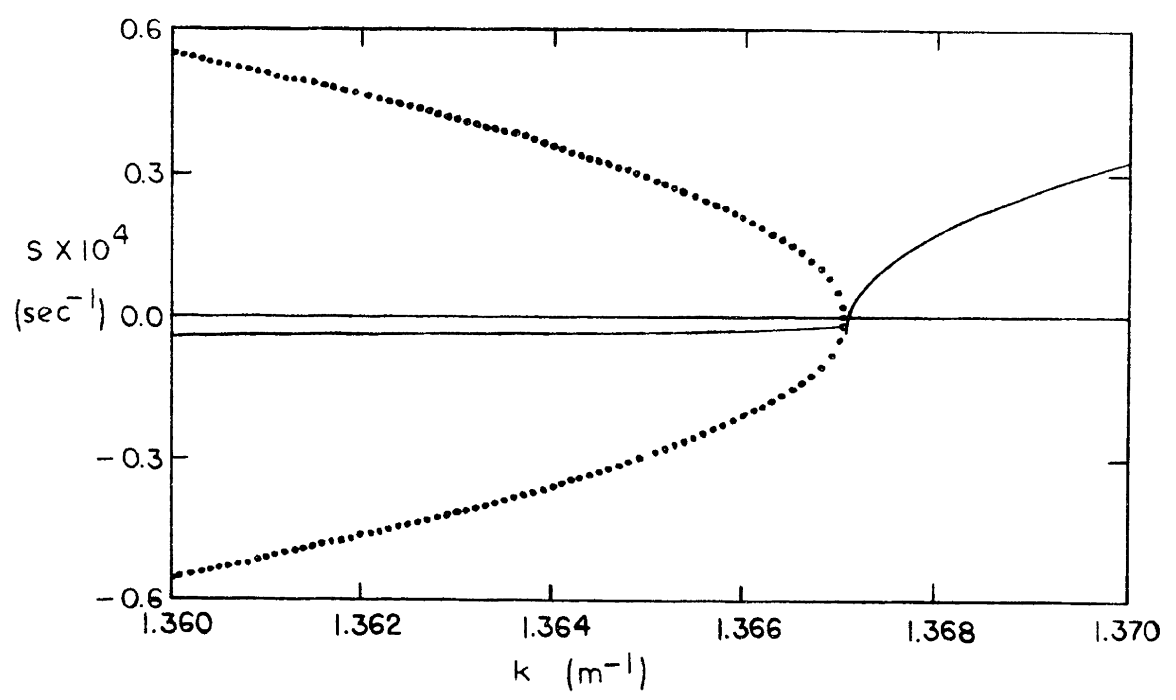


Figure 9
s versus k, $[\rho]/\rho = 10^{-7}$ ($1.36 \leq k \leq 1.37$)

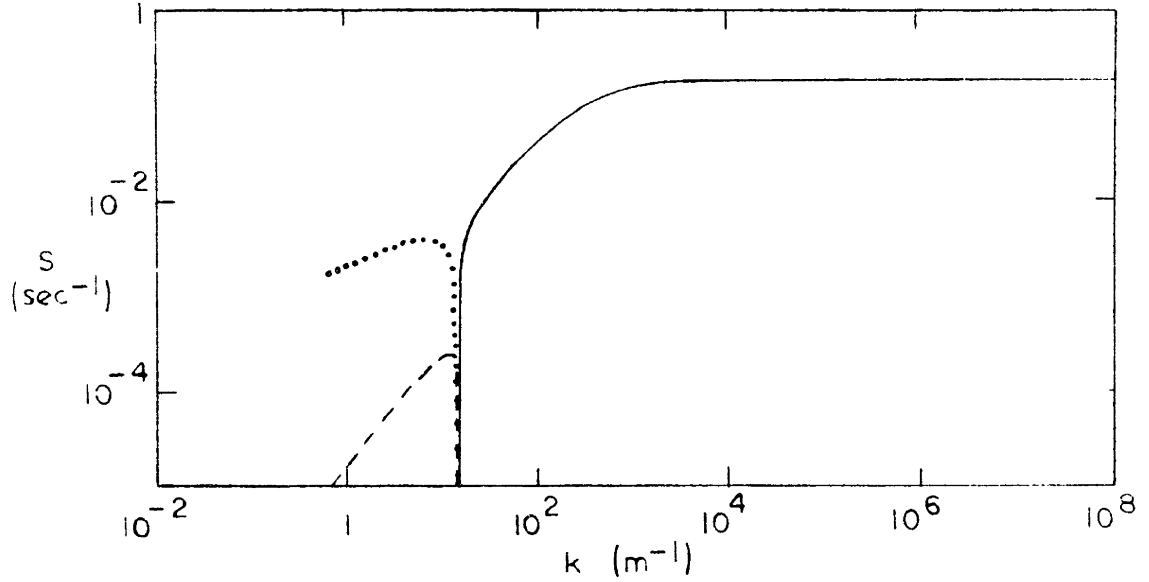


Figure 10

s versus k , $[\rho]/\rho = 10^{-6}$ ($1 \leq k \leq 10^8$)

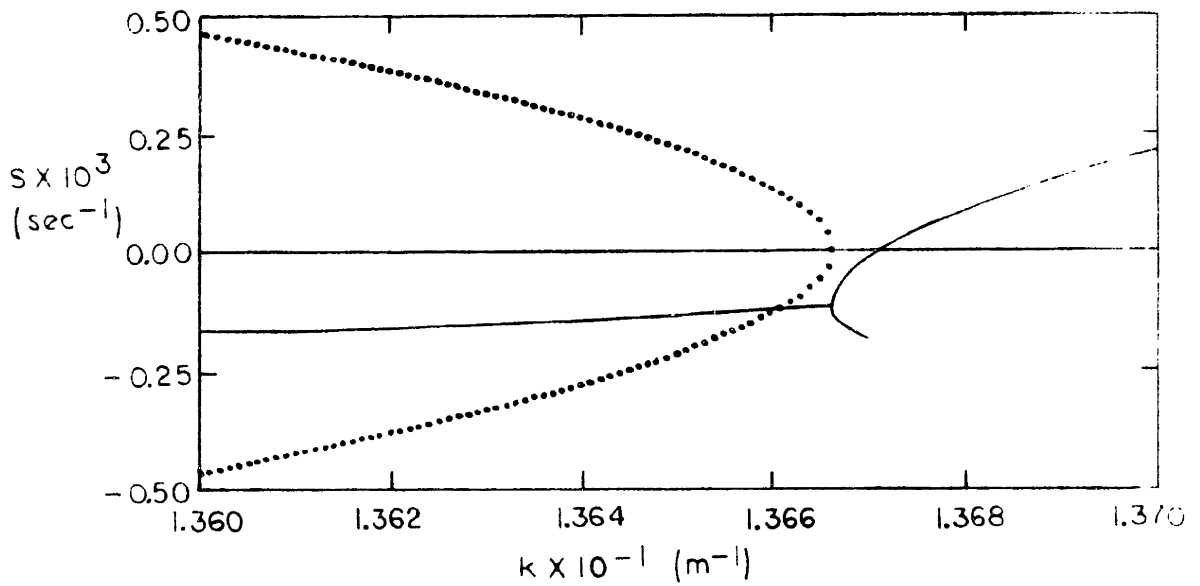


Figure 11

s versus k , $[\rho]/\rho = 10^{-6}$ ($13.6 \leq k \leq 13.7$)

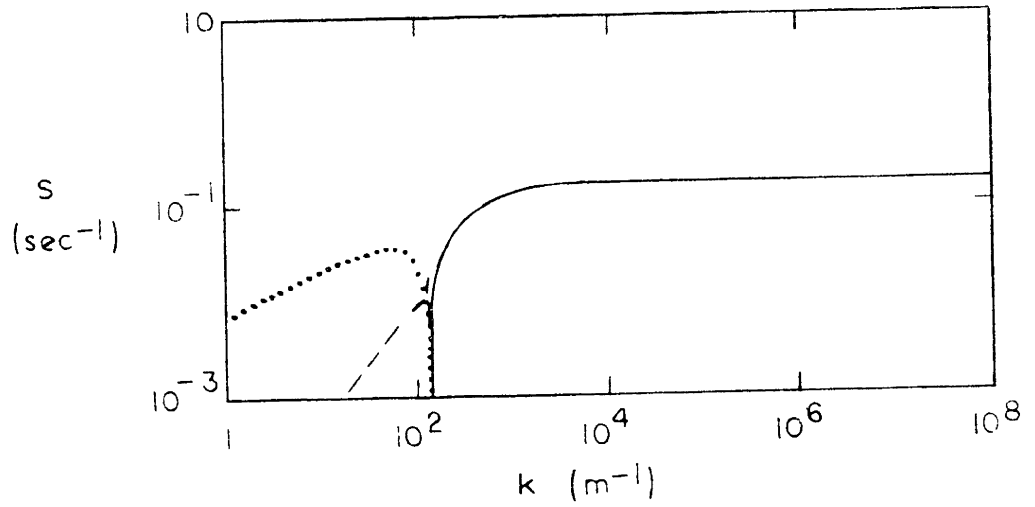


Figure 12

s versus k , $[\rho]/\rho = 10^{-5}$ ($1 \leq k \leq 10^8$)

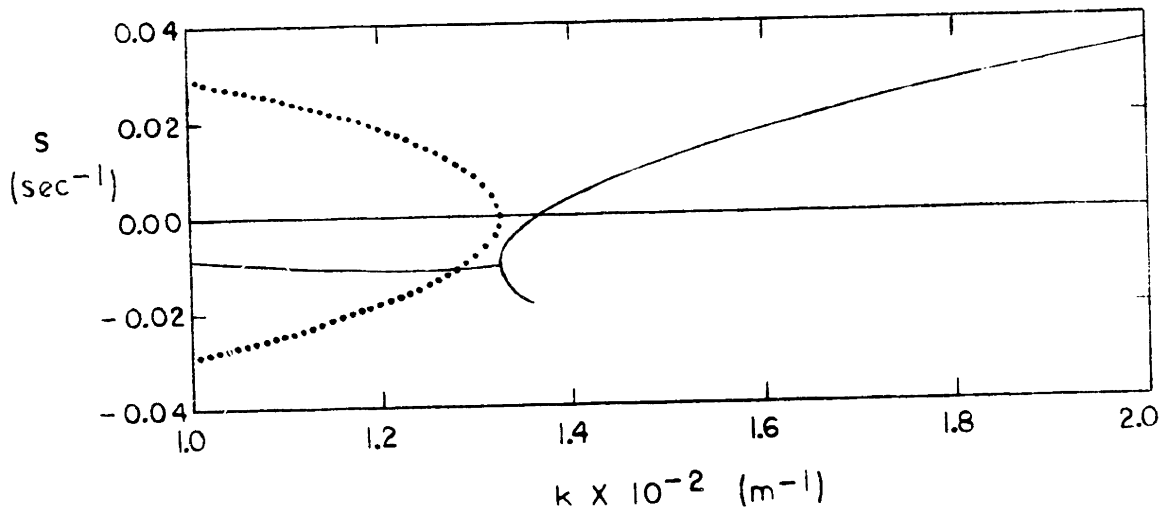


Figure 13

s versus k , $[\rho]/\rho = 10^{-5}$ ($100 \leq k \leq 200$)

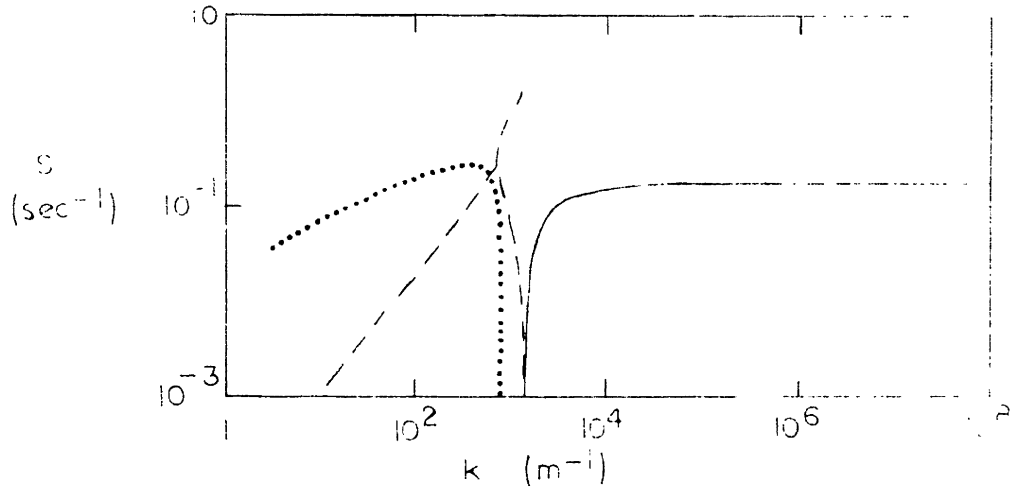


Figure 14

s versus k , $\frac{\rho_0}{\rho} = 10^{-4}$ ($10 \leq k \leq 10^8$)

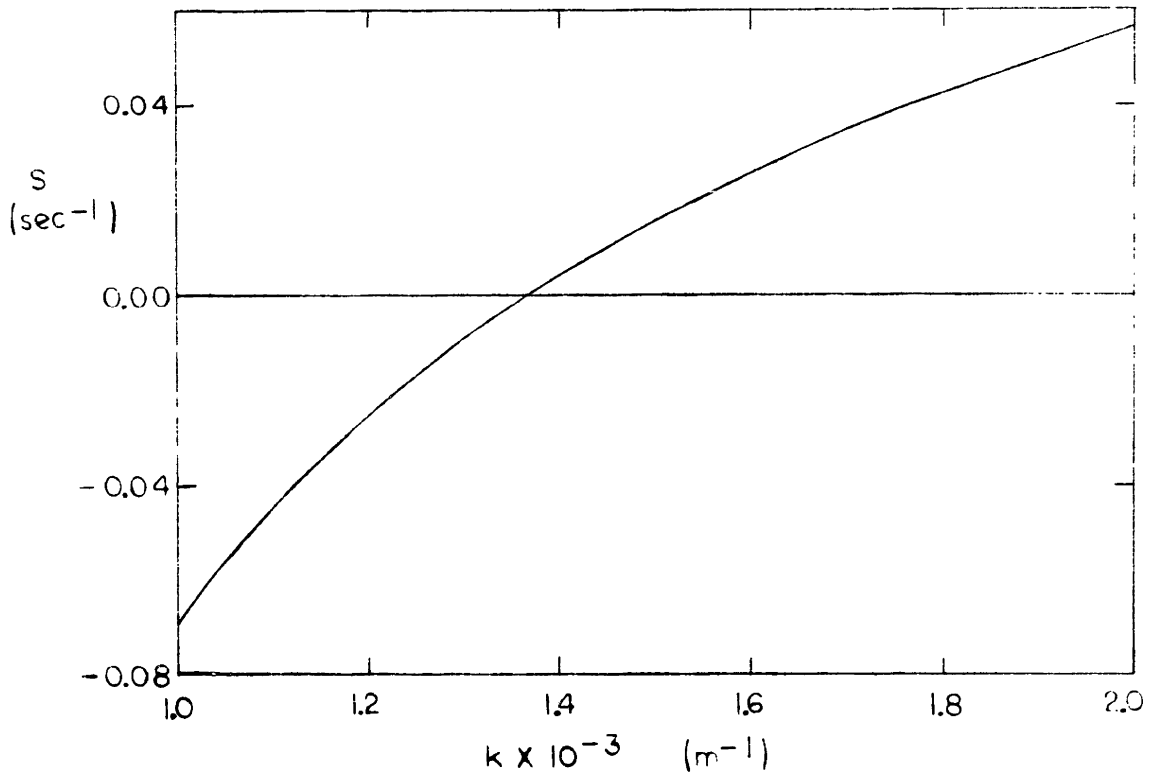


Figure 15

s versus k , $\frac{\rho_0}{\rho} = 10^{-4}$ ($1000 \leq k \leq 2000$)

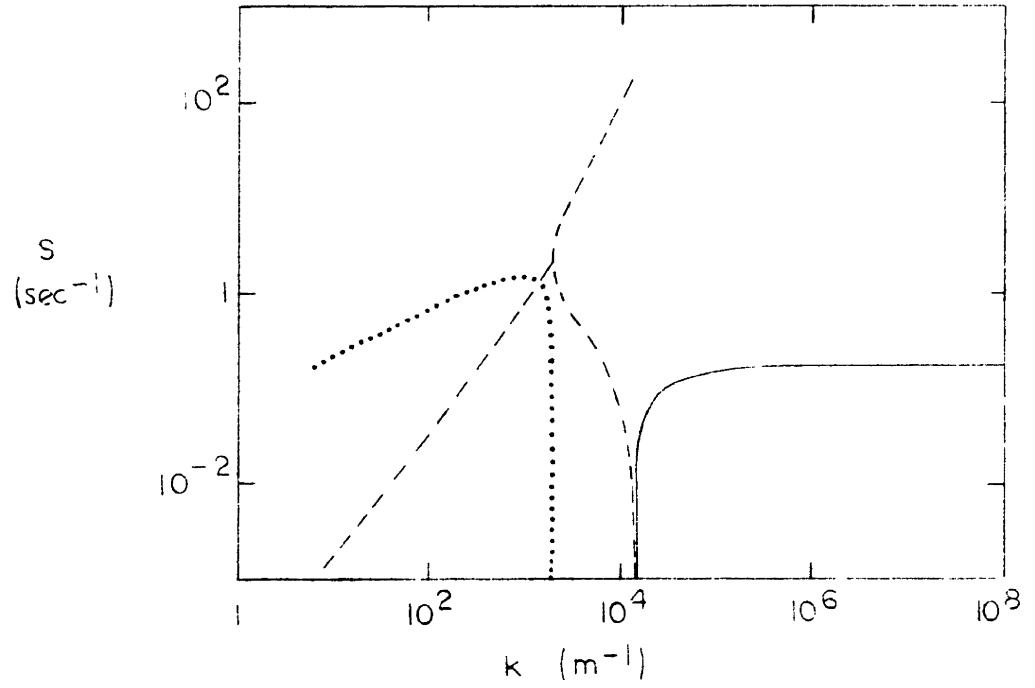


Figure 16: s versus k , $\rho_0/\rho = 10^{-3}$ ($10 \leq k \leq 10^8$)

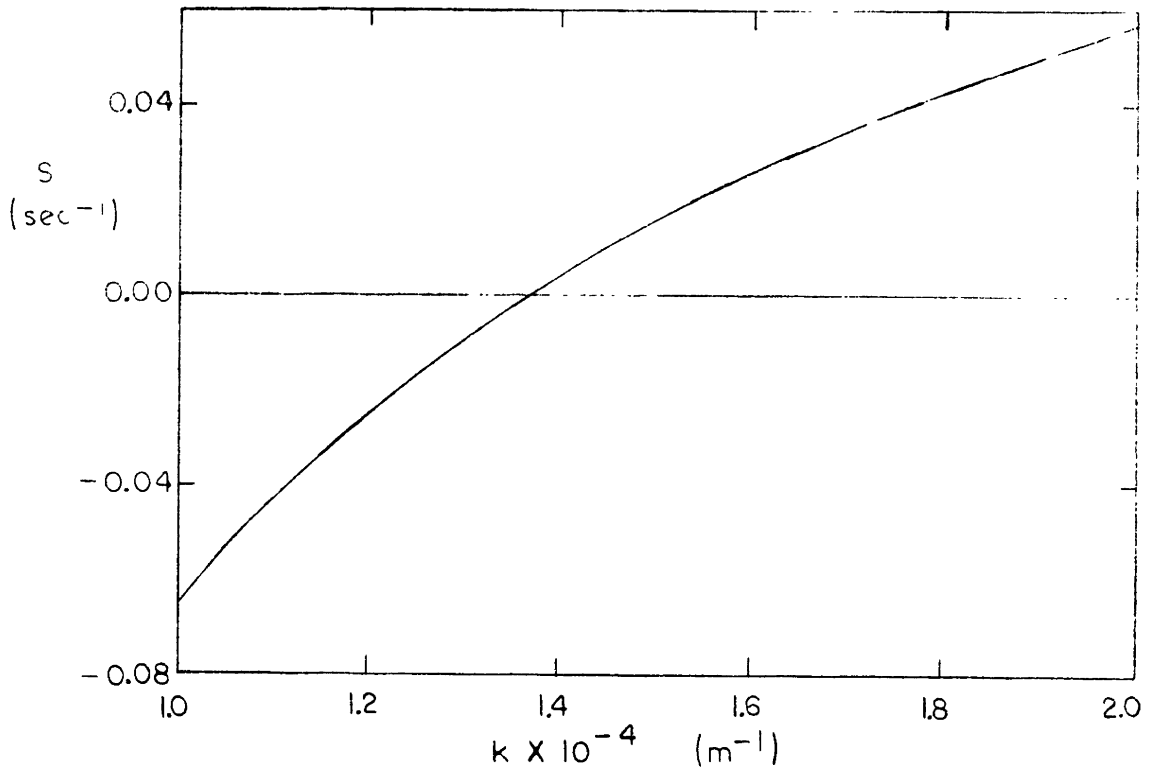


Figure 17

s versus k , $\rho_0/\rho = 10^{-3}$ ($10^4 \leq k \leq 2 \times 10^4$)

the less negative solution is shown in the region of two pure decaying solutions.)

C. Equilibrium Tangential Electric Field

A plane interface bounds two incompressible fluid half-spaces, stressed by an initially tangential electric field, $\vec{E}_0 \vec{i}_z$, as shown in Fig. 18.

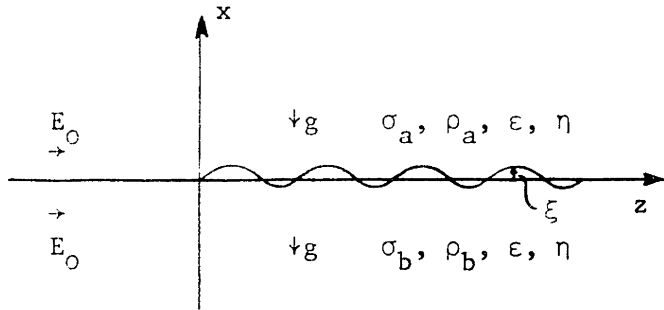


Figure 18 .

Tangential Field Geometry

The situation is identical to that considered in Section III.B, except that the equilibrium field has been changed from normal to tangential to the interface. Again, we are concerned, physically, with two miscible fluids, one doped to increase its conductivity. The same approximation concerning small density difference, $[\rho]$ is made. We seek the dispersion relation for small-amplitude sinusoidal interface motions,

$$\xi = \text{Re } \hat{\xi} e^{(st-jkz)} \quad . \quad (3.74)$$

As in Section III.B, mechanical stress balance from Eq. (2.75) requires:

$$[S_{ij}]n_j + [T_{ij}]n_j = 0 \quad (3.75)$$

with the interface normal defined by:

$$n_x = 1 \quad (3.76)$$

$$n_z = -\frac{\partial \xi}{\partial z} = \text{Re } \frac{jk}{s} \hat{v}_x(\alpha) e^{(st-jkz)} \quad . \quad (3.77)$$

In equilibrium, Eq. (75) is satisfied by:

$$\llbracket \rho^E \rrbracket = 0 \quad . \quad (3.78)$$

Subject to interface perturbation, we obtain for the $i = x$ and $i = z$ components of Eq. (75), respectively:

$$\hat{S}_x^{(\alpha)} - \hat{S}_x^{(\beta)} - \epsilon E_0 \hat{E}_z^{(\alpha)} + \epsilon E_0 \hat{E}_z^{(\beta)} = 0 \quad (3.79)$$

$$\hat{S}_z^{(\alpha)} - \hat{S}_z^{(\beta)} + \epsilon E_0 \hat{E}_x^{(\alpha)} - \epsilon E_0 \hat{E}_x^{(\beta)} = 0 \quad (3.80)$$

The boundary conditions on perturbation fluid velocity, from Eqs. (2.73) and (2.74), are:

$$\hat{v}_x^{(\alpha)} = \hat{v}_x^{(\beta)} \quad (3.81)$$

$$\hat{v}_z^{(\alpha)} = \hat{v}_z^{(\beta)} \quad (3.82)$$

The boundary condition on tangential electric field at the interface is, from Eq. (2.10)

$$\bar{n} \times \llbracket \bar{E} \rrbracket = 0 \quad (3.83)$$

Subject to perturbations, we obtain for Eq. (83):

$$\hat{E}_z^{(\alpha)} = \hat{E}_z^{(\beta)} \quad . \quad (3.84)$$

The boundary condition on normal electric field at the interface, recalling the assumption of instantaneous charge relaxation, is from Eq. (2.12):

$$\bar{n} \cdot \llbracket \sigma \bar{E} \rrbracket = 0 \quad . \quad (3.85)$$

Writing out Eq. (85) for the assumed equilibrium and perturbation yields:

$$\sigma_a \hat{E}_x^{(\alpha)} - \sigma_b \hat{E}_x^{(\beta)} + \llbracket \sigma \rrbracket E_0 \frac{jk}{s} \hat{v}_x^{(\alpha)} = 0 \quad . \quad (3.86)$$

The manipulations required to express the transfer relations -- Eqs. (2.63), (2.64), (2.104) and (2.105) in terms of the interface variables appearing in the boundary conditions just derived are identical to those performed in Section III.B. Immediately applicable are Eqs. (18), (19), (20) and (21). Combining Eqs. (79) and (84) we arrive at:

$$\hat{S}_x^{(\alpha)} = \hat{S}_x^{(\beta)} \quad . \quad (3.87)$$

Combining Eqs. (20), (21), (81) and (87):

$$\left[2\eta \frac{q}{k}(k+q) - \frac{g \llbracket \rho \rrbracket}{s} \right] \hat{v}_x^{(\alpha)} = 0 \quad . \quad (3.88)$$

For non-trivial solutions, then, we require the dispersion relation:

$$2\eta \frac{q}{k}(k+q) - \frac{g \llbracket \rho \rrbracket}{s} = 0. \quad (3.89)$$

Equation (89) may be derived in a more systematic manner by algebraically combining Eqs. (84), (86), (18) and (19) to obtain $\hat{E}_x^{(\alpha)}$, $\hat{E}_x^{(\beta)}$, $\hat{E}_z^{(\alpha)}$ and $\hat{E}_z^{(\beta)}$, each in terms of $\hat{v}_x^{(\alpha)}$ and substituting these four equations, as well as (81) and (82), into Eqs. (79), (80), (20) and (21) to yield six homogeneous equations in six unknowns. Setting the determinant of the coefficient matrix to zero then results in Eq. (89).

Melcher and Schwarz⁽²⁾ have considered the problem of two fluid half-spaces stressed by an initially tangential electric field in greater generality than in the analysis presented above. We may check Eq. (89) by

considering the appropriate limit of the relation in Reference (2).

Setting $\rho_a = \rho_b$ in all terms except the gravitational, which involves

$g[\rho]$, $\epsilon_a = \epsilon_b = \epsilon$, $v_a = v_b = 2\eta/[\rho_a + \rho_b]$, and $T = 0$, we obtain a simplified version of Eq. (34) of Reference (2):

$$\left[1 - \frac{gk[\rho]}{2\rho s^2} \right] [q - k] + k = 0 \quad . \quad (3.90)$$

Using Eq. (22), we see that Eqs. (89) and (90) are identical.

Note that Eq. (89) is identical to Eq. (31) in the special case $J = 0$ of that equation, and that E_0 does not appear in Eq. (89). Physically, we have found that the tangential field system involves no electromechanical coupling. We expect the system to exhibit only decaying modes in time for any given wavenumber, k . These modes are identical to those found in the normal field system of Section III.B in the limit $J = 0$. Although we may not use the normalization of Section III.B in this limit ($\tau_E \rightarrow \infty$), we note that the parameter e defined by Eq. (41) becomes simply:

$$e = (\tau_v/\tau_g)^{3/2} \quad (3.91)$$

and is always positive. Figure 2 then indicates that s always has a negative real part.

The nature of the decaying solutions changes from pure decay to oscillatory decay at

$$e = c_+ \approx 0.61968 \quad (3.92)$$

or, combining Eqs. (91), (92), (43) and (44), at

$$k \equiv k_{gv} = \left[\frac{-g[\rho]/2\rho}{c_+ v^2} \right]^{1/3} \approx 1.1729 \left[\frac{-g[\rho]}{2\rho v^2} \right]^{1/3} \quad (3.93)$$

For $k > k_{gv}$, $e < c_+$ and there are two negative pure real (decaying) solutions for s . For $k < k_{gv}$, $e > c_+$ and there are two complex conjugate solutions with negative real part (decaying, oscillatory).

We may further characterize the slowly decaying solution in the region $k > k_{gv}$ when k is large enough so that $|s/k^2\nu| \ll 1$. Then, the definition of q , Eq. (22), may be approximated:

$$q = \sqrt{k^2 + s/\nu} \approx k \left(1 + \frac{s}{2k^2\nu} \right) \quad . \quad (3.94)$$

Substituting Eq. (94) into the fourth order equation for q [Eq. (36) with $J = 0$], and retaining only first order terms in $s/k^2\nu$:

$$s \approx \frac{g[\rho]}{4\rho\nu k} \quad . \quad (3.95)$$

It is to be recognized, at this point, that the absence of electro-mechanical coupling in a linearized analysis does not preclude the physical possibility of a surface-coupled electrohydrodynamic instability. Such an instability, however, must arise from nonlinear coupling terms.

CHAPTER III BIBLIOGRAPHY

1. Melcher, James R. and Smith, Charles V., Jr., "Electrohydrodynamic Charge Relaxation and Interfacial Perpendicular-Field Instability", Phys. Fluids, v. 12, #4, April, 1969, pp. 778-790.
2. Melcher, James R., and Schwarz, Wilfred, J., Jr., "Interfacial Relaxation Overstability in a Tangential Electric Field", Phys. Fluids, v. 11, #12, December, 1968, pp. 2604-2616.

CHAPTER IV. EXPONENTIAL CONDUCTIVITY DISTRIBUTION IN TANGENTIAL FIELD

A. Layer Transfer Relations

The interfacial discontinuity models presented in Chapter III clearly cannot account for effects occurring on the scale of the thickness of the interface itself. It is our aim, now, to relax the restriction that the region over which conductivity variation occurs at the junction between fluids be thin compared with lengths describing instability dynamics. We consider a layer of fluid, as shown in Fig. 1, extending from $x = 0$ to $x = \Delta$, over which an equilibrium conductivity distribution, $\sigma_0(x)$ is given, experiencing a uniform equilibrium tangential electric field, $E_0 \bar{i}_z$.

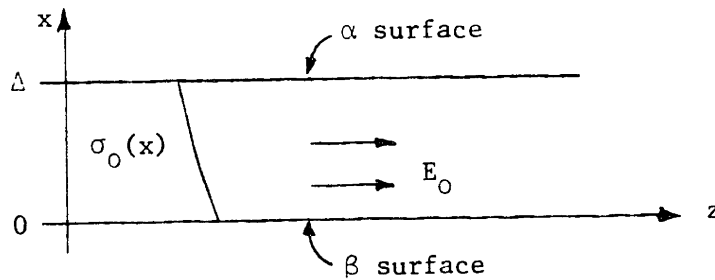


Figure 1. Layer of varying conductivity in tangential field.

It is to be emphasized that the discussion at the beginning of Section III.A still pertains here. That is, we continue to assume that diffusion times are long compared to times describing instability dynamics, so that we may describe the layer by an equilibrium conductivity distribution, itself evolving slowly with time, and subject to electrohydrodynamic instability as modeled in a situation of static equilibrium.

In equilibrium, the fluid is static:

$$\frac{\nabla E}{\nu} = 0 \tag{4.1}$$

and charge free:

$$\rho_f^E = 0 \quad . \quad (4.2)$$

We consider perturbations with z-t dependence $e^{(st-jkz)}$. The perturbation dynamics of the incompressible, viscous layer are described, mechanically, by Eq. (2.71), with the convective inertia term on the left absent due to linearization. The electrical drive term on the right, subject to perturbation is, using Eq. (2.1) and linearizing:

$$[\nabla \times (\rho_f \bar{E})]_y = [\nabla \rho_f \times \bar{E}]_y \approx -E_0 \frac{\partial \rho_f}{\partial x} \quad . \quad (4.3)$$

Thus, combining Eqs. (2.71) and (4.3) in terms of complex amplitudes:

$$s\rho[D^2 - k^2]\hat{\psi} = \eta[D^2 - k^2]^2\hat{\psi} - E_0 D\hat{\rho}_f \quad (4.4)$$

where:

$$D \equiv \frac{d}{dx} \quad . \quad (4.5)$$

Poisson's equation (2.5) relates perturbation charge to potential:

$$(D^2 - k^2)\hat{\phi} = -\hat{\rho}_f/\epsilon \quad . \quad (4.6)$$

Combining Eqs. (4) and (6):

$$[D^2 - k^2][(D^2 - k^2 - \frac{s\rho}{\eta})\hat{\psi} + \frac{\epsilon E_0}{\eta} D\hat{\phi}] = 0 \quad . \quad (4.7)$$

The return coupling, i.e., the effect of fluid motion on potential distribution, derives from the equation of charge conservation, neglecting charge relaxation, Eq. (2.49):

$$\sigma \frac{\rho_f}{\epsilon} + \bar{E} \cdot \nabla \sigma = 0 \quad . \quad (4.8)$$

Linearizing Eq. (8) in terms of complex amplitudes:

$$\sigma_0 \frac{\hat{\rho}_f}{\varepsilon} - jkE_0 \hat{\sigma} + \hat{E}_x D\sigma_0 = 0 \quad . \quad (4.9)$$

Subject to the assumptions that led to Eq. (2.41), we finally state that the conductivity of an elemental volume of fluid of fixed identity remains constant:

$$\frac{\partial \sigma}{\partial t} + \bar{v} \cdot \nabla \sigma = 0 \quad (4.10)$$

or, linearizing Eq. (10) in terms of complex amplitudes:

$$s\hat{\sigma} - jk\psi D\sigma_0 = 0 \quad . \quad (4.11)$$

Combining Eqs. (6), (9), (11) and (2.4), we arrive at a relation between the electric potential and the velocity stream function:

$$[\sigma_0(D^2 - k^2) + (D\sigma_0)D]\hat{\phi} = \frac{k^2}{s} E_0 (D\sigma_0)\hat{\psi} \quad . \quad (4.12)$$

Equations (7) and (12) represent the two-way linkage between electrical and mechanical subsystems characteristic of electrohydrodynamic phenomena. Combining them to obtain one homogeneous equation in $\hat{\phi}$:

$$[D^2 - k^2] \left[(D^2 - k^2 - \frac{s\rho}{\eta}) \left(\frac{\sigma_0}{D\sigma_0} [D^2 - k^2] + D \right) + \frac{k^2}{s} \frac{\varepsilon E_0^2}{\eta} D \right] \hat{\phi} = 0 \quad . \quad (4.13)$$

Characteristic of bulk-coupled models involving inhomogeneous equilibrium property distributions, Eq. (13) is a non-constant coefficient differential equation in the independent variable x . For a general equilibrium conductivity distribution $\sigma_0(x)$, we would necessarily resort to a numerical integration procedure to determine a solution. There is, however, one non-trivial distribution for which Eq. (13) has constant

coefficients, i.e:

$$\sigma_0(x) = \sigma_\beta \left(\frac{\sigma_\alpha}{\sigma_\beta} \right)^{x/\Delta} \quad (3.14)$$

Here, σ_α and σ_β represent known values of conductivity at the upper and lower surfaces of the layer respectively, and the variation has an exponential character across the layer. For this distribution, the factor involving $\sigma_0(x)$ in Eq. (13) takes on a value independent of x :

$$\frac{\sigma_0(x)}{D\sigma_0(x)} = - \frac{\Delta}{\ln R} \quad (4.15)$$

where

$$R \equiv \frac{\sigma_\beta}{\sigma_\alpha} \quad (4.16)$$

We shall analyze the layer with exponential equilibrium conductivity distribution in detail in this chapter.

Substituting Eq. (15) into (13), and assuming solutions of the form $e^{\gamma x}$, we find, for non-zero $\hat{\phi}$, a sixth-order equation in γ :

$$[\gamma^2 - k^2] \left[(\gamma^2 - k^2 - \frac{s\rho}{\eta}) \left(- \frac{\Delta}{\ln R} [\gamma^2 - k^2] + \gamma \right) + \frac{k^2}{s} \frac{\epsilon E_0^2}{\eta} \gamma \right] = 0, \quad (4.17)$$

or, in normalized form:

$$[\underline{\gamma}^2 - \underline{k}^2] \left[(\underline{\gamma}^2 - \underline{k}^2 - \underline{s} \frac{T}{\tau}) (\underline{\gamma}^2 - \underline{\gamma} \ln R - \underline{k}^2) - \frac{\underline{k}^2}{\underline{s}} \underline{\gamma} \ln R \right] = 0 \quad (4.18)$$

where: $\underline{k} \equiv k\Delta$ (4.19)

$\underline{\gamma} \equiv \gamma\Delta$ (4.20)

$T \equiv \rho\Delta^2/\eta$ (4.21)

$$\tau \equiv \eta/\epsilon F_0^2 \quad (4.22)$$

$$\underline{s} \equiv s\tau \quad . \quad (4.23)$$

Note the appearance, as a parameter, of the ratio T/τ of the two characteristic times introduced and discussed in Section II.B.2.

Two of the six solutions to Eq. (18) are immediately apparent:

$$\underline{\gamma} = +\underline{k} \quad (4.24)$$

and

$$\underline{\gamma} = -\underline{k} \quad (4.25)$$

Remaining is a fourth-order equation in $\underline{\gamma}$:

$$\begin{aligned} \underline{\gamma}^4 - \underline{\gamma}^3 \ln R - \underline{\gamma}^2 \left[2\underline{k}^2 + \underline{s} \frac{T}{\tau} \right] + \underline{\gamma} \ln R \left[\underline{k}^2 + \underline{s} \left(\frac{T}{\tau} - \frac{\underline{k}^2}{\underline{s}^2} \right) \right] \\ + \underline{k}^2 \left[\underline{k}^2 + \underline{s} \frac{T}{\tau} \right] = 0 . \end{aligned} \quad (4.26)$$

For any given wavenumber \underline{k} , growth rate \underline{s} , and parameters T/τ and R , it is straightforward to numerically solve the quartic Eq. (26) for the remaining roots in $\underline{\gamma}$.

Denote the six solutions to Eq. (18) by $\underline{\gamma}_1, \underline{\gamma}_2, \underline{\gamma}_3, \underline{\gamma}_4, \underline{\gamma}_5$ and $\underline{\gamma}_6$. We proceed now to express the various electrical and mechanical perturbation complex amplitudes within the layer in terms of these six $\underline{\gamma}$'s. Our objective is a set of transfer relations, determining stresses and normal current densities in terms of velocities and potentials at the layer surfaces. The potential and stream function distributions are expressed as linear combinations of solutions of the form $e^{\underline{\gamma}x}$:

$$\hat{\phi} = \sum_{n=1}^6 \hat{\phi}_n e^{\underline{\gamma}_n x/\Delta} \quad (4.27)$$

$$\hat{\psi} = \sum_{n=1}^6 \hat{\psi}_n e^{\underline{\gamma}_n x/\Delta} \quad (4.28)$$

Equation (12), with (15) substituted in, permits determination of the six coefficients $\hat{\psi}_n$ in terms of $\hat{\phi}_n$:

$$\hat{\psi}_n = -\frac{\underline{s}}{\underline{k}^2} \frac{\Delta}{\tau E_0} \frac{1}{\ln R} [\underline{\gamma}_n^2 - \underline{\gamma}_n \ln R - \underline{k}^2] \hat{\phi}_n \quad (4.29)$$

Defining normalized perturbation complex amplitudes:

$$\hat{\phi} \equiv \frac{\hat{\phi}}{E_0 \Delta} \quad (4.30) \quad \hat{\underline{v}}_x \equiv \hat{\underline{v}}_x \frac{\tau}{\Delta} \quad (4.35)$$

$$\hat{\underline{\phi}}_n \equiv \frac{\hat{\phi}_n}{E_0 \Delta} \quad (4.31) \quad \hat{\underline{v}}_z \equiv \hat{\underline{v}}_z \frac{\tau}{\Delta} \quad (4.36)$$

$$\hat{\underline{\psi}} \equiv \hat{\underline{\psi}} \frac{\tau}{\Delta^2} \quad (4.32) \quad \hat{\underline{S}}_x \equiv \frac{\hat{S}_{xx}}{\epsilon E_0^2} \quad (4.37)$$

$$\hat{\underline{\psi}}_n \equiv \hat{\underline{\psi}}_n \frac{\tau}{\Delta^2} \quad (4.33) \quad \hat{\underline{S}}_z \equiv \frac{\hat{S}_{xz}}{\epsilon E_0^2} \quad (4.38)$$

$$\hat{\underline{p}} \equiv \frac{\hat{p}}{\epsilon E_0^2} \quad (4.34) \quad \hat{\underline{J}}_x \equiv \frac{\hat{J}_x}{\sigma_\alpha E_0} \quad (4.39)$$

we may rewrite Eq. (29) in normalized form as:

$$\hat{\underline{\psi}}_n = -\frac{\underline{s}}{\underline{k}^2} \frac{1}{\ln R} [\underline{\gamma}_n^2 - \underline{\gamma}_n \ln R - \underline{k}^2] \hat{\underline{\phi}}_n \quad (4.40)$$

Using the stream function definition, Eq. (2.68), the normalizations, Eqs. (33), (35) and (36) and Eqs. (28) and (40), we have:

$$\hat{\underline{v}}_x = \sum_{n=1}^6 \frac{j\underline{s}}{\underline{k}} \frac{1}{\ln R} [\underline{\gamma}_n^2 - \underline{\gamma}_n \ln R - \underline{k}^2] \hat{\underline{\phi}}_n e^{\underline{\gamma}_n x/\Delta} \quad (4.41)$$

$$\hat{v}_z = \sum_{n=1}^6 \frac{s \gamma_n}{k^2} \frac{1}{\ln R} \left[\gamma_n^2 - \gamma_n \ln R - k^2 \right] \hat{\phi}_n e^{\gamma_n x/\Delta} \quad (4.42)$$

The interface potential and velocity perturbation complex amplitudes, then, are expressed in terms of the six coefficients $\hat{\phi}_n$ by evaluating Eqs. (27), (41) and (42) at $x = 0$ and $x = \Delta$. We express the results in matrix form below, with superscript α denoting the upper surface ($x = \Delta$) and superscript β denoting the lower surface ($x = 0$):

$$[V] = [H][A] \quad (4.43)$$

where

$$[V] \equiv \begin{bmatrix} \hat{v}_x^\alpha \\ \hat{v}_x^\beta \\ \hat{v}_z^\alpha \\ \hat{v}_z^\beta \\ \hat{\phi}^\alpha \\ \hat{\phi}^\beta \end{bmatrix} \quad (4.44) \quad [A] \equiv \begin{bmatrix} \hat{\phi}_1 \\ \hat{\phi}_2 \\ \hat{\phi}_3 \\ \hat{\phi}_4 \\ \hat{\phi}_5 \\ \hat{\phi}_6 \end{bmatrix} \quad (4.45)$$

and $[H]$ is a 6×6 matrix, with entries defined by:

$$H_{1n} = \frac{js}{k} \frac{1}{\ln R} [\gamma_n^2 - \gamma_n \ln R - k^2] e^{\gamma_n} \quad (4.46)$$

$$H_{2n} = \frac{js}{k} \frac{1}{\ln R} [\gamma_n^2 - \gamma_n \ln R - k^2] \quad (4.47)$$

$$H_{3n} = \frac{sY_n}{\underline{k}^2} \frac{1}{\ln R} [\underline{Y}_n^2 - \underline{Y}_n \ln R - \underline{k}^2] e^{\underline{Y}_n} \quad (4.48)$$

$$H_{4n} = \frac{sY_n}{\underline{k}^2} \frac{1}{\ln R} [\underline{Y}_n^2 - \underline{Y}_n \ln R - \underline{k}^2] \quad (4.49)$$

$$H_{5n} = e^{\underline{Y}_n} \quad (4.50)$$

$$H_{6n} = 1 \quad (4.51)$$

The perturbation normal current density distribution is determined by

$$\hat{J}_x = \sigma_0 \hat{E}_x \quad . \quad (4.52)$$

Using the potential definition , Eq. (2.4), the normalizations, Eqs. (31) and (39), and Eqs. (27) and (52), we have:

$$\hat{J}_x = \sum_{n=1}^6 - R^{(1-x/\Delta)} \underline{Y}_n \underline{\phi}_n e^{\underline{Y}_n x/\Delta} \quad . \quad (4.53)$$

Finally, we determine the perturbation stress complex amplitudes. From Eq. (2.72) and the normalizations, Eqs. (37) and (38), the perturbation stress tensor components are:

$$\hat{S}_x = 2\Delta \underline{D}\hat{v}_x - \hat{p} \quad (4.54)$$

$$\hat{S}_z = \Delta \underline{D}\hat{v}_z - jk \hat{v}_x \quad . \quad (4.55)$$

To obtain \hat{p} for use in Eq. (54), we return to the Navier-Stokes Equation (2.66). Writing out the z-component in linearized form, we have:

$$- jk \hat{p} = - s \rho \hat{v}_z + \eta (D^2 - k^2) \hat{v}_z + \hat{\rho}_f E_0 \quad . \quad (4.56)$$

Combining Eqs. (6) and (56):

$$\hat{p} = \frac{j\eta}{k} \left[(D^2 - k^2 - \frac{s\rho}{\eta}) \hat{v}_z - \frac{\epsilon E_0}{\eta} (D^2 - k^2) \hat{\phi} \right] \quad (4.57)$$

or, using Eqs. (30), (34) and (36) to normalize:

$$\hat{p} = \frac{j}{k} \left[(\Delta^2 D^2 - \underline{k}^2 - \frac{s}{\tau} T) \hat{v}_z - (\Delta^2 D^2 - \underline{k}^2) \hat{\phi} \right] \quad (4.58)$$

Using Eqs. (41), (42) and (58) in Eqs. (54) and (55) we have:

$$\begin{aligned} \hat{\underline{S}}_x = \sum_{n=1}^6 \frac{1}{k} \left[-\frac{1}{\ln R} \frac{j s Y_n}{k^2} (Y_n^2 - Y_n \ln R - \underline{k}^2) (Y_n^2 - 3\underline{k}^2 - \frac{s}{\tau} T) \right. \\ \left. + j(Y_n^2 - \underline{k}^2) \right] \hat{\phi}_n e^{Y_n x/\Delta} \end{aligned} \quad (4.59)$$

$$\hat{\underline{S}}_z = \sum_{n=1}^6 \frac{s}{k^2} \frac{1}{\ln R} [Y_n^2 + \underline{k}^2] [Y_n^2 - Y_n \ln R - \underline{k}^2] \hat{\phi}_n e^{Y_n x/\Delta} \quad (4.60)$$

The interface normal current and stress perturbation complex amplitudes, then, are expressed in terms of the six coefficients $\hat{\phi}_n$ by evaluating Eqs. (53), (59), and (60) at $x = 0$ and $x = \Delta$. The result, expressed in matrix form, is:

$$[S] = [G][A] \quad (4.61)$$

where

$$[S] \equiv \begin{bmatrix} \hat{\underline{S}}_x^\alpha \\ \hat{\underline{S}}_x^\beta \\ \hat{\underline{S}}_z^\alpha \\ \hat{\underline{S}}_z^\beta \\ \hat{\underline{J}}_x^\alpha \\ \hat{\underline{J}}_x^\beta \end{bmatrix} \quad (4.62)$$

[A] is defined by Eq. (45) and [G] is a 6×6 matrix, with entries defined by:

$$G_{1n} = \frac{1}{\underline{k}} \left[-\frac{1}{\ln R} \frac{j\underline{s} \underline{Y}_n}{\underline{k}^2} (\underline{Y}_n^2 - \underline{Y}_n \ln R - \underline{k}^2) (\underline{Y}_n^2 - 3\underline{k}^2 - \frac{\underline{s}}{\underline{\tau}}) + j(\underline{Y}_n^2 - \underline{k}^2) \right] e^{\underline{Y}_n} \quad (4.63)$$

$$G_{2n} = \frac{1}{\underline{k}} \left[-\frac{1}{\ln R} \frac{j\underline{s} \underline{Y}_n}{\underline{k}^2} (\underline{Y}_n^2 - \underline{Y}_n \ln R - \underline{k}^2) (\underline{Y}_n - 3\underline{k}^2 - \frac{\underline{s}}{\underline{\tau}}) + j(\underline{Y}_n^2 - \underline{k}^2) \right] \quad (4.64)$$

$$G_{3n} = \frac{1}{\ln R} \frac{\underline{s}}{\underline{k}^2} [\underline{Y}_n^2 + \underline{k}^2] [\underline{Y}_n^2 - \underline{Y}_n \ln R - \underline{k}^2] e^{\underline{Y}_n} \quad (4.65)$$

$$G_{4n} = \frac{1}{\ln R} \frac{\underline{s}}{\underline{k}^2} [\underline{Y}_n^2 + \underline{k}^2] [\underline{Y}_n^2 - \underline{Y}_n \ln R - \underline{k}^2] \quad (4.66)$$

$$G_{5n} = -\underline{Y}_n e^{\underline{Y}_n} \quad (4.67)$$

$$G_{6n} = -R \underline{Y}_n \quad (4.68)$$

We may now write a set of transfer relations to describe the layer in terms of perturbation complex amplitudes at its surfaces. Inverting Eq. (43):

$$[A] = [H]^{-1} [V] \quad (4.69)$$

Combining Eqs. (61) and (69):

$$[S] = [G][H]^{-1}[V] \equiv [Q][V] \quad (4.70)$$

Equation (70) expresses the desired relations. For given values of \underline{k} , \underline{s} , T/τ , and R , the 36 elements of the transfer matrix $[Q]$ are determined as follows: numerically solving the quartic, Eq. (26) for four roots, and adding the two extra roots given by Eqs. (24) and (25) yields \underline{y}_n ($n = 1, \dots, 6$). Then, Eqs. (46)-(51) and (63)-(68) determine the 36 elements of $[H]$ and the 36 elements of $[G]$. Inverting $[H]$ and premultiplying by $[G]$, the desired transfer matrix $[Q]$ is computed.

B. Half-Space Boundaries

Having determined transfer relations for a viscous layer with exponentially varying equilibrium conductivity distribution in an equilibrium uniform tangential electric field in Section IV.A, we are ready to generalize the tangential field analysis presented in Section III.C. We envisage a physical situation involving two miscible fluids of identical viscosity, permittivity, and density, but with the lower fluid doped so as to have higher conductivity. Provided the region of conductivity variation is thin and perturbation wavelengths short compared to the thickness of the fluid layers, we may model the regions bounding the layer of varying conductivity as half spaces. In contrast to the model considered in Section III.C, lengths characterizing the instability dynamics are now of the same order as the thickness of the region of conductivity variation.

Of course, the exponential conductivity distribution of our viscous layer does not accurately represent the diffusive distribution which actually joins the two regions of uniform conductivity. Figure 2 shows $\sigma_0(x)$ versus x/Δ for an exponential junction between two external layers of conductivities in the ratio $R=e$; (e is the natural logarithm base

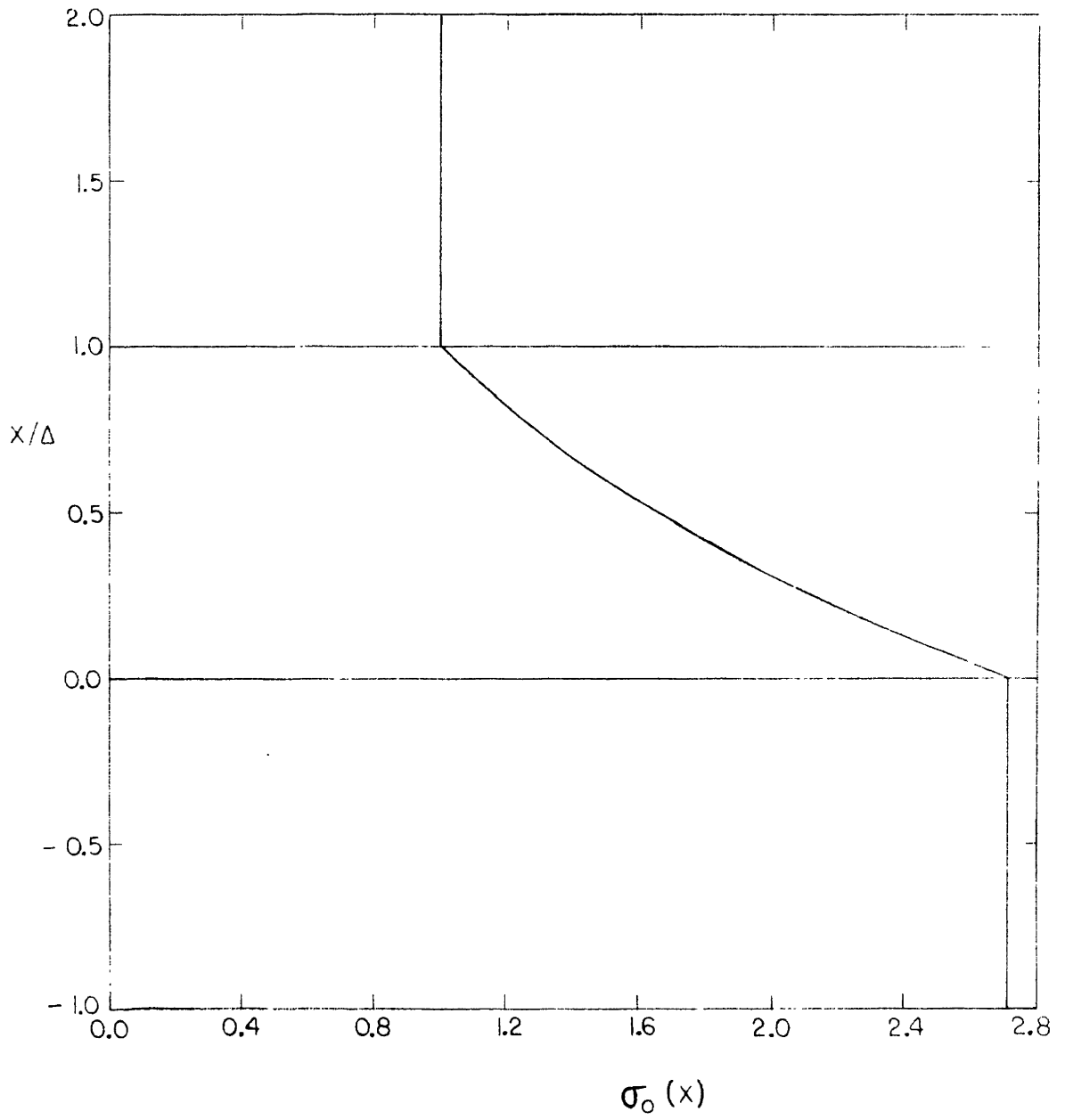


Figure 2. $\sigma_0(x)$ versus x for $R = e$

≈ 2.7183). Note that, in contrast to the actual distribution, the slope here is discontinuous at the surfaces of the varying layer. Such a discontinuity implies no surface charge density or surface force density, and is of no consequence except as regards the detailed structure of the equilibrium conductivity distribution. The stability analysis to follow is not expected to be sensitive to the details of this distribution.

We consider, then, a model as shown in Fig. 3.

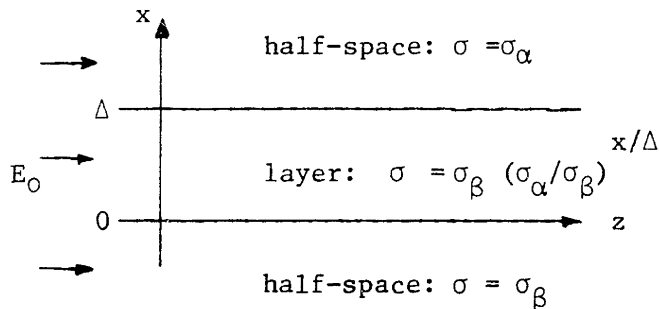


Figure 3

Exponential Conductivity Layer Bounded by Half-spaces

Our aim is to couple the viscous layer with exponentially varying equilibrium conductivity to viscous half-spaces of constant conductivities, above and below. The entire system experiences an equilibrium tangential electric field, $E_0 \bar{i}_z$. Because we do not include gravity in this analysis, and because there is no equilibrium electrical force density, according to the discussion at the end of Section II.B.3, no distinction need be made between perturbation quantities evaluated at equilibrium and at perturbation positions of the interfaces. Having analyzed the half-spaces electrically in Section II.A.4 and mechanically in II.B.3, and the varying

conductivity layer in Section IV.A, our remaining task in arriving at a dispersion relation for the system of Fig. 3 is to splice together the regions at the boundaries $x=0$ and $x = \Delta$. The boundary conditions, from Eqs. (2.10), (2.12) in the instantaneous relaxation limit, (2.73) (2.74) and (2.75) respectively, are that $\hat{\phi}$, \hat{J}_{-x} , \hat{v}_{-x} , \hat{v}_{-z} , \hat{S}_{-x} and \hat{S}_{-z} be continuous across the boundaries. Thus, we require that the layer α variables be identical to the upper half space α variables and the layer β variables be identical to the lower half-space β variables. At this point, we rewrite the half-space transfer relations, using Eqs. (30), (35), (36), (37), (38) and (39) to normalize the various perturbation complex amplitudes. At the upper and lower surfaces, the perturbation normal current densities are, respectively:

$$\hat{J}_x^\alpha = \sigma_\alpha \hat{E}_x^\alpha \quad (4.71)$$

and

$$\hat{J}_x^\beta = \sigma_\beta \hat{E}_x^\beta \quad (4.72)$$

From Eqs. (2.60), (2.63) plus (30), (39) and (71):

$$\hat{J}_{-x}^\alpha = \underline{k} \hat{\phi}^\alpha \quad (4.73)$$

From Eqs. (2.62), (2.64) and (30), (39) and (72):

$$\hat{J}_{-x}^\beta = -R \underline{k} \hat{\phi}^\beta \quad (4.74)$$

From Eqs. (2.104), (35), (36), (37) and (38):

$$\begin{bmatrix} \hat{S}_x^\alpha \\ \hat{S}_z^\alpha \end{bmatrix} = \begin{bmatrix} -\frac{q}{k} (\underline{k} + \underline{q}) & j(\underline{k} - \underline{q}) \\ j(\underline{q} - \underline{k}) & -(\underline{q} + \underline{k}) \end{bmatrix} \begin{bmatrix} \hat{v}_x^\alpha \\ \hat{v}_z^\alpha \end{bmatrix} \equiv [P^\alpha] \begin{bmatrix} \hat{v}_x^\alpha \\ \hat{v}_z^\alpha \end{bmatrix} \quad (4.75)$$

From Eqs. (2.105), (35), (36), (37) and (38):

$$\begin{bmatrix} \hat{S}_x^\beta \\ \hat{S}_z^\beta \end{bmatrix} = \begin{bmatrix} \frac{q}{k} (\underline{k} + \underline{q}) & j(\underline{k} - \underline{q}) \\ j(\underline{q} - \underline{k}) & (\underline{q} + \underline{k}) \end{bmatrix} \begin{bmatrix} \hat{v}_x^\beta \\ \hat{v}_z^\beta \end{bmatrix} \equiv [P^\beta] \begin{bmatrix} \hat{v}_x^\beta \\ \hat{v}_z^\beta \end{bmatrix} \quad (4.76)$$

where, from Eqs. (2.93), (19), (21), (22) and (23):

$$q \equiv \sqrt{k^2 + \underline{s} T/\tau} \quad , \quad (\text{Re } \underline{q} > 0) \quad . \quad (4.77)$$

The splicing of regions is now accomplished by simply writing out Eqs. (70), (73), (74), (75) and (76) simultaneously:

$$\hat{S}_x^\alpha = Q_{11} \hat{v}_x^\alpha + Q_{12} \hat{v}_x^\beta + Q_{13} \hat{v}_z^\alpha + Q_{14} \hat{v}_z^\beta + Q_{15} \hat{\phi}^\alpha + Q_{16} \hat{\phi}^\beta = P_{11}^\alpha \hat{v}_x^\alpha + P_{12}^\alpha \hat{v}_z^\alpha \quad (4.78)$$

$$\hat{S}_x^\beta = Q_{21} \hat{v}_x^\alpha + Q_{22} \hat{v}_x^\beta + Q_{23} \hat{v}_z^\alpha + Q_{24} \hat{v}_z^\beta + Q_{25} \hat{\phi}^\alpha + Q_{26} \hat{\phi}^\beta = P_{11}^\beta \hat{v}_x^\beta + P_{12}^\beta \hat{v}_z^\beta \quad (4.79)$$

$$\hat{S}_z^\alpha = Q_{31} \hat{v}_x^\alpha + Q_{32} \hat{v}_x^\beta + Q_{33} \hat{v}_z^\alpha + Q_{34} \hat{v}_z^\beta + Q_{35} \hat{\phi}^\alpha + Q_{36} \hat{\phi}^\beta = P_{21}^\alpha \hat{v}_x^\alpha + P_{22}^\alpha \hat{v}_z^\alpha \quad (4.80)$$

$$\hat{S}_z^\beta = Q_{41} \hat{v}_x^\alpha + Q_{42} \hat{v}_x^\beta + Q_{43} \hat{v}_z^\alpha + Q_{44} \hat{v}_z^\beta + Q_{45} \hat{\phi}^\alpha + Q_{46} \hat{\phi}^\beta = P_{21}^\beta \hat{v}_x^\beta + P_{22}^\beta \hat{v}_z^\beta \quad (4.81)$$

$$\hat{\underline{J}}_{\underline{x}}^{\alpha} = Q_{51} \hat{\underline{v}}_{\underline{x}}^{\alpha} + Q_{52} \hat{\underline{v}}_{\underline{x}}^{\beta} + Q_{53} \hat{\underline{v}}_{\underline{z}}^{\alpha} + Q_{54} \hat{\underline{v}}_{\underline{z}}^{\beta} + Q_{55} \hat{\underline{\phi}}^{\alpha} + Q_{56} \hat{\underline{\phi}}^{\beta} = \underline{k} \hat{\underline{\phi}}^{\alpha} \quad (4.82)$$

$$\hat{\underline{J}}_{\underline{x}}^{\beta} = Q_{61} \hat{\underline{v}}_{\underline{x}}^{\alpha} + Q_{62} \hat{\underline{v}}_{\underline{x}}^{\beta} + Q_{63} \hat{\underline{v}}_{\underline{z}}^{\alpha} + Q_{64} \hat{\underline{v}}_{\underline{z}}^{\beta} + Q_{65} \hat{\underline{\phi}}^{\alpha} + Q_{66} \hat{\underline{\phi}}^{\beta} = -\underline{Rk} \hat{\underline{\phi}}^{\beta} \quad (4.83)$$

Combining like terms in Eqs. (78)-(83), we have in matrix form:

$$[F][V] = [0] \quad (4.84)$$

where $[V]$ is defined by Eq. (44), $[0]$ is a column matrix of six zeros, and:

$$[F] = \begin{bmatrix} Q_{11} - P_{11}^{\alpha} & Q_{12} & Q_{13} - P_{12}^{\alpha} & Q_{14} & Q_{15} & Q_{16} \\ Q_{21} & Q_{22} - P_{11}^{\beta} & Q_{23} & Q_{24} - P_{12}^{\beta} & Q_{25} & Q_{26} \\ Q_{31} - P_{21}^{\alpha} & Q_{32} & Q_{33} - P_{22}^{\alpha} & Q_{34} & Q_{35} & Q_{36} \\ Q_{41} & Q_{42} - P_{21}^{\beta} & Q_{43} & Q_{44} - P_{22}^{\beta} & Q_{45} & Q_{46} \\ Q_{51} & Q_{52} & Q_{53} & Q_{54} & Q_{55} - \underline{k} & Q_{56} \\ Q_{61} & Q_{62} & Q_{63} & Q_{64} & Q_{65} & Q_{66} + \underline{Rk} \end{bmatrix} \quad (4.85)$$

For non-trivial solutions to Eq. (84), we require:

$$D \equiv \det [F] = 0 \quad (4.86)$$

Equation (86) is the dispersion relation for the coupled system of Fig. 3. For a given \underline{k} , \underline{s} , T/τ , and R , the procedure for computing D is straightforward. For a given \underline{k} , T/τ , and R , we must carry out a search procedure

in the complex \underline{s} plane, looking for values of \underline{s} where Eq. (86) is satisfied.

Assuming, for the time being, that $D(\underline{s})$ is an analytic function, we follow Betchov and Criminale⁽¹⁾, doing a Taylor Series expansion for a small increment $\Delta \underline{s}$, and retaining only up to the first order term in $\Delta \underline{s}$:

$$D(\underline{s} + \Delta \underline{s}) = D(\underline{s}) + \left. \frac{dD}{d\underline{s}} \right|_{\underline{s}} \Delta \underline{s} \quad . \quad (4.87)$$

If \underline{s} is near a zero of D , we choose $\Delta \underline{s}$ so as to move closer to the zero by making

$$D(\underline{s} + \Delta \underline{s}) = 0 \quad . \quad (4.88)$$

Combining Eqs. (87) and (88):

$$\Delta \underline{s} = - \frac{D(\underline{s})}{\left. \frac{dD}{d\underline{s}} \right|_{\underline{s}}} \quad . \quad (4.89)$$

In an iterative search procedure, if the initial starting point \underline{s} is too far from the zero being sought, the routine will not converge. Convergence can be improved by reducing the magnitude of the steps taken in the direction of the zero. Thus, we modify Eq. (89):

$$\Delta \underline{s} = - \lambda \frac{D(\underline{s})}{\left. \frac{dD}{d\underline{s}} \right|_{\underline{s}}} \quad (4.90)$$

where $\lambda \leq 1$.

To determine $dD/d\underline{s}|_{\underline{s}}$, we take a small exploratory step, $\delta\underline{s}$, some fraction of the previous $\Delta\underline{s}$:

$$\delta\underline{s} = \mu\Delta\underline{s} \tag{4.91}$$

where $\mu < 1$. Then:

$$\left. \frac{dD}{d\underline{s}} \right|_{\underline{s}} \approx \frac{D(\underline{s} + \delta\underline{s}) - D(\underline{s})}{\delta\underline{s}} \tag{4.92}$$

Equation (91) is used so as to reduce the size of the exploratory step used to determine the derivative as the zero is approached. Normally, we set $\mu = 0.1$ and $\lambda = 1$, but when there is difficulty with convergence, we reset $\lambda = 0.5$.

The procedure employed in determining eigenfrequencies \underline{s} such that $D(\underline{s}) = 0$ for a given \underline{k} , T/τ , and R is as follows: values of D are computed at grid points in the \underline{s} plane, with the grid size varied over many orders of magnitude. In this way, some "feel" for the complex function $D(\underline{s})$ is gained and we obtain initial estimates for the positions of zeroes. We may then use the search routine described above to converge in on the zeroes. We proceed now to describe the complex function $D(\underline{s})$ using information learned empirically by computing its value at grid points in the \underline{s} plane.

First, the function has complex conjugate symmetry about the real \underline{s} axis. That is, the value of D at a point $\underline{s}_r + j\underline{s}_i$ is the complex conjugate of the value at the point $\underline{s}_r - j\underline{s}_i$. In particular, then, when we find a zero in the upper half-plane, we know immediately that

there is another zero, mirrored through the real axis, in the lower half-plane. Thus, we need only carry out a search for zeroes in the upper half-plane.

Second, the function has a branch cut, extending leftward along the \underline{s}_r axis from a branch point at $\underline{s} = -\underline{k}^2/(T/\tau) + j0$ to negative infinity. To the left of the branch point, in crossing the negative real axis, when \underline{s} is changed incrementally from $\underline{s}_r + j\epsilon$ to $\underline{s}_r - j\epsilon$, the function D has a discontinuous imaginary part; i.e., it jumps from $D_r + jD_i$ to $D_r - jD_i$, where D_i is nonzero.

The nonanalyticity of $D(\underline{s})$ can be traced back to two distinct steps in the computation procedure. First, recall the numerical routine for finding the roots, \underline{Y}_n , to Eq. (26). If we picture a listing, in four columns, of the four roots \underline{Y}_1 , \underline{Y}_2 , \underline{Y}_3 , and \underline{Y}_4 , as functions of \underline{s} as \underline{s} is incremented in steps along a contour in the complex plane, the functions will appear continuous until the contour crosses a branch cut. Upon crossing, two columns will suffer discontinuities. If, however, these two columns were interchanged for values of \underline{s} beyond the branch cut crossing, the functions would appear continuous throughout. That is, the branch cut represents only a reordering of the names, \underline{Y}_1 , \underline{Y}_2 , \underline{Y}_3 , \underline{Y}_4 , of the four solutions. In the computation of the matrices $[H]$ and $[G]$, this is equivalent to an interchanging of two columns, hence a reversal in sign of $\det [H]$ and $\det [G]$. Because $\det [H]$ and $\det [G]$ also have complex conjugate symmetry about the real s axis (in the same sense as does D), this necessarily implies that both functions are pure imaginary along the branch cut. The matrix $[Q] = [G][H]^{-1}$, nevertheless, has a

determinant which is analytic across the branch cut in $\det [H]$ and $\det [G]$.

The second step in the computation procedure for D which involves a non-analytic function is the determination of \underline{q} , the viscous decay number, defined by Eq. (77). The defining restriction $\text{Re } \underline{q} > 0$ implies a branch cut in the function \underline{q} which is coincident with the branch cut in D , i.e., extending from a branch point at $\underline{s} = -\underline{k}^2/(T/\tau) + j0$, along the negative real axis to negative infinity. We see this by writing out Eq. (77):

$$\underline{q} = \sqrt{\left(\underline{k}^2 + \frac{T}{\tau} \underline{s}_r\right) + j\left(\frac{T}{\tau} \underline{s}_i\right)} \quad , \quad (\text{Re } \underline{q} > 0) \quad . \quad (4.93)$$

Now, the function $\underline{q} = \sqrt{z}$, ($\text{Re } \underline{q} > 0$) has a branch cut consisting of the entire negative real z axis and a branch point at the origin. Thus, from Eq. (93), we see that the branch point in the \underline{s} plane is at $\underline{s} = -\underline{k}^2/(T/\tau) + j0$, and the branch cut extends leftward along the negative real \underline{s} axis. It is the nonanalyticity across the branch cut of $\underline{q}(\underline{s})$ which is used in computing the elements of $[P^\alpha]$ and $[P^\beta]$, defined by Eqs. (75) and (76) respectively, which leads to a branch cut in $D(\underline{s})$.

Finally, computation of $D(\underline{s})$ at grid points in the \underline{s} plane leads to the discovery of zeroes [eigenfrequency solutions to Eq. (86)] in the right half-plane with non-zero \underline{s}_i (corresponding to oscillatory growth in time). Recall that, for any one zero in the upper half-plane, there is a corresponding mirror image zero in the lower half-plane. Henceforth, we confine our discussion to the set of zeroes in the upper half-plane. Of all the zeroes, we shall call the one with largest \underline{s}_r the first eigenfrequency, the one with second largest \underline{s}_r the second eigenfrequency, and so on. We find that the first eigenfrequency also has the largest value of \underline{s}_i (oscillates most rapidly), and so on. Characteristic of internal

mode problems, there is an infinite set of eigenfrequencies in the right upper half plane, all within a rectangular region with corners at the first eigenfrequency and the origin. (See Fig. 4.) Any one eigenfrequency has an infinite set of eigenfrequencies between itself and the origin. No zeroes are found in the left half-plane.

To better understand the significance of the various eigenfrequencies, it is desirable to determine the distributions of perturbation complex amplitudes of physical quantities as functions of the x-coordinate (the eigenfunctions). This may be accomplished as follows.

Having found a value of \underline{s} where Eq. (86) is satisfied, we desire a nontrivial column matrix $[V]$ satisfying Eq. (84). It is a straightforward matter to perform matrix manipulations on $[F]$ (taking linear combinations of rows) so as to produce zero entries everywhere below the main diagonal. Having performed such manipulations, because $D = 0$, the 6,6 element will become zero. Thus, the last equation represented by (84) is satisfied by an arbitrary entry for the bottom element of $[V]$. We arbitrarily give this element the value $1 + j0$, i.e.,

$$\hat{\phi}^{\beta} = 1 + j0 \quad . \quad (4.94)$$

Then, the manipulated set of equations derived from Eq. (84) may be used to determine the values of all the other variables in $[V]$, consistent with Eq. (94). We emphasize that (94) was set arbitrarily. We could just as well have set any one of the other elements of $[V]$ to any desired value. The arbitrariness, here, reflects the fact that when Eq. (86) is satisfied, any $[V]$ satisfying Eq. (84) can be multiplied by any complex

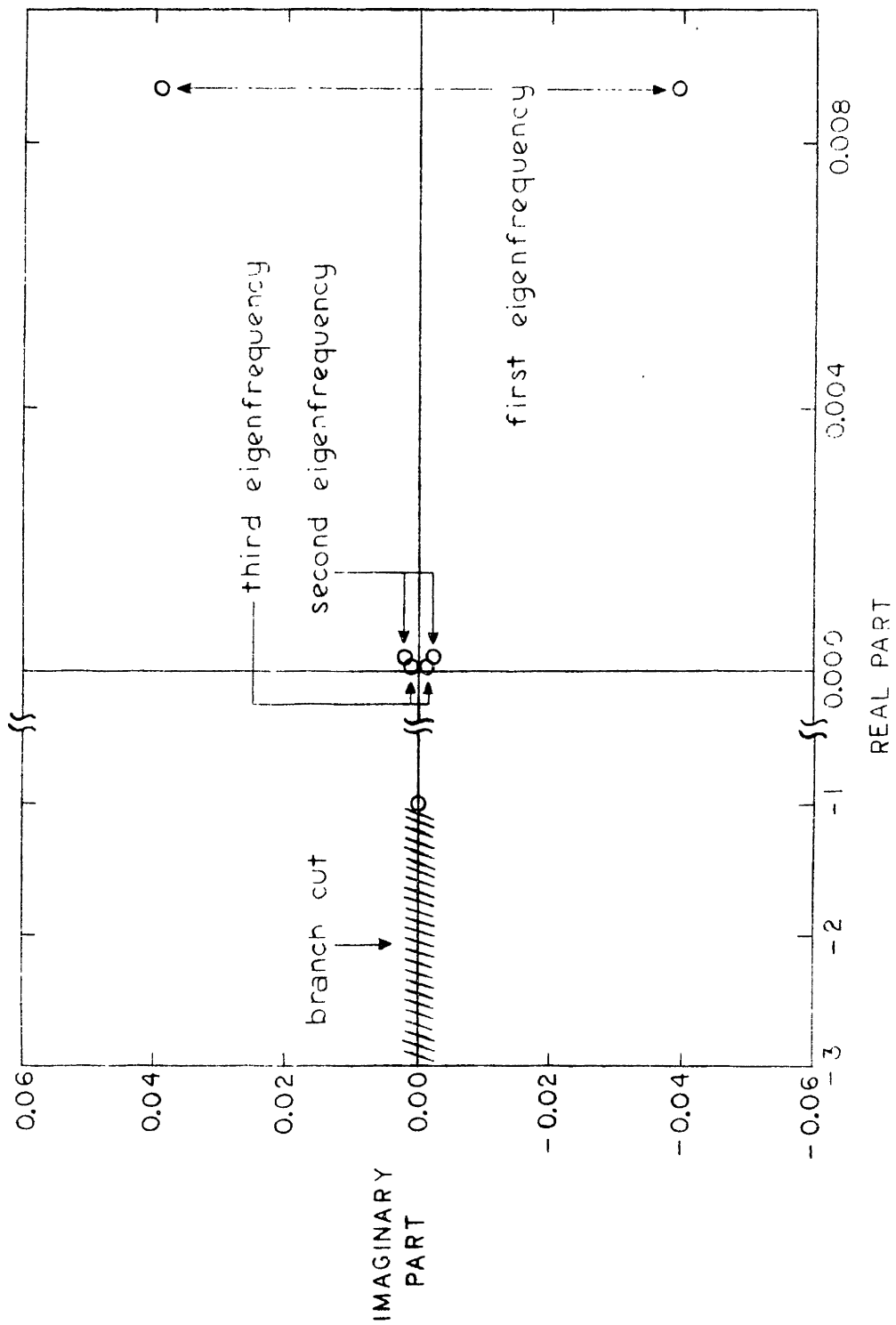


Figure 4. The Function D in the complex s -plane

constant with Eq. (84) still satisfied. Physically, we can excite an eigenmode at an amplitude and phase of our choice.

Having determined a $[V]$, Eq. (69) allows us to compute the corresponding $[A]$, i.e., the $\hat{\phi}_n$. The various physical quantities, $\hat{\phi}$, \hat{v}_x , \hat{v}_z , \hat{J}_x , \hat{S}_x and \hat{S}_z are then given, in terms of the $\hat{\phi}_n$, as functions of position through the varying conductivity layer, by Eqs. (27), (41), (42) (53), (59) and (60). In the half space bounding regions, we use Eqs. (30) through (39) to normalize the spatial distributions defined by Eqs. (2.57), (2.58), (2.94), (2.96), (2.97), (2.98) and (2.101) and arrive at the following distributions:

In the upper half-space, define:

$$x' \equiv x - \Delta \quad . \quad (4.95)$$

Then:

$$\hat{\phi}(x') = \hat{\phi}^\alpha e^{-\underline{k} x' / \Delta} \quad (4.96)$$

$$\hat{J}_x(x') = \underline{k} \hat{\phi}^\alpha e^{-\underline{k} x' / \Delta} \quad (4.97)$$

$$\begin{bmatrix} \hat{v}_x(x') \\ \hat{v}_z(x') \end{bmatrix} = \begin{bmatrix} -j\underline{k} e^{-\underline{k} x' / \Delta} & -j\underline{k} e^{-\underline{q} x' / \Delta} \\ \underline{k} e^{-\underline{k} x' / \Delta} & \underline{q} e^{-\underline{q} x' / \Delta} \end{bmatrix} \begin{bmatrix} \hat{\psi}_1^u \\ \hat{\psi}_2^u \end{bmatrix} \quad (4.98)$$

$$\begin{bmatrix} \hat{S}_x(x') \\ \hat{S}_z(x') \end{bmatrix} = \begin{bmatrix} j(2\underline{k}^2 + \underline{s} \frac{T}{\tau}) e^{-\underline{k} x' / \Delta} & j2\underline{k} \underline{q} e^{-\underline{q} x' / \Delta} \\ -2\underline{k}^2 e^{-\underline{k} x' / \Delta} & -(\underline{k}^2 + \underline{q}^2) e^{-\underline{q} x' / \Delta} \end{bmatrix} \begin{bmatrix} \hat{\psi}_1^u \\ \hat{\psi}_2^u \end{bmatrix} \quad (4.99)$$

where

$$\begin{bmatrix} \hat{\Psi}_1^u \\ \hat{\Psi}_2^u \end{bmatrix} = \frac{j(\underline{q} + \underline{k})}{\underline{s} T/\tau} \begin{bmatrix} \underline{q}/\underline{k} & j \\ -1 & -j \end{bmatrix} \begin{bmatrix} \hat{v}_x^\alpha \\ \hat{v}_z^\alpha \end{bmatrix} \quad (4.100)$$

In the lower half-space:

$$\hat{\phi}(x) = \hat{\phi}^\beta e^{\underline{k} x/\Delta} \quad (4.101)$$

$$\hat{J}_x(x) = -R\underline{k} \hat{\phi}^\beta e^{\underline{k} x/\Delta} \quad (4.102)$$

$$\begin{bmatrix} \hat{v}_x(x) \\ \hat{v}_z(x) \end{bmatrix} = \begin{bmatrix} -j\underline{k} e^{\underline{k} x/\Delta} & -j\underline{k} e^{\underline{q} x/\Delta} \\ -\underline{k} e^{\underline{k} x/\Delta} & -\underline{q} e^{\underline{q} x/\Delta} \end{bmatrix} \begin{bmatrix} \hat{\Psi}_1^\ell \\ \hat{\Psi}_2^\ell \end{bmatrix} \quad (4.103)$$

$$\begin{bmatrix} \hat{S}_x(x) \\ \hat{S}_z(x) \end{bmatrix} = \begin{bmatrix} -j(2\underline{k}^2 + \underline{s} \frac{T}{\tau}) e^{\underline{k} x/\Delta} & -j2\underline{k} \underline{q} \\ -2\underline{k}^2 e^{\underline{k} x/\Delta} & -(\underline{k}^2 + \underline{q}^2) e^{\underline{q} x/\Delta} \end{bmatrix} \begin{bmatrix} \hat{\Psi}_1^\ell \\ \hat{\Psi}_2^\ell \end{bmatrix} \quad (4.104)$$

where:

$$\begin{bmatrix} \hat{\Psi}_1^\ell \\ \hat{\Psi}_2^\ell \end{bmatrix} = \frac{j(\underline{q} + \underline{k})}{\underline{s} T/\tau} \begin{bmatrix} \underline{q}/\underline{k} & -j \\ -1 & j \end{bmatrix} \begin{bmatrix} \hat{v}_x^\beta \\ \hat{v}_z^\beta \end{bmatrix} \quad (4.105)$$

The various physical quantities, $\hat{\phi}$, \hat{v}_x , \hat{v}_z , \hat{J}_x , \hat{S}_x and \hat{S}_z are given, in terms of the elements of [V], as functions of position in the upper and lower half-spaces, by Eqs. (95)-(105).

Figures 5, 6, 7, 8, 9, and 10 display the eigenfunctions $\hat{\phi}$, \hat{J}_x , \hat{v}_x , \hat{v}_z , \hat{S}_x , and \hat{S}_z respectively, for the first eigenfrequency (hereafter called

the first eigenfunctions) at $\underline{k} = 1$, $\frac{T}{\tau} = 1$, and $R = e$. In each case, real and imaginary parts are shown as functions of x across the varying conductivity layer and one layer thickness into the half-spaces on either side of the layer. (Real and imaginary parts describe the distributions, as real functions of x , at two values of z spaced $\pi/2k$ apart, or at two values of t spaced $\pi/2s_1$ apart.) The ordinate scales on these plots, and on all eigenfunction plots to follow, are of no significance. All that is relevant is the relative magnitudes of the various quantities as functions of position across the layer.

Figures 11 and 12 display the second eigenfunctions for $\hat{\phi}$ and \hat{v}_x and Figs. 13 and 14 the third eigenfunctions for $\hat{\phi}$ and \hat{v}_x , all at $\underline{k} = 1$, $\frac{T}{\tau} = 1$, and $R = e$. Comparison of Figs. 5, 11, and 13, and of Figs. 7, 12, and 14, gives physical significance to the first three eigenfrequencies. The most rapidly growing mode involves the least variation of physical quantities across the layer. Higher (less rapidly growing) modes involve more and more points of zero slope within the layer.

Figures 15 and 16 show the first eigenfunctions for $\hat{\phi}$ and \hat{v}_x at $\underline{k} = 0.1$ and Figs. 17 and 18 the first eigenfunctions for $\hat{\phi}$ and \hat{v}_x at $\underline{k} = 10$. ($T/\tau = 1$ and $R = e$ in both cases.) As we would expect, increasing \underline{k} causes more rapid variation of the eigenfunctions as functions of x . The simplest components of these modes are the Laplacian solutions, varying as $e^{\underline{k} x/\Delta}$ and $e^{-\underline{k} x/\Delta}$. The other four roots, $\underline{\gamma}_n$, although more complicated functions of \underline{k} , still have the basic character of increasing in magnitude as \underline{k} is increased. It is essential not to confuse the rapid variation of eigenfunctions in Figs. 17 and 18, due to a large value of

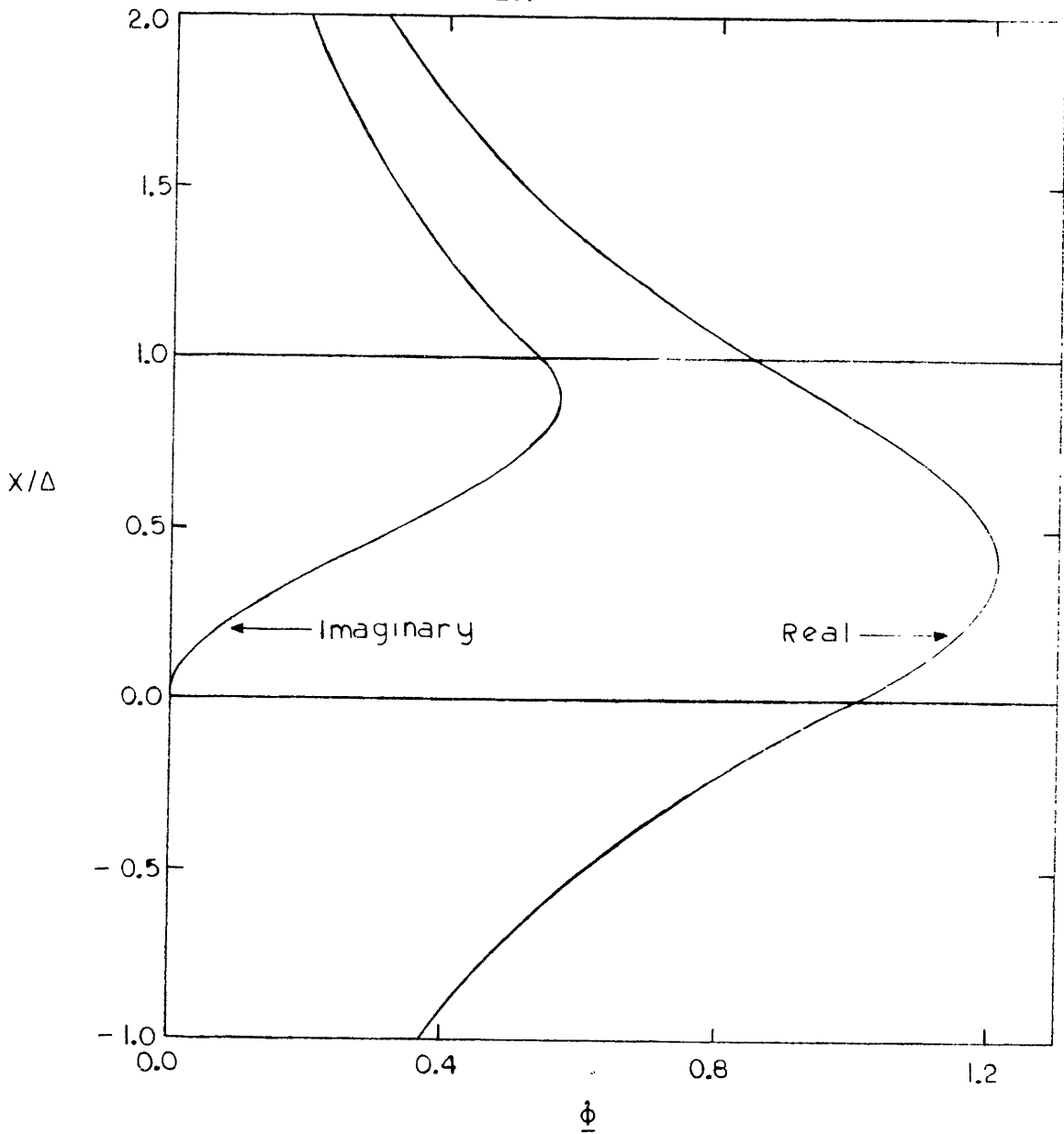


Figure 5. $\hat{\phi}$ versus x/Δ , first eigenfunction, $k=1$, $T/\tau=1$, $R=e$

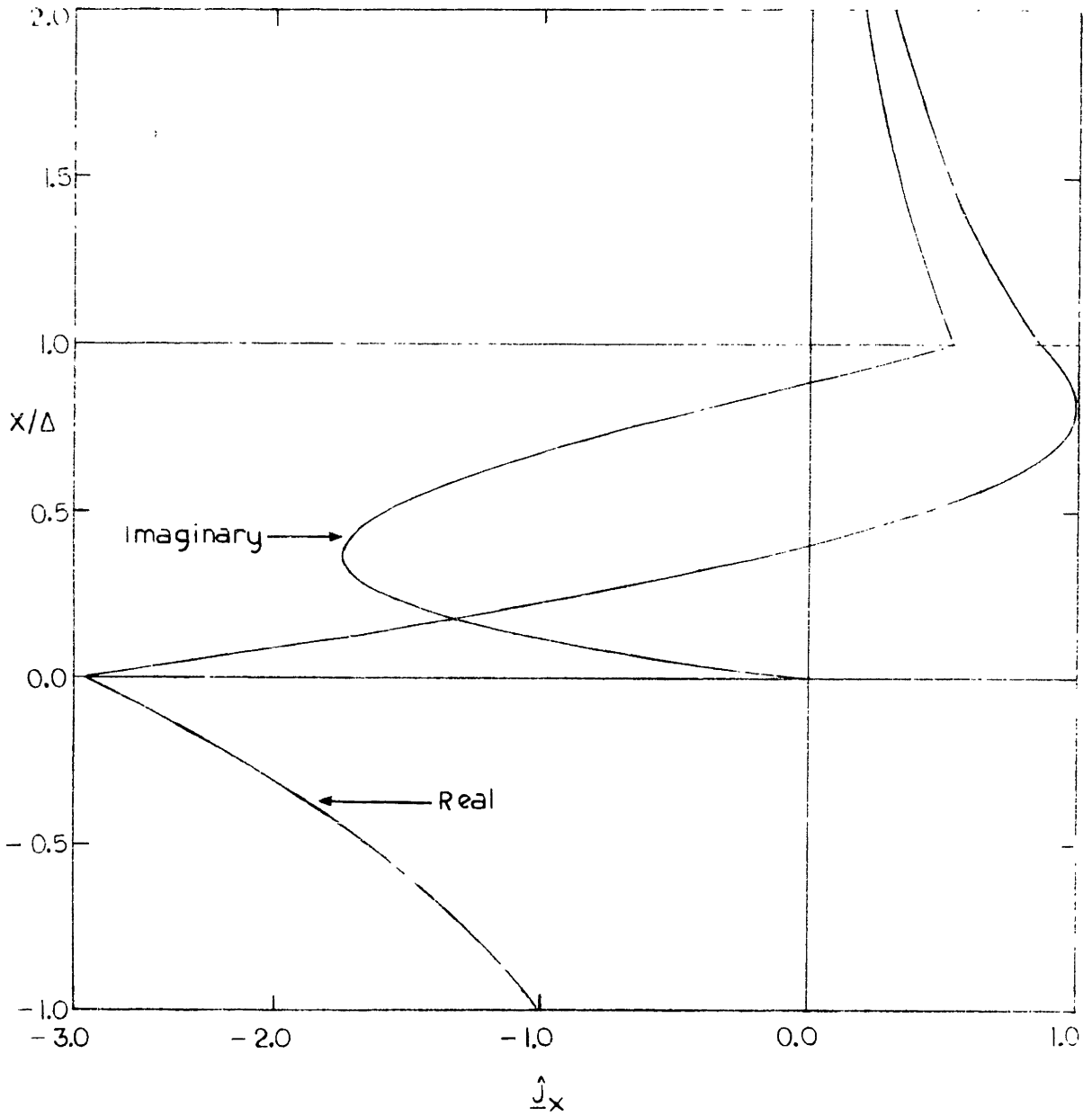


Figure 6. \hat{J}_x versus x/Δ , first eigenfunction, $k=1$, $T/\tau=1$, $R=e$

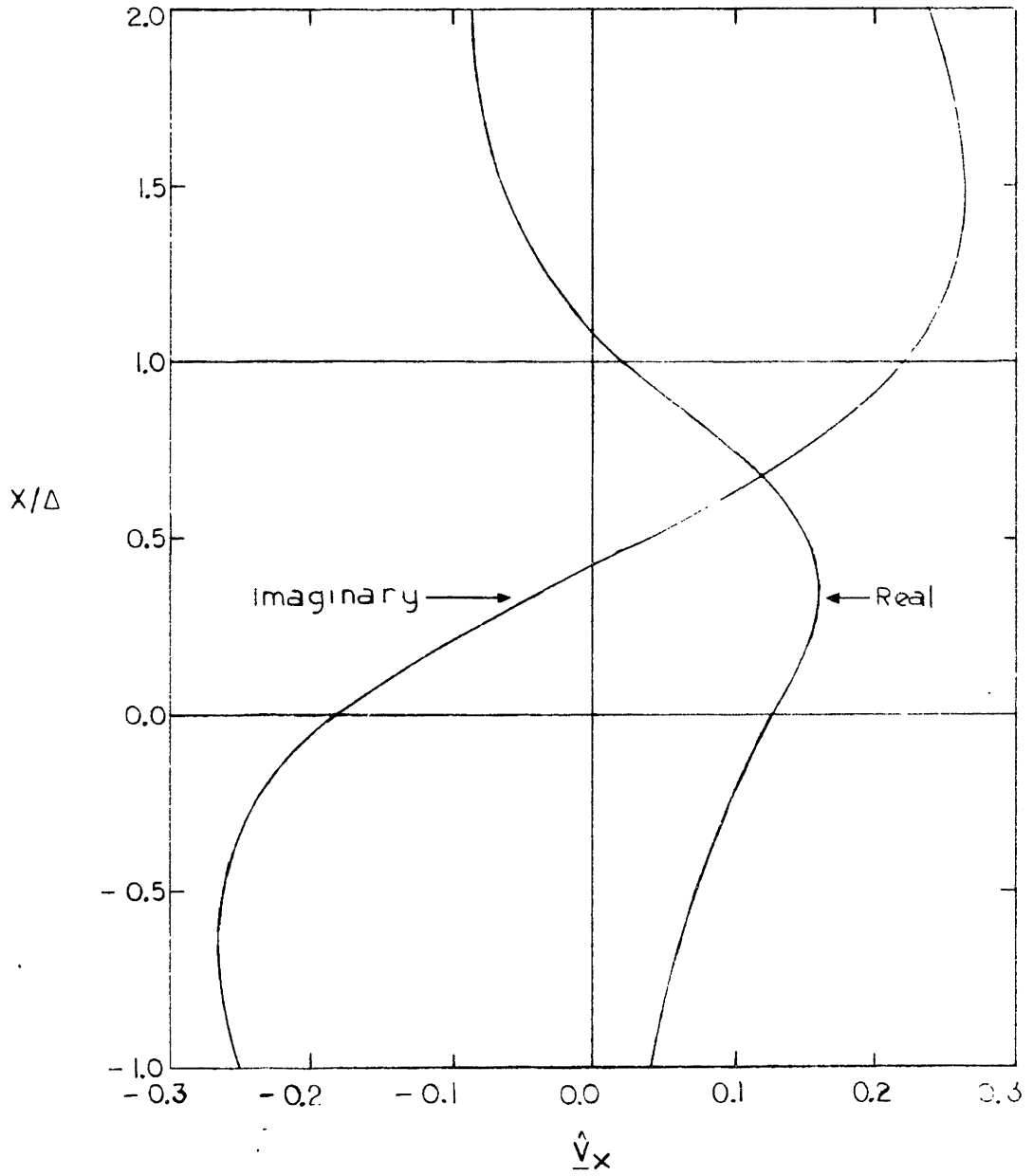


Figure 7. \hat{v}_x versus x/Δ , first eigenfunction, $k=1$, $T/\tau=1$, $R=e$

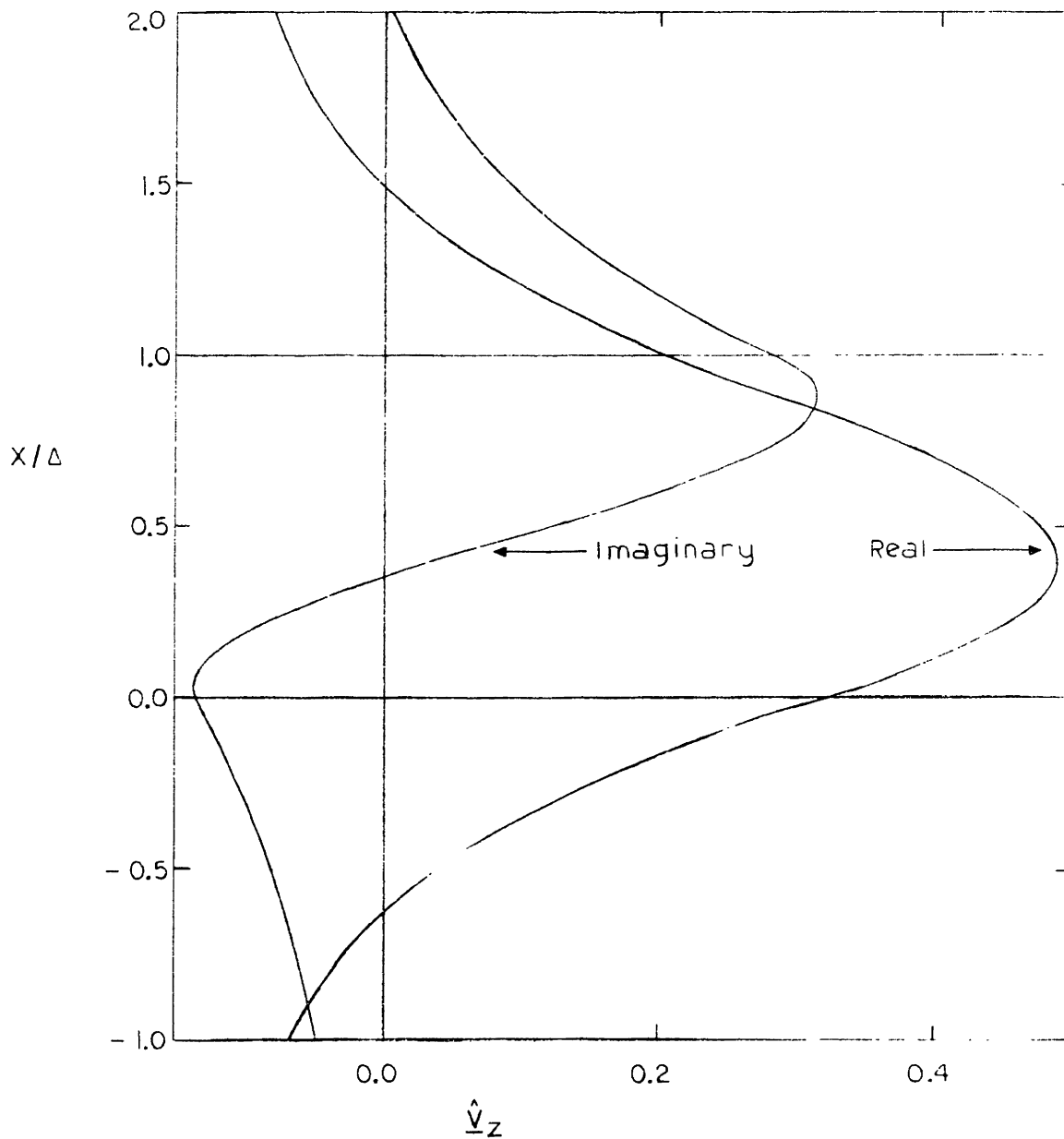


Figure 8. \hat{v}_z versus x/Δ , first eigenfunction, $k=1$, $T/\tau=1$, $R=e$

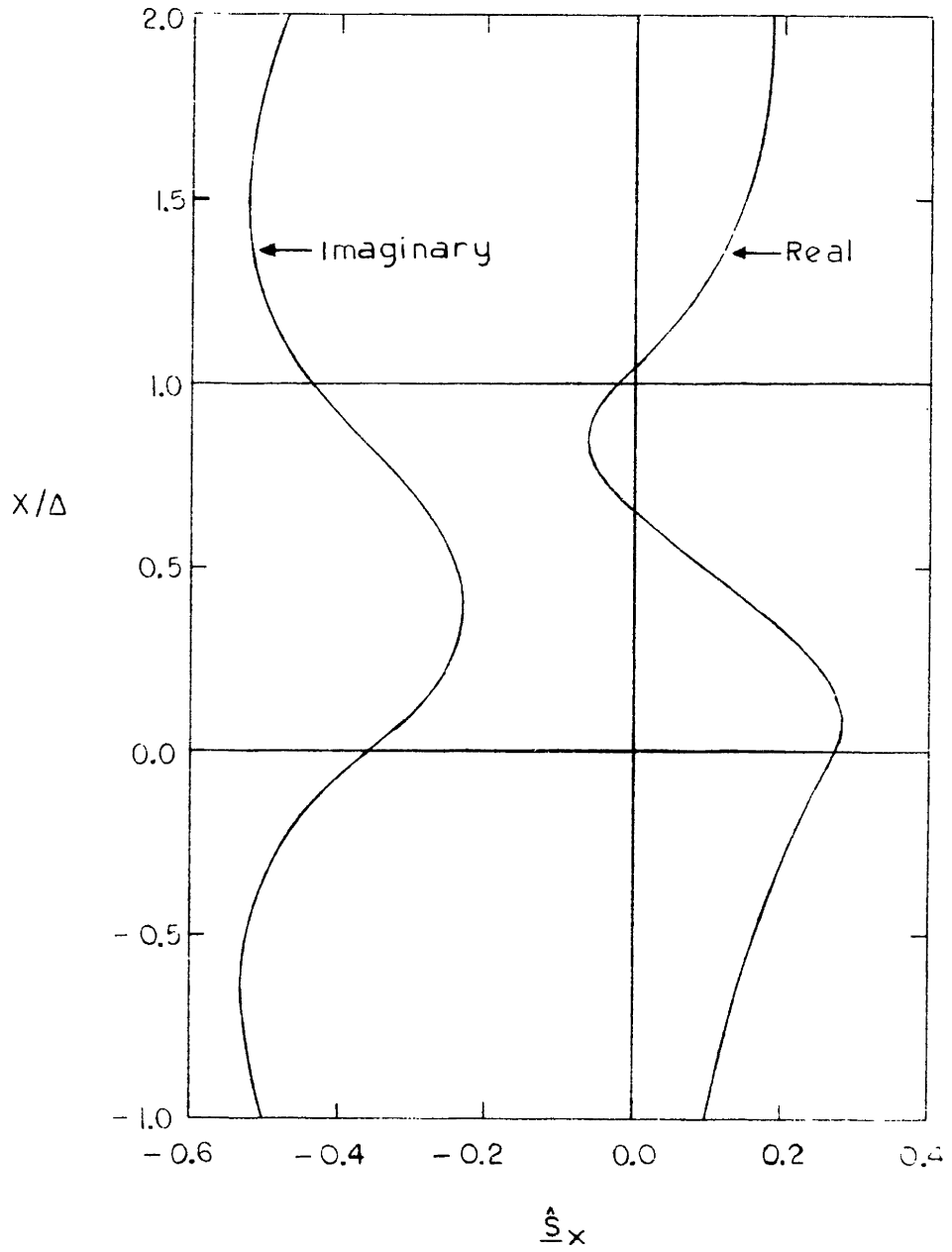


Figure 9. \hat{S}_x versus x/Δ , first eigenfunction, $k=1$, $T/\tau=1$, $R=e$

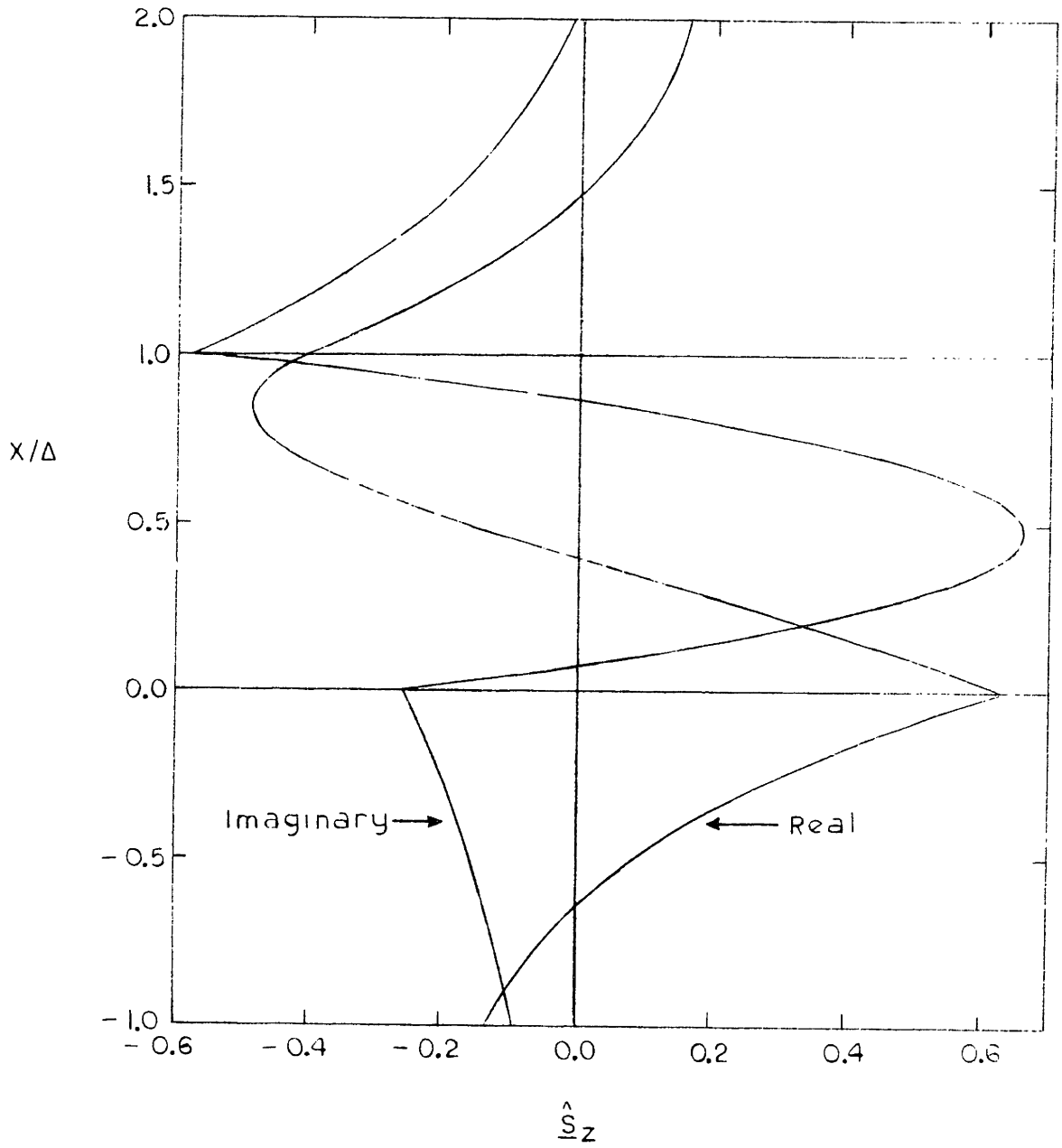


Figure 10. \hat{S}_z versus x/Δ , first eigenfunction, $\underline{k}=1$, $T/\tau=1$, $R=e$

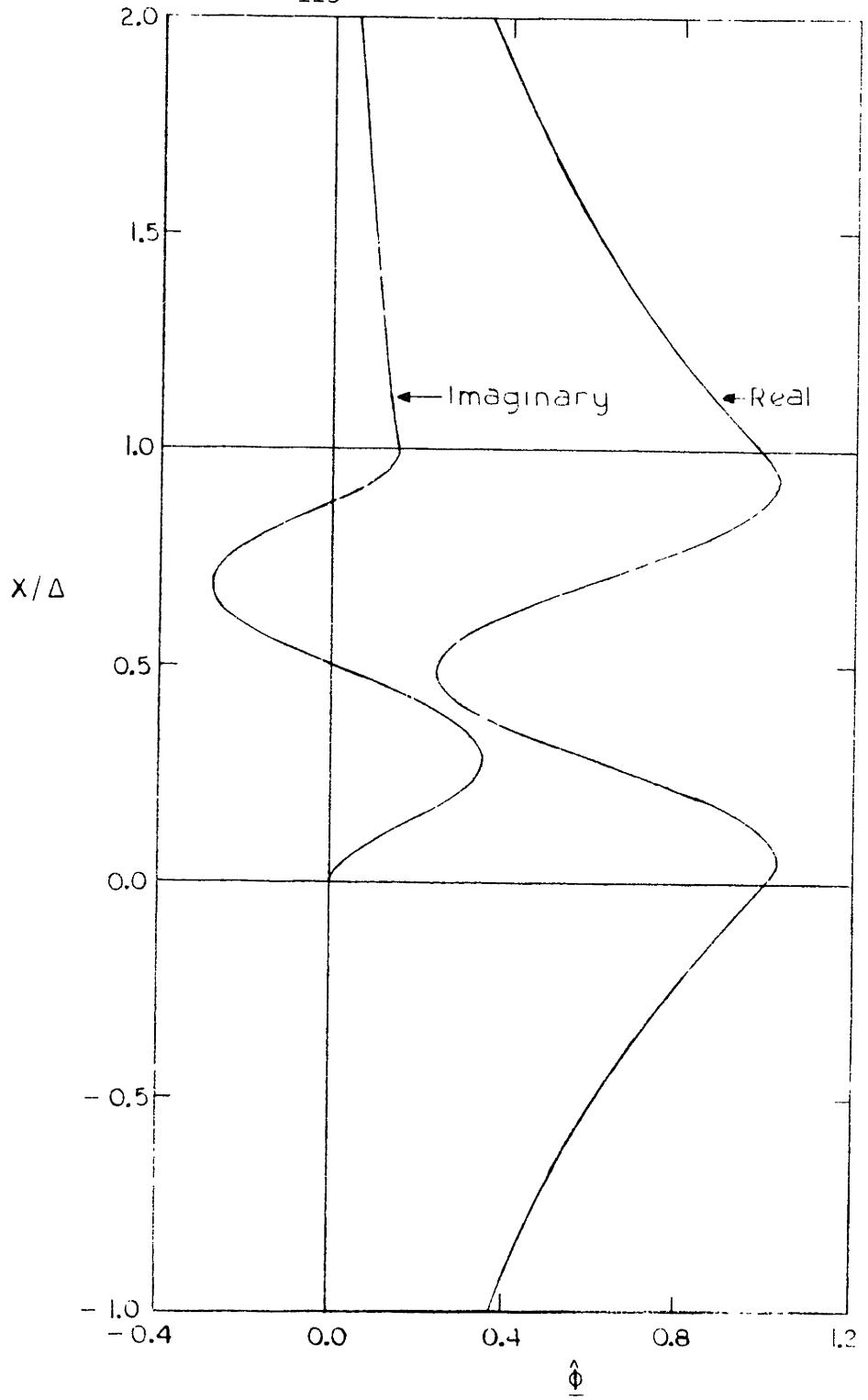


Figure 11. $\hat{\phi}$ versus x/Δ , second eigenfunction, $\underline{k}=1$, $T/\tau=1$, $R=e$

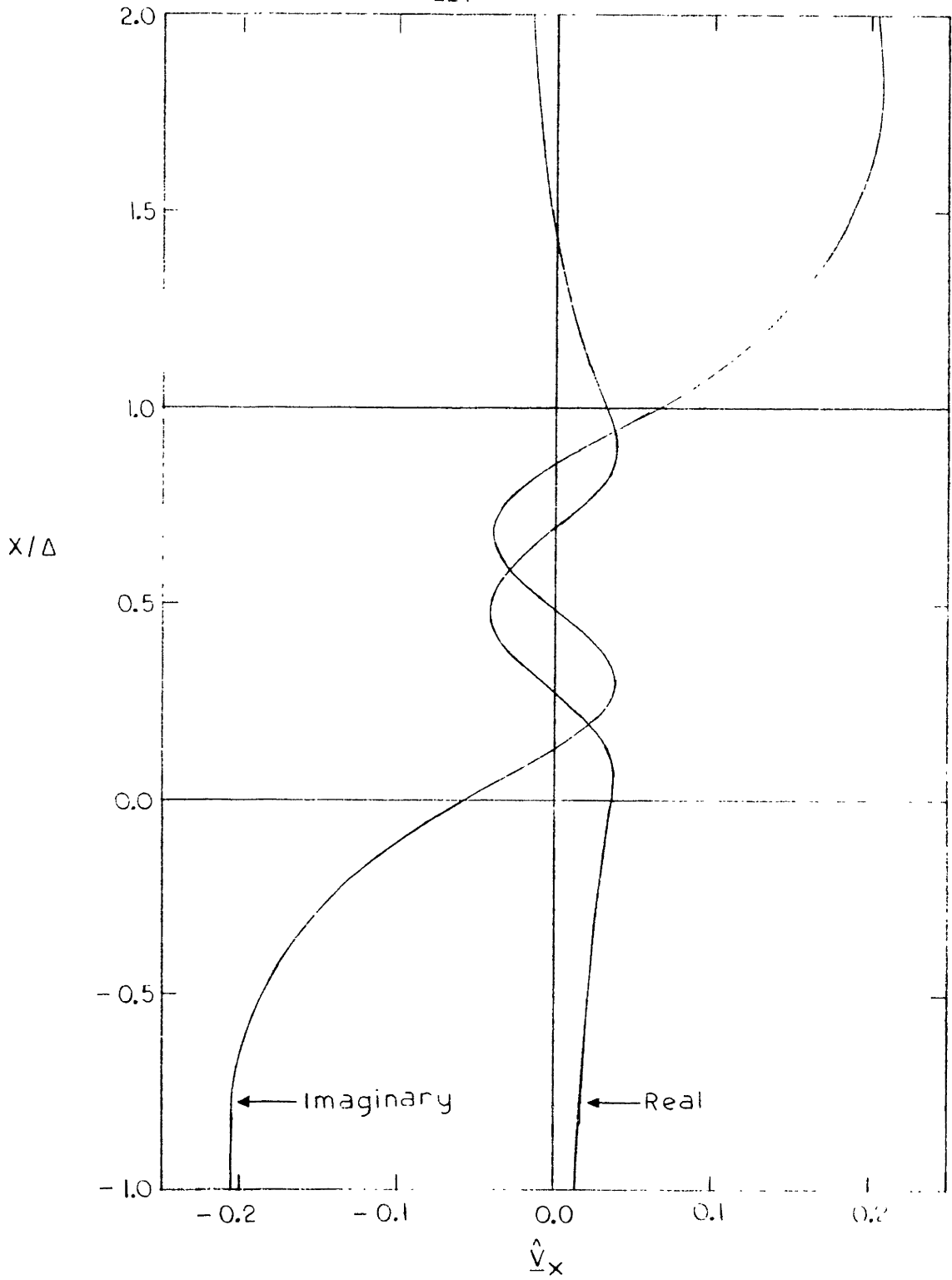


Figure 12. \hat{v}_x versus x/Δ , second eigenfunction, $\underline{k}=1$, $T/\tau=1$, $R=e$

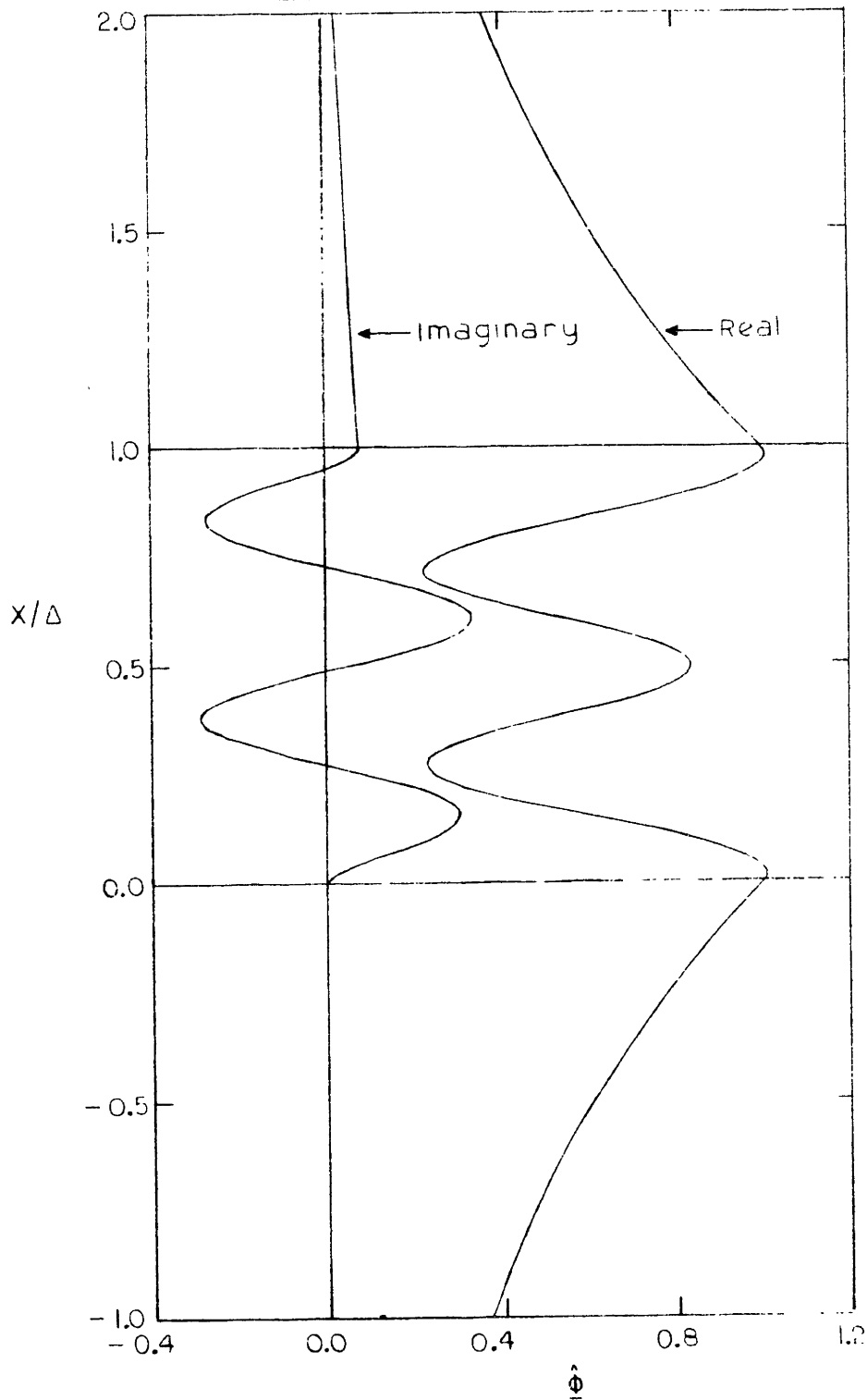


Figure 13. $\hat{\phi}$ versus x/Δ , third eigenfunction, $k=1$, $1/\tau=1$, $R=e$

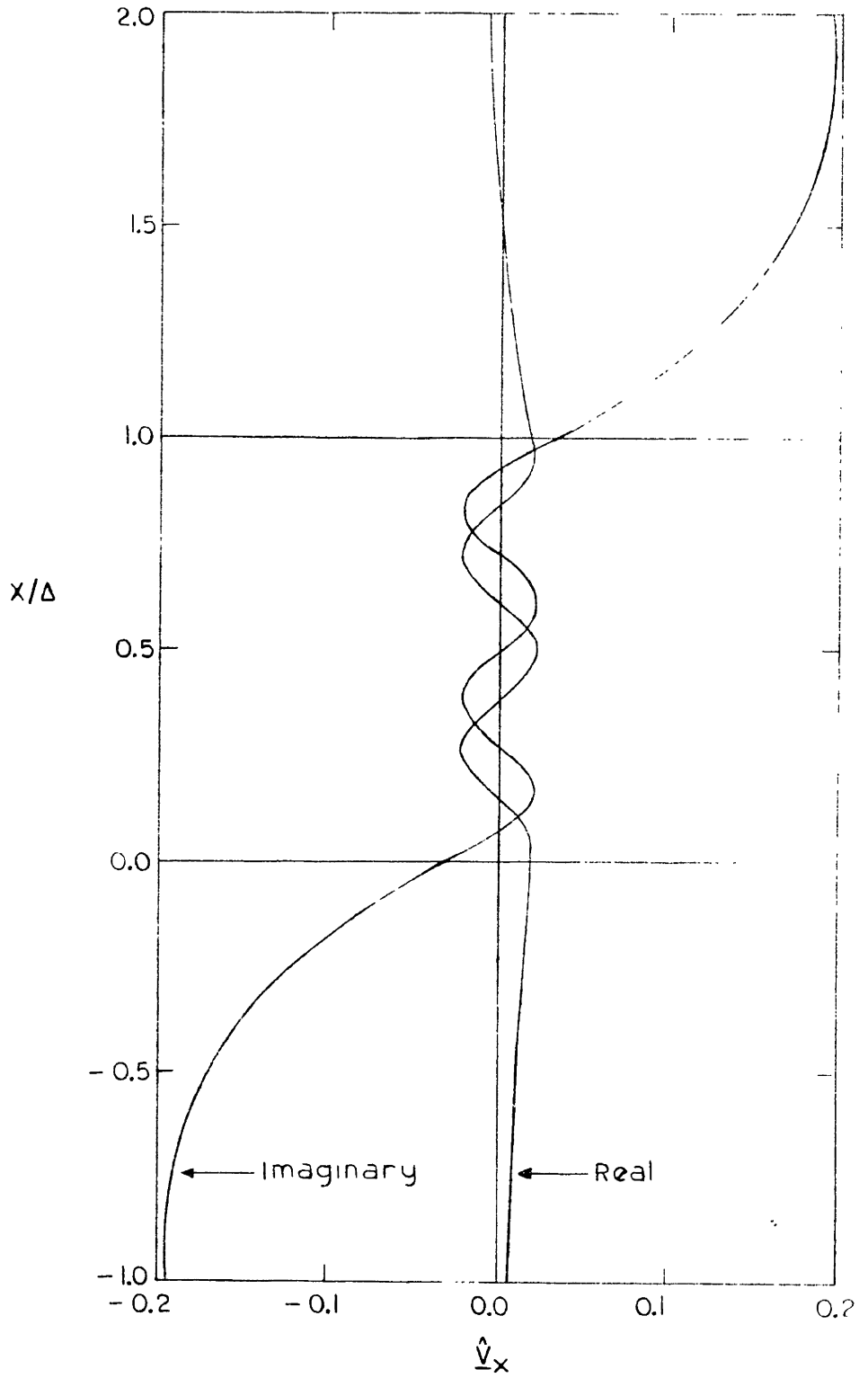


Figure 14. \hat{v}_x versus x/Δ , third eigenfunction, $\underline{k}=1$, $T/\tau=1$, $R=e$

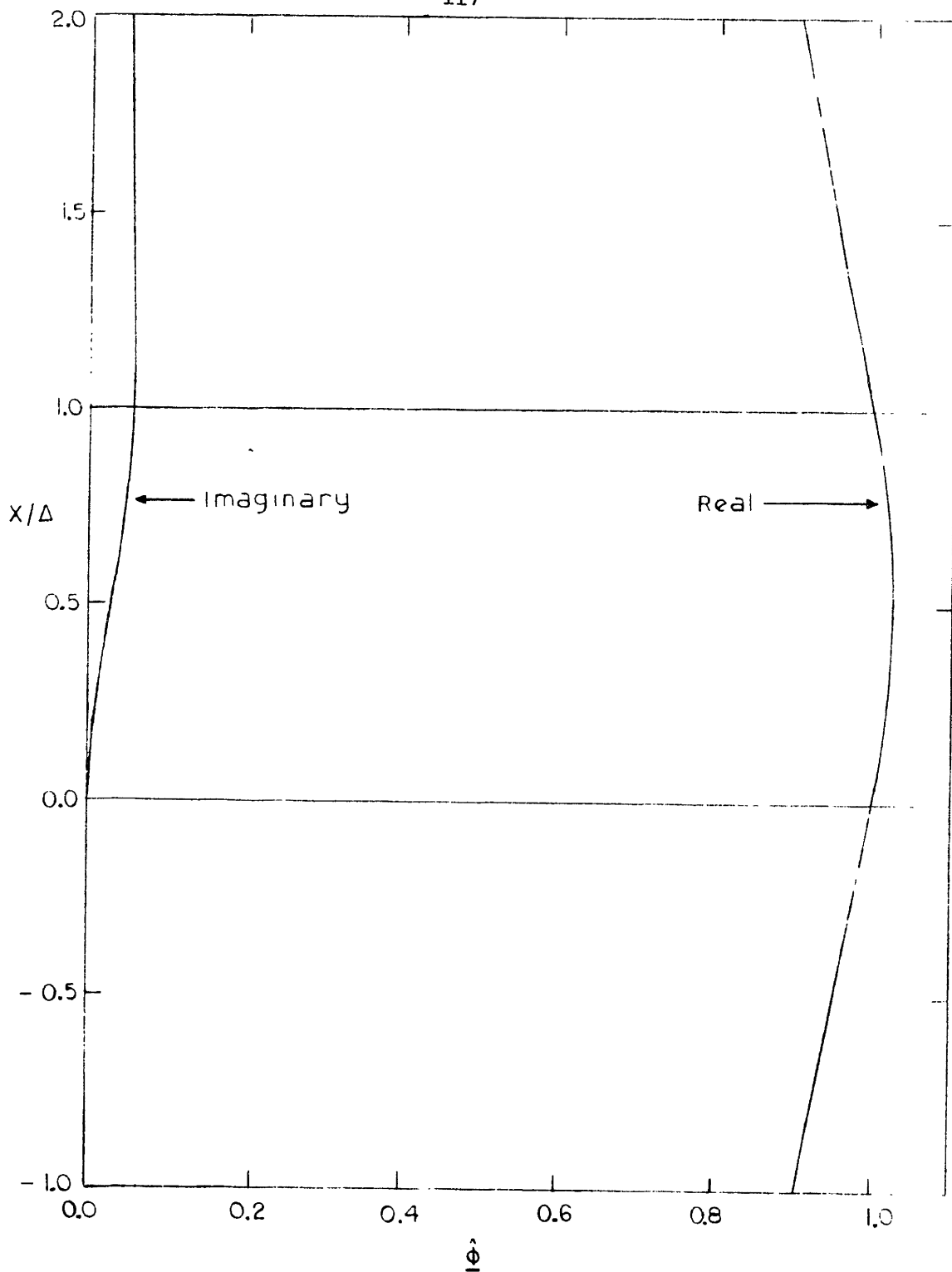


Figure 15. $\hat{\phi}$ versus x/Δ , first eigenfunction, $k=0.1$, $T/\tau=1$, $R=e$

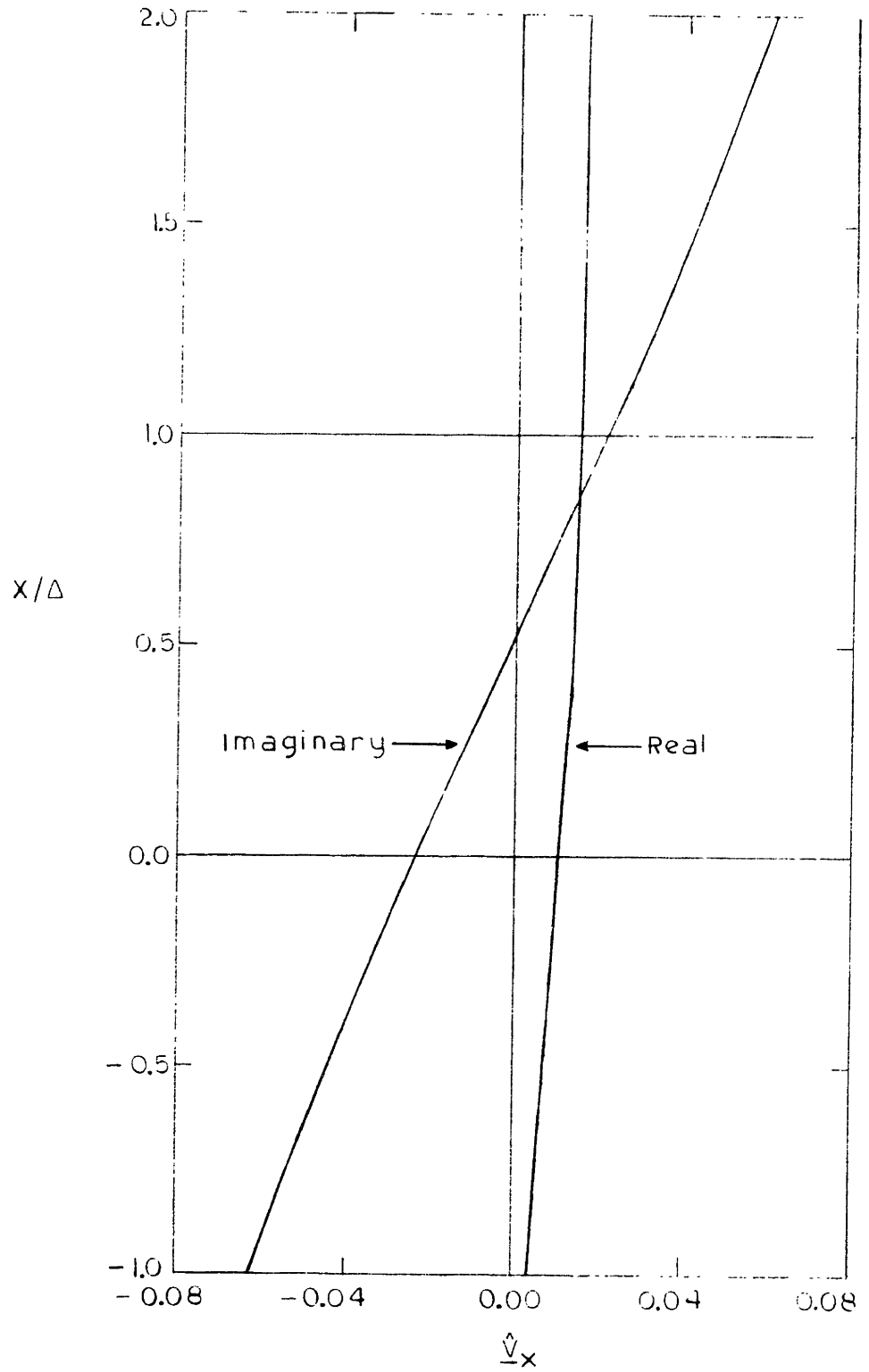


Figure 16. \hat{v}_x versus x/Δ , first eigenfunction, $k=0.1$, $T/\tau=1$, $R=e$

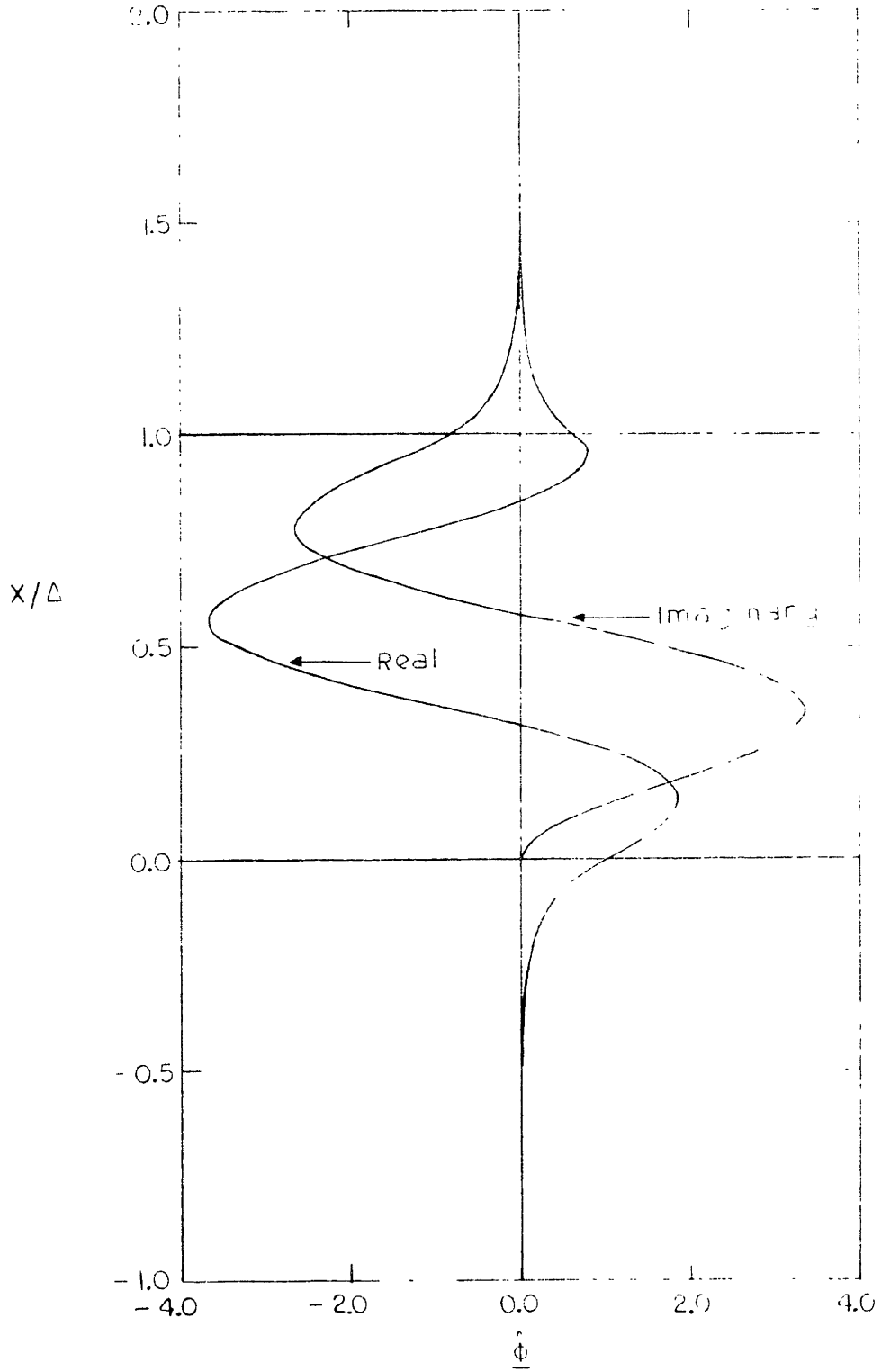


Figure 17. $\hat{\phi}$ versus x/Δ , first eigenfunction, $k=10$, $T/\tau=1$, $R=e$

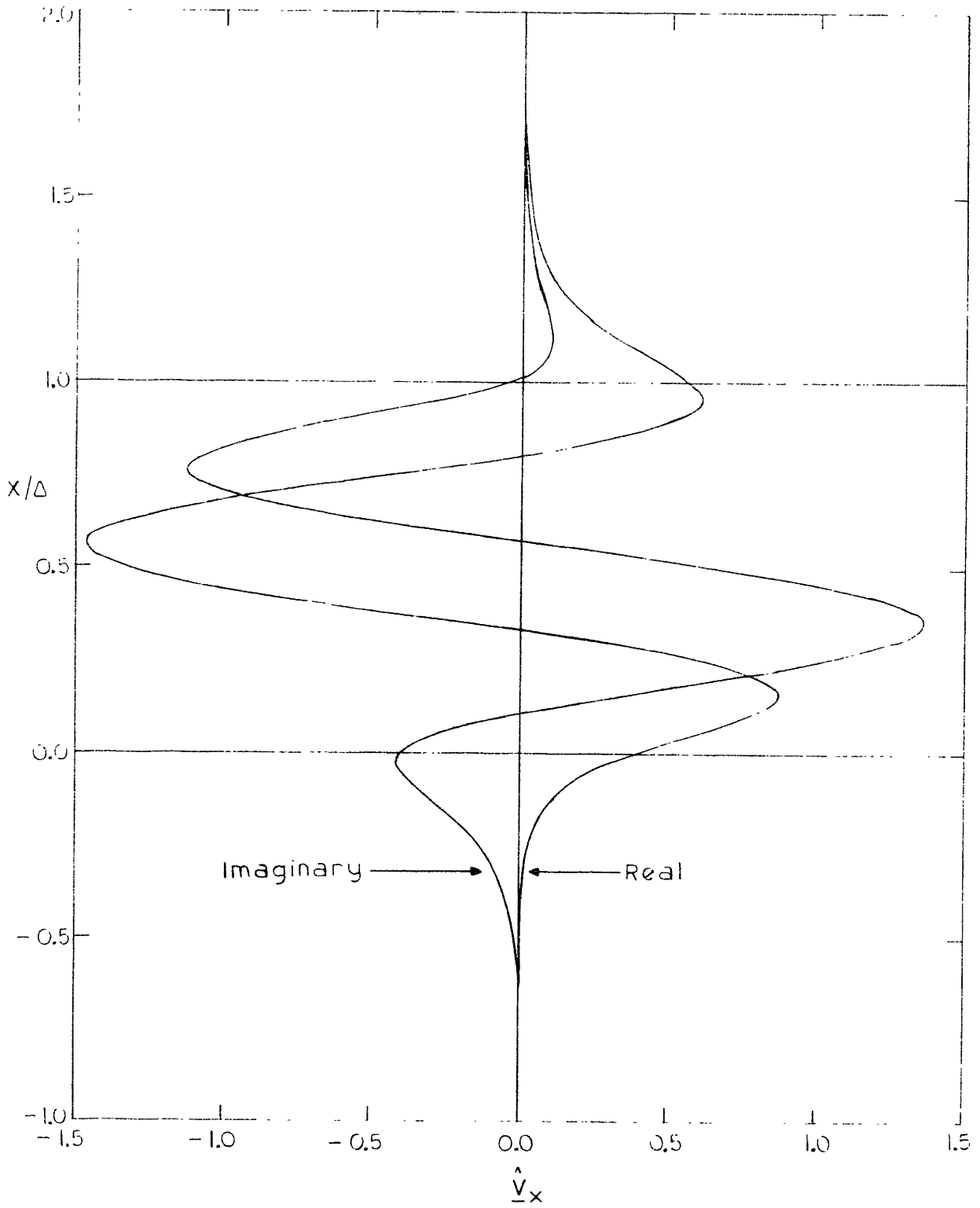


Figure 18. \hat{v}_x versus x/Δ , first eigenfunction, $\underline{k}=10$, $T/\tau=1$, $R=e$

\underline{k} , with that in Figs. 13 and 14, where we are observing a higher eigenfunction. The mode displayed in Figs. 17 and 18 is the fastest-growing one at $\underline{k} = 10$, and involves the least variation of all the eigenmodes at that wavenumber. It has evolved directly from the eigenmode shown in Figs. 15 and 16 as \underline{k} changed from 0.1 to 10.

Having identified a set of eigenfrequencies for one set of parameters, \underline{k} , T/τ , R , we now wish to follow the eigenfrequencies as functions of \underline{k} , with the other parameters, T/τ and R , held fixed. (As a practical matter, we specifically identify the first three eigenfrequencies.) We need not "start from scratch" for each new \underline{k} , printing out a grid to obtain initial estimates for the positions of zeroes of $D(\underline{s})$. Rather, provided we increment \underline{k} in small enough steps, we can start the search for each zero at the position of that zero for the previous value of \underline{k} . The result is a pair of plots of the real and imaginary parts of \underline{s} for the first three eigenfrequencies as functions of \underline{k} , as shown in Figs. 19 and 20.

Several characteristics of these curves are to be noted. First, for small \underline{k} (waves long compared to the layer thickness), all eigenfrequencies approach zero. In this limit, the situation approaches the model of Section III.C -- i.e., an abrupt interface, with no first-order electromechanical coupling. In the opposite extreme, for large \underline{k} , where the eigenfunctions vary rapidly across the layer thickness, all eigenfrequencies approach zero asymptotically. At some intermediate \underline{k} ($\underline{k} \sim 1$), the real and imaginary parts take on maximum values. For the same mode, the maxima of real and imaginary parts occur at different values of \underline{k} . Maxima occur at increasing values of \underline{k} for higher modes.

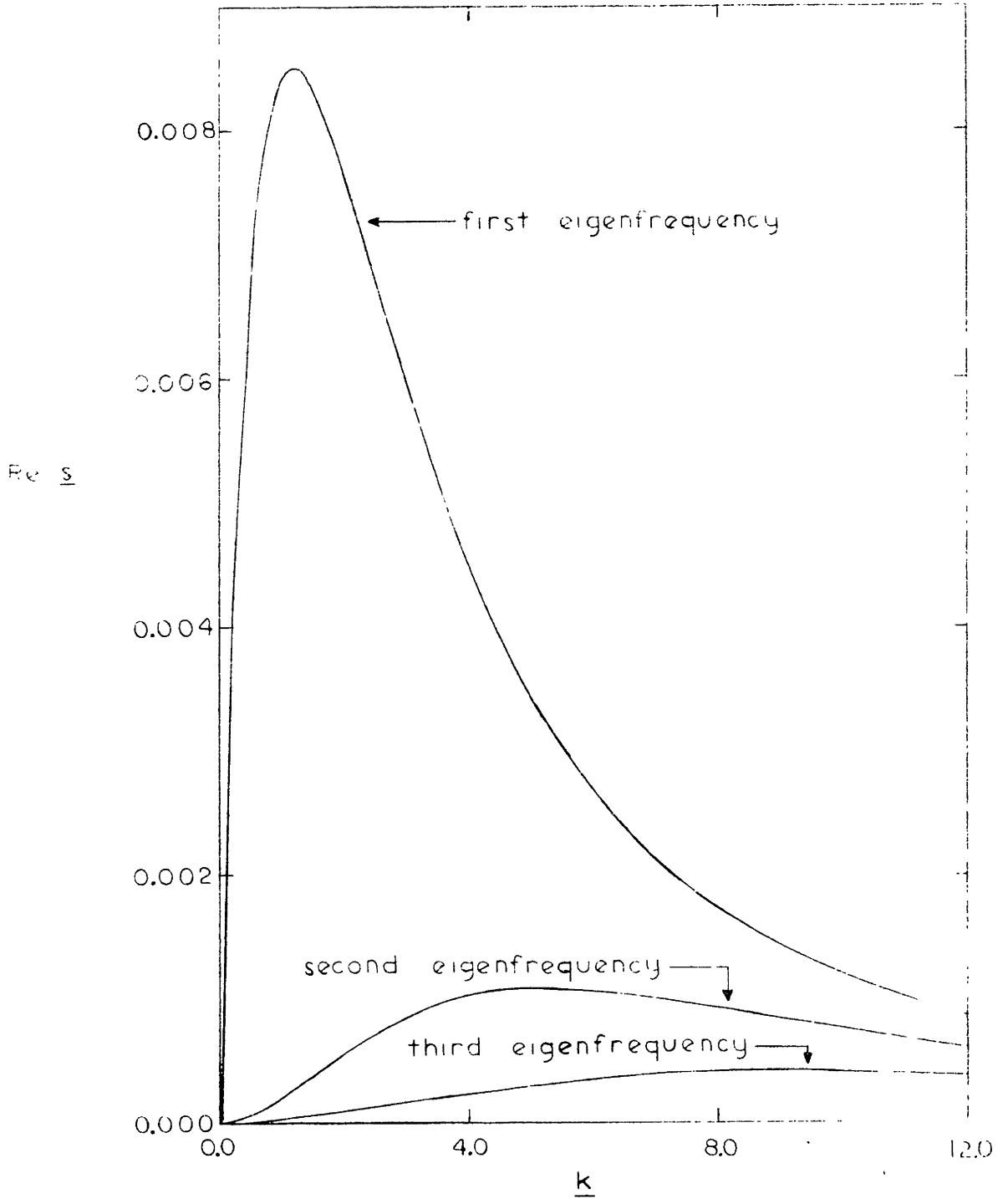


Figure 19. $Re\ s$ versus k , $T/\tau = 1$, $R = e$

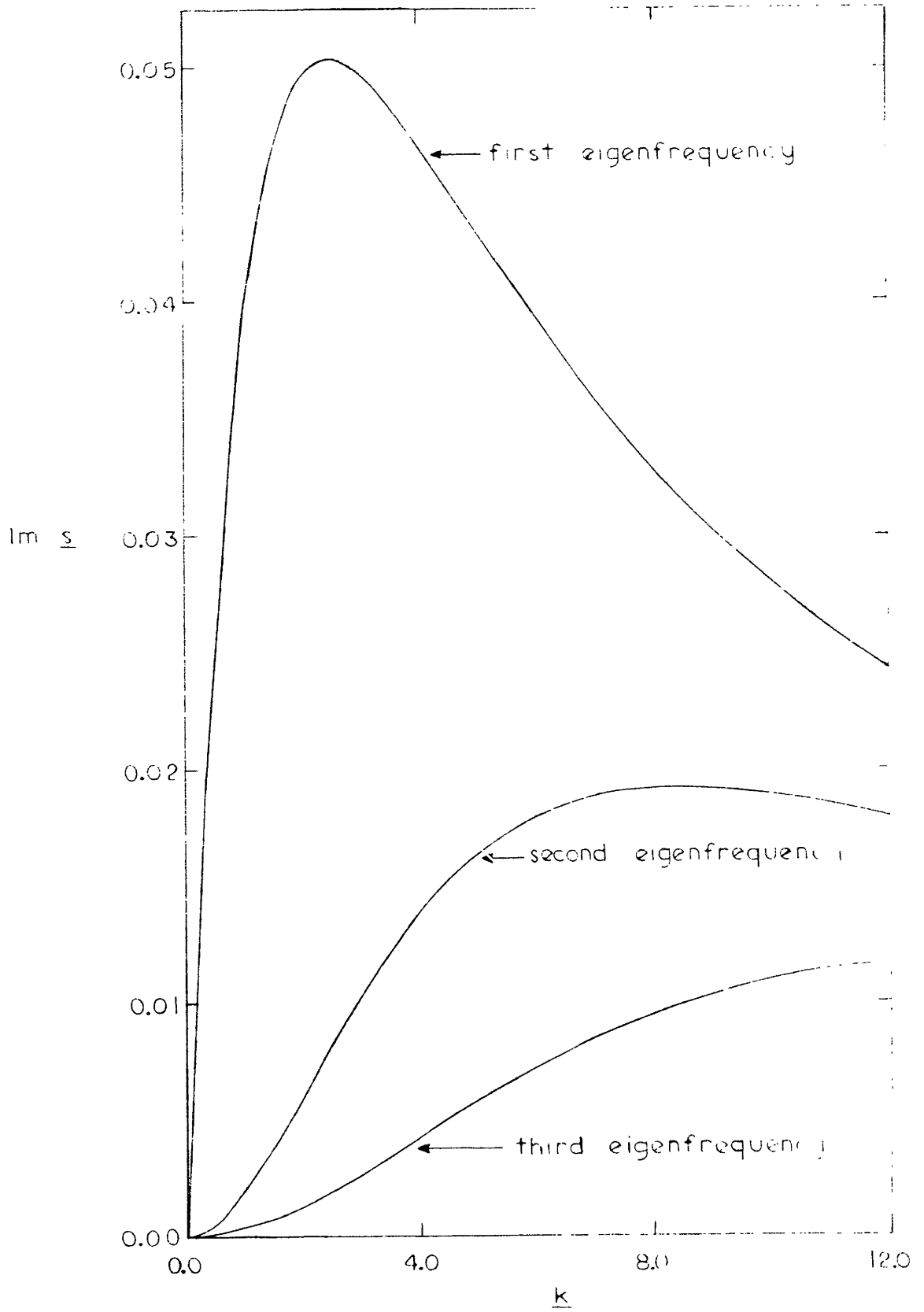


Figure 20. $\text{Im } \underline{s}$ versus \underline{k} , $T/\tau = 1$, $R = e$

To display the dependence of such plots on the parameter T/τ , we show the same information, $\text{Re } \underline{s}$ and $\text{Im } \underline{s}$ versus \underline{k} for the first eigenfrequency, in Figs. 21 and 22 for $T/\tau = 10^{-2}$ and in Figs. 23 and 24 for $T/\tau = 10^2$.

It is at the value of \underline{k} where $\text{Re } \underline{s}$ has its maximum that we predict fastest growth in time for any given T/τ and R . Denote this value \underline{k}^* , and the first eigenfrequency at this value \underline{s}^* . Then, to describe the maximum growth rate and wavenumber as functions of the parameters, we desire plots of \underline{k}^* , $\text{Re } \underline{s}^*$, and $\text{Im } \underline{s}^*$ as functions of T/τ for various values of R . To obtain this information for a given R , without an inordinate amount of computation, we determine three points near the maximum on the $\text{Re } \underline{s}$ versus \underline{k} curve for any one given T/τ , fit the points with a quadratic and locate the maximum of the quadratic. That maximum must lie within the range of values of \underline{k} used to define the quadratic in order for the fit to be deemed acceptable. The values of \underline{k} and \underline{s} at the maximum, then, are \underline{k}^* and \underline{s}^* . We use the same technique in searching for the position of a zero as we increment T/τ as we did in incrementing \underline{k} . Specifically, \underline{k} is held constant at the value of \underline{k}^* for the previous T/τ , and \underline{s}^* is used as the initial estimate of the zero in $D(\underline{s})$ for a new T/τ . Plots of \underline{k}^* , $\text{Re } \underline{s}^*$, and $\text{Im } \underline{s}^*$ versus T/τ on a log scale are shown in Figs. 25 and 26, respectively, for five values of R :

$$\begin{array}{ll}
 R = e^{(0.1)} \approx 1.11 & R = e^5 \approx 148. \\
 R = e \approx 2.72 & \text{and} \\
 R = 25.9 & R = e^{10} \approx 22,000.
 \end{array}$$

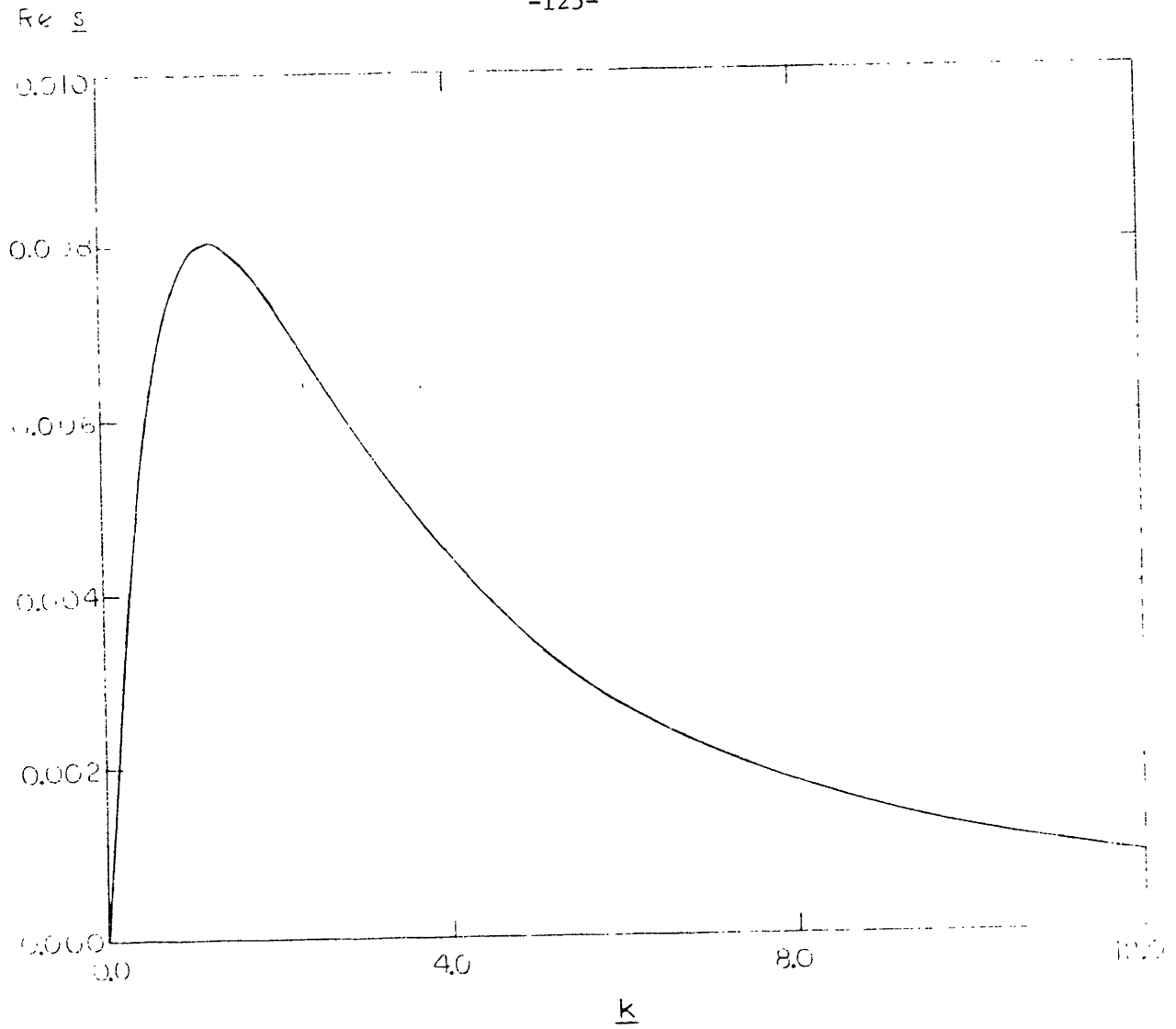


Figure 21. $\text{Re } s$ versus k , $T/\tau = 10^{-2}$, $R = e$

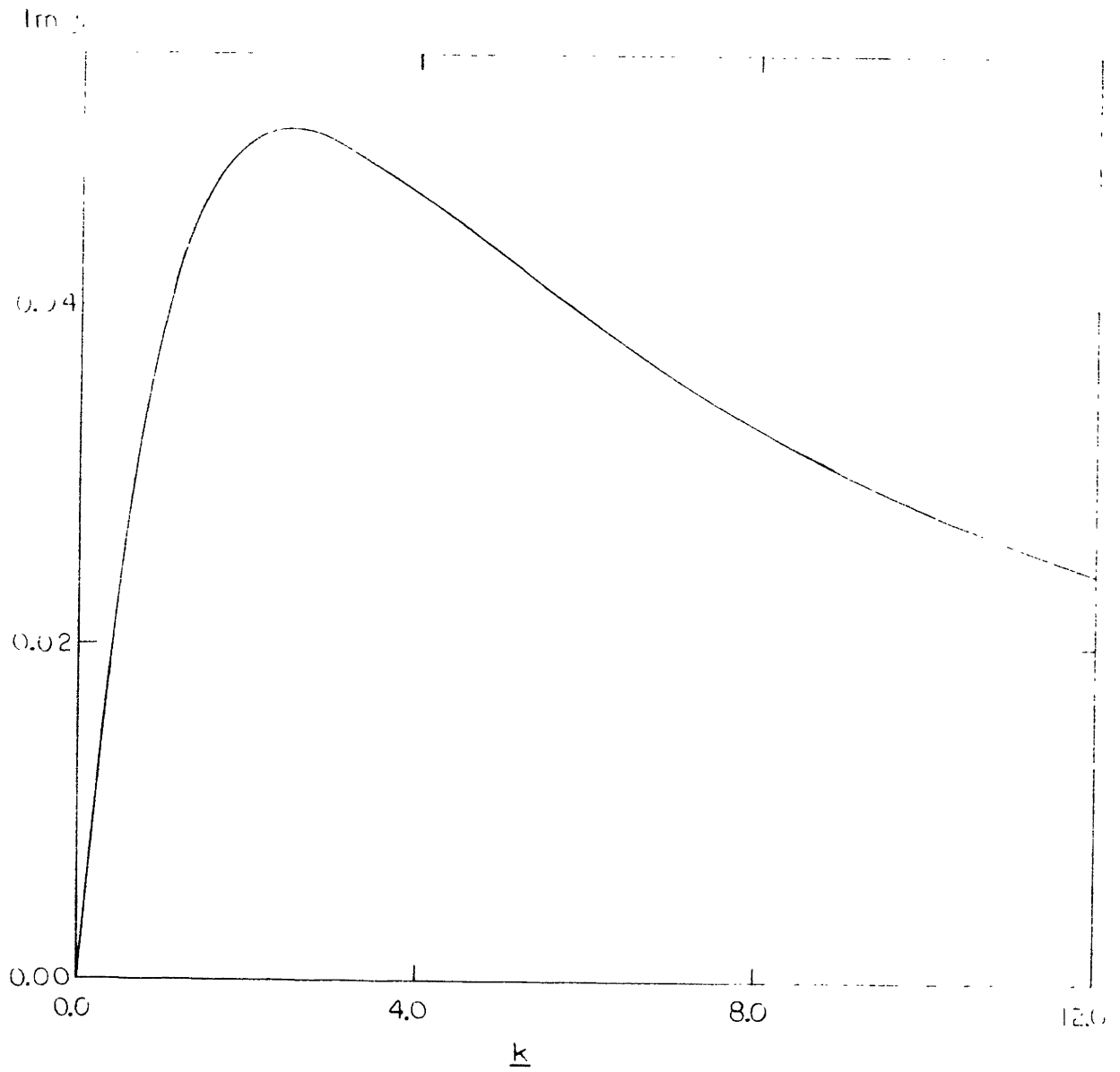


Figure 22. $\text{Im } s$ versus k , $T/\tau = 10^{-2}$, $R = e$

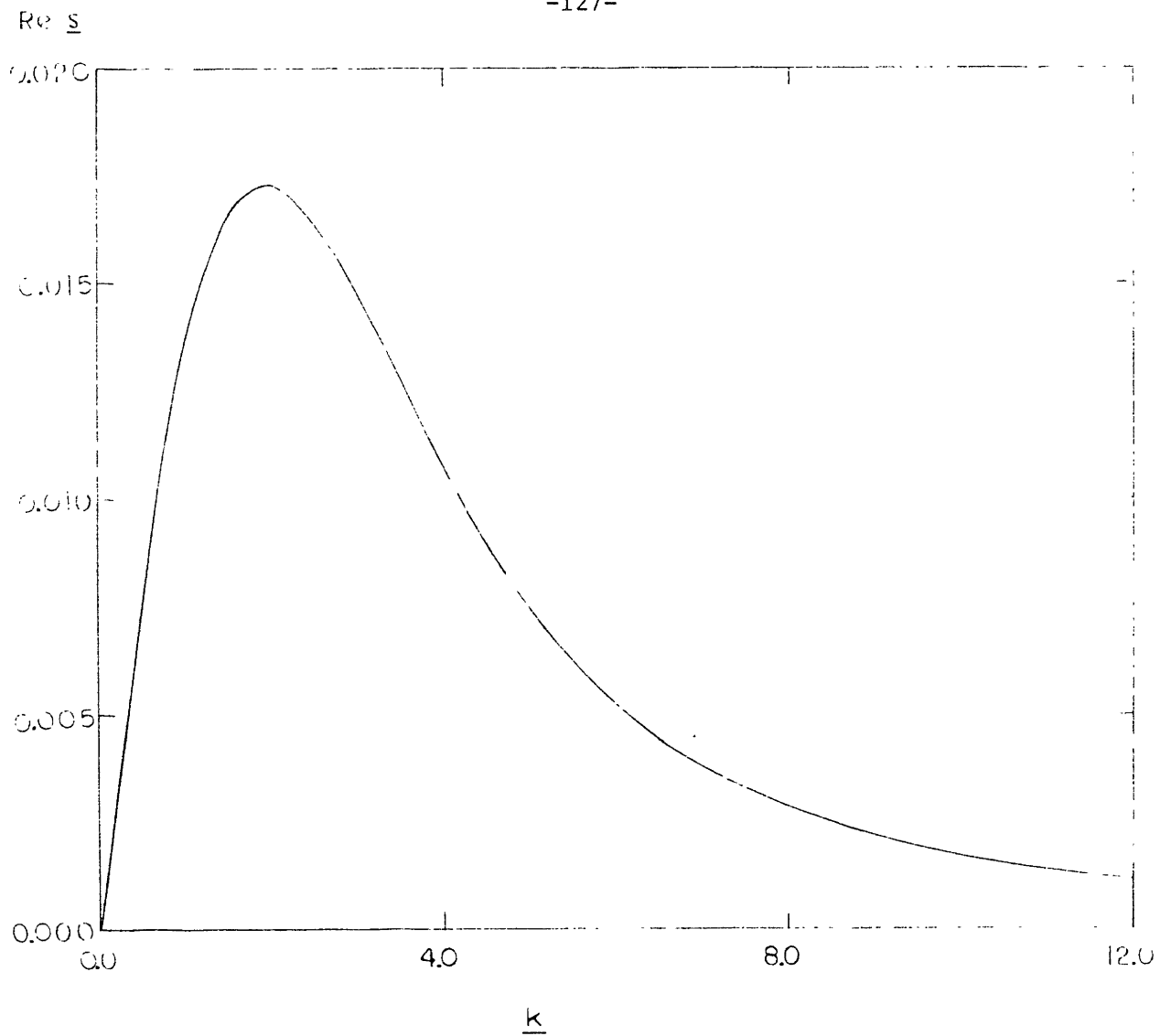


Figure 23. $\text{Re } s$ versus k , $T/\tau = 10^2$, $R = e$

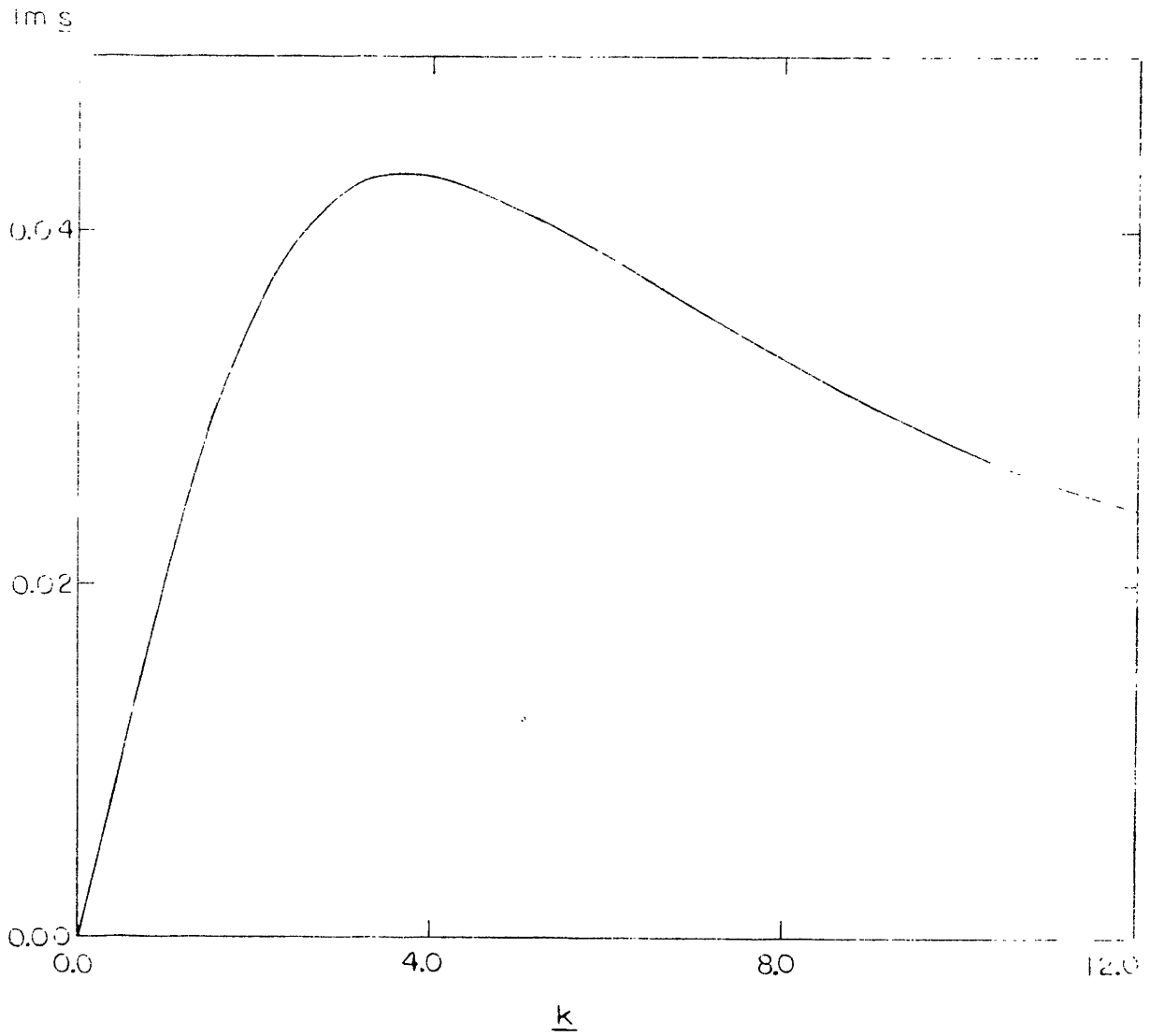


Figure 24. $\text{Im } \underline{s}$ versus \underline{k} , $T/\tau = 10^2$, $R = e$

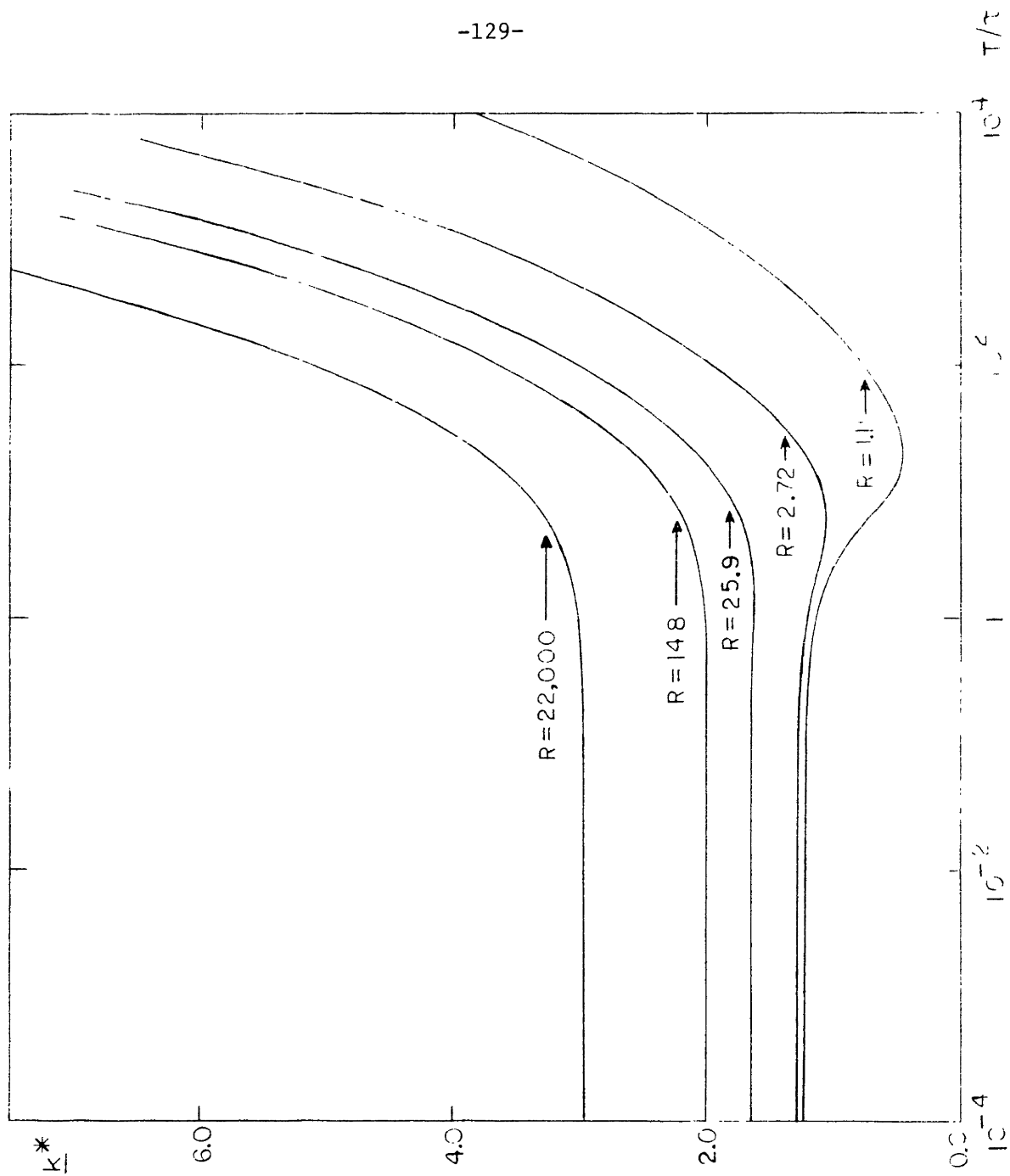


Figure 25. k^* versus T/τ

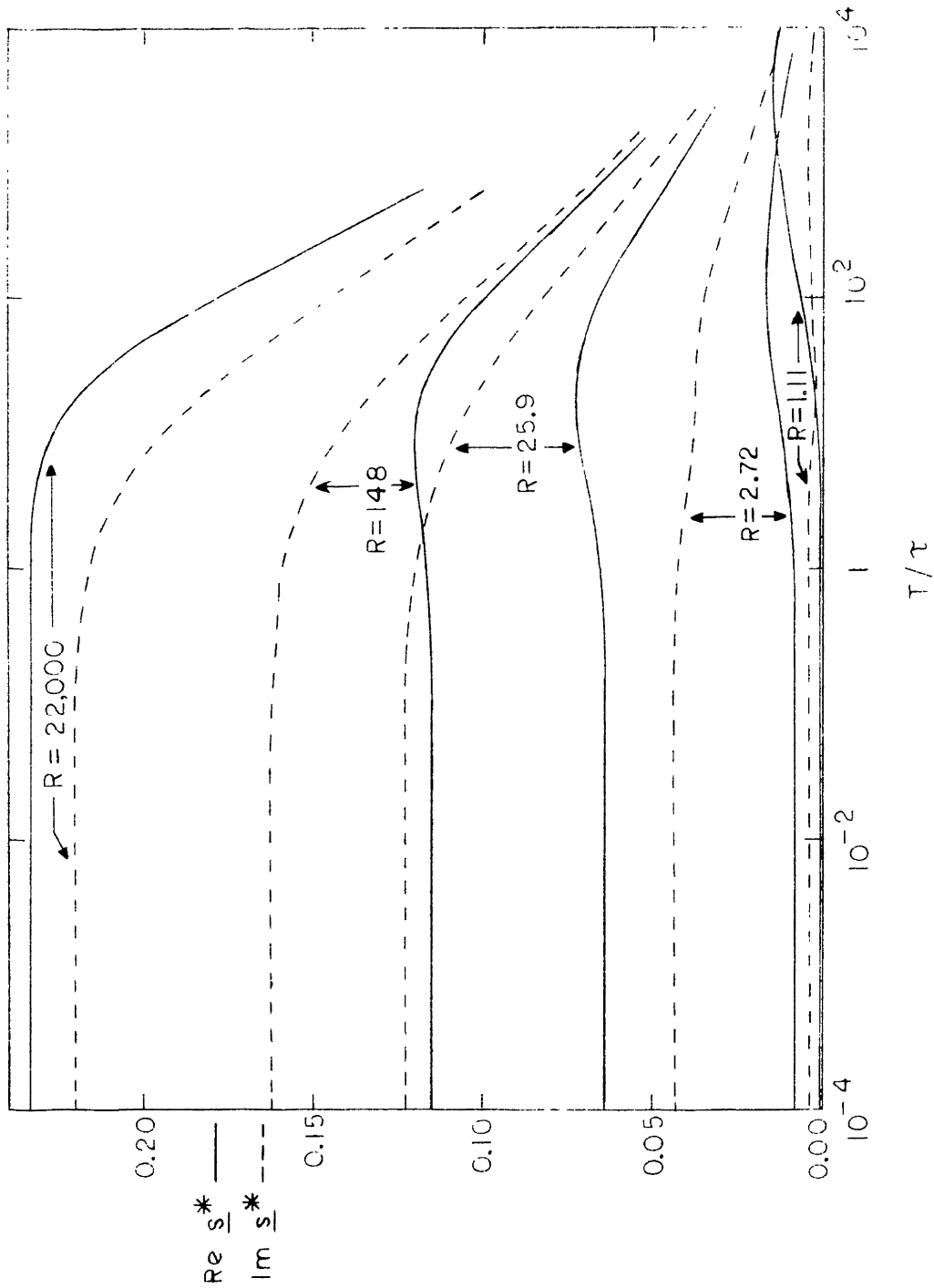


Figure 26. $\text{Re } s^*$ and $\text{Im } s^*$ versus T/τ

Using Eqs. (19), (21), (22) and (23), we write out T/τ in terms of physical parameters, and unnormalize \underline{k} and \underline{s} :

$$\frac{T}{\tau} = \frac{\epsilon \rho}{\eta^2} (E_0 \Delta)^2 \quad (4.106)$$

$$k^* = \underline{k}^* / \Delta \quad (4.107)$$

$$s^* = \underline{s}^* \frac{\epsilon E_0^2}{\eta} \quad (4.108)$$

For $T/\tau \ll 1$, viscous effects dominate over inertia, and \underline{k}^* and \underline{s}^* are independent of T/τ . Thus, if we think of varying T/τ in this range by varying E_0 , holding all other parameters constant, k^* remains constant while s^* increases quadratically with E_0 . Alternatively, if we vary T/τ by varying Δ , k^* decreases as $1/\Delta$ while s^* remains constant.

For $T/\tau \gg 1$, inertia plays an important role in the instability dynamics, and \underline{k}^* increases while $\text{Re } \underline{s}^*$ and $\text{Im } \underline{s}^*$ decrease with T/τ . Note, however, that because T/τ is plotted on a log scale in Figs. 25 and 26, the functions are relatively insensitive to T/τ . Thus, if again we think of increasing E_0 , k^* increases slowly while $\text{Re } s^*$ and $\text{Im } s^*$ increase less rapidly than quadratically with E_0 . If we hold E_0 constant and increase Δ , k^* decreases less rapidly than $1/\Delta$ and $\text{Re } s^*$ and $\text{Im } s^*$ decrease.

Finally, we see that k^* , $\text{Re } s^*$ and $\text{Im } s^*$ are relatively insensitive to R , but that all three functions increase with R , with one exception. For large T/τ , $\text{Re } \underline{s}^*$ first decreases, then increases with R .

C. Physical Mechanism

The physical nature of the instability described in Section IV.B is made apparent by plotting velocity streamlines at \underline{k}^* and \underline{s}^* , with T/τ small enough so that the flow is viscous dominated. Figures 27 and 28 are plots of real and imaginary parts of the first eigenfunctions, \hat{v}_x and \hat{v}_z respectively, at \underline{k}^* and \underline{s}^* , for $T/\tau = 10^{-4}$ and $R = e$. Here, we have used the eigenfrequency which has $\text{Im } \underline{s}^* < 0$ to establish the physical significance of mirror-image eigenfrequencies. The corresponding velocity streamlines are plotted across the layer width and one layer thickness into each of the bounding half-spaces in Fig. 29. The negative imaginary part of \underline{s}^* indicates propagation of the entire picture to the left. The corresponding eigenfrequency with positive imaginary part would have streamlines slanted to the right, with the entire picture propagating to the right.

The physical mechanism responsible for overstable modes in the configuration described may be understood with the help of Fig. 30. Within the range of varying conductivity, bounded above and below by half-spaces, slanted layers of alternating low and high conductivities σ^α and σ^β are postulated. Application of an electric field in the horizontal direction in the leftmost layer leads to surface charge accumulation at the slanted interfaces, so as to yield a continuous normal current density. Interfaces bounded on the left by low conductivity and on the right by high conductivity experience an upward-directed shear force due to the tangential electric field component. Similarly, interfaces bounded on the left by high conductivity and on the right by low conductivity experience a downward-directed shear force. The resulting cellular fluid motions, then, alter the conductivity distribution by drawing in less conducting fluid from the upper half-

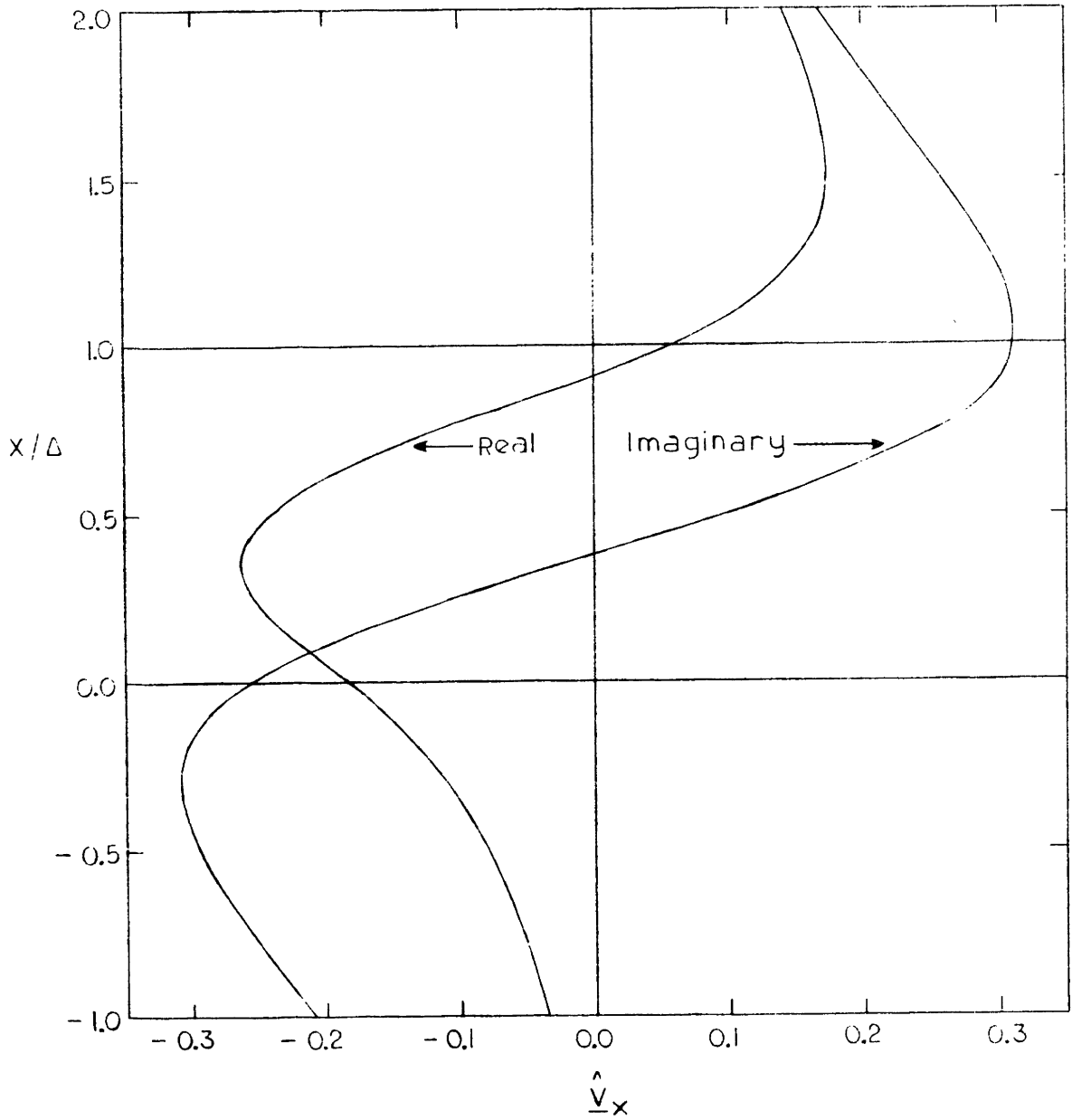


Figure 27. \hat{v}_x versus x/Δ , first eigenfunction, $\underline{k}=\underline{k}^*=1.6412$,
 $T/\tau = 10^{-4}$, $R = 25.9$

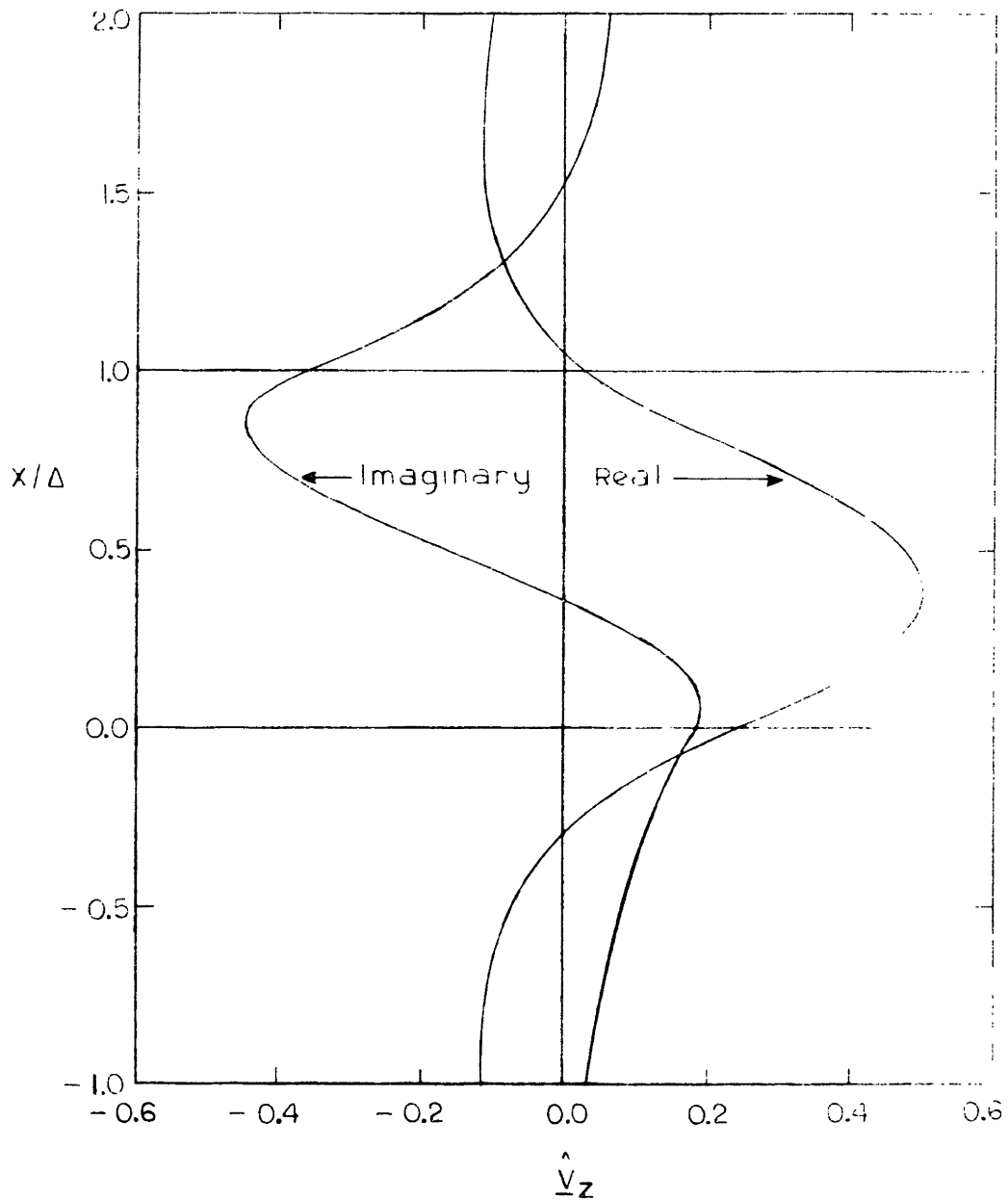


Figure 28. \hat{v}_z versus x/Δ , first eigenfunction, $\underline{k} = \underline{k}^* = 1.6412$,
 $T/\tau = 10^{-4}$, $R = 25.9$

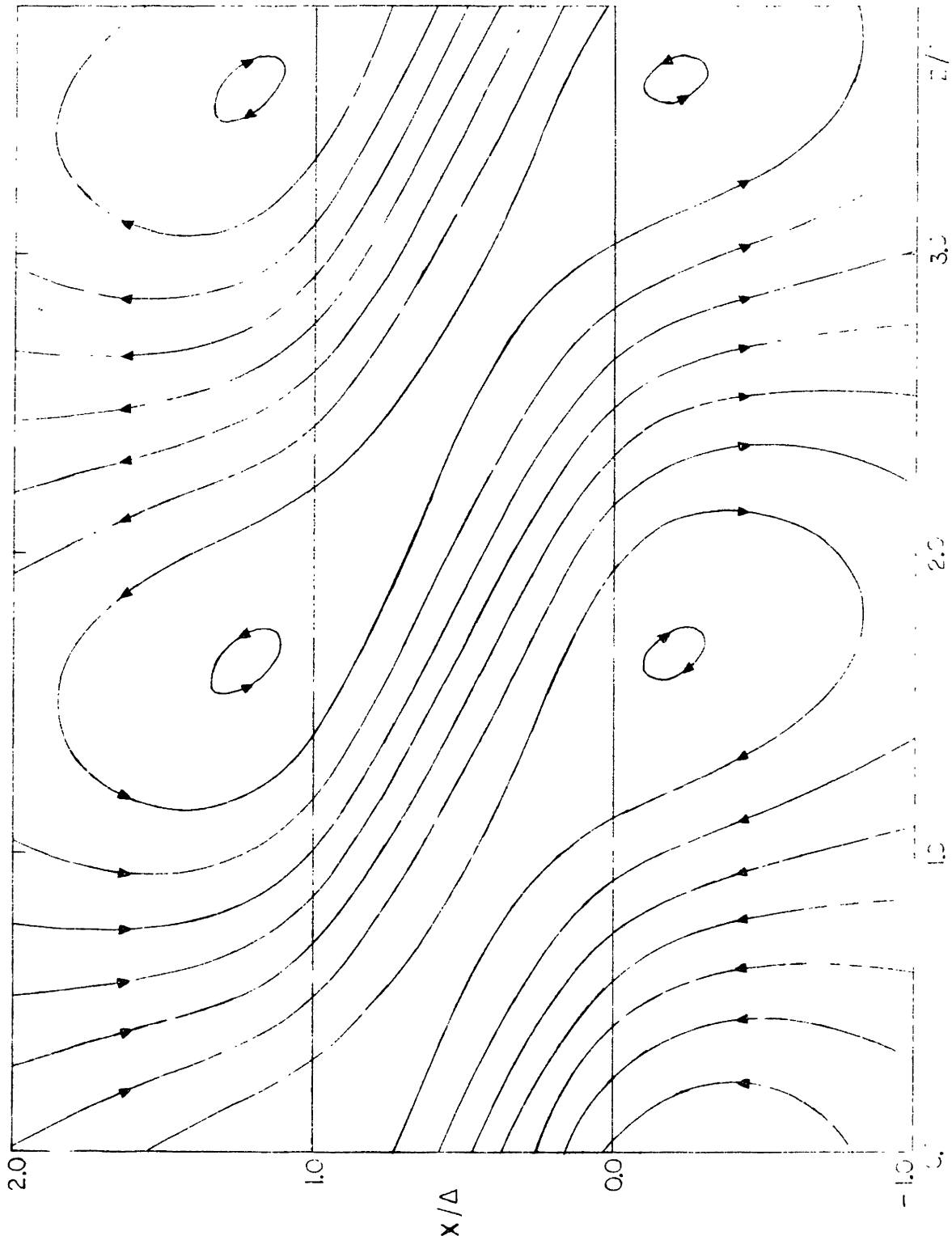


Figure 29. Velocity streamlines, $\underline{k} = \underline{k}^* = 1.6412$, $T/\tau = 10^{-4}$,

$R = 25.9$

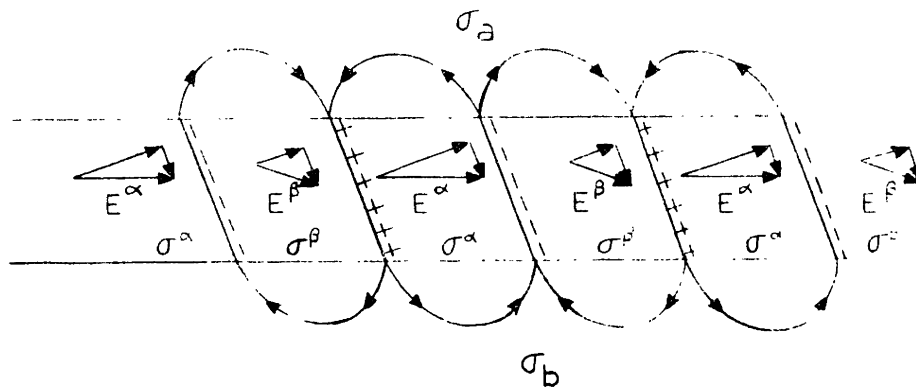


Figure 30. Physical Mechanism

space and more conducting fluid from the lower half-space. This effectively propagates the slanted layer structure to the left. This corresponds to eigenvalue solutions with $s_i < 0$.

If rightward-slanted layers are postulated at the outset, the resulting surface charge accumulations, fluid motions, and conductivity alterations lead to a rightward-propagating structure, corresponding to the mirror-image eigenvalue solutions with $s_i > 0$.

Reversal of the equilibrium electric field direction does not alter the physical mechanism as described here. The propagation direction depends only upon the assumed direction of slant and orientation of high and low conductivity regions. Maximum growth rate as a function of wavenumber is attained by optimizing cell size (and resulting slant angle) with respect to the competition between electrically driven shearing forces and retarding viscous drag and inertia.

The direction of propagation for a given slant direction is, in general, defined as follows: If $\nabla\sigma_0$ is a vector normal to the interface and pointing toward the region of higher conductivity, and $\bar{\kappa}$ is a vector obtained by crossing the direction of slant through an acute angle into the horizontal direction, then the layers propagate in the direction of the vector $\nabla\sigma_0 \times \bar{\kappa}$.

It is important to realize that we have characterized mathematically, in Section, IV.B, and physically in this section, an instability associated with the region of conductivity variation between two regions of constant conductivity. An abrupt discontinuity model, as presented in Section III.C, can never account for this sort of internal instability. In the language

of that section, the coupling mechanism is "within the interface itself". Nevertheless, the constant conductivity regions bounding the layer are disturbed by the instability. That is, the eigenfunctions -- potential, current, velocity, and stress distributions -- extend into the bounding regions. Thus, the instability provides an electrohydrodynamic mechanism for conductivity, mass, and momentum transport across the layer. Our analysis provides a clear indication that, in situations involving conductivity gradients normal to an applied electric field, internal electrohydrodynamic coupling can result in an instability tending to augment the conductivity diffusion process.

D. Rigid, Equipotential Boundaries

To further distinguish the instability modeled in Sections IV.B and IV.C from a surface-coupled instability, we remove the fluid half-spaces and bound the varying conductivity layer in equilibrium tangential electric field with rigid, equipotential (in the perturbation sense) boundaries. In this way, we isolate the "interface" region, identifying mechanisms to be identified solely with the internal dynamics of the layer.

The boundary conditions become, simply:

$$\hat{\phi}_{\alpha} = \hat{\phi}_{\beta} = 0 \quad (4.109)$$

$$\hat{\frac{v}{x}}_{\alpha} = \hat{\frac{v}{x}}_{\beta} = 0 \quad (4.110)$$

$$\hat{\frac{v}{z}}_{\alpha} = \hat{\frac{v}{z}}_{\beta} = 0 \quad (4.111)$$

or, in terms of the matrix notation of Eq. (44):

$$[V] = [0] \quad (4.112)$$

where $[0]$ is a column matrix of six zeroes. Rewriting the transfer relations which describe the layer, Eq. (70), we have:

$$[V] = [Q]^{-1}[S] \quad . \quad (4.113)$$

Thus, combining Eqs. (112) and (113), we have, for non-trivial $[S]$:

$$D' \equiv \text{Det } [Q]^{-1} = 0 \quad . \quad (4.114)$$

Equation (114) is the dispersion relation for the layer bounded by rigid, perfectly conducting walls. From Eq. (70):

$$[Q]^{-1} = [H][G]^{-1} \quad . \quad (4.115)$$

In order for (114) to be satisfied, then, either

$$D'' \equiv \text{Det } [H] = 0 \quad (4.116)$$

or
$$\text{Det } [G]^{-1} = 0 \quad . \quad (4.117)$$

The search for zeroes in D' , then, may be carried out without doing a matrix multiplication by searching for solutions to Eqs. (116) and (117). No solutions to Eq. (117) are found in the finite \underline{s} plane, and thus (116) determines all the solutions to (114).

The procedure used to search for solutions to Eq. (116) is identical to that used in Section IV.B. to search for solutions to Eq. (86). In characterizing the functions $D'(\underline{s})$ and $D''(\underline{s})$ empirically by computing their values at grid points in the \underline{s} plane, we find the following:

D' is analytic throughout. However, D'' has a branch cut extending from a branch point on the negative real axis, leftward to infinity. The branch point corresponds to an occurrence of double roots in the solution of Eq. (26). For example, for the choice of parameters $T/\tau = 1$, $R = e$, we can determine directly that, at $\underline{s} = -\underline{k} + j0$, the roots of Eq. (26) are:

$$\underline{\gamma} = \underline{k}, \underline{k}, -\underline{k}, 1-\underline{k} \quad . \quad (4.118)$$

The branch cut in the four roots to Eq. (26), $\underline{\gamma}_n$, due to a reordering of the names $\underline{\gamma}_1, \underline{\gamma}_2, \underline{\gamma}_3, \underline{\gamma}_4$, leads directly to a branch cut in $D''(\underline{s})$. As described in Section IV.B, D'' is pure imaginary and reverses sign along the branch cut.

Computation of D'' at grid points in the \underline{s} plane leads to the discovery of a set of eigenfrequency solutions to Eq. (116) -- and, hence, to Eq. (114) -- in the right half-plane similar to the set found in the half-space bounded model of Section IV.B. As was the case for that model, there is an infinite set of eigenfrequencies in the right upper half-plane (with mirror images in the lower half plane), and any one eigenfrequency has an infinite set of eigenfrequencies between itself and the origin.

In addition, for the present problem, a set of zeroes lying directly on the negative real \underline{s} axis (superimposed on the branch cut) is found. These eigenfrequencies correspond to pure decay (no oscillation) in time. One such zero has the least negative $\text{Re } \underline{s}$ (slowest decay), and the set extends leftward along the real \underline{s} axis without bound. That is, there is no most rapidly decaying eigenfrequency. Note that, because D'' is not analytic across the branch cut, the search routine described in IV.B need not necessarily converge on zeroes lying on the branch cut. Nonetheless,

as it happens, it does. Whenever there is doubt as to the validity of a search for a particular zero, or as to whether all valid zeroes have been found due to the existence of the branch cut, we simply resort to dealing with $D'(\underline{s})$, a function involving no branch cut. We find, however, that D' and D'' have the same set of zeroes, with one exception. This occurs at the branch point where D'' has a zero, but D' does not. We might jump to the conclusion that this zero in D'' represents an unobservable mode, i.e., one which involves internal motions of the layer, but for which the surface stresses and normal current densities are zero. This, however, is not the case. To understand this situation, we must, as in Section IV.B., determine the distributions of perturbation complex amplitudes of physical quantities as functions of the x-coordinate (the eigenfunctions). For the present problem, this is accomplished as follows:

Having found a value of \underline{s} where Eq. (116) is satisfied, we desire a non-trivial column matrix $[A]$ satisfying Eq. (43). Analogous to the manipulations performed on $[F]$ in Section IV.B, we take linear combinations of rows in $[H]$ so as to produce zero entries everywhere below the main diagonal. Having performed such manipulations, because $D'' = 0$, the 6,6 element will be zero. The last equation represented by Eq. (43) is satisfied by an arbitrary entry for the bottom element of $[A]$. We arbitrarily give this element the value $1 + j0$, i.e.,

$$\hat{\phi}_6 = 1 + j0 \quad . \quad (4.119)$$

Then, the manipulated set of equations derived from Eq. (43) may be used to determine the values of all the other variables in $[A]$, consistent with Eq. (119). We are herein setting directly one of the coefficients of the

$e^{\underline{\gamma}_n x/\Delta}$ components of $\hat{\phi}$, i.e., $\hat{\phi}_6$. By contrast, in Section IV.B., we set the entire function, evaluated at one surface, i.e., $\hat{\phi}^\beta$. This distinction is immaterial to the characterization of eigenfunctions. We desire only, in one way or another, to excite the eigenfunctions and observe the spatial distributions they imply.

We return now to the branch point, where D'' has a zero but D' does not, and consider the eigenfunctions corresponding to this apparent eigenfrequency in $D''(\underline{s})$. We recognize, first, that this zero in D'' has occurred as a result of a double root in the solutions, $\underline{\gamma}_n$, to Eq. (26). The double root and the dependence of the i^{th} column of $[H]$ on only γ_i (see Eqs. (46)-(51), defining the elements of $[H]$) immediately imply two identical columns in $[H]$, and hence $D'' = 0$. Similarly, the double root implies $\text{Det } [G] = 0$, and thus, a singularity in $\text{Det } [G]^{-1}$. For this reason, we may have $D'' = 0$ with $D' \neq 0$.

Now, consider the matrix manipulations involved in determining the eigenfunctions. To be specific, call the double root $\underline{\gamma}_5 = \underline{\gamma}_6$. Then, the fifth and sixth columns of $[H]$ are identical. Manipulations on Eq. (43) then will yield the form:

$$\begin{bmatrix} 1 & H'_{12} & H'_{13} & H'_{14} & H'_{15} & H'_{15} \\ 0 & 1 & H'_{23} & H'_{24} & H'_{25} & H'_{25} \\ 0 & 0 & 1 & H'_{34} & H'_{35} & H'_{35} \\ 0 & 0 & 0 & 1 & H'_{45} & H'_{45} \\ 0 & 0 & 0 & 0 & 1 & 1 \\ 0 & 0 & 0 & 0 & 0 & 0 \end{bmatrix} \begin{bmatrix} \hat{\phi}_1 \\ \hat{\phi}_2 \\ \hat{\phi}_3 \\ \hat{\phi}_4 \\ \hat{\phi}_5 \\ \hat{\phi}_6 \end{bmatrix} = \begin{bmatrix} 0 \\ 0 \\ 0 \\ 0 \\ 0 \\ 0 \end{bmatrix} \quad (4.120)$$

Thus, $\hat{\phi}_6$ is arbitrary. Now, constructing the other elements of $\{A\}$, using Eq. (120):

$$\hat{\phi}_5 = -\hat{\phi}_6 \quad (4.121)$$

$$\hat{\phi}_4 = \hat{\phi}_3 = \hat{\phi}_2 = \hat{\phi}_1 = 0 \quad (4.122)$$

Also, from Eqs. (40), (121) and (122):

$$\hat{\psi}_5 = -\hat{\psi}_6 \quad (4.123)$$

$$\hat{\psi}_4 = \hat{\psi}_3 = \hat{\psi}_2 = \hat{\psi}_1 = 0 \quad (4.124)$$

Thus, from Eqs. (27) and (28):

$$\hat{\phi} = \hat{\phi}_5 e^{\gamma_5 x/\Delta} + \hat{\phi}_6 e^{\gamma_6 x/\Delta} = 0 \quad (4.125)$$

$$\hat{\psi} = \hat{\psi}_5 e^{\gamma_5 x/\Delta} + \hat{\psi}_6 e^{\gamma_6 x/\Delta} = 0 \quad (4.126)$$

The eigenfunctions, then, are trivial-- i.e., identically zero across the layer. The situation may be further complicated by other double roots, or even triple roots, but the same manipulations will always lead to trivial solutions. Thus, having discounted the zero in D'' at the branch point, we find that D' and D'' have the same set of non-trivial eigenfrequencies.

Figures 31 and 32 describe the functions D' and D'' in the complex \underline{s} plane. Figures 33, 34, and 35 display the first eigenfunction $\hat{\underline{v}}_x$ at $T/\tau = 1$, $R = e$ and $\underline{k} = 10^{-3}$, 1, and 10, respectively. As in Section IV.B., Fig. 35 shows more variation across the layer of the first eigenfunction, due to a large value of \underline{k} . The second function, at the same value of \underline{k} ,

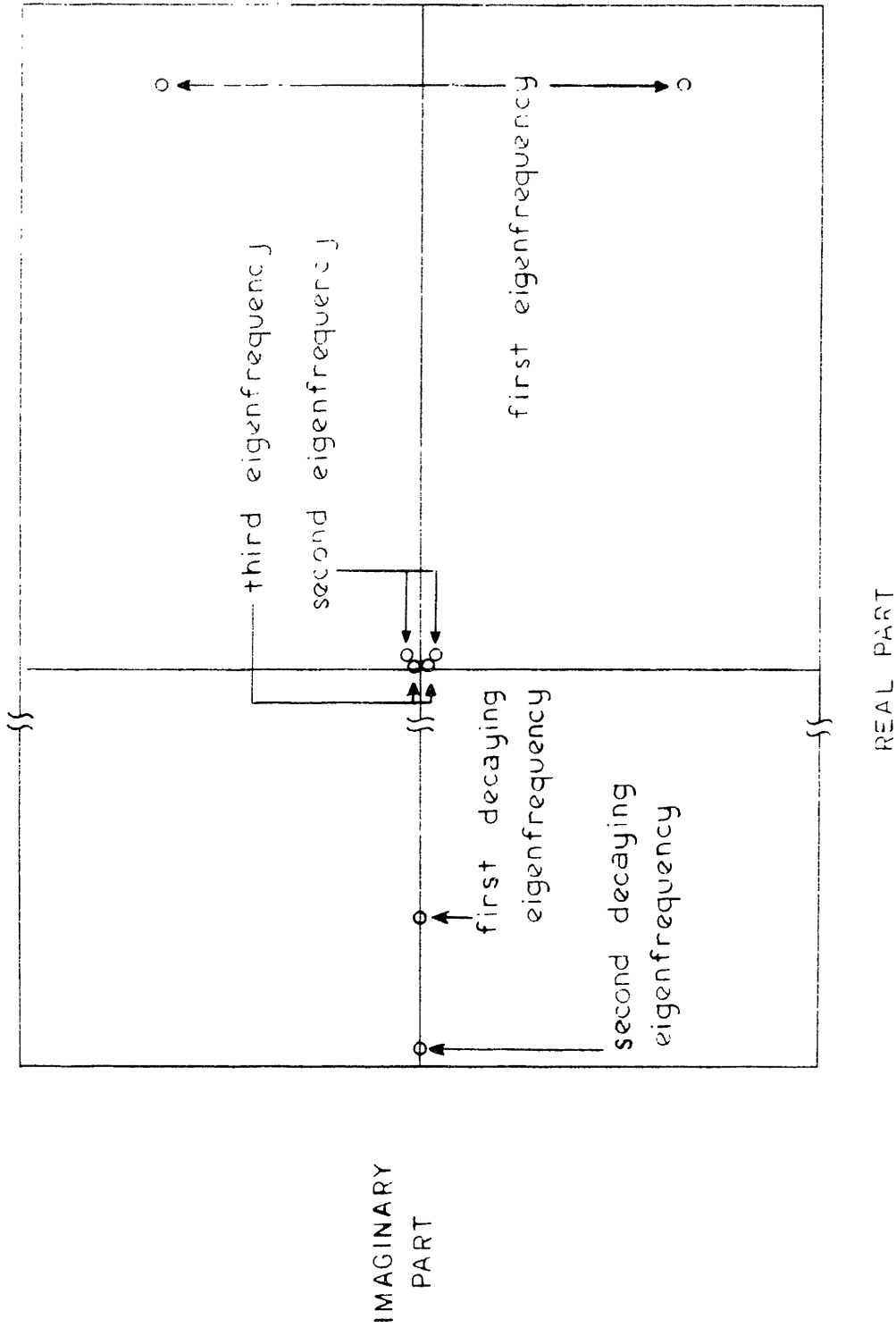


Figure 31. The function D' in the complex s -plane

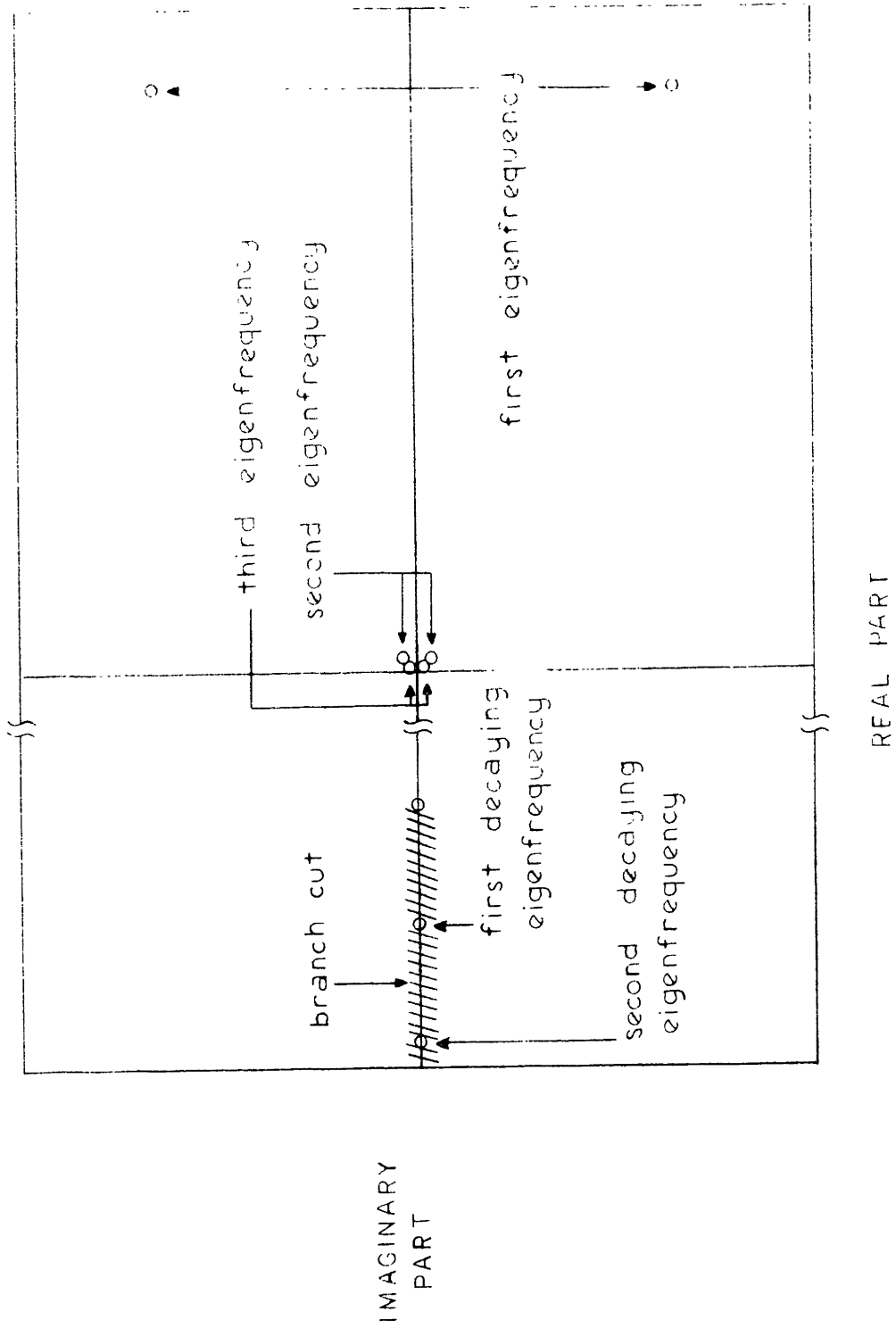


Figure 32. The function D'' in the complex s -plane

displays even more variation, as shown in Fig. 36, where we plot the second eigenfunction \hat{v}_x at $T/\tau = 1$, $R = e$, $\underline{k} = 10$.

The first two eigenfunctions (real and imaginary parts in separate figures) are shown at $T/\tau = 1$, $R = e$, $\underline{k} = 1$, for \hat{v}_x in Figs. 37 and 38 and for $\hat{\phi}$ in Figs. 39 and 40. Note, in Figs. 39 and 40, that the potential distribution provides no obvious indication as to which eigenfunction corresponds to the first and which to the second eigenfrequency. On the other hand, the velocity distributions in Figs. 37 and 38 characteristically involve more variation for the second eigenfrequency. As in Section IV.B., we emphasize that the ordinate scales in these eigenfrequency plots are without meaning. Even the relative magnitudes of two modes, shown on the same figure, must not be compared, since they provide only an indication of the importance of the $e^{\frac{\gamma_6}{\Delta} x}$ component of the function (the one excited to amplitude $1 + j0$) in each case. Only the shapes of the functions of x are of importance.

Finally, we describe the decaying eigenfrequencies by plotting the two slowest decaying eigenfunctions at $T/\tau = 1$, $R = e$, $\underline{k} = 1$, for $|\hat{v}_x|$ and $|\hat{\phi}|$ in Figs. 41 and 42, respectively. Note in Fig. 41 that $|\hat{v}_x|$ is, as far as we can see, symmetric about the center of the layer. The fluid mechanics for this mode apparently is essentially uncoupled from the asymmetric electrical subsystem. The coupling from the electrical to the mechanical subsystem, as manifested in the electrical force contribution to the Navier-Stokes equation, is negligible. This is due to the fact that, even for the slowest decaying mode, the eigenfrequency is relatively large in magnitude. Because the coupling term enters with a $1/\underline{g}$ dependence, it

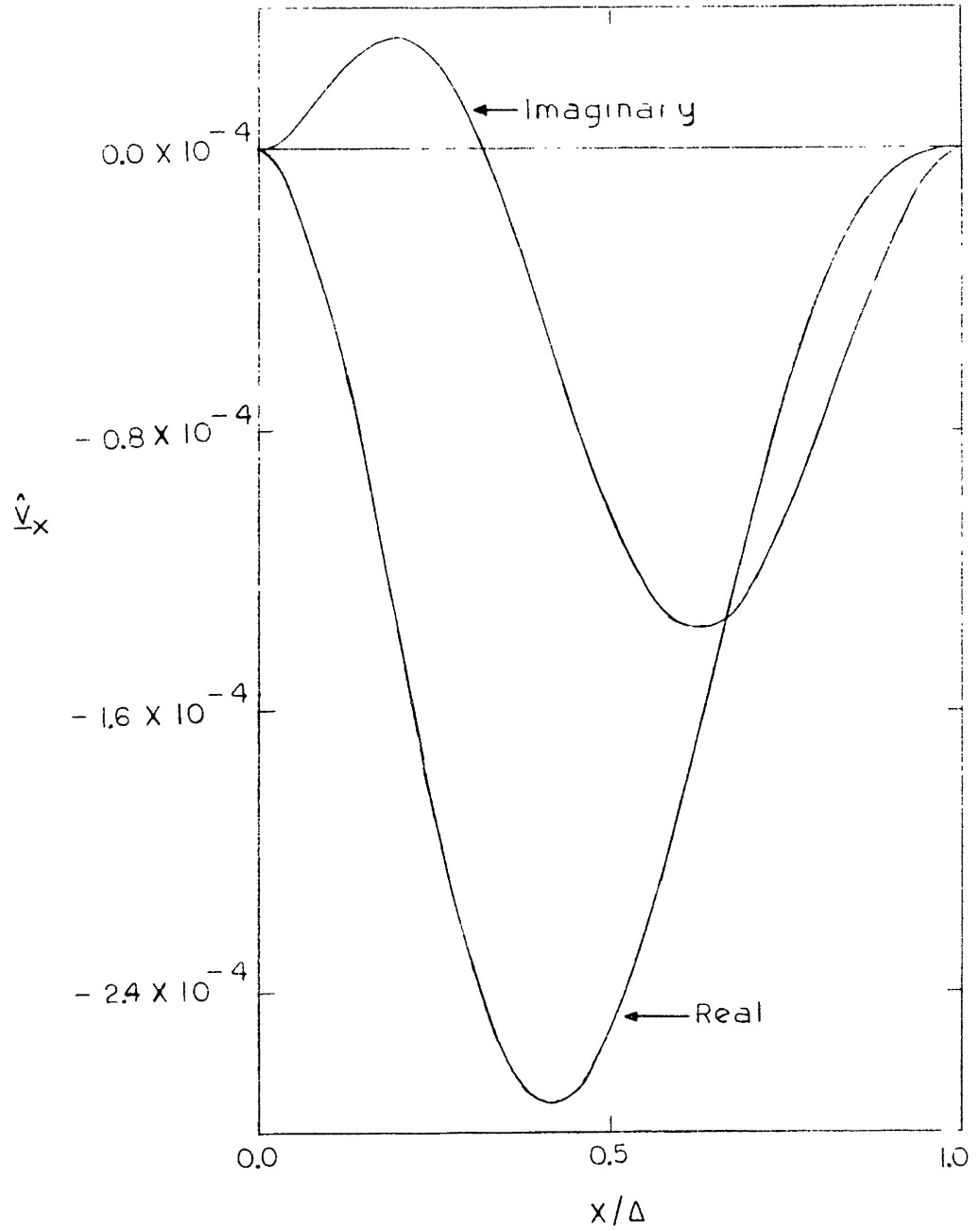


Figure 33. \hat{v}_x versus x/Δ , first eigenfunction, $\underline{k}=10^{-3}$, $T/\tau=1$, $R=e$

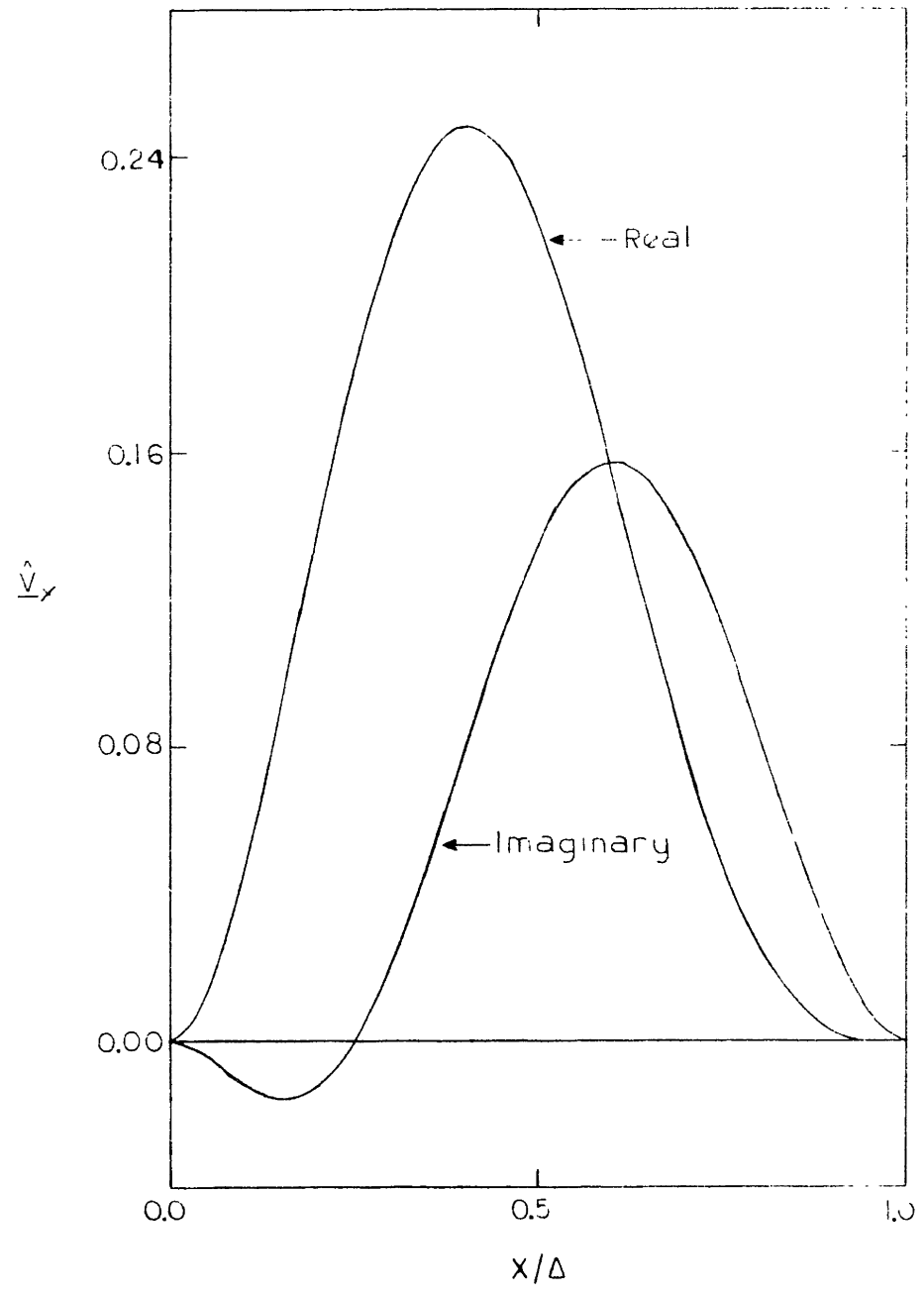


Figure 34. \hat{v}_x versus x/Δ , first eigenfunction, $\underline{k}=1$, $T/\tau=1$, $R=e$

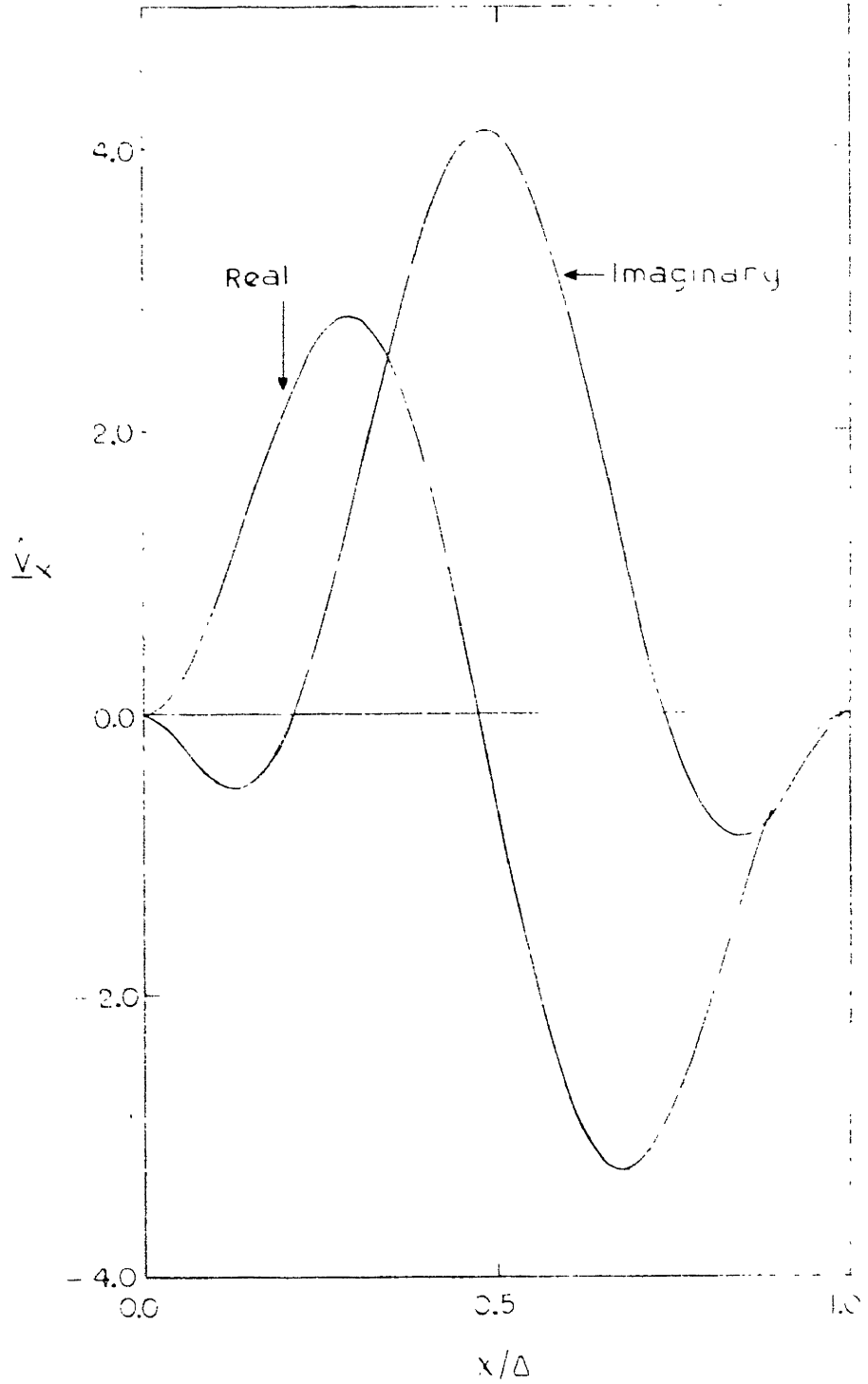


Figure 35. \hat{v}_x versus x/Δ , first eigenfunction, $k = 10$, $T/\tau=1$, $R=e$

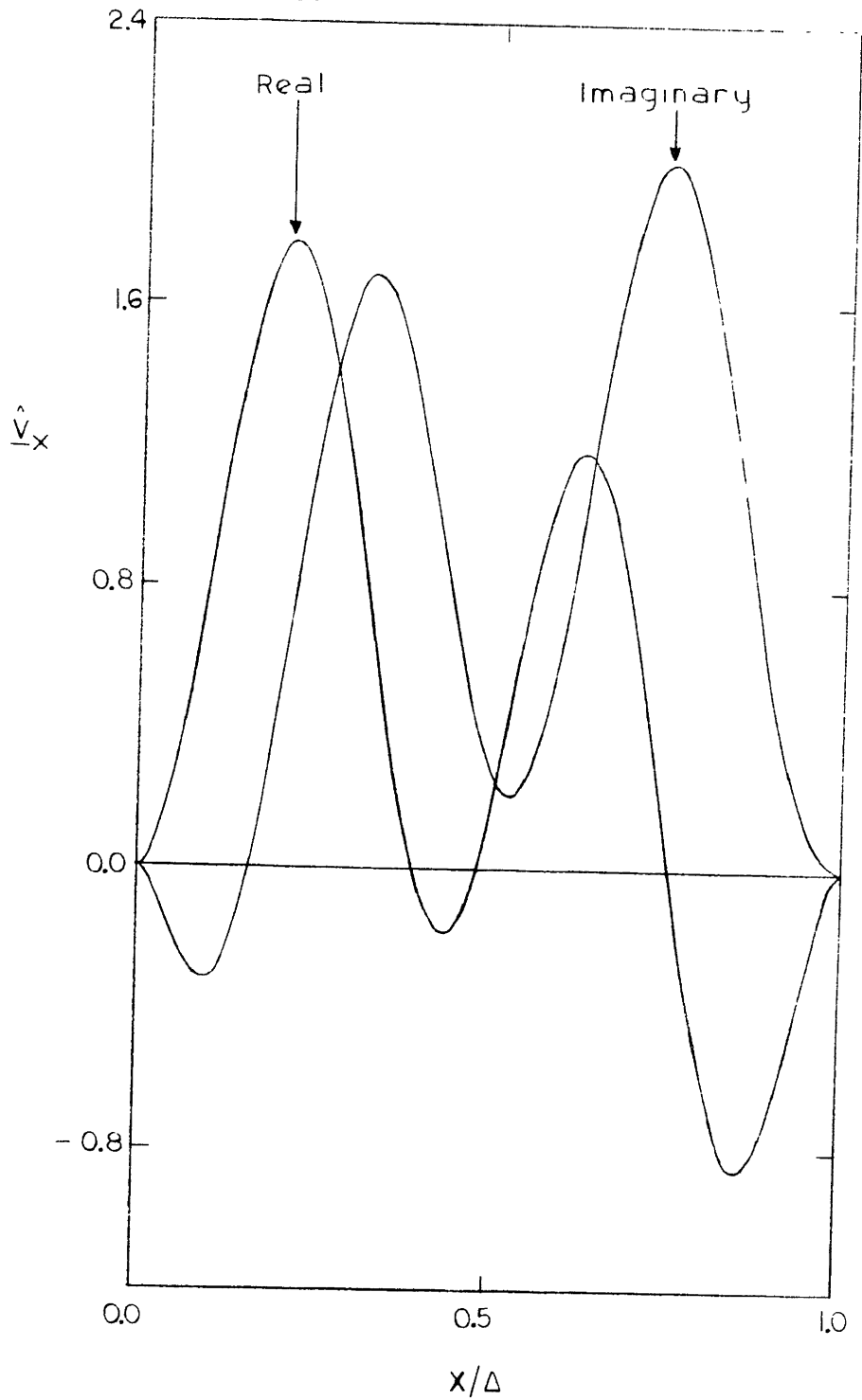


Figure 36. \hat{v}_x versus x/Δ , second eigenfunction, $k=10$, $T/\tau=1$, $R=e$

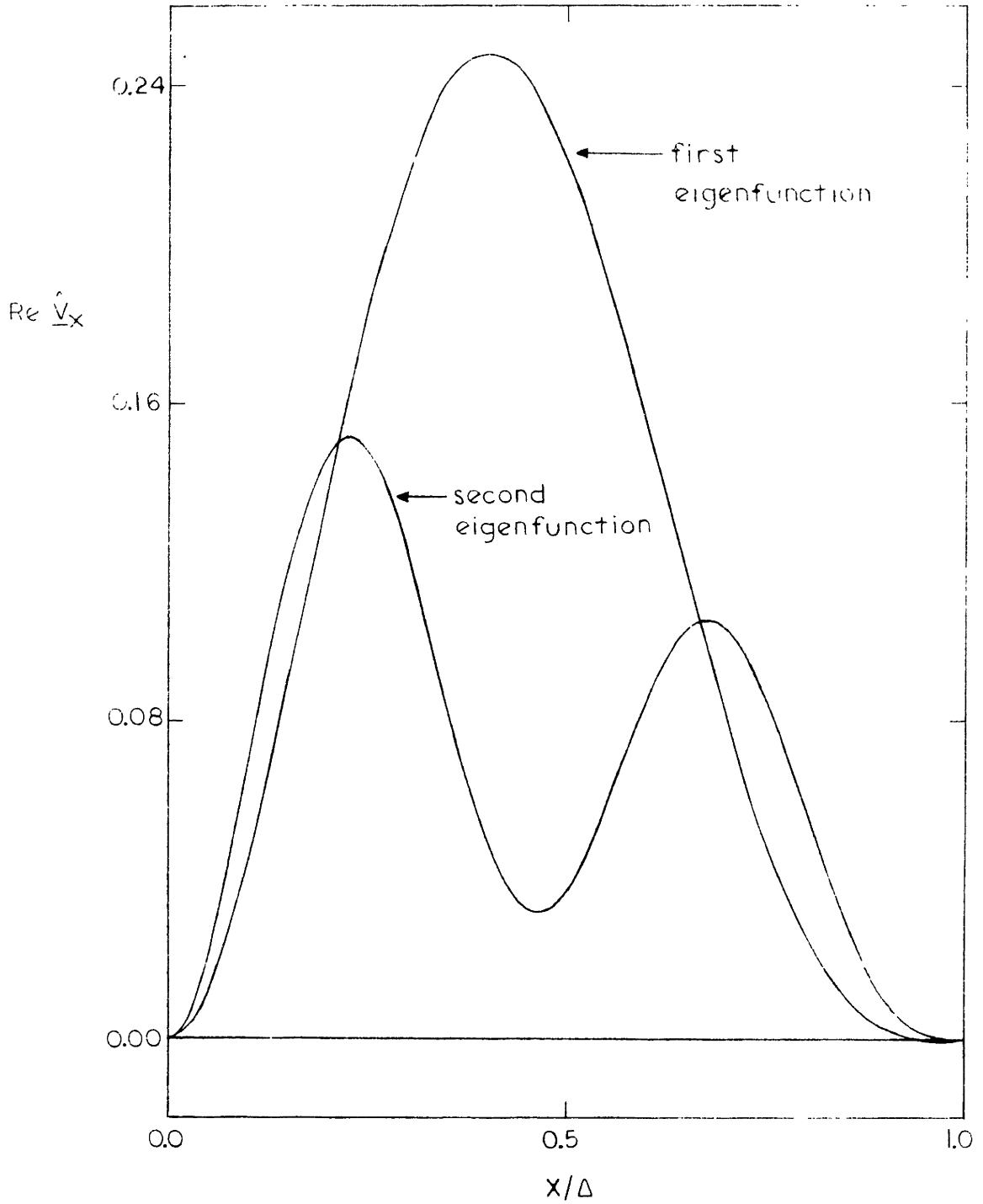


Figure 37. $Re \hat{v}_x$ vs. x/Δ , first & second eigenfunctions, $k=1$,

$$T/\tau = 1, R = e$$

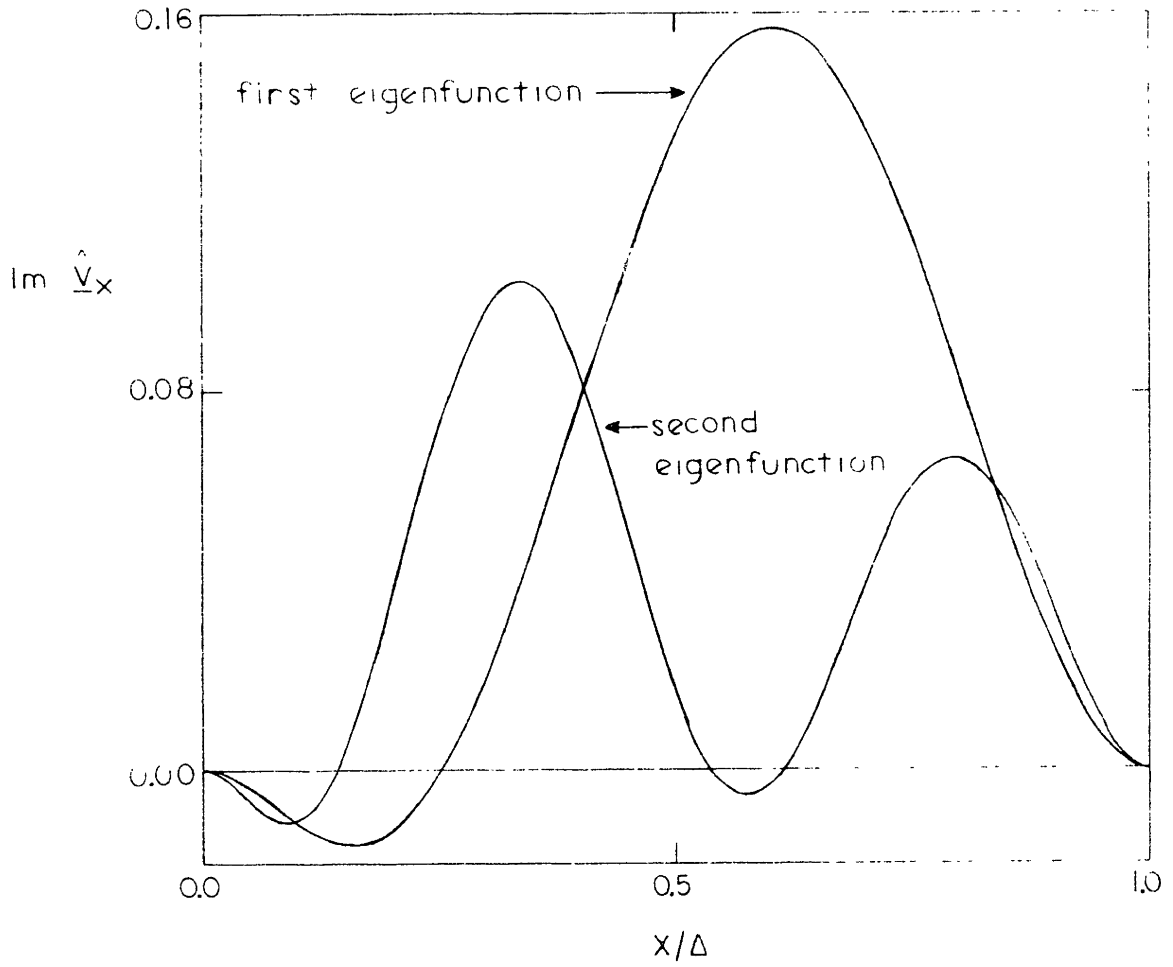


Figure 38. $\text{Im } \hat{v}_x$ versus x/Δ , first and second eigenfunctions,
 $\underline{k} = 1, T/\tau = 1, R = e$

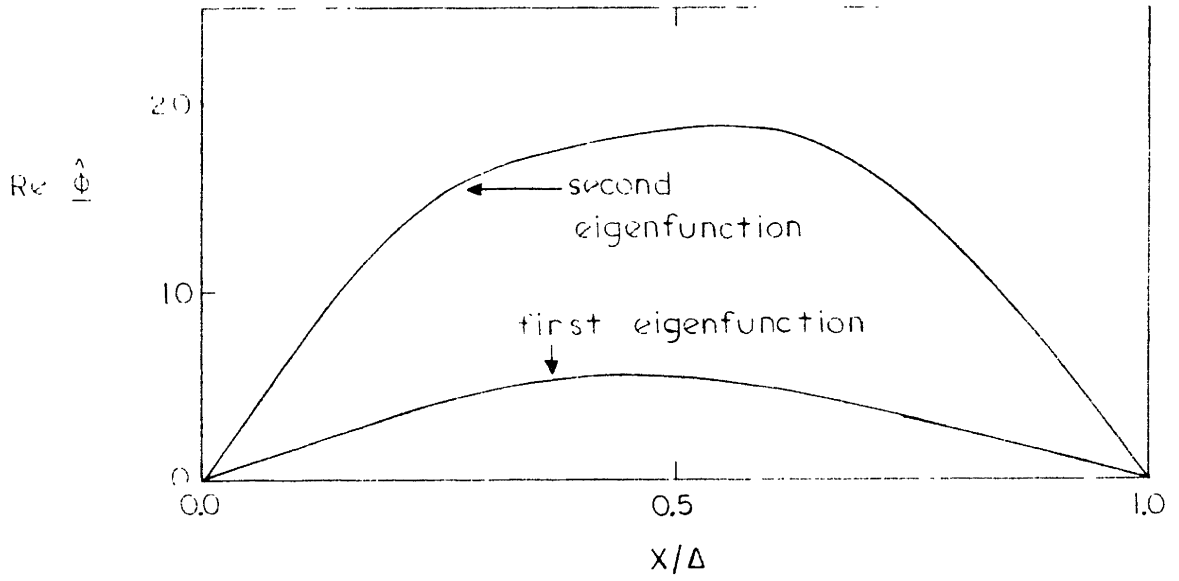


Figure 39. $\text{Re } \hat{\phi}$ versus x/Δ , first and second eigenfunctions,
 $\underline{k} = 1, T/\tau = 1, R = e$

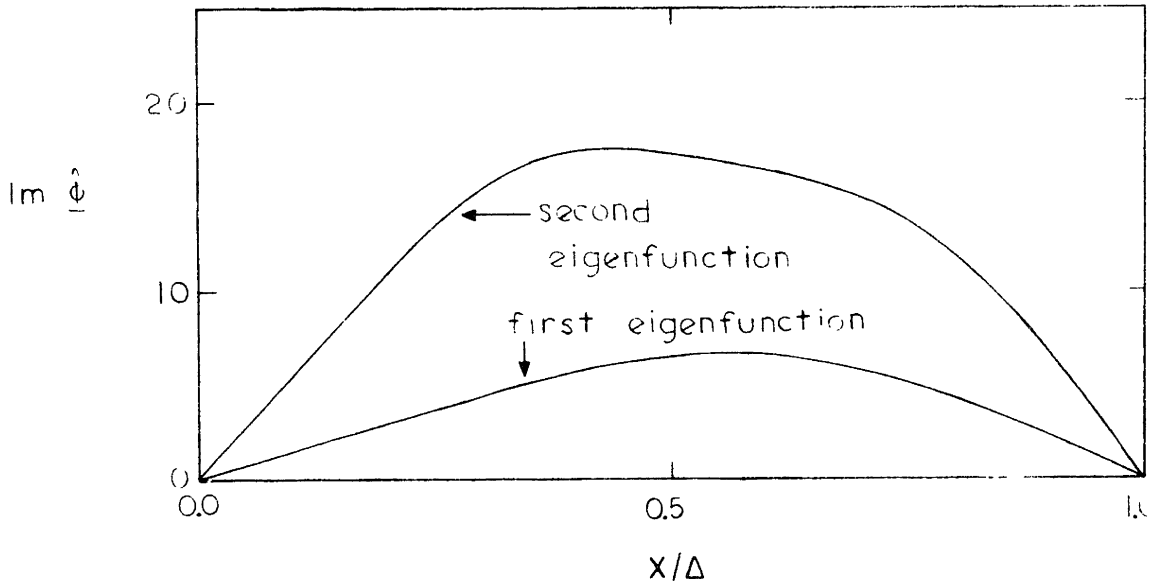


Figure 40. $\text{Im } \hat{\phi}$ versus x/Δ , first and second eigenfunctions,
 $\underline{k} = 1, T/\tau = 1, R = e$

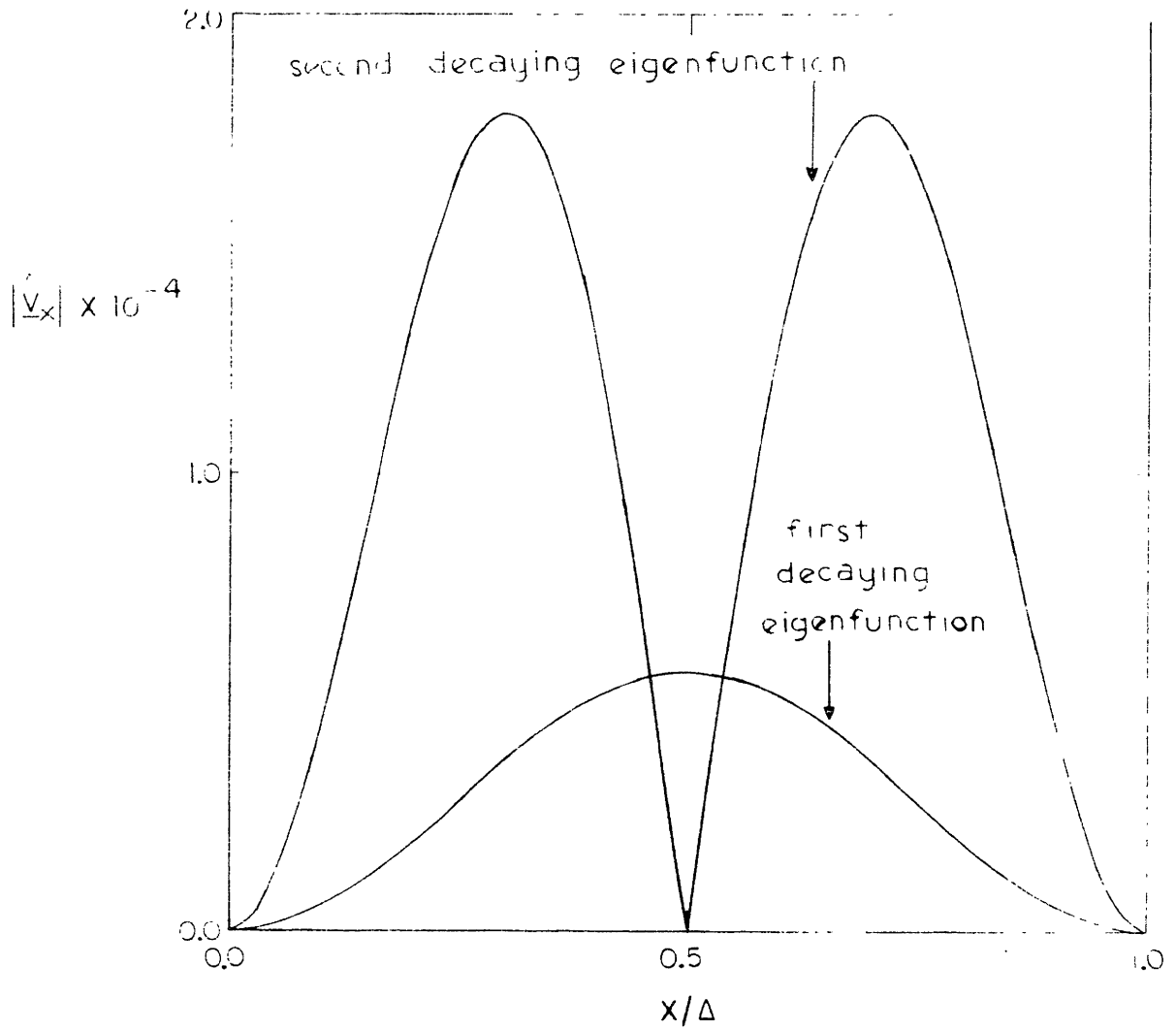


Figure 41. $|\hat{v}_x|$ versus x/Δ , first and second decaying eigenfunctions,
 $\underline{k} = 1, T/\tau = 1, R = e$

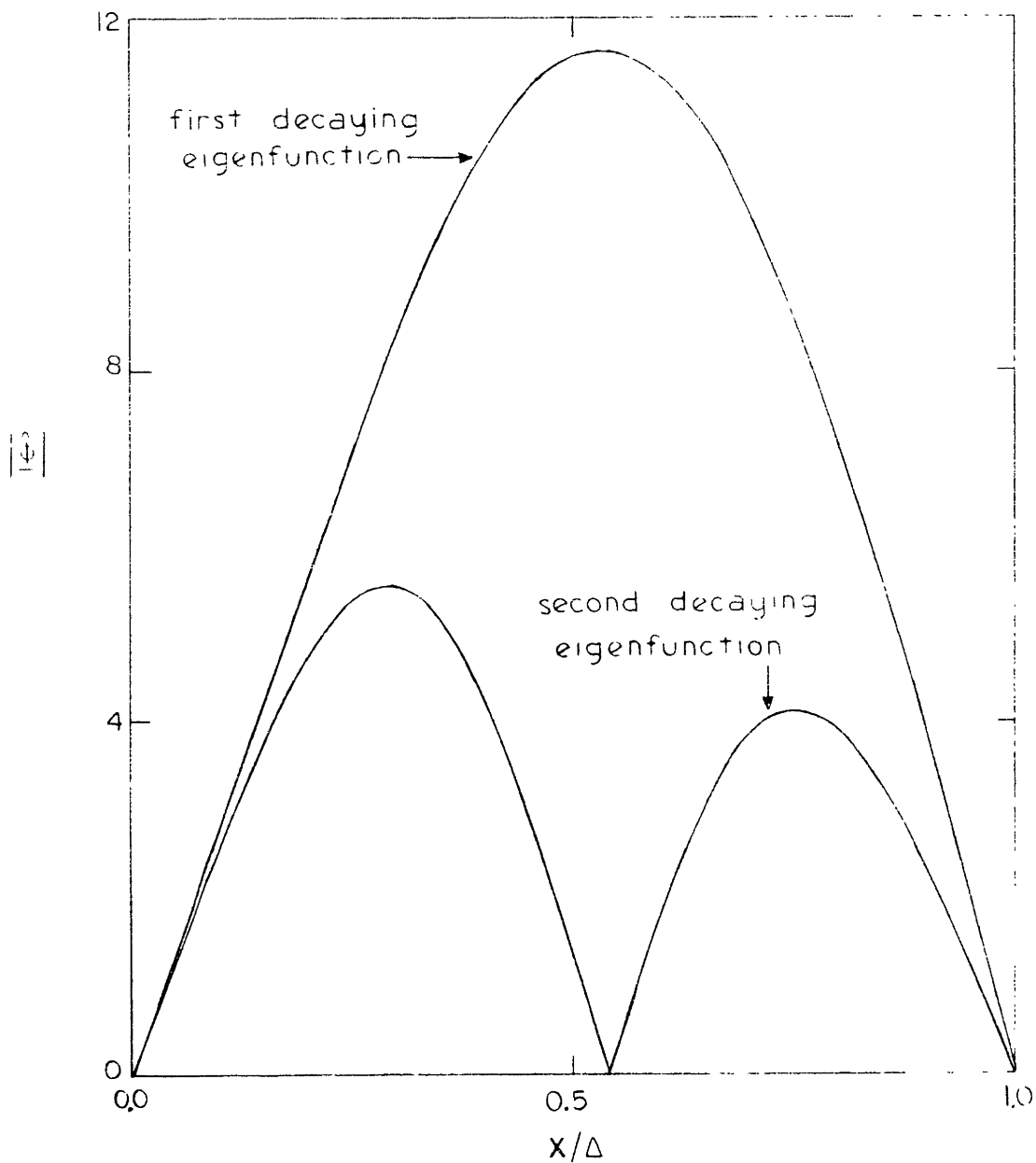


Figure 42. $|\hat{\phi}|$ versus x/Δ , first and second decaying eigenfunctions,
 $\underline{k} = 1, T/\tau = 1, R = e$

is small compared to the other terms in Eq. (18). Thus, the velocity eigenfunctions are the same as would be found with no electrical force in the model.

The return coupling, i.e., the effect of the fluid mechanics on the electrical subsystem through convection of the conductivity gradient, is still present. The potential distribution in Fig. 42 is, of course, sensitive to the equilibrium conductivity gradient; hence, it is not symmetric about the center of the layer. If we were to solve the purely fluid mechanical problem of a viscous layer bounded by rigid walls, we would find a set of purely decaying eigenfrequencies, essentially coincident with those found here. Only to the extent that the electrical-to-mechanical coupling link remains finite is there a shift in position of the eigenfrequencies.

The behavior of $\text{Re } \underline{s}$, for the first two growing eigenfrequencies, as a function of \underline{k} , is displayed in Fig. 43 for $T/\tau = 1$, $R = e$. The curves have forms much like those obtained in the half-space-bounded problem of Section IV.B., going to zero at small \underline{k} and at large \underline{k} , and peaking at an intermediate \underline{k}^* . It would be straightforward to proceed with an analysis like that of Section IV.B., determining \underline{k}^* and \underline{s}^* as functions of the parameters T/τ and R . However, our intention here is not to solve the rigid, equipotential boundary problem in detail; we have demonstrated that the region of conductivity variation, even when isolated and rigidly bounded, displays growing (unstable) modes.

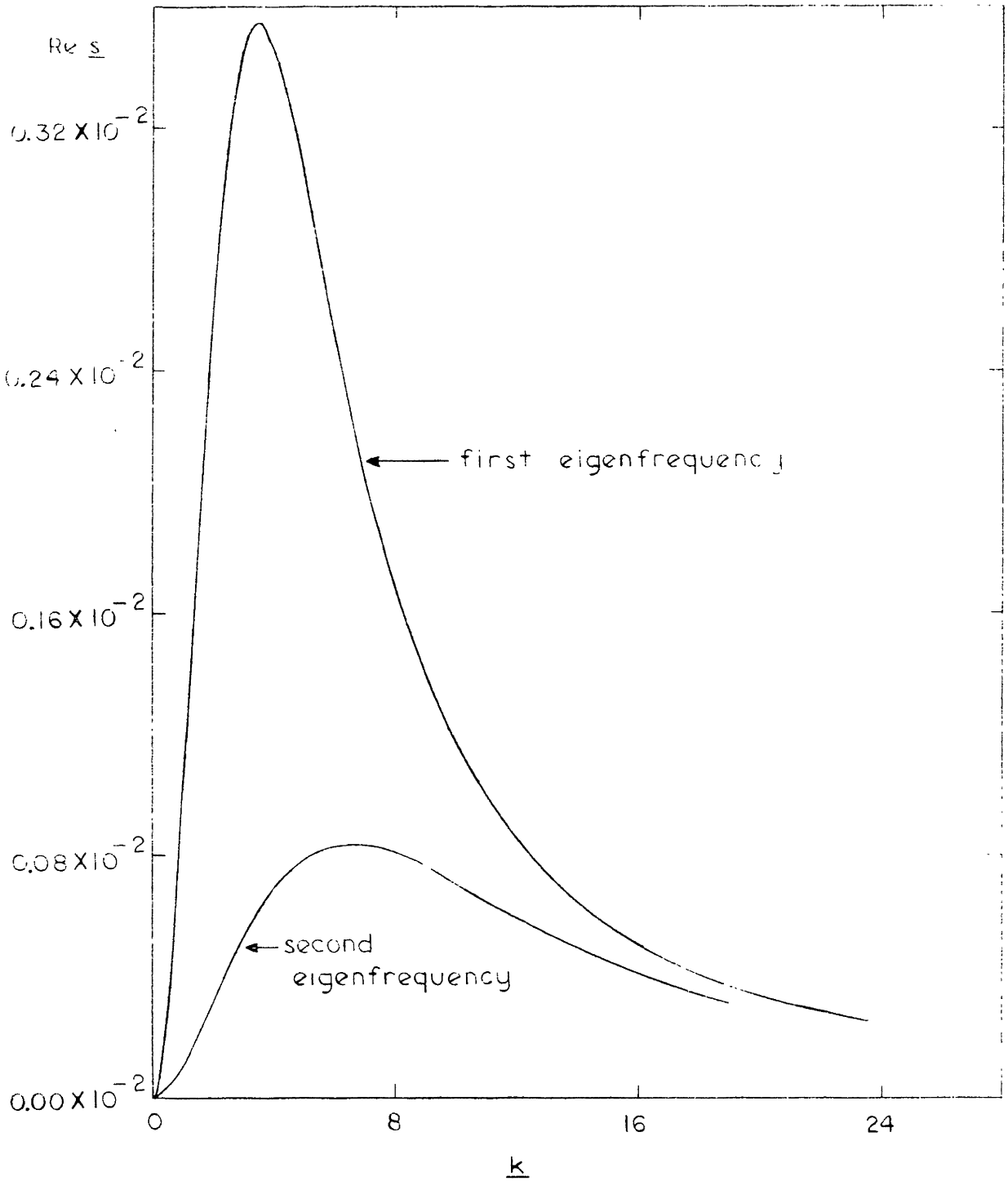


Figure 43. $\text{Re } s$ versus k , $T/\tau = 1$, $R = e$

CHAPTER IV BIBLIOGRAPHY

1. Betchov, Robert, and Criminale, William O., Jr., Stability of Parallel Flows, New York: Academic Press, 1967, p. 78.

CHAPTER V. NUMERICAL INTEGRATION TECHNIQUE FOR SMOOTHLY INHOMOGENEOUS LAYERS

A. Varying Permittivity Layer

An electromechanical problem involving coupling throughout the bulk between electric or magnetic fields and a continuous medium, in which the equilibrium material properties are smoothly varying functions of position, generally results in differential equations with non-constant coefficients. Thus, although such a problem may be well specified, a straightforward analytic solution of the governing equations is not, in general, possible. Consider, as an example involving no mechanics, a planar region with permittivity a function of the x-coordinate, as shown in Fig. 1:

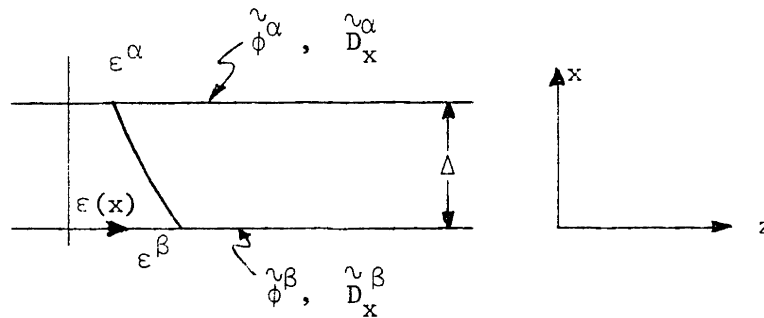


Figure 1. Planar region with permittivity a function of transverse coordinate

Spatially periodic potentials have complex amplitudes $\tilde{\phi}^\alpha$ and $\tilde{\phi}^\beta$ in the planes $x = \Delta$ and $x = 0$, respectively (both arbitrary functions of time since the governing equations will involve no dynamics).

$$\phi(x = \Delta) = \text{Re } \tilde{\phi}^\alpha e^{-jkz} \tag{5.1}$$

$$\phi(x = 0) = \text{Re } \tilde{\phi}^\beta e^{-jkz} \tag{5.2}$$

Our object is to determine transfer relations, specifying the normal electric displacement amplitudes, $\tilde{D}_x^\alpha = \epsilon^\alpha \tilde{E}_x^\alpha$ and $\tilde{D}_x^\beta = \epsilon^\beta \tilde{E}_x^\beta$ in terms of $\tilde{\phi}^\alpha$ and $\tilde{\phi}^\beta$. Due to the presence of a polarization charge density, the potential variation across the layer will be other than Laplacian.

The governing differential equations for the layer are Eqs. (2.2), with no free charge, ρ_f , and (2.4):

$$\nabla \cdot \epsilon \bar{E} = 0 \quad (5.3)$$

$$\bar{E} = -\nabla \phi \quad . \quad (5.4)$$

In terms of complex amplitudes, Eq. (4) becomes

$$\tilde{E}_x = -D\tilde{\phi} \quad (5.5)$$

and

$$\tilde{E}_z = jk\tilde{\phi} \quad (5.6)$$

(where $D \equiv d/dx$).

Expanding Eq. (3):

$$\epsilon \nabla \cdot \bar{E} + \bar{E} \cdot \nabla \epsilon = 0 \quad (5.7)$$

or, because $\nabla \epsilon = \bar{i}_x D\epsilon$:

$$\epsilon [D\tilde{E}_x - jk\tilde{E}_z] + \tilde{E}_x D\epsilon = 0 \quad . \quad (5.8)$$

Combining Eqs. (5), (6) and (8):

$$[D^2 + \frac{D\epsilon}{\epsilon} D - k^2] \tilde{\phi} = 0 \quad . \quad (5.9)$$

Equation (9) is a linear differential equation with non-constant coefficients. In the special case $\epsilon = \text{constant}$, $D\epsilon = 0$ and Eq. (9) reduces to Laplace's equation.

To gain some insight into the effect of a nonuniform permittivity, we recognize, before proceeding with a numerical technique for integrating Eq. (9), that one particular permittivity distribution does yield a constant coefficient $D\epsilon/\epsilon$, and hence permits straightforward analytic solution -- that is, exponentially varying. If we take

$$\epsilon(x) = \epsilon^\beta \left(\frac{\epsilon^\alpha}{\epsilon^\beta} \right)^{x/\Delta} \quad (5.10)$$

we have:

$$\frac{D\epsilon}{\epsilon} = - \frac{\ln R}{\Delta} \quad (5.11)$$

where $R \equiv \epsilon^\beta / \epsilon^\alpha$. (5.12)

Combining Eqs. (9) and (11):

$$[D^2 - \frac{\ln R}{\Delta} D - k^2] \overset{\sim}{\phi} = 0 \quad (5.13)$$

Equation (13) is linear with constant coefficients. Assuming solutions of the form

$$\overset{\sim}{\phi}(x) = e^{\gamma x} \quad (5.14)$$

we have

$$\gamma = \frac{1}{2} \left[-\frac{\ln R}{\Delta} \pm \frac{1}{\delta} \right] \equiv \gamma_{\pm} \quad (5.15)$$

where:

$$\frac{1}{\delta} \equiv \sqrt{\left(\frac{\ln R}{\Delta} \right)^2 + 4k^2} \quad (5.16)$$

Writing out $\overset{\sim}{\phi}(x) = \phi_1 e^{\gamma_+ x} + \phi_2 e^{\gamma_- x}$, (5.17)

solving for the coefficients ϕ_1 and ϕ_2 subject to the conditions

$$\overset{\sim}{\phi}(0) = \overset{\sim}{\phi}^\beta \quad \text{and} \quad \overset{\sim}{\phi}(\Delta) = \overset{\sim}{\phi}^\alpha, \quad \text{and computing } \tilde{D}_x^\alpha \quad \text{and} \quad \tilde{D}_x^\beta, \quad \text{we find:}$$

$$\begin{bmatrix} -\frac{\tilde{D}}{x} \alpha \\ \frac{\tilde{D}}{x} \beta \end{bmatrix} = \frac{1}{e^{\gamma_+ \Delta} - e^{\gamma_- \Delta}} \begin{bmatrix} \epsilon^\alpha (\gamma_+ e^{\gamma_+ \Delta} - \gamma_- e^{\gamma_- \Delta}) & -\epsilon^{\beta/\delta} \\ -\epsilon^{\beta/\delta} & -\epsilon^\beta (\gamma_- e^{\gamma_+ \Delta} - \gamma_+ e^{\gamma_- \Delta}) \end{bmatrix} \begin{bmatrix} \phi^\alpha \\ \phi^\beta \end{bmatrix} \quad (5.18)$$

It is convenient to normalize Eq. (18) as follows:

$$\left. \begin{aligned} \text{Define: } \underline{\tilde{\phi}} &\equiv \tilde{\phi} ; \quad \underline{k} \equiv k\Delta ; \quad \underline{\tilde{D}}_x \equiv \frac{\Delta}{\epsilon^\alpha} \tilde{D}_x ; \quad \underline{\frac{1}{\delta}} \equiv \frac{\Delta}{\delta} = \sqrt{(\ln R)^2 + 4k^2} \\ \underline{\gamma}_+ &\equiv \gamma_+ \Delta = \frac{1}{2} \left[\ln R + \frac{1}{\underline{\delta}} \right] ; \quad \underline{\gamma}_- \equiv \gamma_- \Delta = \frac{1}{2} \left[\ln R - \frac{1}{\underline{\delta}} \right] \end{aligned} \right\} (5.19)$$

Then:

$$\begin{bmatrix} -\frac{\underline{\tilde{D}}}{x} \alpha \\ \frac{\underline{\tilde{D}}}{x} \beta \end{bmatrix} = \begin{bmatrix} T_{11} & T_{12} \\ T_{21} & T_{22} \end{bmatrix} \begin{bmatrix} \underline{\tilde{\phi}}^\alpha \\ \underline{\tilde{\phi}}^\beta \end{bmatrix} \quad (5.20)$$

$$\text{where: } \left. \begin{aligned} T_{11} &= \frac{\underline{\gamma}_+ e^{\underline{\gamma}_+} - \underline{\gamma}_- e^{\underline{\gamma}_-}}{e^{\underline{\gamma}_+} - e^{\underline{\gamma}_-}} & T_{22} &= -R \frac{\underline{\gamma}_- e^{\underline{\gamma}_+} - \underline{\gamma}_+ e^{\underline{\gamma}_-}}{e^{\underline{\gamma}_+} - e^{\underline{\gamma}_-}} \\ T_{12} &= T_{21} = -\frac{R/\underline{\delta}}{e^{\underline{\gamma}_+} - e^{\underline{\gamma}_-}} \end{aligned} \right\} (5.21)$$

We now proceed with a technique for numerically integrating Equation (9), and hence for determining the transfer matrix in the case of an arbitrarily prescribed (smoothly varying) permittivity. We begin by writing finite difference equations for a thin layer, of thickness d , as shown in Fig. 2, with variables at the lower and upper boundaries of the incremental layer identified by subscripts i and $i+1$ respectively:

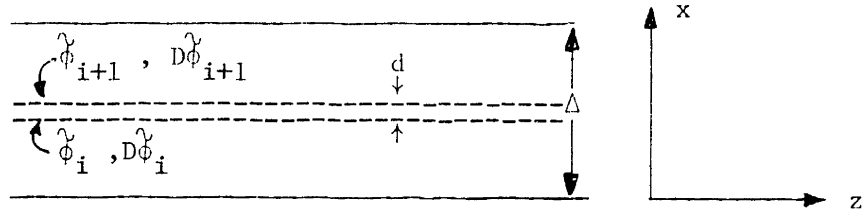


Figure 2. Variables at boundaries of an incremental layer.

$$D\tilde{\phi}_i = \frac{\tilde{\phi}_{i+1} - \tilde{\phi}_i}{d} \quad (5.22)$$

and
$$D^2\tilde{\phi}_i = \frac{D\tilde{\phi}_{i+1} - D\tilde{\phi}_i}{d} \quad (5.23)$$

Using Eq. (9) to express $D^2\tilde{\phi}_i$ in terms of $D\tilde{\phi}_i$ and $\tilde{\phi}_i$, and rewriting Eqs. (22) and (23):

$$\begin{bmatrix} \tilde{\phi}_{i+1} \\ D\tilde{\phi}_{i+1} \end{bmatrix} = \begin{bmatrix} 1 & d \\ dk^2 & 1 - d\left(\frac{D\varepsilon}{\varepsilon}\right)_i \end{bmatrix} \begin{bmatrix} \tilde{\phi}_i \\ D\tilde{\phi}_i \end{bmatrix} \quad (5.24)$$

or, in normalized form:

$$\underline{\tilde{\phi}}_{i+1} \equiv \tilde{\phi}_{i+1} ; \quad \underline{D\tilde{\phi}}_{i+1} \equiv \Delta D\tilde{\phi}_{i+1} ; \quad \underline{d} \equiv \frac{d}{\Delta} ; \quad \underline{k} \equiv k\Delta \quad (5.25)$$

$$\begin{bmatrix} \underline{\tilde{\phi}}_{i+1} \\ \underline{D\tilde{\phi}}_{i+1} \end{bmatrix} = \begin{bmatrix} 1 & \underline{d} \\ \underline{d} \underline{k}^2 & 1 - \underline{d}\left(\Delta \frac{D\varepsilon}{\varepsilon}\right)_i \end{bmatrix} \begin{bmatrix} \underline{\tilde{\phi}}_i \\ \underline{D\tilde{\phi}}_i \end{bmatrix} \quad (5.26)$$

Equation (26) tells us how to compute $\underline{\tilde{\phi}}$ and $\underline{D\tilde{\phi}}$ at the upper boundary of an incremental layer, given the same quantities at the lower boundary.

Applied repeatedly it allows us to find $\underline{\phi}$ and $\underline{D\phi}$ through the bulk of the layer in terms of $\underline{\gamma}^\beta$ and $\underline{D\phi}^\beta$ by repeated matrix multiplications. If the layer is broken into n increments of equal thickness, $\underline{d} = 1/n$, then after ℓ successive multiplications, $x = \ell \underline{d}$, and:

$$\begin{bmatrix} \underline{\phi}(x) \\ \underline{D\phi}(x) \end{bmatrix} = \begin{bmatrix} 1 & \underline{d} \\ \underline{dk}^2 & 1 - \underline{d} \left(\Delta \frac{D\epsilon}{\epsilon} \right)_{\ell-1} \end{bmatrix} \begin{bmatrix} 1 & \underline{d} \\ \underline{d} \underline{k}^2 & 1 - \underline{d} \left(\Delta \frac{D\epsilon}{\epsilon} \right)_{\ell-2} \end{bmatrix} \dots \begin{bmatrix} 1 & \underline{d} \\ \underline{d} \underline{k}^2 & 1 - \underline{d} \left(\Delta \frac{D\epsilon}{\epsilon} \right)_0 \end{bmatrix} \begin{bmatrix} \underline{\gamma}^\beta \\ \underline{D\phi}^\beta \end{bmatrix} \quad (5.27)$$

or,

$$\begin{bmatrix} \underline{\phi}(x) \\ \underline{D\phi}(x) \end{bmatrix} = \begin{bmatrix} L_{11}(x) & L_{12}(x) \\ L_{21}(x) & L_{22}(x) \end{bmatrix} \begin{bmatrix} \underline{\gamma}^\beta \\ \underline{D\phi}^\beta \end{bmatrix} \quad (5.28)$$

When $\ell = n$, $x = \Delta$ and:

$$\begin{bmatrix} \underline{\phi}^\alpha \\ \underline{D\phi}^\alpha \end{bmatrix} = \begin{bmatrix} M_{11} & M_{12} \\ M_{21} & M_{22} \end{bmatrix} \begin{bmatrix} \underline{\gamma}^\beta \\ \underline{D\phi}^\beta \end{bmatrix} \quad (5.29)$$

where $M_{ij} = L_{ij}(\Delta)$. (5.30)

Finally, rearranging Eq. (29) and computing the normalized displacements:

$$\begin{bmatrix} -\frac{D^2}{dx^2} \alpha \\ \frac{D^2}{dx^2} \beta \end{bmatrix} = \frac{1}{\epsilon^\alpha} \begin{bmatrix} \epsilon^\alpha & \underline{D\phi}^\alpha \\ -\epsilon^\beta & \underline{D\phi}^\beta \end{bmatrix} = \begin{bmatrix} T_{11} & T_{12} \\ T_{21} & T_{22} \end{bmatrix} \begin{bmatrix} \underline{\phi}^\alpha \\ \underline{\phi}^\beta \end{bmatrix} \quad (5.31)$$

where

$$\left. \begin{aligned} T_{11} &= \frac{M_{22}}{M_{12}} & ; & & T_{12} &= M_{21} - \frac{M_{11} M_{22}}{M_{12}} \\ T_{21} &= -R \frac{1}{M_{12}} & ; & & T_{22} &= R \frac{M_{11}}{M_{12}} \end{aligned} \right\} \quad (5.32)$$

and, as before, $R \equiv \epsilon^\beta / \epsilon^\alpha$. Equations (27)-(30) allow us, by marching across the layer of varying permittivity, to obtain variables at the $x = \Delta$ plane in terms of those at the $x = 0$ plane. Rearrangement then yields the transfer relations in their conventional form... Eqs. (31)-(32).

Note that we have a check on the accuracy of this numerical technique for the special case of an exponential permittivity distribution, the exact solution being expressed in Eqs. (20)-(21). An even simpler check may be performed in the case of uniform permittivity, where the transfer relations are simply LaPlacian. In terms of the above-introduced normalization and transfer matrix as defined in Eq. (31), the matrix entries for the uniform permittivity case are:

$$\left. \begin{aligned} T_{11} &= T_{22} = \underline{k} \coth \underline{k} \\ T_{12} &= T_{21} = -\frac{\underline{k}}{\sinh \underline{k}} \end{aligned} \right\} \quad (5.33)$$

In fact, for both the constant and exponential permittivity distributions, it may be shown that the exact solutions, rewritten in the stepwise form of Eq. (24) and specialized to layers of thickness $d \ll 1/k$, yield the same finite difference integration formulas given by Eq. (24.)

Another check upon the accuracy of the numerical integration technique is available by comparing the cross terms, T_{12} and T_{21} , of Eq. (31).

Regardless of the permittivity distribution, energy considerations require the reciprocity condition $T_{12} = T_{21}$. This condition is numerically satisfied to a degree dependent upon the step size \underline{d} used.

As examples of the use of the numerical integration technique, Figures 3 and 4 present results for three different permittivity distributions. In Fig. 3, the elements of the matrix L, as defined by Eq. (28), are plotted as functions of position through the bulk of the layer x/Δ , for constant permittivity, and for permittivities decreasing linearly and exponentially from bottom to top, reaching a value at the upper surface $1/5$ as large as at the lower. (In the cases of constant and exponential distributions, numerical integration results are in agreement with those obtained by evaluation of the exact solutions.) For this plot, in each case, $\underline{k} = 1$. Note that it is only the last values of the elements of L, i.e., those at $x/\Delta = 1$, that matter in computing the elements of T. Further note that $L_{12} = L_{21}$ for the constant and exponential distributions, but that the cross elements become distinct for the linear distribution.

In Fig. 4, the elements of the matrix T, as defined in Eqs. (31) and (32), are plotted on log-log paper as functions of \underline{k} for the same three permittivity distributions. The elements T_{11} and T_{22} are positive while T_{12} and T_{21} are negative for each of the distributions.

B. Varying Conductivity Layer in Equilibrium Tangential Electric Field-- Finite Difference Equations

The transfer relation technique used to characterize the exponentially varying conductivity layer in equilibrium tangential electric field in Chapter IV can, at least in principle, be extended to configurations described by non-constant coefficient differential equations,

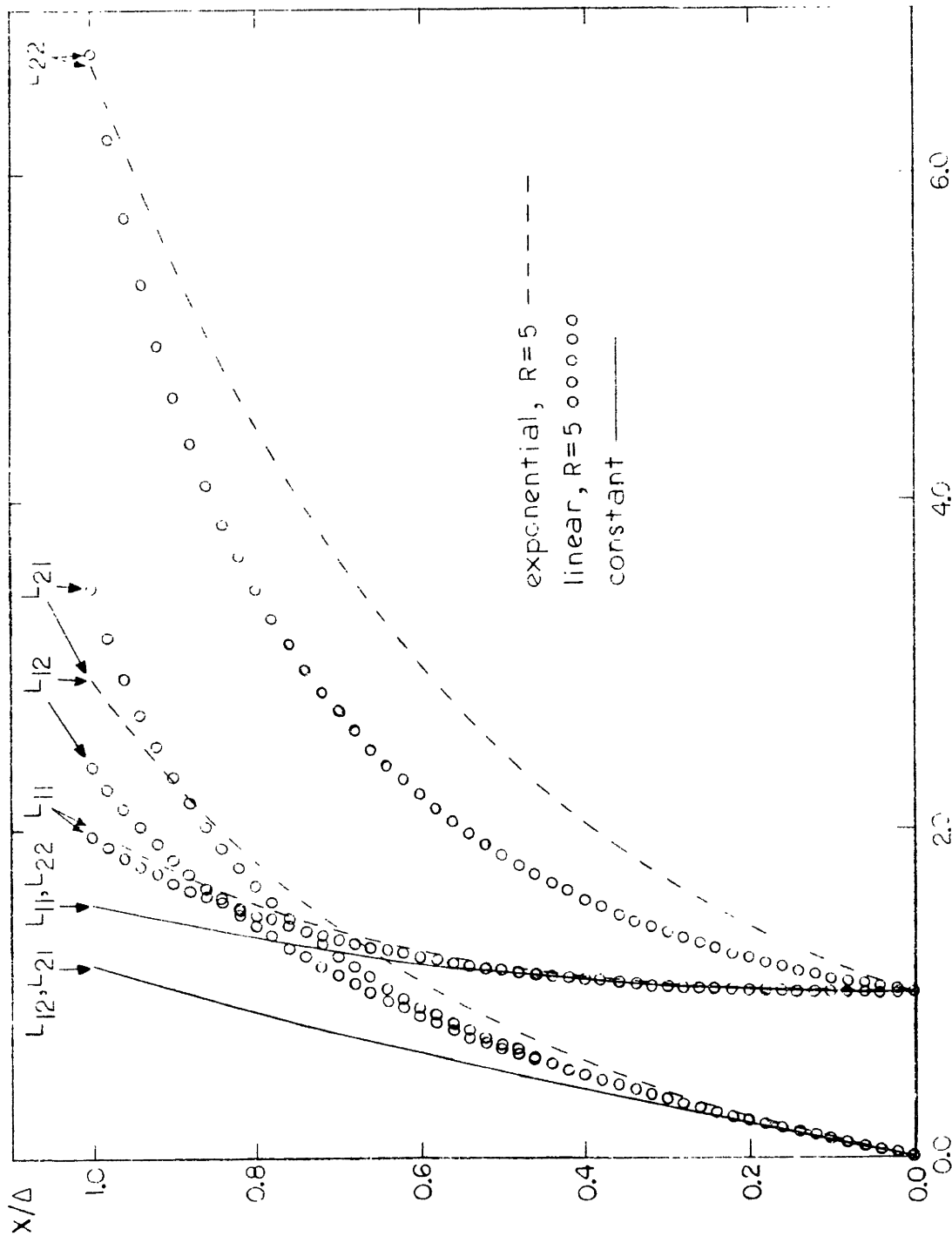


Figure 3. Elements of the matrix L as functions of x/Δ

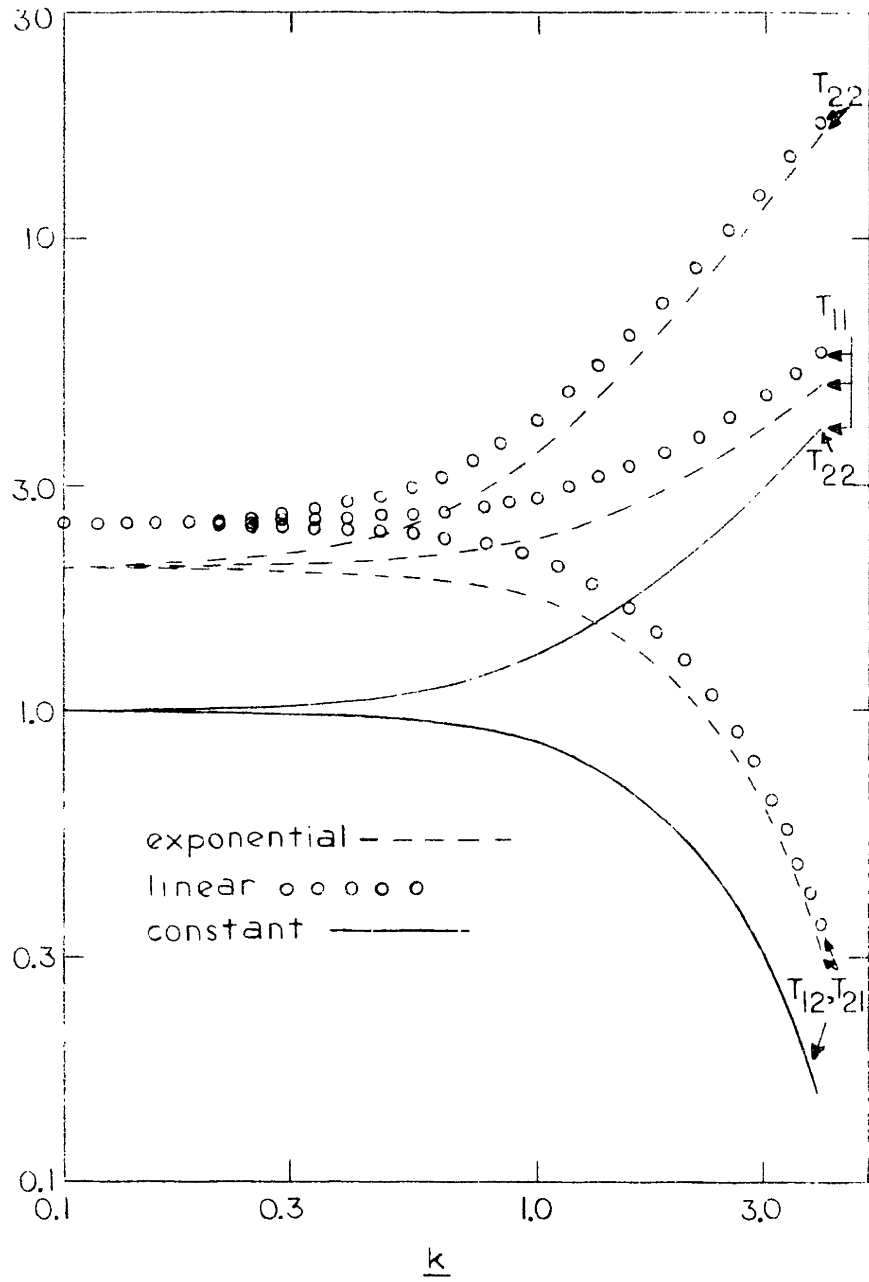


Figure 4. Elements of the matrix T as functions of \underline{k}

using a numerical integration technique analogous to that described in Section V.A. Thus, the situation is exactly that described in Section IV.A., where we allow $\sigma_0(x)$ to remain a general function. In order to deal with differential equations no higher than first order, we use, instead of Eqs. (4.7) and (4.12), a set of ten first order equations in ten unknowns. The x and z components of the Navier-Stokes equation (2.66) are:

$$s \rho \hat{v}_x = D \hat{S}_{xx} - jk \hat{S}_{xz} \quad (5.34)$$

$$s \rho \hat{v}_z = D \hat{S}_{xz} - jk \hat{S}_{zz} + E_0 \hat{\rho}_f \quad (5.35)$$

where we have written the equations in terms of perturbation stress tensor components \hat{S}_{xx} , \hat{S}_{xz} and \hat{S}_{zz} , defined by:

$$\hat{S}_{xx} = - \hat{p} + 2\eta D \hat{v}_x \quad (5.36)$$

$$\hat{S}_{xz} = \eta [D \hat{v}_z - jk \hat{v}_x] \quad (5.37)$$

$$\hat{S}_{zz} = - \hat{p} - 2\eta jk \hat{v}_z \quad (5.38)$$

The incompressibility condition, Eq. (2.65), yields:

$$D \hat{v}_x - jk \hat{v}_z = 0 \quad (5.39)$$

A curl-free electric field, Eq. (2.1), requires:

$$jk \hat{E}_x + D \hat{E}_z = 0 \quad (5.40)$$

and Gauss' Law, Eq. (2.2), becomes:

$$D\hat{E}_x - jk\hat{E}_z = \hat{\rho}_f/\epsilon \quad (5.41)$$

The equation of charge conservation, neglecting charge relaxation -- Eq. (2.49)--- yields:

$$\frac{\sigma_0}{\epsilon} \hat{\rho}_f - jkE_0 \hat{\sigma} + (D\sigma_0)\hat{E}_x = 0 \quad (5.42)$$

Finally, from Eq. (2.41) the constant conductivity condition is:

$$s\hat{\sigma} + (D\sigma_0)\hat{v}_x = 0 \quad (5.43)$$

Algebraic elimination of the four variables \hat{p} , \hat{S}_{zz} , $\hat{\rho}_f$ and $\hat{\sigma}$ leaves a system of six first order differential equations in the six variables \hat{v}_x , \hat{v}_z , \hat{E}_z , \hat{S}_{xx} , \hat{S}_{xz} and \hat{E}_x :

$$D\hat{v}_x = jk\hat{v}_z \quad (5.44)$$

$$D\hat{v}_z = jk\hat{v}_x + \frac{1}{\eta} \hat{S}_{xz} \quad (5.45)$$

$$D\hat{E}_z = -jk\hat{E}_x \quad (5.46)$$

$$D\hat{S}_{xx} = s\rho \hat{v}_x + jk \hat{S}_{xz} \quad (5.47)$$

$$D\hat{S}_{xz} = \frac{jk\epsilon}{s} E_0^2 \frac{D\sigma_0}{\sigma_0} \hat{v}_x + [s\rho + 4\eta k^2] \hat{v}_z + jk\hat{S}_{xx} + \epsilon E_0 \frac{D\sigma_0}{\sigma_0} \hat{E}_x \quad (5.48)$$

$$D\hat{E}_x = -\frac{jk}{s} E_0 \frac{D\sigma_0}{\sigma_0} \hat{v}_x + jk\hat{E}_z - \frac{D\sigma_0}{\sigma_0} \hat{E}_x \quad (5.49)$$

We proceed, next, to define a set of normalized variables:

$$\begin{aligned} \tau &\equiv \eta/\epsilon E_0^2 ; \quad T \equiv \frac{\rho \Lambda^2}{\eta} ; \quad \xi \equiv x/\Delta \\ \underline{d} &\equiv \frac{d}{\Delta} ; \quad \underline{k} \equiv k\Delta ; \quad \underline{s} \equiv s\tau \\ \underline{\hat{v}}_x &\equiv \hat{v}_x \frac{\tau}{\Delta} ; \quad \underline{\hat{v}}_z \equiv \hat{v}_z \frac{\tau}{\Delta} ; \quad \underline{\hat{S}}_x \equiv \frac{\hat{S}_{xx}}{\epsilon E_0^2} ; \quad \underline{\hat{S}}_z \equiv \frac{\hat{S}_{xz}}{\epsilon E_0^2} \\ \underline{\hat{\phi}} &\equiv \frac{\hat{\phi}}{E_0 \Delta} ; \quad \underline{\hat{E}}_x \equiv \frac{\hat{E}_x}{E_0} ; \quad \underline{\hat{E}}_z \equiv \frac{\hat{E}_z}{E_0} ; \quad \underline{\hat{J}}_x \equiv \frac{\hat{J}_x}{\sigma_\alpha E_0} \\ \underline{h}_0 &\equiv \frac{\sigma_0}{\sigma_\alpha} ; \quad \underline{h}_1 \equiv \frac{\Delta D \sigma_0}{\sigma_0} = \frac{1}{\underline{h}_0} \frac{dh_0}{d\xi} \end{aligned} \quad (5.50)$$

Finally, Eqs. (44)-(50) are used to write a set of finite difference equations for an incremental layer of thickness d , identified by superscripts i and $i+1$ at lower and upper boundaries respectively:

$$\underline{\hat{v}}_x^{i+1} = \underline{\hat{v}}_x^i + j \underline{k} \underline{d} \underline{\hat{v}}_z^i \quad (5.51)$$

$$\underline{\hat{v}}_z^{i+1} = j \underline{k} \underline{d} \underline{\hat{v}}_x^i + \underline{\hat{v}}_z^i + \underline{d} \underline{\hat{S}}_z^i \quad (5.52)$$

$$\underline{\hat{E}}_z^{i+1} = \underline{\hat{E}}_z^i - j \underline{k} \underline{d} \underline{\hat{E}}_x^i \quad (5.53)$$

$$\underline{\hat{S}}_x^{i+1} = \underline{s} \frac{T}{\tau} \underline{d} \underline{\hat{v}}_x^i + \underline{\hat{S}}_x^i + j \underline{k} \underline{d} \underline{\hat{S}}_z^i \quad (5.54)$$

$$\underline{\hat{S}}_z^{i+1} = \frac{j \underline{k} \underline{d}}{\underline{s}} \underline{h}_1^i \underline{\hat{v}}_x^i + \underline{d} [\underline{s} \frac{T}{\tau} + 4 \underline{k}^2] \underline{\hat{v}}_z^i + j \underline{k} \underline{d} \underline{\hat{S}}_x^i + \underline{\hat{S}}_z^i + \underline{d} \underline{h}_1^i \underline{\hat{E}}_x^i \quad (5.55)$$

$$\underline{\hat{E}}_x^{i+1} = - \frac{j \underline{k} \underline{d}}{\underline{s}} \underline{h}_1^i \underline{\hat{v}}_x^i + j \underline{k} \underline{d} \underline{\hat{E}}_z^i + [1 - \underline{d} \underline{h}_1^i] \underline{\hat{E}}_x^i \quad (5.56)$$

Equations (51)-(56) allow us to compute the six variables $\underline{\hat{v}}_x$, $\underline{\hat{v}}_z$, $\underline{\hat{E}}_z$, $\underline{\hat{S}}_x$, $\underline{\hat{S}}_z$, and $\underline{\hat{E}}_x$ at the upper surface of an incremental layer when the same variables are known at the lower surface. Applied repeatedly, they may be

used to "march" across the thickness Δ , and determine \hat{v}_x^α , \hat{v}_z^α , \hat{E}_z^α , \hat{S}_x^α , \hat{S}_z^α and \hat{E}_x^α in terms of \hat{v}_x^β , \hat{v}_z^β , \hat{E}_z^β , \hat{S}_x^β , \hat{S}_z^β , and \hat{E}_x^β . The results, then, are the 36 elements of a matrix [L], defined by:

$$\begin{bmatrix} \hat{v}_x^\alpha \\ \hat{v}_z^\alpha \\ \hat{E}_z^\alpha \\ \hat{S}_x^\alpha \\ \hat{S}_z^\alpha \\ \hat{E}_x^\alpha \end{bmatrix} = \begin{bmatrix} L_{11} & L_{12} & L_{13} & L_{14} & L_{15} & L_{16} \\ L_{21} & L_{22} & L_{23} & L_{24} & L_{25} & L_{26} \\ L_{31} & L_{32} & L_{33} & L_{34} & L_{35} & L_{36} \\ L_{41} & L_{42} & L_{43} & L_{44} & L_{45} & L_{46} \\ L_{51} & L_{52} & L_{53} & L_{54} & L_{55} & L_{56} \\ L_{61} & L_{62} & L_{63} & L_{64} & L_{65} & L_{66} \end{bmatrix} \begin{bmatrix} \hat{v}_x^\beta \\ \hat{v}_z^\beta \\ \hat{E}_z^\beta \\ \hat{S}_x^\beta \\ \hat{S}_z^\beta \\ \hat{E}_x^\beta \end{bmatrix} \quad (5.57)$$

Knowing the elements of [L], a matrix manipulation program, as described in Appendix B, is used to compute the 36 elements of the transfer matrix [T], defined by:

$$\begin{bmatrix} \hat{S}_x^\alpha \\ \hat{S}_x^\beta \\ \hat{S}_z^\alpha \\ \hat{S}_z^\beta \\ \hat{E}_x^\alpha \\ \hat{E}_x^\beta \end{bmatrix} = \begin{bmatrix} T_{11} & T_{12} & T_{13} & T_{14} & T_{15} & T_{16} \\ T_{21} & T_{22} & T_{23} & T_{24} & T_{25} & T_{26} \\ T_{31} & T_{32} & T_{33} & T_{34} & T_{35} & T_{36} \\ T_{41} & T_{42} & T_{43} & T_{44} & T_{45} & T_{46} \\ T_{51} & T_{52} & T_{53} & T_{54} & T_{55} & T_{56} \\ T_{61} & T_{62} & T_{63} & T_{64} & T_{65} & T_{66} \end{bmatrix} \begin{bmatrix} \hat{v}_x^\alpha \\ \hat{v}_x^\beta \\ \hat{v}_z^\alpha \\ \hat{v}_z^\beta \\ \hat{E}_z^\alpha \\ \hat{E}_z^\beta \end{bmatrix} \quad (5.58)$$

Finally, J_x is related to E_x :

$$\hat{\underline{J}}_x = h_0 \hat{\underline{E}}_x \quad (5.59)$$

and $\hat{\underline{E}}_z$ is related to $\hat{\underline{\phi}}$:

$$\hat{\underline{E}}_z = j \underline{k} \hat{\underline{\phi}} \quad (5.60)$$

to determine the layer transfer relations:

$$[S] = [Q][V] \quad (5.61)$$

where

$$[S] \equiv \begin{bmatrix} \hat{\underline{S}}_x^\alpha \\ \hat{\underline{S}}_x^\beta \\ \hat{\underline{S}}_z^\alpha \\ \hat{\underline{S}}_z^\beta \\ \hat{\underline{J}}_x^\alpha \\ \hat{\underline{J}}_x^\beta \end{bmatrix} \quad (5.62) \quad [V] \equiv \begin{bmatrix} \hat{\underline{v}}_x^\alpha \\ \hat{\underline{v}}_x^\beta \\ \hat{\underline{v}}_z^\alpha \\ \hat{\underline{v}}_z^\beta \\ \hat{\underline{\phi}}^\alpha \\ \hat{\underline{\phi}}^\beta \end{bmatrix} \quad (5.63)$$

and $[Q]$ is given by:

$$[Q] \equiv \begin{bmatrix} T_{11} & T_{12} & T_{13} & T_{14} & j\underline{k}T_{15} & j\underline{k}T_{16} \\ T_{21} & T_{22} & T_{23} & T_{24} & j\underline{k}T_{25} & j\underline{k}T_{26} \\ T_{31} & T_{32} & T_{33} & T_{34} & j\underline{k}T_{35} & j\underline{k}T_{36} \\ T_{41} & T_{42} & T_{43} & T_{44} & j\underline{k}T_{45} & j\underline{k}T_{46} \\ T_{51} & T_{52} & T_{53} & T_{54} & j\underline{k}T_{55} & j\underline{k}T_{56} \\ RT_{61} & RT_{62} & RT_{63} & RT_{64} & j\underline{k}RT_{65} & j\underline{k}RT_{66} \end{bmatrix} \quad (5.64)$$

C. Varying Conductivity Layer in Equilibrium Normal Electric Field --
Finite Difference Equations

Provided we use a numerical integration technique to deal with the governing differential equations, we can describe a varying conductivity layer with equilibrium electric field oriented normal to the layer surfaces as shown in Fig. 5:

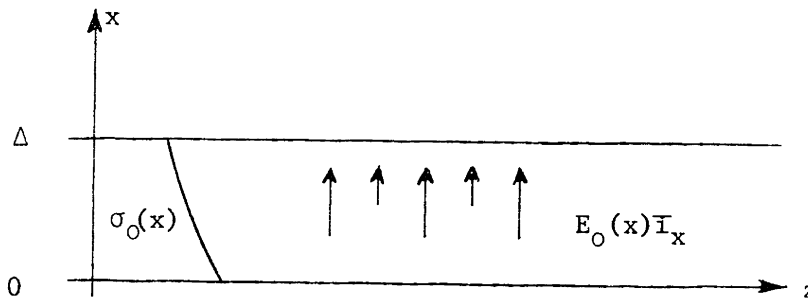


Figure 5. Layer of varying conductivity in normal field.

In equilibrium, the fluid is static:

$$\frac{-E}{v} = 0 \quad (5.65)$$

and supports constant current density $J_0 \mathbf{I}_x$. Thus:

$$E_0(x) = J_0 / \sigma_0(x) \quad (5.66)$$

Gauss' Law, Eq. (2.2), then determines the equilibrium charge density distribution:

$$\rho_{f0}(x) = - \frac{\epsilon J_0}{\sigma_0(x)} \frac{D\sigma_0(x)}{\sigma_0(x)} = - \epsilon E_0(x) \frac{D\sigma_0(x)}{\sigma_0(x)} \quad (5.67)$$

The corresponding equilibrium pressure distribution, defined such that $p = p_0$ when $E_0 = 0$, is:

$$p = p_0 + \frac{1}{2} \epsilon E_0^2(x) \quad . \quad (5.68)$$

We consider perturbations with z - t dependence $e^{(st-jkz)}$. The dynamics are described by first order differential equations deriving from the Navier-Stokes equation, stress tensor component definitions, incompressibility condition, electroquasistatic Faraday's law, Gauss' law, charge conservation, and constant conductivity condition, in correspondence with Eqs. (34)-(43) of Section V.B., thus

$$\hat{s} \rho \hat{v}_x = D \hat{S}_{xx} - jk \hat{S}_{xz} + \rho_{f0} \hat{E}_x + E_0 \hat{\rho}_f \quad (5.69)$$

$$\hat{s} \rho \hat{v}_z = D \hat{S}_{xz} - jk \hat{S}_{zz} + \rho_{f0} \hat{E}_z \quad (5.70)$$

$$\hat{S}_{xx} = -\hat{p} + 2\eta D \hat{v}_x \quad (5.71)$$

$$\hat{S}_{xz} = \eta [D \hat{v}_z - jk \hat{v}_x] \quad (5.72)$$

$$\hat{S}_{zz} = -\hat{p} - 2\eta jk \hat{v}_z \quad (5.73)$$

$$D \hat{v}_x - jk \hat{v}_z = 0 \quad (5.74)$$

$$jk \hat{E}_x + D \hat{E}_z = 0 \quad (5.75)$$

$$D \hat{E}_x - jk \hat{E}_z = \hat{\rho}_f / \epsilon \quad (5.76)$$

$$\frac{\sigma}{\epsilon} \hat{\rho}_f + \frac{\rho_{f0}}{\epsilon} \hat{\sigma} + E_0 D \hat{\sigma} + (D \sigma_0) \hat{E}_x = 0 \quad (5.77)$$

$$\hat{s} \hat{\sigma} + (D \sigma_0) \hat{v}_x = 0 \quad . \quad (5.78)$$

Our development proceeds in complete analogy with the analysis for the tangential field equations of Section V.B. Algebraic elimination of

the four variables $\hat{\rho}$, \hat{S}_{zz} , $\hat{\rho}_f$ and $\hat{\sigma}$ leaves a system of six first order equations in the six variables \hat{v}_x , \hat{v}_z , \hat{E}_z , \hat{S}_{xx} , \hat{S}_{xz} , and \hat{E}_x :

$$D\hat{v}_x = jk\hat{v}_z \quad (5.79)$$

$$D\hat{v}_z = jk\hat{v}_x + \frac{1}{\eta} \hat{S}_{xz} \quad (5.80)$$

$$D\hat{E}_z = -jk\hat{E}_x \quad (5.81)$$

$$\begin{aligned} D\hat{S}_{xx} = & \left[s\rho - \frac{\epsilon E_0^2}{s} \frac{D^2\sigma_0}{\sigma_0} - \frac{\rho_{f0}E_0}{s} \frac{D\sigma_0}{\sigma_0} \right] \hat{v}_x \\ & - \frac{jk}{s} \epsilon E_0^2 \frac{D\sigma_0}{\sigma_0} \hat{v}_z + jk\hat{S}_{xz} + \left[\epsilon E_0 \frac{D\sigma_0}{\sigma_0} - \rho_{f0} \right] \hat{E}_x \end{aligned} \quad (5.82)$$

$$D\hat{S}_{xz} = \left[s\rho + 4\eta k^2 \right] \hat{v}_z - \rho_{f0} \hat{E}_z + jk\hat{S}_{xx} \quad (5.83)$$

$$\begin{aligned} D\hat{E}_x = & \frac{1}{s} \left[E_0 \frac{D^2\sigma_0}{\sigma_0} + \frac{\rho_{f0}}{\epsilon} \frac{D\sigma_0}{\sigma_0} \right] \hat{v}_x + \frac{jk}{s} E_0 \frac{D\sigma_0}{\sigma_0} \hat{v}_z + jk\hat{E}_z \\ & - \frac{D\sigma_0}{\sigma_0} \hat{E}_x \end{aligned} \quad (5.84)$$

We use the normalized variables:

$$\tau \equiv \frac{\eta}{\epsilon(E^\alpha)^2} ; \quad T \equiv \frac{\rho\Delta^2}{\eta} ; \quad \xi \equiv x/\Delta$$

$$\underline{d} \equiv \frac{d}{\Delta} ; \quad \underline{k} \equiv k\Delta ; \quad \underline{s} \equiv s\tau$$

$$\underline{\hat{v}}_x \equiv \hat{v}_x \frac{\tau}{\Delta} ; \quad \underline{\hat{v}}_z \equiv \hat{v}_z \frac{\tau}{\Delta} ; \quad \underline{\hat{S}}_x \equiv \frac{\hat{S}_{xx}}{\epsilon(E^\alpha)^2} ; \quad \underline{\hat{S}}_z \equiv \frac{\hat{S}_{xz}}{\epsilon(E^\alpha)^2} \quad (5.85)$$

$$\underline{\hat{\phi}} \equiv \frac{\hat{\phi}}{E^\alpha \Delta} ; \quad \underline{\hat{E}}_x \equiv \frac{\hat{E}_x}{E^\alpha} ; \quad \underline{\hat{E}}_z \equiv \frac{\hat{E}_z}{E^\alpha} ; \quad \underline{\hat{J}}_x \equiv \frac{\hat{J}_x}{\sigma^\alpha E^\alpha}$$

$$\underline{h}_0 \equiv \frac{\sigma_0}{\sigma^\alpha} ; \quad \underline{h}_1 \equiv \frac{\Delta D\sigma_0}{\sigma_0} = \frac{1}{\underline{h}_0} \frac{d\underline{h}_0}{d\xi}$$

$$\underline{h}_2 \equiv \frac{\Delta^2 D^2 \sigma_0}{\sigma_0} = \frac{1}{\underline{h}_0} \frac{d^2 \underline{h}_0}{d\xi^2} ; \quad \frac{1}{\underline{h}_0} = \frac{E_0}{E^\alpha}$$

where $\sigma^\alpha \equiv \sigma_0(x = \Delta)$ and $E^\alpha \equiv E_0(x = \Delta)$ (5.86)

to write a set of finite difference equations for an incremental layer of thickness d , identified by superscripts i and $i+1$ at lower and upper boundaries respectively:

$$\underline{v}_x^{i+1} = \underline{v}_x^i + jk d \underline{v}_z^i \quad (5.87)$$

$$\underline{v}_z^{i+1} = jk d \underline{v}_x^i + \underline{v}_z^i + d \underline{S}_z^i \quad (5.88)$$

$$\underline{E}_z^{i+1} = \underline{E}_z^i - jk d \underline{E}_x^i \quad (5.89)$$

$$\begin{aligned} \underline{S}_x^{i+1} = d \left[\underline{s} \frac{T}{\tau} - \frac{1}{\underline{s}} \frac{\underline{h}_2^i}{\{\underline{h}_0^i\}^2} + \frac{1}{\underline{s}} \left\{ \frac{\underline{h}_1^i}{\underline{h}_0^i} \right\}^2 \right] \underline{v}_x^i - j \frac{k d}{\underline{s}} \left[\frac{\underline{h}_1^i}{\{\underline{h}_0^i\}^2} \right] \underline{v}_z^i \\ + \underline{S}_x^i + jk d \underline{S}_z^i + 2d \left[\frac{\underline{h}_1^i}{\underline{h}_0^i} \right] \underline{E}_x^i \end{aligned} \quad (5.90)$$

$$\underline{S}_z^{i+1} = d \left[\underline{s} \frac{T}{\tau} + 4k^2 \right] \underline{v}_z^i + d \left[\frac{\underline{h}_1^i}{\underline{h}_0^i} \right] \underline{E}_z^i + jk d \underline{S}_x^i + \underline{S}_z^i \quad (5.91)$$

$$\underline{E}_x^{i+1} = \frac{d}{\underline{s}} \left[\frac{\underline{h}_2^i - \{\underline{h}_1^i\}^2}{\underline{h}_0^i} \right] \underline{v}_x^i + \frac{jk d}{\underline{s}} \left[\frac{\underline{h}_1^i}{\underline{h}_0^i} \right] \underline{v}_z^i + jk d \underline{E}_z^i + [1 - \underline{d} \underline{h}_1^i] \underline{E}_x^i \quad (5.92)$$

Successive use of Eqs. (87)-(92) yields the 36 elements of the matrix $[L]$, defined by Eq. (57). The matrix manipulations given in Appendix B yield the elements of the matrix $[T]$, defined by Eq. (58).

Finally, \underline{J}_x is related to \underline{E}_x :

$$\hat{\underline{J}}_{\underline{x}} = \frac{\hat{h}}{\underline{0}} \hat{\underline{E}}_{\underline{x}} - \frac{\hat{h}_1}{\underline{s}} \hat{\underline{v}}_{\underline{x}} \quad (5.93)$$

and $\hat{\underline{E}}_{\underline{z}}$ is related to $\hat{\underline{\phi}}$:

$$\hat{\underline{E}}_{\underline{z}} = \underline{jk} \hat{\underline{\phi}} \quad (5.94)$$

to determine the elements of the matrix [Q], defined by Eq. (61), in terms of the elements of [T]:

$$[Q] = \begin{bmatrix} T_{11} & T_{12} & T_{13} & T_{14} & \underline{jkT}_{15} & \underline{jkT}_{16} \\ T_{21} & T_{22} & T_{23} & T_{24} & \underline{jkT}_{25} & \underline{jkT}_{26} \\ T_{31} & T_{32} & T_{33} & T_{34} & \underline{jkT}_{35} & \underline{jkT}_{36} \\ T_{41} & T_{42} & T_{43} & T_{44} & \underline{jkT}_{45} & \underline{jkT}_{46} \\ \left\{ T_{51} - \frac{\hat{h}_1^\alpha}{\underline{s}} \right\} T_{52} & T_{53} & T_{54} & \underline{jkT}_{55} & \underline{jkT}_{56} \\ RT_{61} \left\{ RT_{62} - \frac{\hat{h}_1^\beta}{\underline{s}} \right\} RT_{63} & RT_{64} & \underline{jk} RT_{65} & \underline{jkRT}_{66} \end{bmatrix} \quad (5.95)$$

CHAPTER VI. TANGENTIAL FIELD EXPERIMENTS

A. Low Field Instability and Correspondence with Theory

Experimental studies involving the application of an electric field tangential to the interface between two miscible fluids of identical mechanical properties but disparate electrical conductivities lead to unexpected phenomena. Figure 1 shows a drawing of an electrohydrodynamic flow cell.

Microscope slides allow optical projection through the cell from a tungsten arc point light source. Two fluids enter via respective inlet tubes at the top and bottom. Removal via the outlet tubes at the sides allows formation of a clean horizontal interface midway up the cell. An electric field is applied tangential to the interface by means of wire electrodes running vertically along the sides.

The liquid used is Mazola corn oil. Pure corn oil enters at the bottom inlet tube. That entering at the top inlet tube is doped in electrical conductivity with Shell anti-static fluid ASA-3 (85001) and dyed with Fisher Scientific Flaming Red Dye A-801 (Lot 770942). Depending upon the experiment to be performed, the lower fluid is used straight, as doped and dyed, or diluted with pure corn oil to 1/20 concentration by volume. The various physical properties are listed in Table I.

Still photographs obtained by projecting the image of the cell directly onto the shutter of a 35 mm. camera, with relatively low values of applied electric field, are shown in Figs. 2 and 3. The lower (clear) fluid is pure corn oil, while the upper (dark) fluid is the 1/20 mixture of doped and red-dyed corn oil. The conductivity ratio in this case is $R = 25.9$.

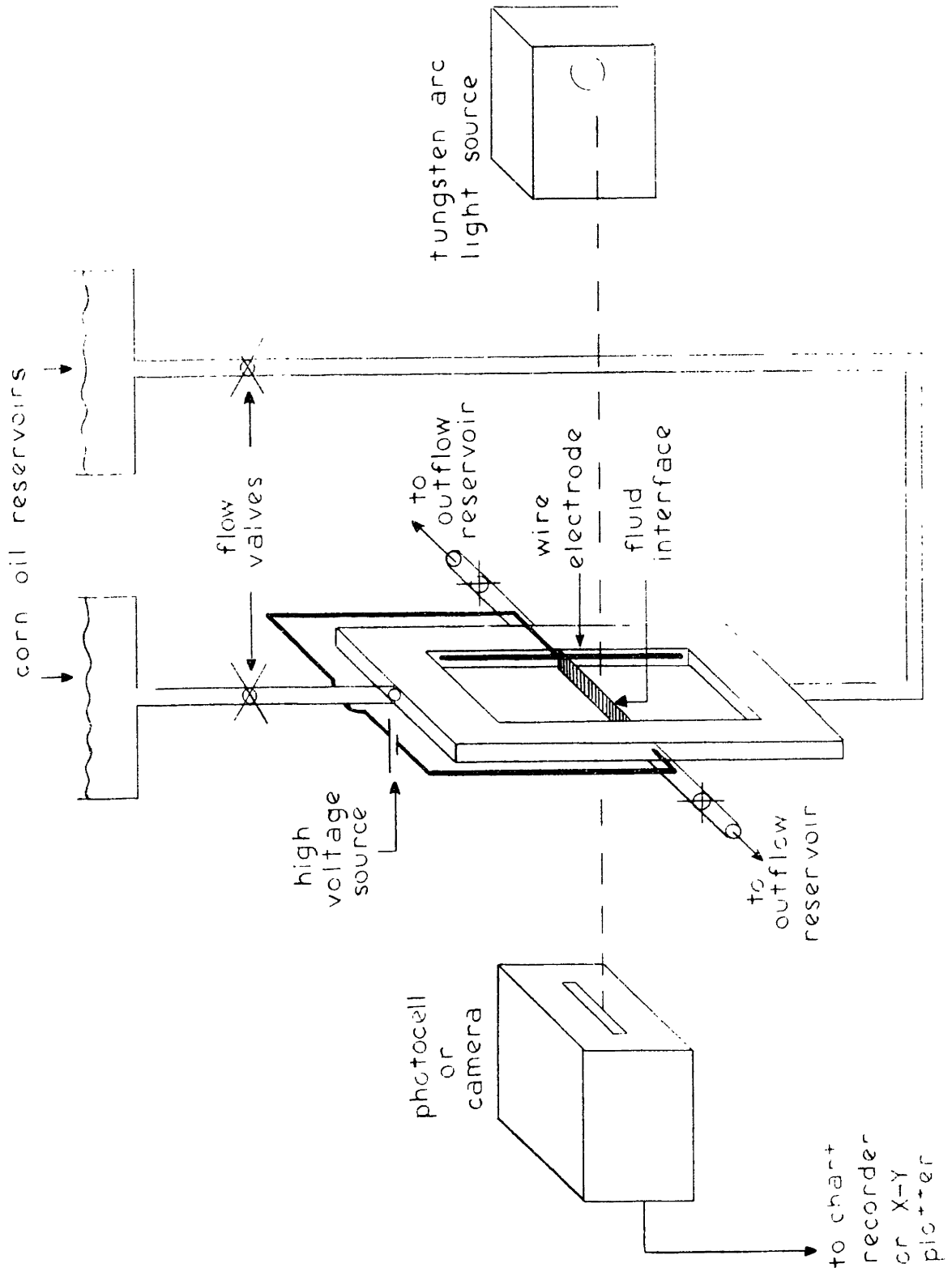


Figure 1. Experimental flow cell and optical configuration

Table I. Corn Oil Properties

Density: $\rho = 0.922 \times 10^3 \text{ Kgm/m}^3$.

Viscosity: $\eta = 6 \times 10^{-2} \text{ Kgm/m-sec.}$

Permittivity: $\epsilon = 3.1 \epsilon_0 = 2.74 \times 10^{-11} \text{ farad/m.}$

Conductivity:

Pure: $\sigma = 4.05 \times 10^{-11} \text{ mho/m.}$

1/20 Mixture: $\sigma = 1.05 \times 10^{-9} \text{ mho/m.}$

Straight doped and dyed: $\sigma = 8.1 \times 10^{-9} \text{ mho/m.}$

For each of the sequences shown, a clean interface is formed, then allowed to diffuse for a known time before application of the field. In each of the four sequences shown in Fig. 2, the interface has diffused one hour; in the first two sequences of Fig. 3, it has diffused four hours; in the last sequence of Fig. 3, it has diffused nine hours. Thus, assuming diffusion is unaffected by the cell walls, the sequences in Fig. 3 begin with interface structures twice and three times as broad as those in Fig. 2. Photographs are taken at the indicated times after the instant the electrical source is switched on.

In each sequence, note the appearance, at the scale of the interface structure, of slanted fronts, originating at the outer edges and propagating toward the center. The distances between fronts in the sequences in Fig. 3 are, respectively, approximately twice and three times those in Fig. 2. Distance between fronts appears to be independent of the value of electric field, depending only on the initial interface structure.

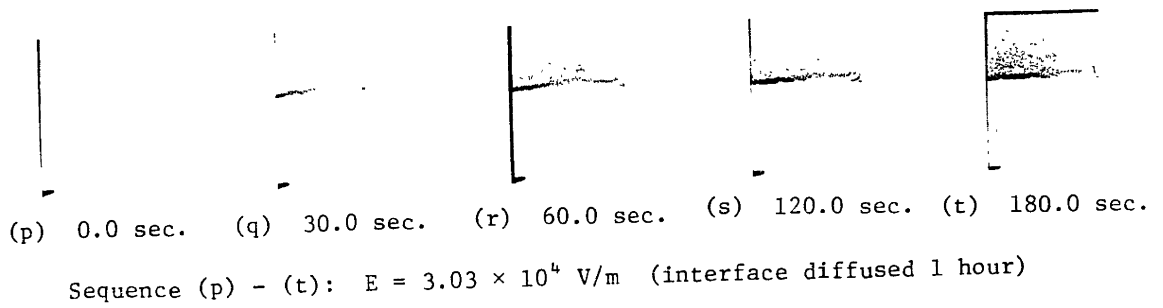
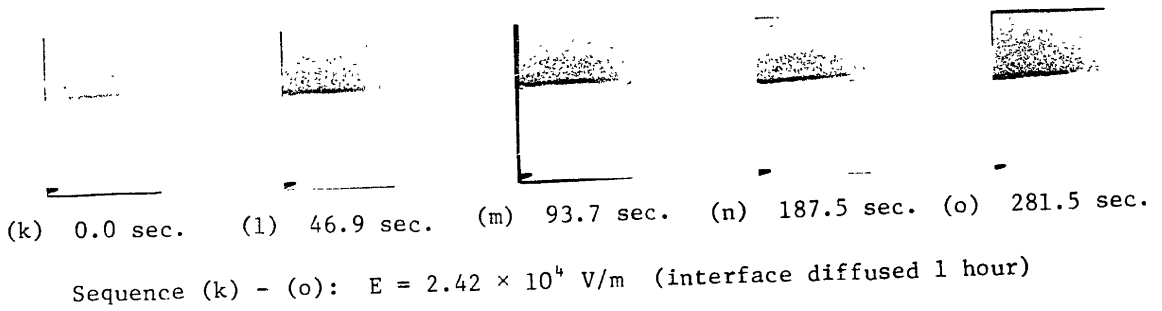
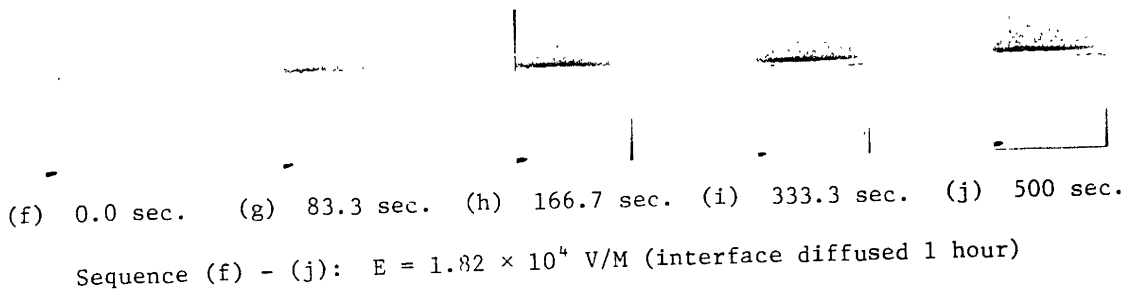
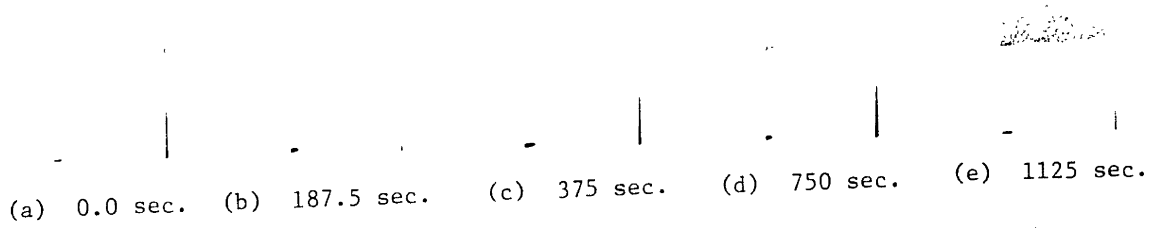


Figure 2. Photographs of experimental cell fluid component distributions

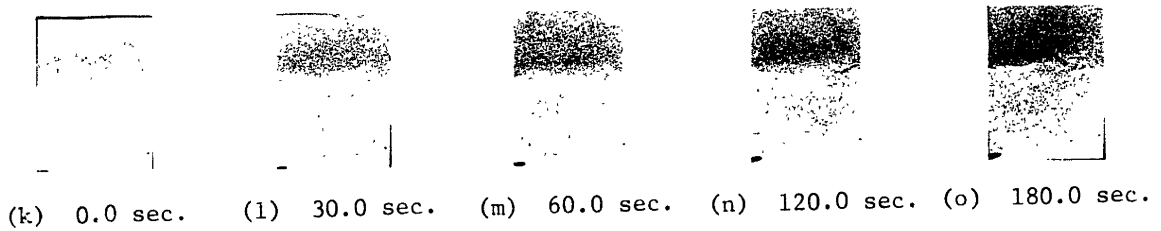
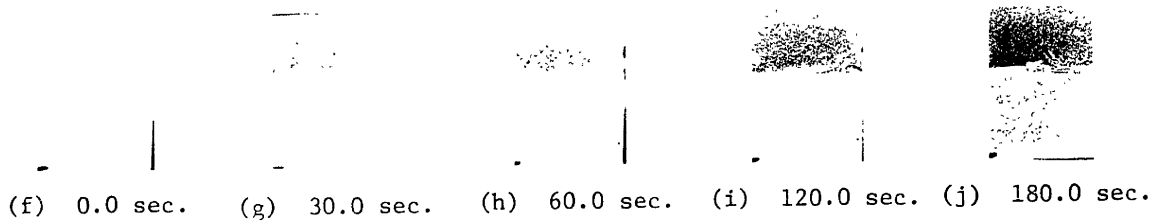
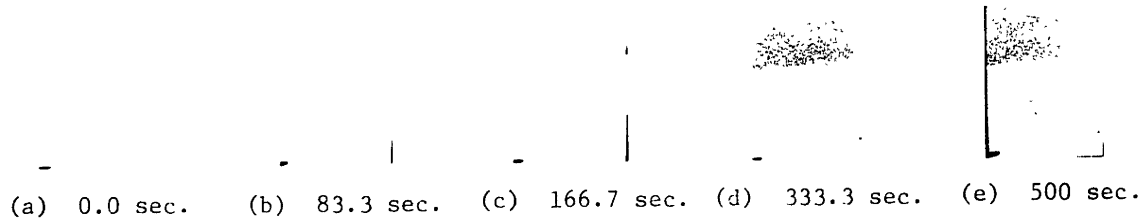


Figure 3. Photographs of experimental cell fluid component distributions

The slant angles of fronts vary between photographs, but lie in the range of $20^\circ - 30^\circ$.

The respective time intervals between photographs are scaled to $1/E^2$. Note that, with this scaling, the sequence of events appears quite similar for sequences with identically diffuse initial interfaces. In real time, for example, the first sequence in Fig. 2 evolves over a period $6\frac{1}{4}$ times as long as the last.

The phenomena observed in Figs. 2 and 3 are, presumably, associated with electrohydrodynamic instability at the scale of the structure of the interface. Thus, it is natural to consider the degree of correspondence between experimental observations and the theory of Chapter IV.

Comparison of the slanted fronts in Figs. 2 and 3 with the cells in Fig. IV.29 requires that the photographs be turned upside down, so that the more conducting fluid is on the bottom. Alternatively, the cross-product defined in Section IV.C. may be used to see that the fronts slant and propagate in the manner described by the theory for fluid cells.

It is essential to recognize here that detailed correlation between experiment and theory cannot be claimed for two reasons: first, the experimental configuration is not well enough controlled, at the scale of the processes described. Second, the detailed evolution of the instability from initial noise is not simply determined by the fastest growing wave-number. There is, however, strong evidence that the experimentally observed fine-scale processes find explanation in the physical mechanism identified by the theory. The slant angle in the center of the cells of Fig. IV.29 (27°) falls within the experimentally determined range ($20^\circ - 30^\circ$)

The wavenumber, k , as mentioned above, is independent of the value of electric field and is halved when the interface is allowed to diffuse to double its initial thickness. This corresponds to $\underline{k}^* = k_i =$ one known number, dependent only on R and T/τ in the theory.

Finally, it is possible, by starting with two different bits of experimental data and working back through the theory, to arrive by two different routes at an estimate of the initial interface thickness. Considering, for example, the first sequence in Fig. 3:

$$\begin{aligned} E_0 &= 1.82 \times 10^4 \text{ V/m} \\ \tau &= \eta/\epsilon E_0^2 = 6.63 \text{ sec.} \\ R &= 25.9 \end{aligned}$$

Assuming $T/\tau \ll 1$, Figs. IV.25 and IV.26 yield:

$$\begin{aligned} \underline{s}_r^* &= 0.064 \\ \underline{s}_i^* &= 0.123 \\ \underline{k}^* &= 1.641 \end{aligned}$$

Measurement of the distance between fronts in Fig. 3d and assumption that it may be identified with the fastest-growing wavenumber yields:

$$2\pi\Delta/k^* = 3.9 \times 10^{-3} \text{ m}$$

which implies $\Delta = 10^{-3}$ m. Measurement of the velocity of the front from Fig. 3.c to 3.d to 3.e and assumption that it may be identified with the phase velocity \underline{s}_i^*/k^* yields:

$$\underline{s}_i^*/\underline{k}^* \tau = 1.2 \times 10^{-5} \text{ m/sec}$$

which also implies $\Delta = 10^{-3}$ m. Checking the validity of the assumption

$\tau/\tau \ll 1$ gives

$$\tau = \frac{\rho\Delta^2}{\eta} = 0.0154 \ll \tau \quad .$$

Thus, the assumption that experimentally observed fronts correspond to the theoretically predicted propagating cells leads to consistent prediction of interface thickness from two separate pieces of experimental data.

Propagating fronts in a region of spatially varying conductivity are suggestive of similar phenomena observed in poorly conducting fluids with thermally induced property gradients.⁽¹⁾ Propagation of phases of unstable modes is, similarly, consistent with a bulk-coupled electrohydrodynamic theory.⁽²⁾

B. High Field Mixing

The photographs shown in Figs. 2 and 3 all correspond to relatively low values of electric field. For relatively higher values, ($E \sim 10^5$ V/m and higher), the interface curves, buckles and folds over on itself. In static equilibrium, there is no electrical force density. The rotational character of the electric force density created by the instability is evident as fluid components roll and swirl into one another.

Figure 4 demonstrates the sort of mixing attainable in relatively short times at relatively high values of electric field. The fluid orientation has been reversed here, with the pure corn oil on top. Straight dyed and doped corn oil is used in the lower part of the cell, yielding a conductivity ratio of $R = 200$. Motions of the kind shown here are of obvious interest with regard to practical mixing operations.⁽³⁾



(a) 60 sec.



(b) 120 sec.



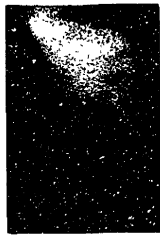
(c) 60 sec.



(d) 120 sec.

(a) - (b): $E = 6.06 \times 10^4$ V/m

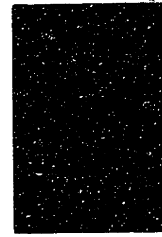
(c) - (d): $E = 1.21 \times 10^5$ V/m



(e) 60 sec.



(f) 120 sec.

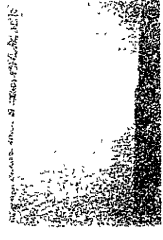
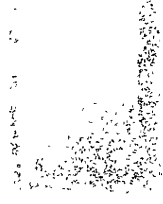
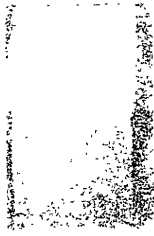


(g) 60 sec.

(e) - (f): $E = 3.03 \times 10^5$ V/m

(g): $E = 6.06 \times 10^5$ V/m

Figure 4. Photographs of experimental cell fluid component distributions at relatively high electric fields



An important consideration in the large-scale processes shown is viscous drag due to the proximity of front and back cell walls.

A quantitative description of the mixing process exemplified by Fig. 4 is accomplished with the use of a photocell, providing an electrical signal with magnitude directly proportional to the intensity of light incident on a narrow slit. The photocell is positioned behind the mixing cell, so that the intensity of light from the tungsten arc source depends upon the optical properties of fluid at a given level in the cell.

Vertical positioning is such that light incident on the photocell slit has passed through the experimental cell just above the interface. As dark fluid is swept up into the region above the initial interface, the light intensity incident on the photocell slit is diminished, and a chart recorder sensing photocell output provides a time history of the mixing process at one vertical position in the cell. (Variations in the horizontal direction are automatically averaged out by this method.)

Figure 5 shows plots of light intensity as a function of time for six different values of electric field. The time scale here is normalized to the electric-viscous time, $\tau = \eta/\epsilon E^2$. It is evident that the mixing process evolves on the scale of the cell over times of the order $10^2\tau$. The point here is that, except for the highest value of electric field, the various normalized curves are reasonably close to one another, even though the run at 0.606×10^5 V/m evolved in real time over a period 40 times as long as the run at 3.84×10^5 V/m. The scaling of the mixing process with τ is thus experimentally confirmed. At the highest field value ($E = 6.06 \times 10^5$ V/m), inertia apparently plays a role in the

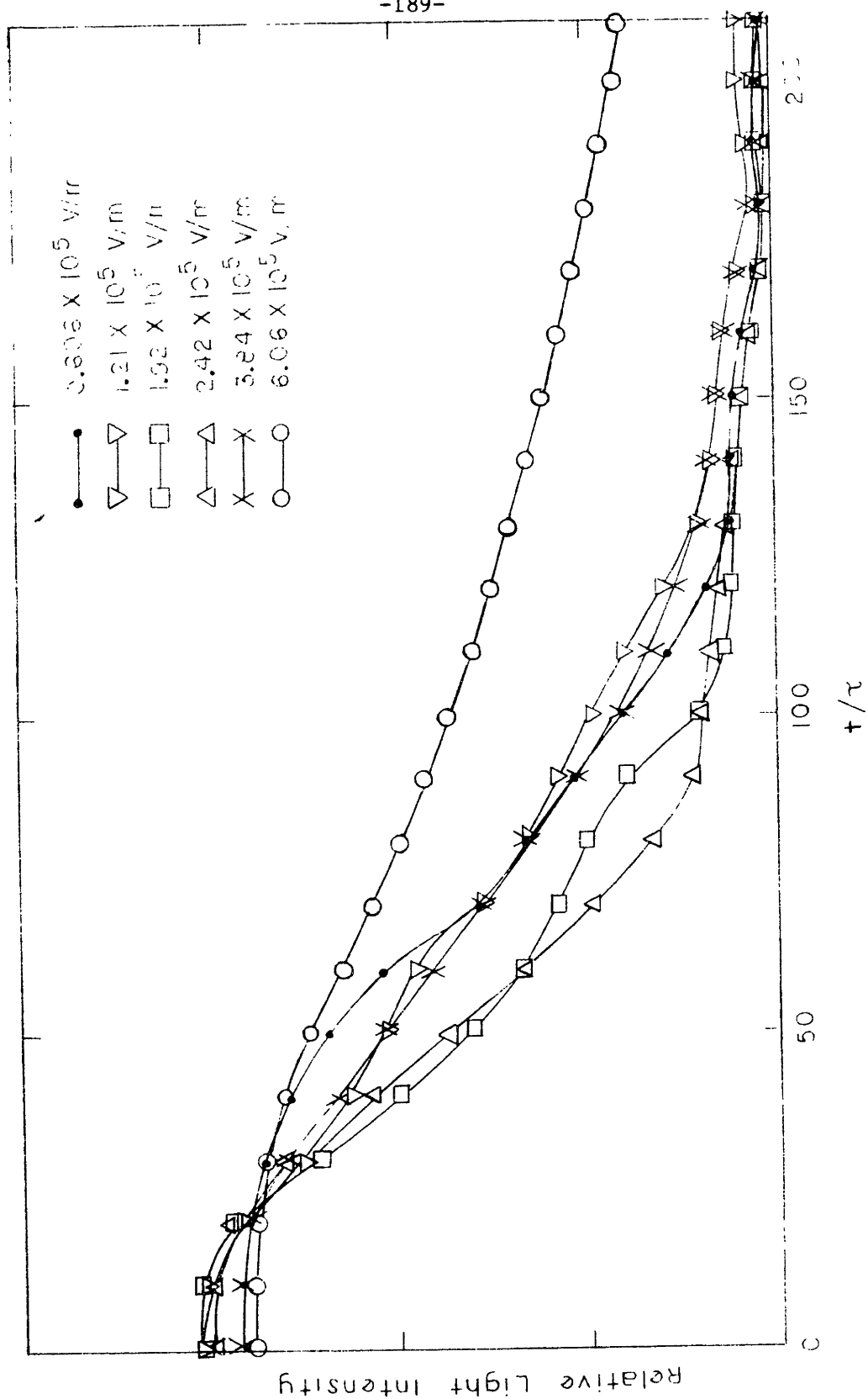


Figure 5. Relative light intensity through experimental cell versus time for various values of electric field

electrohydrodynamic process, with growth occurring less rapidly than would be predicted on the basis of a purely viscous flow.

Further quantitative data are obtained in a second photocell experiment, this time allowing a determination of fluid distribution over the vertical length of the cell. The vertical position of the photocell slit may be varied over a range of 2 cm. on either side of the initial fluid interface. An electrical signal corresponding to cell position drives one scale of an x-y plotter, with light intensity signal driving the second scale. Thus, by running the photocell over the mixing cell length, a curve describing fluid component distribution is obtained. The 1/20 mixture is used for the dark fluid because, for dilutions of 1/20 and less, light intensity through the cell is directly proportional to percentage of clear corn oil in the mixture.

Because the flows involved are viscous-dominated, it is possible to apply an electric field for a given time, switch off the field, take a photocell distribution run, and switch the field back on to continue the experiment. (There is no concern here with lengths small enough for diffusional processes to alter the distribution during the time the field is off.) The fineness with which the distribution may be determined is limited by the photocell slit width (1.6 mm).

Figures 6 through 12 show evolutions of fluid component distributions for values of electric field varying by a factor of 10. In each case, distributions are determined at three times in addition to the initial clean interface distribution. The times at which plots are made are chosen so as to have t/τ take on the same three values in each case.

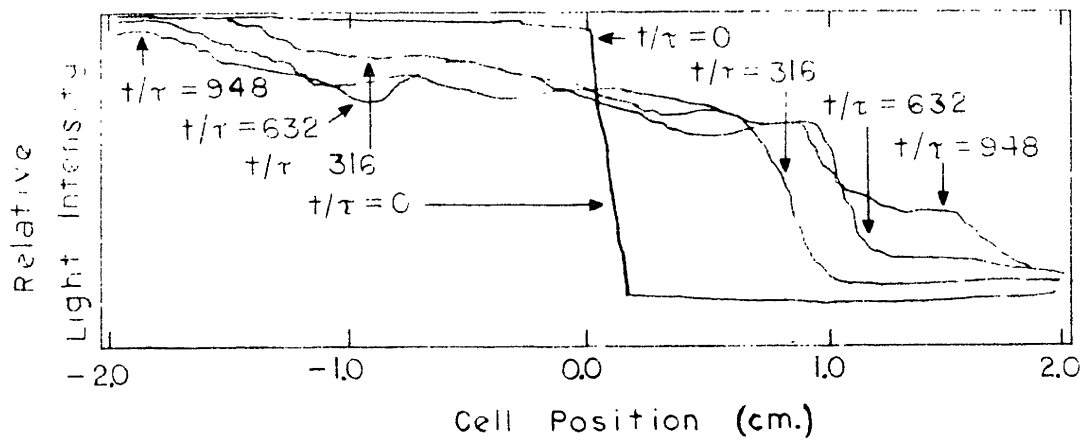


Figure 6. Relative light intensity through experimental cell versus cell position, $E = 0.606 \times 10^5$ V/m

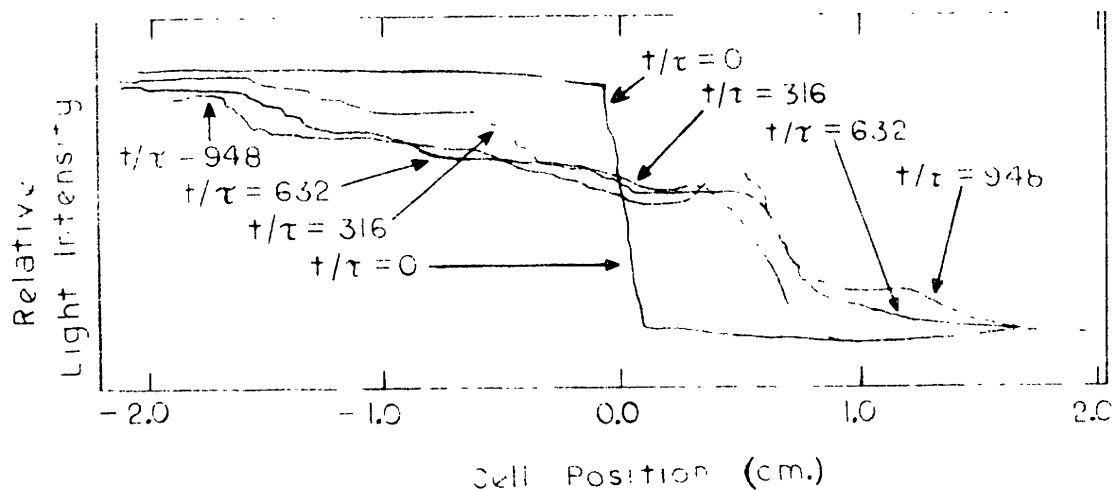


Figure 7. Relative light intensity through experimental cell versus cell position, $E = 1.21 \times 10^5$ V/m

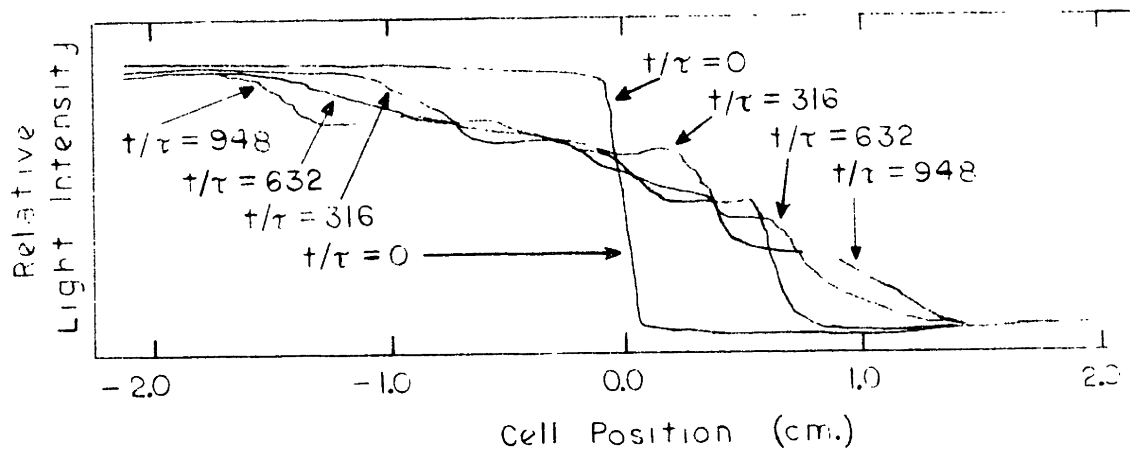


Figure 8. Relative light intensity through experimental cell versus cell position, $E = 1.82 \times 10^5$ V/m

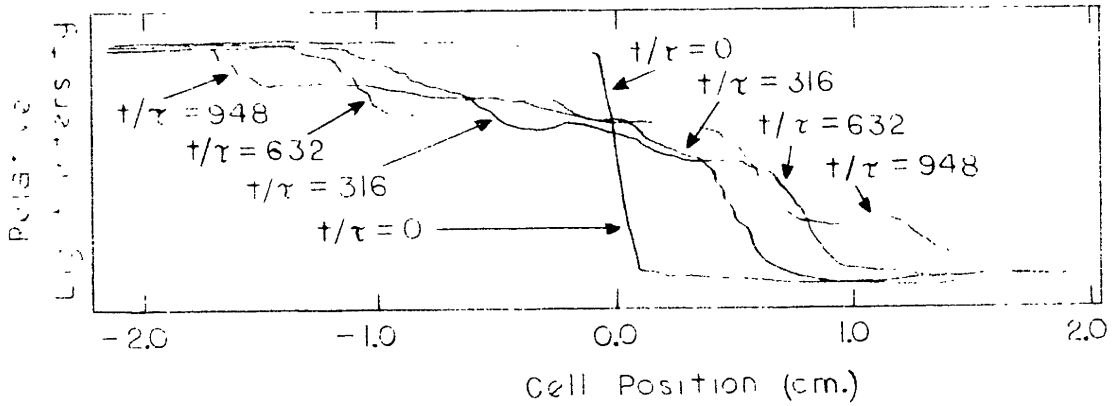


Figure 9. Relative light intensity through experimental cell versus cell position, $E = 2.42 \times 10^5$ V/m

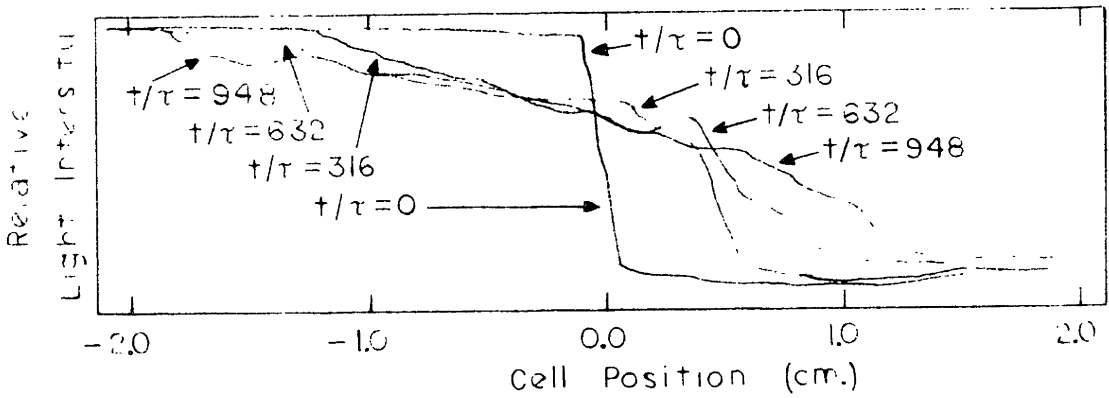


Figure 10. Relative light intensity through experimental cell versus cell position, $E = 3.03 \times 10^5$ V/m

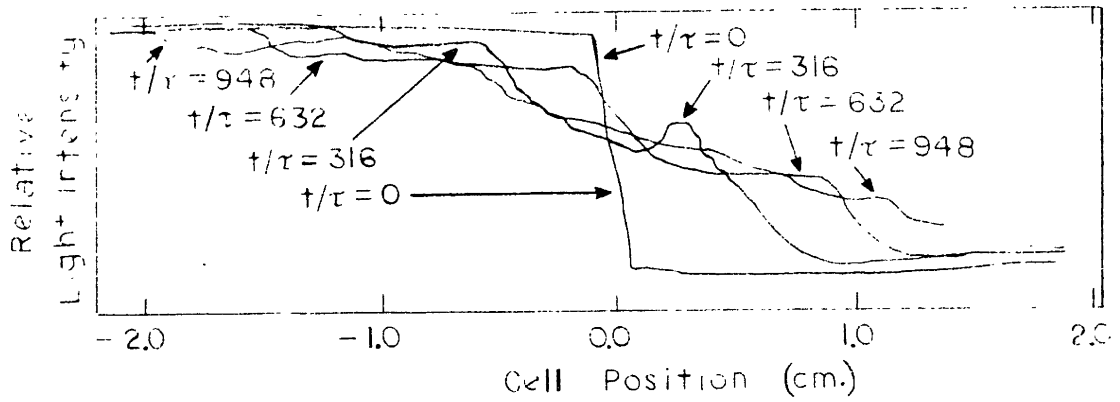


Figure 11. Relative light intensity through experimental cell versus cell position, $E = 4.24 \times 10^5$ V/m

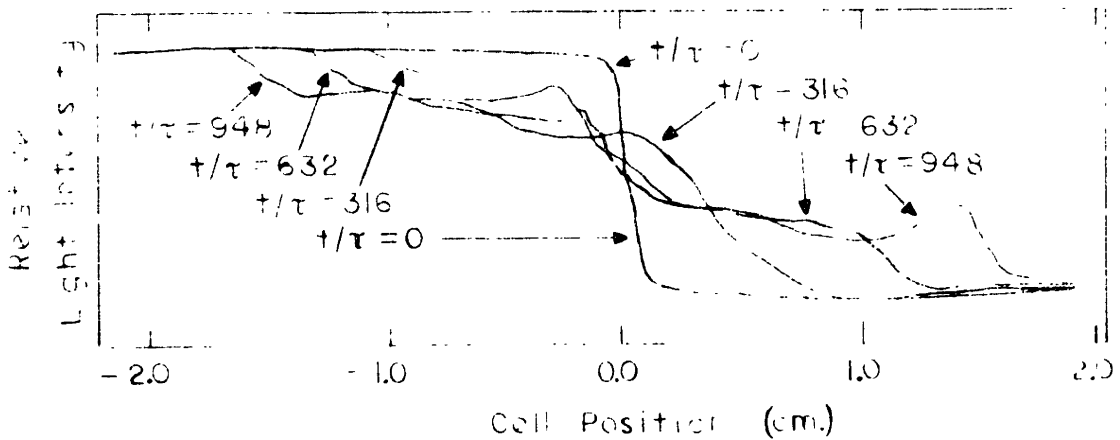


Figure 12. Relative light intensity through experimental cell versus cell position, $E = 6.06 \times 10^5$ V/m

Thus, the lowest field run spans a time period 100 times as long as the highest field run.

Again, strong experimental evidence of scaling of the mixing process with τ is provided by the similarities of evolutions for various values of electric field. At the highest field value, some details of the plots have a somewhat altered character, possibly the result of inertial effects beginning to have a noticeable influence on the motions.

CHAPTER VI. BIBLIOGRAPHY

1. Turnbull, R. J., "Electroconvective Instability with a Stabilizing Temperature Gradient. II. Experimental Results", Phys. Fluids, 11, pp. 2597-2603.
2. Turnbull, R. J., "Electroconvective Instability with a Stabilizing Temperature Gradient. I. Theory", Phys. Fluids, 11, pp. 2588-2596.
3. Uhl, V. W., and Gray, J. B., Mixing Theory and Practice, Volume I, Academic Press, 1966, Chapter I.

APPENDIX A. SOLUTION OF THE QUARTIC EQUATION (3.38)

A general quartic solution⁽¹⁾ is used to determine the four roots of Eq. (3.38) for any given value of the parameter e:

Given a quartic of the form

$$aq^4 + bq^3 + cq^2 + dq + e = 0 \quad (\text{A.1})$$

compute:

$$P \equiv -\frac{3b^2}{8a^2} + \frac{c}{a} \quad (\text{A.2})$$

$$Q \equiv \frac{b^3}{8a^3} - \frac{bc}{2a^2} + \frac{d}{a} \quad (\text{A.3})$$

and
$$R \equiv -\frac{3b^4}{256a^4} + \frac{b^2c}{16a^3} - \frac{bd}{4a^2} + \frac{e}{a} \quad (\text{A.4})$$

For the particular form Eq. (3.38):

$$P = -\frac{11}{8}, \quad Q = -\frac{3}{8}, \quad \text{and } R = \frac{45}{256} + e \quad (\text{A.5})$$

The "reducing cubic" has the form

$$z^3 + \frac{P}{2} z^2 + \left(\frac{P^2}{16} - \frac{R}{4}\right)z - \frac{Q^2}{64} = 0 \quad (\text{A.6})$$

or, for Eq. (3.38):

$$z^3 - \frac{11}{16} z^2 + \left(\frac{19}{256} - \frac{e}{4}\right)z - \frac{9}{4096} = 0 \quad (\text{A.7})$$

A general cubic solution⁽²⁾ is used to determine the three roots of Eq. (A.7). Given a cubic of the form

$$z^3 + P'z^2 + Q'z + R' = 0 \quad (\text{A.8})$$

compute:

$$a' \equiv \frac{1}{9}(3Q' - [P']^2) \quad (\text{A.9})$$

and

$$b' \equiv \frac{1}{54}(2[P']^3 - 9P'Q' + 27R') \quad . \quad (\text{A.10})$$

For Eq. (7):

$$a' = -\frac{1}{36}(1 + 3e), \quad \text{and } b' = -\frac{1}{216}\left(1 + \frac{99}{16}e\right) \quad . \quad (\text{A.11})$$

Next, compute:

$$D \equiv (b')^2 + (a')^3 \quad . \quad (\text{A.12})$$

For Eq. (7):

$$D = -\frac{e}{1728}(e - c_+)(e + c_-) \quad (\text{A.13})$$

where

$$c_+ \equiv \frac{51\sqrt{17} + 107}{512} \approx 0.61968 \quad (\text{A.14})$$

and

$$c_- \equiv \frac{51\sqrt{17} - 107}{512} \approx 0.20172 \quad . \quad (\text{A.15})$$

The sign of D determines the character of the roots of Eq. (8).

For $D \geq 0$, there are one real and two complex conjugate roots. In this case, compute:

$$A \equiv \sqrt[3]{-b' + \sqrt{D}} \quad (\text{A.16})$$

and

$$B \equiv \sqrt[3]{-b' - \sqrt{D}} \quad . \quad (\text{A.17})$$

The three roots of Eq. (8) are then given by

$$Z_1 = -\frac{P'}{3} + A + B \quad (\text{A.18})$$

$$Z_2 = -\frac{P'}{3} - \frac{A+B}{2} + j \frac{A-B}{2} \sqrt{3} \quad (\text{A.19})$$

$$Z_3 = -\frac{P'}{3} - \frac{A+B}{2} - j \frac{A-B}{2} \sqrt{3} \quad (\text{A.20})$$

For the case of Eq. (7), $D \geq 0$ occurs in the regions

$$e \leq -c_- \quad \text{and} \quad 0 \leq e \leq c_+ \quad (\text{A.21})$$

and we have

$$A = \frac{1}{6} \left[\left(1 + \frac{99}{16} e \right) + 9 \left\{ \frac{e}{3} (c_+ - e)(c_- + e) \right\}^{1/2} \right]^{1/3} \quad (\text{A.22})$$

$$B = \frac{1}{6} \left[\left(1 + \frac{99}{16} e \right) - 9 \left\{ \frac{e}{3} (c_+ - e)(c_- + e) \right\}^{1/2} \right]^{1/3} \quad (\text{A.23})$$

For $D < 0$, there are three real and unequal roots. In this case, compute:

$$\phi = \arccos \left[\frac{-b'}{\sqrt{-(a')^3}} \right] \quad (\text{A.24})$$

The three roots of Eq. (8) are then given by

$$Z_1 = -\frac{P'}{3} + 2\sqrt{-a'} \cos \frac{\phi}{3} \quad (\text{A.25})$$

$$Z_2 = -\frac{P'}{3} + 2\sqrt{-a'} \cos \left(\frac{\phi}{3} + \frac{2\pi}{3} \right) \quad (\text{A.26})$$

$$Z_3 = -\frac{P'}{3} + 2\sqrt{-a'} \cos \left(\frac{\phi}{3} - \frac{2\pi}{3} \right) \quad (\text{A.27})$$

For the case of Eq. (7), $D < 0$ occurs in the regions

$$c_- < e < 0 \quad \text{and} \quad c_+ < e \quad (\text{A.28})$$

and we have

$$2 \sqrt{-a'} = \frac{1}{3} \sqrt{1 + 3e} \quad (\text{A.29})$$

$$\phi = \arccos \frac{1 + \frac{99}{16} e}{(1 + 3e)^{3/2}} \quad (\text{A.30})$$

In either case, ($D \geq 0$ or $D < 0$), we have

$$-\frac{P'}{3} = \frac{11}{48} \quad (\text{A.31})$$

Now, returning to the solution of the quartic, (1), and in particular Eq. (3.38):

Determine the square roots of the roots of the reducing cubic, with signs chosen such that:

$$\sqrt{Z_1} \sqrt{Z_2} \sqrt{Z_3} = -\frac{Q}{8} \quad (\text{A.32})$$

For Eq. (3.38) we require

$$\sqrt{Z_1} \sqrt{Z_2} \sqrt{Z_3} = \frac{3}{64} \quad (\text{A.33})$$

Finally, the four roots of Eq. (1) are given by

$$q_1 = \sqrt{Z_1} + \sqrt{Z_2} + \sqrt{Z_3} - \frac{b}{4a} \quad (\text{A.34})$$

$$q_2 = \sqrt{Z_1} - \sqrt{Z_2} - \sqrt{Z_3} - \frac{b}{4a} \quad (\text{A.35})$$

$$q_3 = -\sqrt{Z_1} + \sqrt{Z_2} - \sqrt{Z_3} - \frac{b}{4a} \quad (\text{A.36})$$

$$q_4 = -\sqrt{Z_1} - \sqrt{Z_2} + \sqrt{Z_3} - \frac{b}{4a} \quad (\text{A.37})$$

For Eq. (3.38) we have:

$$-\frac{b}{4a} = -\frac{1}{4} \quad (\text{A.38})$$

APPENDIX A BIBLIOGRAPHY

1. Rektorys, Karel, Editor, Survey of Applicable Mathematics, M.I.T. Press, Cambridge, Mass., 1969, pp. 79-80.
2. Weast, Robert C., Editor-in-Chief, C.R.C. Standard Mathematical Tables, Chemical Rubber Publishing Company, Cleveland, Ohio, 1959, pp. 358-359.

APPENDIX B. MATRIX MANIPULATIONS FOR CHANGING TRANSFER RELATION FORMS

Knowing the elements of [L], the (6 × 6) matrix defined by Eq. (5.57), the elements of [T], the (6 × 6) matrix defined by Eq. (5.58) may be computed according to the following program:

Compute the quantities:

$$\Lambda_{21}, \Lambda_{22}, \Lambda_{23}, \Lambda_{25}, \Lambda_{26}$$

$$\Lambda_{31}, \Lambda_{32}, \Lambda_{33}, \Lambda_{35}, \Lambda_{36}$$

$$\Omega_{21}, \Omega_{22}, \Omega_{23}, \Omega_{24}, \Omega_{26}$$

$$\Omega_{31}, \Omega_{32}, \Omega_{33}, \Omega_{34}, \Omega_{36}$$

$$\text{where } \Lambda_{ab} \equiv L_{14} L_{ab} - L_{a4} L_{1b} \quad (\text{B.1})$$

$$\text{and } \Omega_{ab} \equiv L_{15} L_{ab} - L_{a5} L_{1b} \quad (\text{B.2})$$

$$\text{Then, compute } D_{\Lambda} \equiv \Lambda_{35} \Lambda_{26} - \Lambda_{36} \Lambda_{25} \quad (\text{B.3})$$

$$\text{and } D_{\Omega} \equiv \Omega_{24} \Omega_{36} - \Omega_{34} \Omega_{26} \quad (\text{B.4})$$

Finally, the elements of [T] are given by:

$$T_{21} = (\Omega_{26} L_{35} - \Omega_{36} L_{25}) / D_{\Omega} \quad (\text{B.5})$$

$$T_{22} = (\Omega_{26} \Omega_{31} - \Omega_{36} \Omega_{21}) / D_{\Omega} \quad (\text{B.6})$$

$$T_{23} = \Omega_{36} L_{15} / D_{\Omega} \quad (\text{B.7})$$

$$T_{24} = (\Omega_{26} \Omega_{32} - \Omega_{36} \Omega_{22}) / D_{\Omega} \quad (\text{B.8})$$

$$T_{25} = -\Omega_{26} L_{15} / D_{\Omega} \quad (\text{B.9})$$

$$T_{26} = (\Omega_{26} \Omega_{33} - \Omega_{36} \Omega_{23}) / D_{\Omega} \quad (\text{B.10})$$

$$T_{41} = (\Lambda_{36} L_{24} - \Lambda_{26} L_{34}) / D_{\Lambda} \quad (\text{B.11})$$

$$T_{42} = (\Lambda_{21} \Lambda_{36} - \Lambda_{26} \Lambda_{31}) / D_{\Lambda} \quad (\text{B.12})$$

$$T_{43} = -\Lambda_{36} L_{14} / D_{\Lambda} \quad (\text{B.13})$$

$$T_{44} = (\Lambda_{22} \Lambda_{36} - \Lambda_{26} \Lambda_{32}) / D_{\Lambda} \quad (\text{B.14})$$

$$T_{45} = \Lambda_{26} L_{14} / D_{\Lambda} \quad (\text{B.15})$$

$$T_{46} = (\Lambda_{23} \Lambda_{36} - \Lambda_{26} \Lambda_{33}) / D_{\Lambda} \quad (\text{B.16})$$

$$T_{61} = (\Lambda_{25} L_{34} - \Lambda_{35} L_{24}) / D_{\Lambda} \quad (\text{B.17})$$

$$T_{62} = (\Lambda_{25} \Lambda_{31} - \Lambda_{35} \Lambda_{21}) / D_{\Lambda} \quad (\text{B.18})$$

$$T_{63} = \Lambda_{35} L_{14} / D_{\Lambda} \quad (\text{B.19})$$

$$T_{64} = (\Lambda_{25} \Lambda_{32} - \Lambda_{35} \Lambda_{22}) / D_{\Lambda} \quad (\text{B.20})$$

$$T_{65} = -\Lambda_{25} L_{14} / D_{\Lambda} \quad (\text{B.21})$$

$$T_{66} = (\Lambda_{25} \Lambda_{33} - \Lambda_{35} \Lambda_{23}) / D_{\Lambda} \quad (\text{B.22})$$

$$T_{11} = L_{44} T_{21} + L_{45} T_{41} + L_{46} T_{61} \quad (\text{B.23})$$

$$T_{12} = L_{41} + L_{44} T_{22} + L_{45} T_{42} + L_{46} T_{62} \quad (\text{B.24})$$

$$T_{13} = L_{44} T_{23} + L_{45} T_{43} + L_{46} T_{63} \quad (\text{B.25})$$

$$T_{14} = L_{42} + L_{44} T_{24} + L_{45} T_{44} + L_{46} T_{64} \quad (\text{B.26})$$

$$T_{15} = L_{44} T_{25} + L_{45} T_{45} + L_{46} T_{65} \quad (\text{B.27})$$

$$T_{16} = L_{43} + L_{44} T_{26} + L_{45} T_{46} + L_{46} T_{66} \quad (\text{B.28})$$

$$T_{31} = L_{54} T_{21} + L_{55} T_{41} + L_{56} T_{61} \quad (\text{B.29})$$

$$T_{32} = L_{51} + L_{54} T_{22} + L_{55} T_{42} + L_{56} T_{62} \quad (\text{B.30})$$

$$T_{33} = L_{54} T_{23} + L_{55} T_{43} + L_{56} T_{63} \quad (\text{B.31})$$

$$T_{34} = L_{52} + L_{54} T_{24} + L_{55} T_{44} + L_{56} T_{64} \quad (\text{B.32})$$

$$T_{35} = L_{54} T_{25} + L_{55} T_{45} + L_{56} T_{65} \quad (\text{B.33})$$

$$T_{36} = L_{53} + L_{54} T_{26} + L_{55} T_{46} + L_{56} T_{66} \quad (\text{B.34})$$

$$T_{51} = L_{64} T_{21} + L_{65} T_{41} + L_{66} T_{61} \quad (\text{B.35})$$

$$T_{52} = L_{61} + L_{64} T_{22} + L_{65} T_{42} + L_{66} T_{62} \quad (\text{B.36})$$

$$T_{53} = L_{64} T_{23} + L_{65} T_{43} + L_{66} T_{63} \quad (\text{B.37})$$

$$T_{54} = L_{62} + L_{64} T_{24} + L_{65} T_{44} + L_{66} T_{64} \quad (\text{B.38})$$

$$T_{55} = L_{64} T_{25} + L_{65} T_{45} + L_{66} T_{65} \quad (\text{B.39})$$

$$T_{56} = L_{63} + L_{64} T_{26} + L_{65} T_{46} + L_{66} T_{66} \quad (\text{B.40})$$

BIOGRAPHICAL NOTE

The author was born in Pittsburgh, Pennsylvania, on December 30, 1946. He graduated from Hampton Township High School in Allison Park, Pennsylvania, in 1964, and began his undergraduate education in Electrical Engineering at Drexel University.

While at Drexel, he received the Scott Paper Foundation Award for Leadership in 1966 and the Junior Electrical Engineering Award in 1968, was elected to Tau Beta Pi and Eta Kappa Nu, and was Vice President and Secretary of Delta Sigma Phi fraternity. He did research on application of the method of characteristics at the Wave Propagation Research Center.

Graduating with a B.S. in Electrical Engineering in 1969, he was awarded a National Science Foundation Fellowship, and began his graduate education at Massachusetts Institute of Technology. He received his S.M. and E.E. degrees in 1971, with Master's thesis entitled "Modes of Behavior of Water on High Voltage Transmission Lines". He received the Carlton E. Tucker Award for Excellence in Teaching in 1972, was elected to Sigma Xi, and was Appointed an Instructor in 1973.

His interests include electromagnetic field theory, discrete electro-mechanical systems, and continuum electromechanics.